Transparent conductive oxides for perovskite/silicon tandem solar cells by sputter deposition - model-based characterization of sputter damage, material development and device implementation

vorgelegt von

M. Sc.

Marlene Sophie Härtel

ORCID: 0000-0002-1251-9745

an der Fakultät IV – Elektrotechnik und Informatik
der Technischen Universität Berlin
zur Erlangung des akademischen Grades

Doktorin der Ingenieurwissenschaften
– Dr.-Ing. –

genehmigte Dissertation

Promotionsausschuss:

Vorsitzender:	Prof. Dr. Bernd Rech
Gutachter:	Prof. Dr. Bernd Szyszka
Gutachter:	Prof. Dr. Steve Albrecht
Gutachterin:	Prof. Dr. Monica Morales-Masis

Tag der wissenschaftlichen Aussprache: 16. Dezember 2022

Berlin 2023

Abstract

Multi-junction solar cells can enable efficiencies beyond the state-of-the-art single junction efficiency limits. Two or more sub-cells make up a multi-junction. Perovskite solar cells, for example, can easily be combined with conventional silicon-based solar cell technologies in monolithically integrated tandem devices. Furthermore, perovskite solar cells offer tremendous potential due to their low material and production costs. The scope of the thesis is the optimization of the transparent front-electrode in perovskite/silicon tandem solar cells and the investigation and reduction of damage during the sputter deposition of the transparent electrode onto the perovskite (sub-)cell. Tin oxide (SnO_2) buffer layers made by thermal atomic layer deposition (ALD) are typically used to shield the perovskite solar cells' sensitive layers from sputter damage. However, this method causes parasitic absorption. We present techniques for sputter damage mitigation that eliminate the need for a SnO_2 buffer layer. Thereby we offer pathways for boosting the tandem device's efficiency further while also simplifying their processing.

Several strategies to reduce sputter damage based on established considerations presented in the literature were tested - a low power process, a high-pressure process, and an indirect process. These strategies are in contrast to our standard sputter process, which was initially developed without taking sputter damage into account, concentrating only on the thin film quality. Indium zinc oxide (IZO) served as transparent front-electrode material. Prior to the integration into solar cell devices, we varied the oxygen flow ratio during the sputter processes of the standard process and the various low-damage deposition strategies to optimize the optoelectrical properties of the IZO films. The optimization focused on a good agreement between low parasitic absorption and high electrical conductivity with regard to the application in tandem devices.
The low-damage IZO deposition techniques were subsequently tested on semitransparent single-junction perovskite solar cells and compared to the standard IZO deposition. The protective SnO_2-buffer layer was thus removed in order to study how effectively the low-damage techniques reduce sputter damage. One of the studied low-damage techniques, the low power process, exhibited a statistically higher open circuit voltage (V_{OC}) of ~13 mV and a statistically higher fill factor (FF) of ~3 %, compared to the standard IZO deposition process. We then performed light intensity-dependent current density-voltage (J-V) measurements to reveal the correlation between sputter damage and recombination losses.

Furthermore, the interactions between different solar cell surface materials and the

growing thin film were investigated. The aim was to analyze how the electron transport layer (ETL)/transparent conductive oxide (TCO) interface dynamics and the growth of the TCO are influenced by the choice of the substrate layer on which the TCO is deposited. Therefore, we studied semitransparent perovskite solar cell devices with a low-damage IZO front-electrode deposited on different ETL designs - precisely a C_{60}-only ETL and C_{60}/SnO_2 and C_{60}/PEIE (polyethyleneimine ethoxylated) double layer ETLs. Three key conclusions were drawn from the J-V analysis: 1. when IZO is deposited directly on C_{60}, the resulting J-V curve forms an s-shape; 2. the s-shape formation can be prevented by interlayers, such as SnO_2 or PEIE; 3. the interlayer PEIE leads to an even better performance than the SnO_2 interlayer. The findings were further studied via light intensity-dependent J-V measurements, transient opto-electrical measurements in the all-in-one *Paios* tool, contact angle analysis, and in-situ grazing incidence small angle x-ray diffraction scattering (GISAXS) measurements during the sputter deposition, monitoring the initial growth behavior of IZO on the various ETL-designs. We found no correlation between the electrical performance and the initial IZO thin film growth.
Based on electrical simulations with the SCAPS-1D program, we deduced that the s-shape behavior in C_{60}-only ETL devices results from a potential barrier between the electrode and the ETL. We also found that interfacial non-radiative recombination is not necessarily reflected in the ideality factor. In contrast, interlayers, such as SnO_2 or PEIE, seem to improve charge extraction.

Lastly, we transferred our findings into monolithic perovskite/silicon tandem devices. Our goal was to reduce optical losses in tandem devices by removing the protective buffer layer and instead circumvent sputter damage by applying a low-damage IZO deposition process, thereby pushing the overall efficiency and reducing the thermal load. Additionally, this makes the fabrication less time-intense, cheaper, and less complex. Firstly, we performed optical simulations with the MATLAB-based tool GenPro4 of tandem devices with and without a SnO_2-buffer layer to study the optical gain. We observed an overall potential current density gain of 0.6 mA/cm^2 for the sum of both sub-cell currents by removing the SnO_2-buffer layer in the simulation.
In the next step, we built monolithic two-terminal tandem devices with a C_{60}/SnO_2 and a C_{60}/PEIE double layer ETL and applied a low-damage IZO deposition process. The superior optics, originating from replacing 20 nm SnO_2 with the ultra-thin ~2 nm PEIE, led to a PCE improvement from 27.4 % to 28.4 % in the tandem devices. The current density loss analysis based on EQE and reflection measurements revealed a gain of 0.58 mA/cm^2 for the sum of the respective sub-cell currents originating from reduced reflec-

tion and reduced parasitic absorption. Eventually, we performed long-term stability tests on both tandem device designs to study how the stability of the devices is affected by omitting SnO_2.

This work highlights difficulties and offers suitable approaches and implications for depositing the transparent front electrode in ALD SnO2-buffer layer-free perovskite/silicon tandem systems by industry-relevant means. Additionally, we show the possibility of enhancing the efficiency of tandem solar cells. The results are significant for the development of perovskite/silicon tandem solar cells and will boost the growth of the photovoltaics industry.

Zusammenfassung

Mehrfachsolarzellen weisen Wirkungsgrade auf, die über die Grenzen des Wirkungsgrads von Einzelzellen hinausgehen. Eine Mehrfachsolarzelle besteht aus zwei oder mehr Teilzellen. Perowskit-Solarzellen lassen sich beispielsweise problemlos mit herkömmlichen Silizium-basierten Solarzellentechnologien in monolithisch integrierten Tandemsolarzellen kombinieren. Darüber hinaus bieten Perowskit-Solarzellen aufgrund ihrer geringen Material- und Produktionskosten ein enormes Potenzial. Gegenstand der Arbeit ist die Optimierung der transparenten Frontelektrode in Perowskit/Silizium-Tandemsolarzellen und die Untersuchung und Reduzierung der Schädigung während der Sputterabscheidung der transparenten Elektrode auf der Perowskit-(Sub-)Zelle. Zinnoxid (SnO_2) Pufferschichten, die durch thermische Atomlagenabscheidung (ALD) hergestellt werden, werden üblicherweise verwendet, um die empfindlichen Schichten der Perowskit-Solarzellen vor Sputterschäden zu schützen. Diese Methode führt jedoch zu parasitärer Absorption. Wir stellen Techniken zur Abschwächung von Sputterschäden vor, die die Notwendigkeit einer SnO_2-Pufferschicht überflüssig machen. Dadurch bieten wir Möglichkeiten, den Wirkungsgrads der Tandem-Bauelemente weiter zu steigern und gleichzeitig ihre Verarbeitung zu vereinfachen.

Es wurden mehrere Strategien zur Verringerung von Sputterschäden getestet, die auf in der Literatur dargelegten Überlegungen beruhen: ein Verfahren mit geringerer Leistung, ein Hochdruckverfahren und ein indirektes Verfahren. Diese Strategien stehen unserem Standard-Sputterprozess gegenüber, der ursprünglich ohne Berücksichtigung von Sputterschäden entwickelt wurde und sich nur auf die Qualität der gesputterten Dünnschicht konzentrierte. Indiumzinkoxid (IZO) diente als transparentes Frontelektrodenmaterial. Vor der Integration in Bauelemente variierten wir das Sauerstoffflussverhältnis während des Standardprozesses und der verschiedenen schadensarmen Sputterprozesse, um die optoelektrischen Eigenschaften der IZO-Schichten zu optimieren. Die Optimierung konzentrierte sich auf eine gute Übereinstimmung zwischen geringer parasitärer Absorption und hoher elektrischer Leitfähigkeit im Hinblick auf die Anwendung in Tandembauelementen.
Die beschädigungsarmen IZO-Abscheidungstechniken wurden anschließend an halbtransparenten Perowskit-Einzelsolarzellen getestet und mit der Standard-IZO-Abscheidung verglichen. Die schützende SnO_2-Pufferschicht wurde dabei entfernt, um zu untersuchen, wie effektiv die schadensarmen Techniken Sputterschäden reduzieren. Eine der untersuchten schädigungsarmen Techniken, der so genannte „Low-Power“-Prozess, wies eine statistisch höhere Leerlaufspannung (V_{OC}) von ~13 mV und einen statistisch höheren Füllfaktor

(FF) von ~3 % auf, verglichen mit dem Standard-IZO-Abscheidungsprozess. Anschließend führten wir beleuchtungsintensitätsabhängige Stromdichte-Spannungs-Messungen (J-V Messungen) durch, um die Korrelation zwischen Sputterschäden und Rekombinationsverlusten aufzuzeigen.

Im weiteren wurden die Wechselwirkungen zwischen den verschiedenen Oberflächenmaterialien der Solarzellen und der wachsenden Dünnschicht untersucht. Ziel war es, zu analysieren, wie die Dynamik der Grenzfläche zwischen Elektronentransportschicht (ETL) und transparentem leitfähigem Oxid (TCO) und das Wachstum des TCOs durch die Wahl der Substratschicht, auf der das TCO abgeschieden wird, beeinflusst wird. Daher untersuchten wir semitransparente Perowskit-Solarzellen mit einer beschädigungsarmen IZO-Front-Elektrode, die auf verschiedenen ETL-Designs abgeschieden wurde - genauer gesagt auf einem reinen C_{60}-ETL sowie auf C_{60}/SnO_2- und C_{60}/PEIE (Polyethylenimin ethoxyliert) Doppelschicht-ETLs. Drei wichtige Schlussfolgerungen wurden aus der J-V-Analyse gezogen: 1. wenn IZO direkt auf C_{60} abgeschieden wird, bildet die resultierende J-V-Kurve eine s-Form; 2. die s-Form-Bildung kann durch Zwischenschichten, wie SnO_2 oder PEIE, verhindert werden; 3. die Zwischenschicht PEIE führt zu einer noch besseren Leistung als die SnO_2-Zwischenschicht. Die Ergebnisse wurden durch beleuchtungsintensitätsabhängige J-V-Messungen, transiente opto-elektrische Messungen mit dem All-in-One-Tool *Paios*, Kontaktwinkelanalysen und In-situ-Röntgenkleinwinkelstreuungsmessungen (GISAXS-Messungen) während der Sputterabscheidung weiter untersucht. In-situ-GISAXS-Messungen untersuchen hierbei das anfängliche Wachstumsverhalten von IZO auf den verschiedenen ETL-Designs. Wir fanden keine Korrelation zwischen der elektrischen Leistung und dem anfänglichen IZO-Dünnschichtwachstum.
Auf der Grundlage elektrischer Simulationen mit dem SCAPS-1D-Programm haben wir abgeleitet, dass das s-förmige Verhalten in reinen C_{60}-ETL-Bauelementen auf eine Potenzialbarriere zwischen der Elektrode und dem ETL zurückzuführen ist. Wir fanden auch heraus, dass sich die nicht-strahlende Rekombination an der Grenzfläche nicht unbedingt im Idealitätsfaktor widerspiegelt. Im Gegensatz dazu scheinen Zwischenschichten wie SnO_2 oder PEIE die Ladungsextraktion zu verbessern.

Schließlich übertrugen wir unsere Erkenntnisse auf monolithische Perowskit/Silizium-Tandembauelemente. Unser Ziel war es, die optischen Verluste in Tandem-Bauelementen zu reduzieren, indem wir die schützende Pufferschicht entfernten und stattdessen die Sputter-Beschädigung durch einen schadensarmen IZO-Abscheidungsprozess umgingen, wodurch

die Gesamteffizienz gesteigert und die thermische Belastung verringert wurde. Außerdem ist die Herstellung dadurch weniger zeitaufwändig, billiger und weniger komplex. Zunächst führten wir mit dem MATLAB-basierten Tool GenPro4 optische Simulationen von Tandembauelementen mit und ohne SnO_2-Pufferschicht durch, um den optischen Gewinn zu untersuchen. Wir beobachteten einen Gesamtgewinn an potenzieller Stromdichte von 0,6 mA/cm^2 für die Summe der Ströme beider Teilzellen, wenn die SnO_2-Pufferschicht in der Simulation entfernt wurde.
Im nächsten Schritt bauten wir monolithische, zweipolige Tandem-Bauelemente mit einem C_{60}/SnO_2- und einem C_{60}/PEIE-Doppel-ETL und wendeten einen beschädigungsarmen IZO-Abscheidungsprozess an. Die überlegene Optik, die aus dem Ersetzen der 20 nm SnO_2-Schicht durch das ultradünne ~2 nm PEIE resultiert, führte zu einer PCE-Verbesserung von 27,4 % auf 28,4 % in den Tandembauteilen. Die Analyse der Stromverluste auf der Grundlage von EQE- und Reflexionsmessungen ergab einen Gewinn von 0,58 mA/cm^2 für die Summe der jeweiligen Teilzellenströme, der auf die verringerte Reflexion und die reduzierte parasitäre Absorption zurückzuführen ist. Schließlich haben wir Langzeitstabilitätstests an beiden Tandem-Bauelementen durchgeführt, um zu untersuchen, wie die Stabilität der Bauelemente durch das Weglassen von SnO_2 beeinflusst wird.

Diese Arbeit zeigt die Schwierigkeiten auf und bietet geeignete Ansätze und Implikationen für die Abscheidung der transparenten Frontelektrode in ALD SnO_2-Pufferschicht-freien Perowskit/Silizium-Tandemsystemen mit industrierelevanten Mitteln. Darüber hinaus zeigen wir eine Möglichkeit auf, den Wirkungsgrad von Tandemsolarzellen zu erhöhen. Die Ergebnisse sind bedeutsam für die Entwicklung von Perowskit/Silizium-Tandemsolarzellen und werden das Wachstum der Photovoltaik-Industrie fördern.

Contents

Chapter 1

Introduction

In recent months, we have experienced how our daily lives are affected by our dependence on political interests. We are all affected by rising energy prices. The steep price development in the most recent time is primarily a reflection of import prices. Between July 2021 and July 2022, the cost of importing natural gas into Germany more than tripled, and electricity even quadrupled [1]. It is therefore of great interest to explore technologies that will allow us to be more independent of transnational conflicts. On top of that, the demand for energy continues to rise as the world's population grows. It is therefore becoming increasingly important to research alternative and renewable energy sources. Germany's gross final energy consumption is increasingly covered by renewable resources. The German government aimed to raise the percentage to 18% by 2020 and 30% by 2030 [2]. With a share of 19.3%, the target value of 18% was exceeded in 2020 [2]. The sun offers great potential for energy delivery by utilizing photovoltaic technologies. Among various photovoltaic materials, perovskite-based solar cells are the most fascinating recent technological innovations. Particularly, monolithic perovskite/silicon tandem solar cells have drawn a lot of attention from the scientific and industrial community because of their likely lower material and production costs and high efficiency potential compared to other commercially available conventional technologies. Just recently, Researchers from the Swiss Center for Electronics and Microtechnology (CSEM) and the École polytechnique fédérale de Lausanne (EPFL) have shown a certified a new power conversion efficiency (PCE) world record for this technology, of 30.93% for a planar device and 31.25% for a fully textured device [3, 4]. The fundamental efficiency limit for monolithic perovskite/silicon tandem solar cells, with ideal band gaps for both sub-cells, was calculated to be 45.1% [5].
Monolithic perovskite/silicon tandem solar cells' PCE can be further improved by identifying the losses limiting the existing PCE and developing methods to overcome them.

This thesis studies potential strategies to increase the efficiency of such devices. The high efficiencies of existing perovskite/silicon tandem devices are typically accomplished by expensive SnO_2 buffer layers, which require a time-consuming deposition process that uses water and keeps the samples at high temperatures, potentially damaging the perovskite. The primary objectives are to reduce sputter damage to the sensitive layers of SnO_2 buffer layer-free perovskite top cells and parasitic optical absorption losses, focusing on the optoelectrical optimization of the top contact. Indium zinc oxide (IZO) is the transparent front-electrode material fabricated in a radio-frequency magnetron sputter deposition process. The optoelectrical properties of IZO can be tuned by the oxygen content in the film. Through deliberate sputter process management, we have attempted to minimize sputter damage. Furthermore, it is important to get a fundamental understanding of the ETL/TCO interface dynamics. Predicting the nature of an interface between two materials is difficult. Already moderate interface interaction, or the impact of sputter deposition of the IZO might affect the interface formation through damage of the substrate's surface, penetration of IZO atoms, strain between the materials, or chemical reactions.
Therefore, this thesis is divided into three major thematic sections:

1. Optimization and deposition of IZO with focus on sputter damage reduction.
2. Interactions between the substrate and the growing thin film and implications for the interface dynamics.
3. Application of low-damage IZO in monolithic perovskite/silicon tandem solar cells - the optical gains of omitting the SnO_2 buffer layer and the study of the long-term stability.

1.1 Outline of this work

This thesis is organized as follows:

Chapter 2 is dedicated to giving a fundamental overview of the physics of transparent conductive oxides, ceramic cathode sputter deposition, and solar cells. Furthermore, several literature reviews will be given to contextualize certain topics.

Chapter 3 outlines the fabrication procedures of the various samples and solar cells examined in this work. Also included are specifics on the experimental characterization techniques used as well as descriptions of the electrical and optical simulation.

Chapter 4 presents the results of this work. This chapter is divided into three main parts. In the first part, strategies to reduce sputter damage, like increasing the process

pressure, decreasing the sputtering power, and indirect coating are studied. The study focuses on IZO film optimization for each approach and examines the effectiveness of each method in reducing sputter damage.
The second part takes a closer look at the interface formation between ETL and TCO. Here, various ETL designs are examined to see how they affect the electrical performance of the solar cell and the layer growth of the IZO. We also provide an assessment, based on electrical simulations, of how the ETL/TCO interface is influencing the solar cell performance.
Finally, the third part, we discuss the application of our findings in tandem devices. Through optical simulations, we estimate the potential current gain that could result from omitting the SnO_2 buffer, whose primary function is to prevent sputter damage. Then, using a low-damage IZO deposition technique, we substitute the conventional SnO_2 buffer layer for an optically superior, ultra-thin PEIE layer. We evaluate the electrical performance and long-term stability of the resultant tandem devices.

Chapter 5 outlines the conclusions of this thesis and provides an outlook for additional future studies.

Chapter 2

Fundamentals

2.1 Transparent conductive oxides

Transparent conductive oxides (TCO) are widely popular front-electrode materials due to their high transparency and, at the same time, high conductivity. A high optical band gap (E_g > 3 eV) is needed to realize high transparency and low parasitic absorption losses in e.g. absorber layers used for solar cell devices. The most common TCOs are n-type materials, such as In_2O_3:Sn (ITO) or In_2O_3-ZnO (IZO). In this chapter, we will present the fundamental optoelectrical properties of TCOs in general. Then, we will present IZO, as it is the core material of this work. Finally, we will give an overview of emerging trends for transparent electrodes, focusing on high-mobility TCOs as they offer a great prospect for tandem solar cell front-electrode application.

2.1.1 Electrical conductivity

A TCO is a metal oxide which is degenerately doped, either by extrinsic (other elements replacing metal or oxygen lattice sites) or intrinsic (typically oxygen vacancies or interstitials) dopants. In such a degenerated semiconductor, the conductivity, which is determined entirely by free electrons (the charge carriers), is defined by the charge carrier density N_e and the charge carrier mobility μ via the equation:

$$\sigma = \frac{1}{\rho} = N_e \cdot \mu \cdot e \tag{2.1}$$

The conditions under which the equation mentioned above is valid are outlined below.

In n-type TCOs, the high charge carrier density, which can be thought of as a free electron gas, reaches charge carrier densities of $N_e \geq 10^{20}\ cm^{-3}$ and causes the fermi level to be moved into the conduction band. The Mott criteria describes the required charge carrier density $N_{e,deg}$ for degenerately doping, which is given by [6]:

$$N_{e,deg}^{1/3} \cdot r_0^* = 0.25 \tag{2.2}$$

r_0^* is the effective Bohr radius, which is described as [7]:

$$r_0^* = \epsilon_0 \epsilon_x \cdot \frac{h^2}{\pi m_e^* e^2} \tag{2.3}$$

where ϵ_0 is the vacuum permittivity, and ϵ_x is the static dielectric constant of the respective host material, m_e^* is the effective electron mass, which is dependent on the overall composing metal oxides, and locally on interstitial atoms and vacancies, and e is the elementary charge. According to Hamberg *et al.* we can assume for In_2O_3 that $m_e^* \approx 0.35 \cdot m_e$, and $\epsilon_x = 8.9$, together with the electron mass m_e and the vacuum permittivity ϵ_0 this results into $r_0^* \approx 1.3$ nm [8]. This leads to the assumption that the threshold carrier concentration to reach free electron gas properties, and thus degenerately doping, is achieved for $N_e > N_{e,deg} \approx 6 \times 10^{18}\ cm^{-3}$. A degenerately doped metal oxide exhibit electrical properties similar to those of a metal.
The movement of electrons (or, in other words, the free electron gas) through such a material can be described by the Drude model [9]. The movement (to be precise: the carrier mobility) of the electrons is limited by several decelerating scattering events. Scattering centers usually are grain boundaries, ionized impurities, defects, and lattice vibrations [8]. The different scattering events contribute to the overall mobility and can be summed according to the Matthiesen rule. The sum of the mobility components resulting from various scattering events is given by [10]:

$$\frac{1}{\mu_H} = \frac{1}{\mu_1} + \frac{1}{\mu_2} + \frac{1}{\mu_3} + ... + \frac{1}{\mu_n} \tag{2.4}$$

where μ_H is the resulting (Hall) mobility of the charge carrier of a material and μ_1, μ_2, μ_3, ..., μ_n describe the different scattering mechanisms. Below the most important scattering mechanisms are listed:

- Ionized impurity scattering events occur in TCOs that are doped by impurity atoms or oxygen vacancies. For high carrier concentrations (for IZO that is $N_e > 5 \times 10^{20}\ cm^{-3}$), it is the predominating scattering process [11]. The impact of this scattering event on the overall charge carrier mobility of a material can be reduced by reducing the number of impurity atoms or oxygen vacancies, hence charge carrier density.

- Non-doped (-ionized) impurities cause neutral impurity scattering in the crystal lattice [12]. For high carrier concentrations, this scattering process is negligible.
- Phonon scattering, caused by lattice vibrations, becomes especially relevant for lower carrier concentrations [13]. It is temperature-dependent, meaning the impact of this scattering event can be reduced by cooling the material [11].
- Grain boundary scattering is mainly relevant in polycrystalline thin film materials. This scattering process is significant for grain sizes of the polycrystalline thin film within the range of the mean free path of the charge carriers [13]. Grain boundary scattering occurs due to the grain boundaries' space charge region, which acts as a potential barrier, scattering electrons as they move across them.

The electrical conductivity, which is defined according to Equ. 2.1, can be enhanced by increasing the charge carrier density N_e or the charge carrier mobility μ, however for reasons as explained above, these two factors cannot always be increased simultaneously. By increasing the charge carrier density, the charge carrier mobility may be limited and even reduced by ionized impurity scattering events. The charge carrier density also impacts the optical porperties of a TCO, which we will explain in the following section.

2.1.2 Optical properties

Optically, materials are characterized by their refractive index. Generally, the refractive index describes the ratio of the wavelength of electromagnetic waves (light) in vacuum to the wavelength in a medium with a certain optical density. The electric field of a location-dependent sinusoidal electromagnetic wave is described as:

$$E(x) = E_0 \cdot e^{ik \cdot x} \tag{2.5}$$

At the interface of two media with different refractive indices, light is refracted and reflected. For non-magnetic media, assuming a perpendicular angle of incidence and in disregard of any absorption of light by either medium, a simplified qualitative description of the reflection is given by the Fresnel equations:

$$R = \left| \frac{E_r}{E_i} \right|^2 = \left| \frac{n_1 - n_2}{n_1 + n_2} \right|^2 \tag{2.6}$$

where E_i is the incident, and E_r the reflected electric field.
And, as a consequence of conservation of energy, the transmittance results from:

$$T = 1 - R \tag{2.7}$$

In order to describe the electromagnetic wave propagation in a medium, as well as its extinction, the complex refractive index is used.

$$n^* = n + i\kappa \tag{2.8}$$

where n, the real part of the refractive index, represents the wavelength dependent phase velocity of the electromagnetic wave, and κ, the complex part, is called extinction coefficient, describing the absorption of light by the medium. The absorption of light in a material can be understood as a wavelength and depth-dependent decrease in light intensity ($I(\lambda,x)$), or the reduction of the electromagnetic wave amplitude. A simple relation between the initial light intensity I_0 and the light intensity $I(\lambda, x)$ reduced by absorption in a medium (neglecting interference) is given by the Lambert-Beer-law:

$$I(\lambda, x) = I_0 \cdot e^{-\alpha(\lambda)x} \tag{2.9}$$

where λ denotes the wavelengths, x the penetration depth of light into the material, I_0 is the initial light intensity before entering the material, and α is the absorption coefficient. The absorption coefficient is related to the extinction coefficient via the following equation:

$$\alpha(\lambda) = \frac{4\pi\kappa}{\lambda} \tag{2.10}$$

However, the experimental determination of α is not straightforward and optical interference effects need to be taken into account.
The optical properties of a TCO thin film are characterized by its interaction with light, resulting in wavelength-dependent reflection, transmittance, and absorption events, as described above. Considering that all the incident light is either reflected (R), transmitted (T), or absorbed (A), the following correlation can be formulated:

$$1 = R(\lambda) + T(\lambda) + A(\lambda) \tag{2.11}$$

For small wavelengths (in the UV spectral region), significant absorption takes place in thin film TCOs. This is due to band gap absorption. Most TCOs exhibit an optical band gap of $E_g > 3$ eV [13]. Incident light with photon energies above the optical band gap ($E_{ph} > E_g$) is absorbed due to band-to-band transitions of electrons creating excitons. In degenerately doped metal oxides, the optical band gap scales with the carrier concentration (N_e) due to the Burstein–Moss shift [14, 15]. In degenerated semiconductors, the lowest conduction band states are populated by additional free electrons, which results in the Fermi level being localized in the conduction band (all states below the Fermi level are occupied). In this case, the optical band gap is the difference between the valence band maximum and the energy of the highest occupied states in the conduction band. An illustration of the Burstein-Moss shift is depicted in Fig. 2.1(a).
The optical band gap can be estimated by the intersection of linear fits to linear parts of

the absorption coefficient (α^x) versus $h\nu$ curves and the x-axis. The kind of transition is indicated by the exponent x [11]. In the case of direct, allowed band transitions (f.e. in the case of IZO), x is assumed to be 2. By applying Lambert-Beer's law, the most frequently employed method to calculate the absorption coefficient is utilizing the transmission and reflection according to:

$$\alpha(\lambda) = -\frac{1}{d} \cdot ln(\frac{T(\lambda)}{1 - R(\lambda)}) \tag{2.12}$$

where d is the thickness of the thin film. However, the absorption does not immediately drop to zero for light with energies below the optical band gap. Absorption below the band gap occurs for a wide range of materials due to so-called Urbach tails. Such tails are well pronounced in the optical absorption spectra of heavily doped and amorphous semiconductors. The Urbach energy (E_U) describes the width of the Urbach tail states and can be extracted following the Urbach relation $\alpha(h\nu) = \alpha_0 \exp(-h\nu/E_U)$, where α_0 and E_U are constants. In the energy spectrum of the absorption coefficient, the Urbach tail appears as an exponential component near the optical band gap. E_U can be calculated from the slope of a linear region below the band gap energy when α is plotted over $h\nu$ in a semi-logarithmic plot. Urbach tails represent disorder or defects in the thin film. In this work, we decided to calculate the absorption coefficient for Urbach energy approximations according to Equ. 6.1. A detailed discussion can be found in Chap. 6.1 of the Supplementary section.
Photons with energies well below the optical band gap ($E < E_g$) cannot excite electrons across the band gap. Here, the absorption reaches a minimum, and only reflection limits the optical performance. For the technological application of TCOs, the optical window, the area of minimal absorption, is essential. Depending on the technology, having a large optical window is desirable.

In the near-infrared (NIR) region of the light spectrum, the absorption rises again as a result of so-called free carrier absorption. In the previous section we estimated that free electron gas conditions (degenerately doping) is achieved for $N_e > N_{e,deg} \approx 6 \times 10^{18}\ cm^{-3}$. Photons in the NIR spectral region cause oscillations of these free carriers, resulting in so-called free carrier absorption. The plasma frequency ω_p is related to the free charge carrier density by the relation [9]:

$$\omega_p = f_p \cdot 2\pi = \sqrt{\frac{(N_e \cdot e^2)}{(\epsilon_0 \cdot m^*)}} \tag{2.13}$$

An increasing free charge carrier density leads to an increasing parasitic absorption due to the plasma frequency ($\lambda_p = c/f_p$ describes the peak position of the absorptance curve in the NIR spectrum) moving to shorter wavelengths. The effect is depict in Fig. 2.1(b).

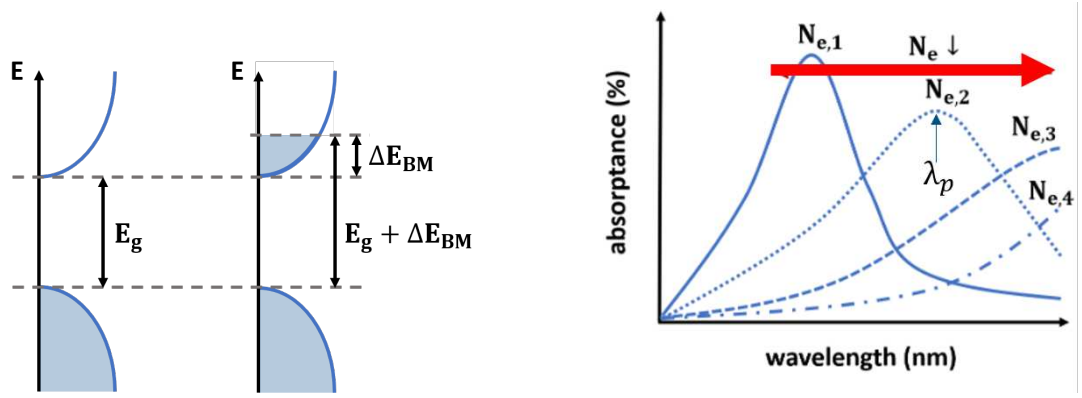

Figure 2.1: (a) Schematic illustrations depicting the Burstein-Moss effect, which states that a moderate filling of the conduction band causes an increase in the band gap; (b) Illustration showing the absorptance as a function of wavelength, with different carrier concentrations and their impact on the plasma frequency (λ_p - exemplarily assigned to one peak). There are three consequences of an decreasing carrier concentration: 1. the peak of the curves moves to longer wavelengths (see red arrow); 2. the height of the curves decreases; 3. the half-width of the absorptance curves increases. Both illustrations are based on [9].

2.1.3 Amorphous indium zinc oxide

Amorphous indium zinc oxide gained much interest as a transparent electrode in recent years, especially for TCOs in perovskite-based tandem solar cells, for several reasons. The primary motivation is the material's exceptional electrical conductivity while being deposited at room temperature [16, 17]. Consequently, IZO is mainly used in its amorphous structure, typically comprised of 90 wt% In_2O_3 and 10 wt% ZnO. Here, the zinc oxide mainly promotes the conservation of an amorphous structure in the indium oxide thin films, with a-IZO maintaining its amorphous state up to annealing temperatures of ~500°C [9, 18].

Conductivity

Without the need for annealing, a-IZO exhibits an unusually high electron mobility, values of $\mu > 50$ cm^2/Vs have been reported in the literature [11, 16, 19]. The spatial overlap of neighboring large spherically symmetric, heavy metal cation ns orbitals is believed to cause the high mobility. Generally, amorphous TCOs exhibit high electron mobilities with an electronic configuration of $(n\text{-}1)d^{10}ns^0$ where $n \geq 4$, and large overlapping orbitals radii, creating coherent conduction paths [9, 10].
According to Equ. 2.1, the conductivity of TCOs can be tuned either by the charge carrier concentration or by the carrier mobility. In the case of IZO, the sources of the charge carriers are believed to be oxygen vacancies V_O^{++}, which are known to act as

doubly charged donors, or interstitial Zn^{2+} ions, according to Ito *et al.* [20]. However, Leenheer *et al.* concluded that the carrier concentration is rather dependent on the oxygen content during sputtering and is less affected by the metal ratio In:Zn [11], which is in line with observations done by others [19, 21, 22]. Leenheer *et al.* also found that for a-IZO, the electron mobility depends primarily on oxygen content during sputtering and thus on the carrier concentration [11]. They reported a maximum electron mobility of 54 cm^2/Vs, at a charge carrier concentration of 1.3×10^{20} cm^{-3}. Here, intrinsic lattice vibration, which causes electron scattering, is the main limitation of the electron mobility. At higher carrier concentrations ($N_e > 5 \times 10^{20}$ cm^{-3}) ionized impurity scattering by oxygen vacancies reduces the carrier mobility significantly. However, a carrier mobility reduction was also observed for carrier concentrations as low as 10^{19} cm^{-3}. They suggested that the charge carriers get trapped in localized states, and the conductivity is dominated by a hopping or percolation mechanism.

Band gap

The optical band gap of In_2O_3 is ~3.7 eV, which is much higher than its fundamental band gap and stems from forbidden transitions from the valence band maximum (VBM) [23]. The fundamental (direct) band gap of In_2O_3 is in the range of 2.6 eV to 2.9 eV, which is ~0.8 eV below the measured optical band gap, a value much too high to be explained by the BMS, according to Walsh *et al.* [23]. Jia *et al.* and Walsh *et al.* suggested that for a-IZO films, the fundamental band gap is about ~2.6 eV [22, 24].

Work function

The work function of the solar cell's electrode is a crucial parameter, as it significantly impacts the interface formation, charge collection, and ultimately the solar cell's efficiency. For efficient charge collection at the electrodes, it is necessary to have an ohmic contact between the electrode and the charge transport layer (CTL). It has been observed that in severe cases of mismatch between the electrode's work function and the energy bands of the respective adjacent functional layers, a Schottky barrier may even be formed, which significantly impacts the charge collection efficiency [25–28]. The efficiency of the solar cell may also be impacted by the built-in potential, which results from the difference in the electrodes' work functions. A sufficiently high built-in potential is desirable as it is the driving force for photogenerated charge carrier extraction through the charge selective contacts [29, 30]. The Schottky barrier, the built-in potential, and their impact on the solar cell will be discussed in detail in section 2.3.2. Several values have been reported for the work function of IZO, which, similar to ITO, can be tuned by the oxygen content in the sputtering gas [31, 32]. Several groups report IZO work functions as high as >5 eV after exposing the thin films to a UV-ozone treatment [31, 33, 34]. Cheun *et al.* measured a value of 4.46 eV while deliberately keeping the oxygen content in the sputtering gas low. In order to confirm the dependency of

the IZO work function value on the oxygen ratio in the sputtering gas, they increased the oxygen content. Consequently, they measured a higher IZO work function value of 4.74 eV. An IZO work function value of 4.37 eV was reported by Liu *et al.* [35]. They also observed a dependency of the IZO work function on the charge carrier density, as their IZO with significantly lower charge carrier density exhibited a much higher IZO work function of 4.81 eV. This observation is in line with the earlier mentioned correlation between the work function and the oxygen content during sputtering.

2.1.4 A review on low temperature high mobility transparent conductive oxides for possible use in perovskite/silicon tandem solar cells

Recently, high mobility TCOs have become increasingly popular electrode materials because they offer a good compromise between high conductivity and high transparency over a broad spectrum. Especially for use as a top electrode in tandem solar cells, transparent electrodes with wide optical band gaps and low free carrier absorption in the near-infrared range are required in order to fully exploit the potential of the top and bottom solar cells. The optical band gap of a TCO is primarily a material feature and can only be minimally modified by the BMS, while the fundamental band gap can be modified by the film's micro-structure and composition. The free carrier density can tune the transparency in the near-infrared range. The conductivity depends on the carrier density and mobility, which are two conflicting properties. Typically, a TCO's free charge carrier density is increased to increase conductivity, sacrificing transparency in the NIR. High mobility TCOs are attractive because they promise excellent conductivity without lower transparency. According to Calnan *et al.*, a TCO (E_g > 3.0 eV, $N_e \geq 10^{20}$ cm^{-3}, $\rho < 10^3$ Ωcm) qualifies as high mobility TCO by having a Hall mobility of $\mu \geq$62.5 $cm^2V^{-1}s^{-1}$ [13]. Unlike IZO, many TCOs require an annealing procedure to achieve high mobilities, which usually involves high temperatures. Annealing a thin film can serve two primary purposes: 1. It is necessary to crystallize the film; 2. It activates dopants. This latter phenomenon, which is usually characterized by higher charge carrier concentrations after annealing, is seen, for instance, for the Sn in ITO [16] and the Hf in IO:Hf films [36].
The selection of high mobility TCOs is severely constrained by the fact that the majority of perovskite top cell designs should not be annealed at temperatures above 100 °C for an extended period of time due to thermal degradation [37]. But also the most common bottom cells in monolithic tandem configuration, silicon hetero-junctions, and CIGS, are limited to processing temperatures below 200 °C. In the case of silicon hetero-junction solar cells, the degradation of the a-Si:H passivation layer begins at a temperature of approximately 200 °C, which subsequently leads to a reduction in the V_{OC} [38]. Flash-lamp annealing (FLA) is a way to circumvent long-term annealing at degrading temperatures and reduce thermal stress on sensitive substrates. Scherg-Kurmes *et al.* managed to produce crystalline IO:H films on silicon wafers by short-term

(about 2.7 ms) flash lamp annealing with equivalent optoelectronic properties to IO:H films annealed at 180 °C for 30 min (see Tab. 2.1 line 8. and 9.) [39]. Also, a high conductivity can be achieved by a clever selection of dopants, which can promote crystallinity. These include dopants such as hydrogen (H) or zirconium (Zr) [39, 40]. In contrast, other dopants, such as zinc, have the opposite effect, so the thin film has a highly temperature-stable amorphous phase [18]. Traditionally, metallic cation dopants, such as Sn^{4+}, Zr^{4+}, or W^{6+} act as electron donors by substitution of In^{3+} sites. Whereas, the anion dopant fluorine is said to lower the transport barrier at the grain boundaries, thereby increasing the carrier mobility [41].
A variety of indium-based TCOs can meet the abovementioned criteria for high mobility. An overview of various indium-based TCOs that can achieve high mobilities at relatively low annealing temperatures, their optoelectrical properties, and their deposition method is given in Tab. 2.1. In some cases, the initial TCO properties before annealing are listed (f.e., lines 12. and 13. show IO:Zr without any temperature treatment and IO:Zr after annealing at 200 °C for 25 min). If presented in the respected study, a band gap value is given. Lines 1. to 4. serve as examples and provide typical values for the two most popular indium-based TCOs, ITO and IZO. DC and RF refer to direct current and radio frequency magnetron sputtering, PLD refers to pulsed laser deposition, and RPD refers to rapid plasma deposition. Except for IO:W in line 18. by Meng *et al.* [42] and IFO:H in line 25. by Han *et al.* [41], which were temperature treated during the deposition, the given annealing temperatures are post-deposition treatment temperatures. Most post-deposition treatments were carried out for 25 to 30 min. For explicit details, we refer to the given references in Tab. 2.1.

Table 2.1: List of various indium-based TCOs that can achieve high mobilities. Their annealing temperatures (T_{ann}), their optoelectrical properties if provided (N_e, μ, ρ, and E_g), their deposition method (RF and DC each refer to cathode sputter deposition variants), and the respective reference is given. *IO:H was treated by flash lamp annealing (FLA, 20 J/cm^2 and 100°C additional substrate heating)

	TCO	T_{ann} (°C)	N_e (10^{20}/cm^3)	μ (cm^2/Vs)	ρ (mΩcm)	E_g (eV)	Method	ref.
1.	ITO	/	0.5	47	2.4	~3.65	DC	[16]
2.	ITO	190	2.4	25	1.0	~3.8	DC	[16]
3.	IZO	/	2.1	58	0.51	3.44	RF	[16]
4.	IZO	190	2.3	60	0.45	3.48	RF	[16]
5.	IO:H	/	3.8	54	0.3	~3.63	RF	[16]
6.	IO:H	190	1.7	115	0.32	~3.87	RF	[16]
7.	IO:H	/	3.45	48	0.38	~3.72	RF	[39]
8.	IO:H	180	1.68	117	0.32	~3.9	RF	[39]
9.	IO:H	~360*	2.11	112	0.26	-	RF	[39]
10.	IO:Hf	/	4.41	50.7	0.37	-	RF	[36]
11.	IO:Hf	230	5.04	79.6	0.38	3.43	RF	[36]
12.	IO:Zr	/	6.18	25.7	0.41	3.55	RF	[40]
13.	IO:Zr	200	3.18	76.9	0.18	3.75	RF	[40]
14.	IO:Zr	/	4.7	21	0.68	-	PLD	[43]
15.	IO:Zr	200	5.5	71	0.21	-	PLD	[43]
16.	IO:Zr	/	6.2	20	0.52	-	RF	[43]
17.	IO:Zr	200	3.2	77	0.27	-	RF	[43]
18.	IO:W	200	1.6	89	0.44	3.83	RPD	[42]
19.	IO:W	200	1.5	90	0.45	-	RPD	[44]
20.	IO:Ce	200	1.4	85	0.55	-	RPD	[44]
21.	IO:W,H	/	3.0	45	0.45	-	RPD	[44]
22.	IO:W,H	250	2.4	84	0.3	-	RPD	[44]
23.	IO:Ce,H	/	3.0	45	0.5	-	RPD	[44]
24.	IO:Ce,H	250	2.4	150	0.2	-	RPD	[44]
25.	IFO:H	105	1.2	87	0.62	3.85	RF	[41]
26.	ITGZO	/	3.67	40.84	0.42	-	RF	[45]
27.	ITGZO	200	1.79	89.04	0.39	3.9	RF	[45]

All the presented TCOs in Tab. 2.1 are exciting candidates for future applications as front-electrodes in monolithic perovskite/silicon tandem devices. Amongst them, IO:H in lines 6. and 8. and ITGZO in line 27. stand out due to their high optical band gaps, which may reduce optical losses in the front layer and, in turn, increase the short-circuit current density (J_{SC}) in the respective solar cell. The lowest resistivities, which lead

to lower transport losses, were shown for FLA IO:H (in line 9.), for IO:Zr annealed at 200°C (in lines 13., 15., and 17.), and IO:Ce,H annealed at 250°C (in line 24.). The lowest thermal stress for the solar cells is probably achieved by FLA, which was used to crystallize IO:H (in line 9.) and the 105°C annealing temperature during the sputter deposition of IFO:H (in line 25.).

2.2 Ceramic cathode sputter deposition of thin films

Sputtering by itself is a low-temperature process in which material is released from the surface of a target due to the bombardment with highly energetic ions. It belongs to the physical vapor deposition techniques (PVD). The ejected material then condenses on a substrate and thus forms a thin layer. The highly energetic ions are generated in a glow discharge and accelerated to the target in the plasma's cathode sheath, with argon generally serving as the inert sputtering gas. The glow discharge is ignited between two electrodes, the target, which is at cathode potential, and the wall of the vacuum chamber, which is at anode potential (earth).
Furthermore, targets are often equipped with magnetrons, whose strong magnetic field confines the charged plasma components close to the target surface. Electrons in the plasma follow the magnetic field lines due to their charge and thus carry out more ionizing collisions with the sputter gas in the target surface vicinity. This results in a higher sputtering rate at a sufficiently low-pressure (and thus little film contamination) [46]. The possibility of large area deposition at high sputter rates makes sputtering a highly attractive, industry-relevant thin film deposition process.

Film growth kinetics
The film growth kinetics during the sputter deposition process depends on the energy of the atoms arriving on the substrate and the nature of the substrate surface. The impinging atoms must have sufficient kinetic energy to diffuse to an energetically favorable position on the substrate surface and allow for dense thin film growth, resulting in a high-quality layer. On the other hand, sputter damage may happen if the particle energy at the substrate is too high. Thornton created a model that is frequently used in order to predict the morphological layer properties of sputtered thin films depending on the sputter parameters [47]. Fig. 2.2 depicts the model, where the variable sputter parameters are argon pressure and substrate temperature.
The zones can be described as followed:

- Zone 1: High process gas pressure and low substrate temperature; because the impinging particles' kinetic energy is insufficient to support surface diffusion, the developing layer has a low density and a rough surface.
- Zone T: Transition area between zone 1 and 2.

- Zone 2: Lower process gas pressure and increased substrate temperature; the impinging atoms have enough kinetic energy to perform surface diffusion, resulting in denser films.
- Zone 3: Very low process gas pressure and substrate temperature corresponds to the melting point of the material; The high kinetic energy of the impinging atoms and the additional energy from the high substrate temperature favors a very dense, crystalline film growth.

The process gas pressure correlates with the mean free path length of the sputtered atoms on their journey from the target to the substrate. The impact on the kinetics of film growth is explained by the fact that a decreased process gas pressure causes the atoms' free path length to increase. A higher kinetic energy of the impinging atoms enables a higher surface free energy to perform surface diffusion.

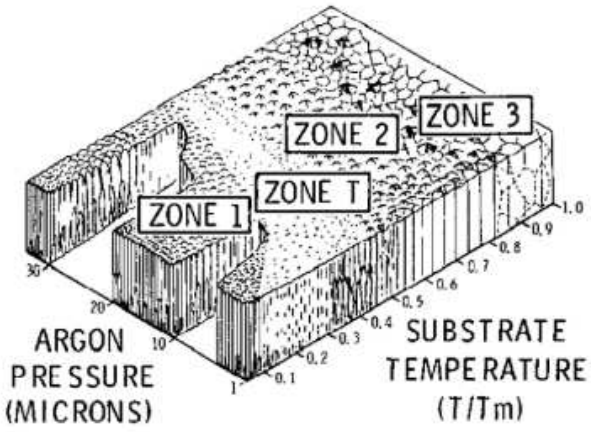

Figure 2.2: The Thornton model: the impact of sputtering parameters on the morphological properties of the growing layer. Source: Reprinted with permission from Annual Reviews from Ref. [47].

The initial nucleation and nature of the thin film growth mode depends on the interaction strength between adatom and surface [46]. Three main thin film growth modes exist:

- Volmer-Weber growth: Island growth; Stronger interactions between the adatoms than between adatoms and surfaces cause three-dimensional adsorbates clusters or islands to form.
- Frank-Van der Merwe growth: Layer-by-layer growth; the growth appears two-dimensional. The films grows by adsorbates forming monolayer after monolayer.
- Stranski-Krastanov growth: Layer-plus-island growth; the initial growth occurs as a layer growth, reaching several monolayers of thickness. With each layer, the influence substrate's surface free energy is reduced, up to a point at which adsorbates are rather attracted to each other than the surface. Then an island-like growth takes over.

2.2.1 Basic principle of radio frequency magnetron sputtering

One popular type of sputter deposition is the radio frequency magnetron sputtering process (RFMS), which is used to produce high-quality transparent contact layers. The name stems from the radio frequency excitation of 13.56 MHz, the oscillation rate of the alternating signal at the target. Due to the much more mobile electrons and the less mobile positive ions in the plasma, a negative bias voltage of the target is established with respect to the grounded chamber wall even while the target is excited through RF. A substantial electron current is attracted to the target while at positive potential. When switching to a negative target potential, a relatively lower Ar^+ ions current reaches the target. On average, over time, this results in a negative target bias voltage. Due to the purging of accumulating charges at the target surface during switching between positive and negative potential, the RFMS offers the advantage of enabling sputtering of non- or poorly conductive ceramic targets so that, in principle, no reactive gas such as oxygen is required to deposit stoichiometric metal oxides, which usually involves very stable process conditions as opposed to direct current (DC) reactive sputtering. The magnetron at the target, which generates a magnetic field in the sputtering chamber, confines the electrons close to the target surface onto circular paths (in the case of round targets). As a result, more ionizing collisions are carried out with the sputter gas, and consequently, a considerable amount of material is removed from the target in this area. Over time, this leads to so-called race tracks on the target surface due to the non-uniform material removal. Magnetron sputter depositions can be performed at a relatively low pressure, resulting in little film contamination. Furthermore, the sputtering chamber is kept at/evacuated to a high vacuum before the deposition to minimize contamination. In order to guarantee clean substrate surfaces, minimize contamination by leftover gas molecules, and avoid target oxidation, such a base pressure is typically lower than 10^{-6} mbar [46]. Argon gas, generally at a pressure of 0.5 - 1 Pa (1 Pa = 1×10^{-2} mbar), is used as the sputtering gas in the chamber (without the magnetron typically higher pressures of 1–5 Pa are necessary) [46].
Besides the possibility of performing very stable depositions using ceramic targets, the RFMS technique is also considered less damaging to sensitive substrates compared to DC sputtering, as the target discharge voltage is commonly higher for DC processes than RF processes.

2.2.2 Sputter damage

In general, sputter damage describes the damaging of a layer through high-energy particle bombardment during the deposition process. Less commonly, literature describes other several interactions with various plasma constituents including electrons, and ultraviolet or vacuum ultraviolet photons, that can have layer-degrading properties [48]. It is assumed that negatively charged oxygen (O^-) is a major cause of sputter

damage [49, 50]. This oxygen originates from the ceramic target as it is knocked out and subsequently negatively ionized on the target surface by free electrons. In front of the target these O^- ions gain kinetic energy, equal to the target potential, accelerating them in the target sheath [50]. Since the target potential is dependent on the applied sputter power, the kinetic energy of the target particles can be controlled. In addition, according to Jia et al. the flux of O^- ions is likewise proportional to the sputtering power [50]. This leads to the first assumption: 1) the impact of sputter damage can be controlled by the applied sputter power, as illustrated in Fig. 2.3.

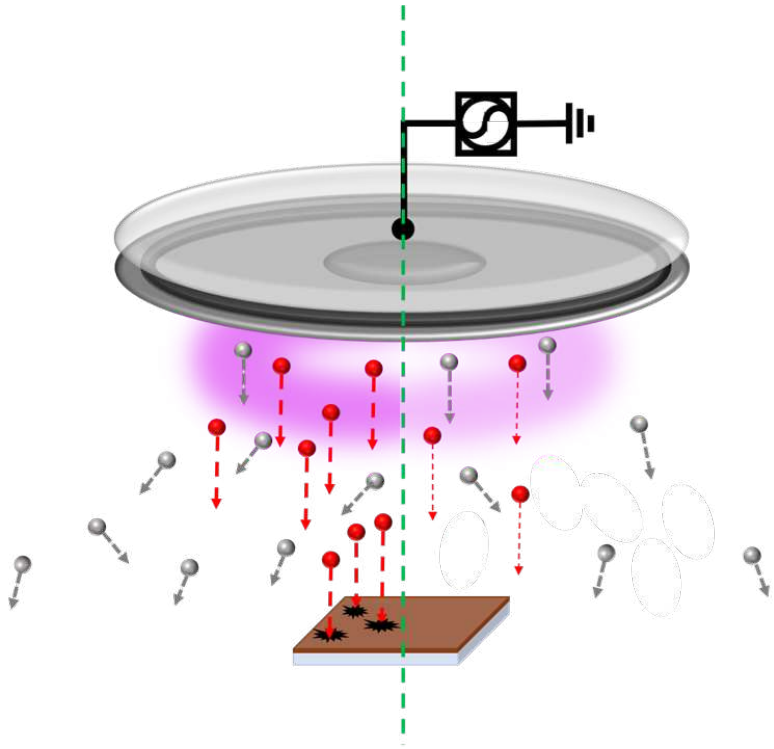

Figure 2.3: Explanatory illustration of the effect of sputter power reduction on the (damaging) target particles.

With a sufficiently high mean free path length, which can be up to several centimeters for conventional sputter processes, it can be assumed that a considerable amount of the damaging species reaches the substrate without colliding with gas particles, which would reduce their kinetic energy [51]. The mean free path length ($\lambda_{1,2}$) between a sputtered particle (1) and a gas particle (2) can be calculated by [46]:

$$\lambda_{1,2} = \frac{1}{\sigma_{1,2} \cdot n_2} \tag{2.14}$$

Where $\sigma_{1,2}$ is the effective collision or scattering cross-section, and n_2 is the density of

the gas particles (number of gas particles per unit volume). Assuming, that the colliding particles are spherical with a radius r, $\sigma_{1,2}$ can be expressed as:

$$\sigma_{1,2} = \pi \cdot (r_1 + r_2)^2 \tag{2.15}$$

n_2 is dependent on the process pressure. By applying the ideal gas law, n_2 is given by:

$$n_2 = N/V = p/k_b T \tag{2.16}$$

This leads to the statement that mean free path length of sputtered particles is inversely proportional to sputtering gas pressure ($\lambda_{1,2} \propto 1/p$). According to above equations, at 0.6 Pa the mean free path length of a sputtered indium atom with the argon gas is $\sim$ 1.5 cm. The number of collisions a sputtered particle performs during its path from target to substrate, is given by:

$$n_{coll.} = d/\lambda_{1,2} \tag{2.17}$$

where d is the distance between target and substrate. Every time a sputtered particle collides with gas particles its kinetic energy is lowered. It is considered completely "thermalized", when its energy is in the same order as the thermal energy. This leads to two prospects to reduce sputter-damage: 1) Increasing the target-to-substrate distance (d), which also increases the number of collisions a sputtered particle will perform on average, and therefore favors the thermalization, and 2) increasing the process gas pressure, therefore reducing the mean free path length, results into the target particles reaching the substrate with less kinetic energy, because they thermalize by multiple collisions.
Tominaga et al. were able to show, that damaging species during sputtering of ceramic targets can mainly be found at the substrate position facing the eroded area of the target, indicating that those particles are ejected in normal direction from the target surface [49]. Similar observations were made by Dewald et al., when analyzing the spatially resolved resistivity of growing films with regard to the racetracks (eroded area) of the magnetron assisted ceramic target [52]. Therefore, the forth and last assumption is: 4) Sputter-damage occurs when the target surface faces the substrate, whereas for an indirect process only scattered particles reach the substrate surface with comparably low energy.
In 2015 Fu and colleagues deposited ZnO:Al as well as In_2O_3:H by radio-frequency magnetron sputtering directly onto the organic hole transport layer [53]. Both TCOs were deposited with different extent of sputter damage (presumably ion bombardment), due to different sputter geometries. In case of In_2O_3:H the process pressure and the substrate-to-target distance was higher than for the ZnO:Al deposition and the substrate was not facing the target directly. As a result, the group observed and concluded that

the deposition of IO:H was less damaging.
A different technical approach to prevent the bombardment of the sensitive substrate by ejection of damaging particles in normal direction from the target surface was shown in 2013 by Jeong et al., who introduced a plasma damage-free linear facing target sputtering (LFTS) technique [54]. The LFTS technique is able to effectively confine the high-density plasma between the surface facing targets and prevents damage of the sensitive substrate by high-energetic particle bombardment, since in normal direction ejected high-energetic particles will be accelerated towards the opposite target surface instead.
In 2006 Kim and colleagues introduced the box cathode sputtering technique as a tool to deposit indium zinc oxide (IZO) as top cathode layer on top of organic light-emitting diodes [55]. Similar to LFTS, by confining high-density plasma between two rectangular magnetrons supported IZO targets they were able to perform plasma damage-free sputtering. The targets are facing each other in a given target-to-target distance. A strong magnetic field is generated between both targets, which is able to confine the high-energetic particles within the box, while the particles reaching the substrate are of low average kinetic energy.
The two previously mentioned techniques have both in common that the target surfaces facing each other, which is a similar approach as for the gas flow sputtering (GFS) technique, which will be explained in the following chapter (2.2.3).

2.2.3 The principle of hollow cathode gas flow sputtering

Hollow cathode gas flow sputtering is a low-damage sputter coating approach with facing target surfaces, which is suitable for large-scale sputter depositions, even of metal oxides. Due to the use of an electric field and geometric confinement, a glow discharge with a high plasma density occurs inside the hollow cathode. Similar to the RFMS, Ar^+ ions bombard and sputter the inside of the cathode surface. In contrast to RFMS, the sputtered target atoms are transported to the substrate by forced convection in the argon flow. The hollow cathode discharge can occur in a tube or a pair of opposing rectangular targets. Thanks to its unique geometry, it achieves fast deposition processes with a comparatively high process pressure in the mbar-range. Due to the high process pressure of the gas flow, the sputtered atoms thermalize during their transport and thus reach the substrate with very low kinetic energy, leading to low bombardment defects. The fast deposition, scalability, and possibility of depositing films on sensitive substrates make the hollow cathode gas flow sputtering a promising technique [56, 57].
In 2000 Höfer *et al.* demonstrated that the gas flow sputtering process is suitable for producing high-quality ITO layers in a gentle process at low temperatures (T_{sub} < 80°C), which is necessary for sputter depositing TCOs on sensitive substrates. A ceramic target with a stoichiometric ratio of [In_2O_3] / [SnO_2] = 90/10 was used [58]. Furthermore, plasma damage to the substrate surface can be further reduced by integrating

a magnetic field shield between the cathode and the substrate. In 2009 Mahrholz and colleagues attached a permanent magnetic shield to the gas flow sputtering aperture. They increased the distance between the source and the substrate to mitigate defects caused by the bombardment of the substrate by high-energy particles [59]. The magnetic field shield had a secondary effect: confinement of the plasma within the hollow cathode, led to a denser plasma and, consequently, to a higher deposition rate. This makes the GFS process a promising sputter deposition technology for sensitive solar cells that require low-damage thin film depositions.

2.3 Solar cells

Solar cells are optoelectronic devices that convert sunlight (hence "solar") into electrical energy via the photovoltaic effect [60]. The light/energy emitted by the sun can be approximated as black body radiation. Black body radiation refers to thermal electromagnetic radiation. In the solar field, the most frequently used incident solar spectrum for calculating solar cell parameters is the AM1.5G. It refers to an air mass (AM), which the sunlight passes through at a latitude of 42.8° that is 1.5 times as thick as the earth's atmosphere at a latitude of 90°. On the other hand, the solar spectrum outside of the earth's atmosphere is referred to as AM0. The integrated spectral irradiance at AM1.5G results in the incident power density for this spectrum of 1000 W/m^2. Fig. 2.4 shows the AM0 and AM1.5G solar spectra. The visible gaps in the AM1.5G solar spectrum stem from the absorption of atmospheric gases at characteristic spectrum regions.

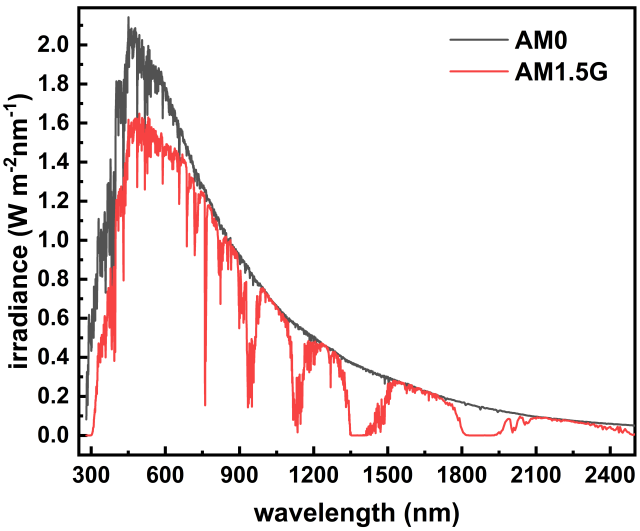

Figure 2.4: Spectral irradiance of the sun at the earth's surface for a solar zenith angle of 48.2° (AM1.5G) in red and outside the atmosphere (AM0) in black. Data according to NREL [4].

The fundamental operations of a solar cell are:

- Generation of electron-hole pairs (excitons) by light absorption.

- The separation of photogenerated charge carriers of opposite types.
- Collection/extraction of photogenerated charge carriers to an external circuit to generate an electrical power.

This chapter outlines the solar cell fundamentals, physical mechanisms, and the electrical and optical device limitations. In the last section (section 2.3.3), it will furthermore introduce the reader to the perovskite solar cell.

2.3.1 Charge carrier generation, extraction and recombination

The semiconductor absorber material's capacity to absorb light to generate electricity is the essential function of solar cells. Typically, semiconductor materials are used as absorbers in solar cells. Unlike the previously described TCOs, common semiconductors used as absorbers consist of a valence band filled with electrons and a conduction band that is mostly empty. The energetic distance between the valence band maximum (VBM) and the conduction band minimum (CBM) is called band gap energy (E_g). The VBM and CBM of semiconductors with direct band gaps are each defined by the same crystal momentum for electrons and holes. These direct semiconductors, like hybrid perovskites, are characterized by a high absorption coefficient (*alpha*), which enables them to effectively absorb light over absorber thicknesses of just a few hundred nm. The band gap energy measures the minimal energy needed to excite an electron to a state in the conduction band. The excitation energy is provided by incident photons with $E_{ph} = h\nu \geq E_g$. Depending on the incident photon energy, the electron is excited from the valence band to a higher-energy state within the conduction band, leaving behind a vacancy (a so-called hole) in the valence band. Any excess energy provided by the incident photon exceeding E_g (which creates hot carriers) is lost, due to carrier cooling to the band edges (thermalization) [61].

Fig. 2.5 gives an overview on the charge carrier dynamics and time-scales in a solar cell. The early-stage events taking place following photoexcitation in the picosecond time-scale are charge generation, relaxation, and transfer (diffusion- or drift-mediated charge movement towards the CTLs). According to Shi *et al.*, the generation of free carriers from excitons in perovskite absorbers happens at timescales between femtoseconds to picoseconds (at a rate of 10^{12} s^{-1}), which is substantially quicker than the charge transport and recombination rates [61]. Like the free carrier generation, the carrier cooling is also ultrafast, time-scales of 1 ps were reported [62]. Because carrier cooling is lost energy, a loss-mechanism described by the Shockley-Queisser limit (detailed explanation follows), there are efforts to extend the lifetime of these hot carriers to utilize the excess energy and reducing voltage losses [61].
On the time-scale of an excited charge carrier, the next event taking place after cooling

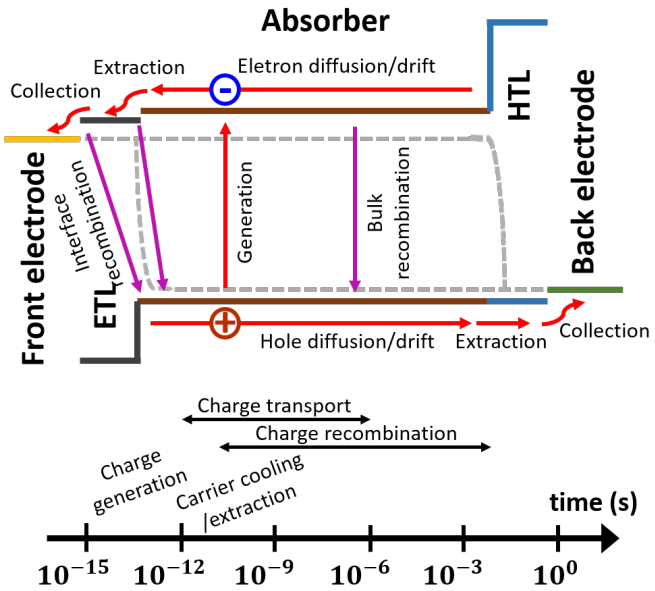

Figure 2.5: Illustration of charge carrier dynamics and time-scales, adopted from [61].

would be its transfer over the absorber interfaces into the CTLs. Usually, this process is diffusion- or drift-mediated, with diffusion lengths for excited carriers of [63]:

$$L_n = \sqrt{D_n \cdot \tau_n} \tag{2.18}$$

where τ_n is the lifetime of the excited carrier and D_n is the diffusion coefficient. In a good absorber L_n is substantially longer than the absorber's film thickness. Furthermore, in many devices, a big-enough built-in potential (originating from the work function difference of the electrodes) provides an electric field that promotes the charge transport. It is a critical process, as a too low transfer rate may result in charge accumulation and recombination, leading to low quantum efficiencies (QE) and photocurrents. There are many reasons for low transfer rates, like for example energetically misaligned [30] or low conducting interfaces [64]. Therefore, interface and material optimization are required to maximize the carrier transfer rate. It was shown that a good energy alignment [30, 65], certain interfacial layers [27, 64–66], CTL doping [67], and increasing the interface contact area improves the charge transfer [68].
Recombination in the absorber of a solar cell device can follow two principle mechanisms. If an electron in the conduction band recombines with a hole in the valence band, it will release its energy (band gap energy) in form of a photon. This is why this process is called "radiative recombination", band-to-band recombination, or bimolecular recombination. In another recombination process, the Auger recombination, the released energy causes excitation of a third charge carrier instead of photon emission. In contrast to the recombination described before, this recombination process is not radiative, therefore, referred to as non-radiative recombination. However, Auger re-

combination processes are not considered a limiting factor in perovskite solar cells in contrast to, for example, silicon solar cells due to their low contribution to losses under one sun condition [69, 70].
Another non-radiative recombination, associated with energy losses, describes the process of charges getting trapped in "deep" energetic states (hence trap states) within the band gap of the absorber, originating from impurities or defects in the material. When charge carriers get trapped in these states, they can either recombine with a carrier of an opposing charge or be discharged to the conduction (electrons) or valence (holes) band. This recombination process is called Shockley-Read-Hall (SRH) or monomolecular recombination.
The charge recombination rate is defined by the ratio of the charge carrier density N_e and the charge carrier lifetime τ_i associated with the respective recombination process. The total charge recombination rate is a superposition of all recombination rates of the different recombination processes R_i [63]:

$$R_{tot} = \frac{\Delta N_e}{\tau_{tot}} = \sum_i R_i = \sum_i \frac{\Delta N_e}{\tau_i} \tag{2.19}$$

R_i refers to different recombination processes, that may take place in the absorber.
The ideality factor n_{id} can be used as an indicator of the type of recombination process. In perovskite solar cells, the ideality factor usually exhibits a value between $n_{id} = 1$ and $n_{id} = 2$. While $n_{id} = 1$ describes bimolecular recombination (radiative band-to-band), $n_{id} = 2$ describes trap-assisted recombination (non-radiative, also called Shockley-Reed-Hall SRH recombination) processes. Typically, a lower ideality factor correlates with a higher V_{OC} due to decreased trap-assisted non-radiative recombination in the bulk [71]. Whereas n_{id} is usually insignificantly influenced by transport losses in the solar cell. It has been shown in the literature that although significant non-radiative second-order surface/interface recombination may limit the V_{OC}, it is, in contrast to SRH recombination in the bulk, not reflected by a high n_{id} [72]. Here, the recombination takes place through charges getting trapped in surface/interface states. Therefore, the ideality factor interpretation may not be straightforward.
Eventually, the power output of a solar cell is solely dependent on the carriers collected by the electrodes. A solar cell's quantum efficiency describes the ratio of extracted charge carriers to incident photons of a certain wavelength. Generally, a distinction is made between two quantum efficiencies, the external quantum efficiency (EQE) and the internal quantum efficiency (IQE). The EQE of a solar cell is defined as the ratio of the incoming photon flux to the electron flux, which is expressed as electrical current at short circuit (J_{SC}) [73]:

$$EQE(\lambda) = \frac{J_{SC}(\lambda)}{q\Phi_{ph}(\lambda)} \tag{2.20}$$

While the EQE is calculated by considering all "external" incident photons and thereby does not account for reflection losses through the front layer surfaces, the IQE only considers the photons that reach the absorber (hence are not reflected) and consequently is mainly limited by internal losses.

$$IQE(\lambda) = \frac{EQE(\lambda)}{1 - R(\lambda)} \tag{2.21}$$

However, since only reflection losses are taken into account when calculating the IQE from the EQE and reflection data, parasitic absorption is not accounted for. Therefore, the true IQE cannot be determined by this method.
In an idealized scenario, the EQE is considered to be 1, meaning all incident photons with energies equal and above the band gap (E_g) are absorbed and produce an electron-hole pair. In contrast, all photons with energies below E_g are not absorbed. It is described as a step-function-like absorptance, which is zero for photon energies below and one for photon energies greater than E_g. The ultimate efficiency of a solar cell assumes a theoretical solar cell temperature of T_c = 0 K illuminated by a black body with a surface temperature of 6000 K, an open-circuit voltage (V_{OC}) equal to the band gap ($V_{OC} = V_g$), and a maximum power equal to the nominal power (FF = 100 %). In such a theoretical scenario, a solar cell with a band gap of E_g = 1.6 eV, which would only be limited by thermalization and transmission losses (assuming 100 % absorption of incident light at the band edge), would result in an efficiency of 40.75 % (calculated with data taken from Ref. [74]). The light blue area in Fig. 2.6 exhibits the ultimate efficiency of such a solar cell. However, for a solar cell with a cell temperature of 300 K illuminated by a black body with a surface temperature of 6000 K, which is a more realistic scenario, the open-circuit voltage is limited to values below the energy gap. Furthermore, the voltage at maximum power is smaller than the open-circuit voltage (FF ≠ 100 %), which is described by the impedance matching factor. This limit is known as the Shockley-Queisser (SQ) limit, or detailed balance limit [75]. For a solar cell with a band gap of E_g = 1.6 eV, the SQ limit efficiency would be η_{SQ} = 30.14 %, which is depicted as dark blue area in Fig. 2.6 [74].

2.3.2 Solar cell parameters

The performance parameters of solar cells are derived from their current density-voltage characteristics (J-V characteristics). Under dark conditions, solar cells behave like classical diodes, exhibiting the characteristic diode curve (see explanations and Fig. 2.7 below). When assuming an ideal solar cell that is illuminated, its characteristic curve shifts along the Y-axis by the photo-generated current density J_{ph}. Fig. 2.7(a) shows the dark J-V curve (dashed line) and the illuminated J-V curve (compact line). Furthermore, it depicts the characteristic values that can be extracted from the illuminated J-V curve: the

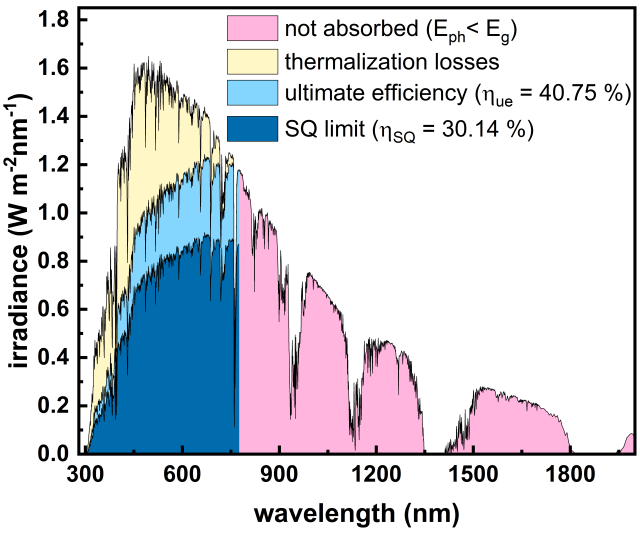

Figure 2.6: The spectral utilization in a perovskite absorber (E_g = 1.6 eV) with regard to the standard AM1.5g spectrum. The light blue area visualizes the absorbed incident power assuming ultimate efficiency (η_{ue} = 40.75 %), while the dark blue area visualizes the absorbed incident power assuming Shockley-Queisser (SQ) limit efficiency (η_{ue} = 30.14 %). The difference between the two blue areas can be considered extraction losses. The yellow area visualizes thermalization losses, and the pink area depicts incident photon energy that is not absorbed due to being lower than the band gap energy.

short-circuit current density (J_{SC}) at V = 0 V; the open-circuit voltage (V_{OC}), measured at unloaded cell conditions (J = 0 mA/cm^2); the Maximum Power Point (MPP), the operating point of the solar cell, where the cell delivers the highest power density (P_{MPP} = $V_{MPP} \times J_{MPP}$).
The voltage-dependent current density that describes the illuminated J-V curve can be expressed according to the following equation:

$$J(V) = J_{ph} - J_0(e^{\frac{qV}{n_{id}kT}} - 1) \tag{2.22}$$

where J_0 is the reverse saturation current density of the diode, n_{id} the ideality factor, q is the elementary charge, k is the Boltzmann constant, and T is the temperature.
The non-ideal J-V characteristics feature losses, expressed by the series resistance (R_{ser}) and the shunt resistance (R_{par}). The equivalent circuit model in Fig. 2.7(b) depicts these parasitic resistances. Accordingly, the solar cell's J-V curve is described by the following equation that takes into account both series and shunt resistances:

$$J(V) = J_{ph} - J_0(e^{\frac{q(V-J\cdot R_{ser})}{n_{id}kT}} - 1) - \frac{V - J \cdot R_{ser}}{R_{par}} \tag{2.23}$$

Generally speaking, the solar cell series resistance (R_{ser}) depends on the device's overall conductivity, which is related to the charge transport through individual layers and interfaces of the solar cell stack as well as the electrodes sheet resistance. On the

other hand, the shunt resistance (R_{par}) is linked to losses due to photogenerated charge carrier recombination within the device and shunts [76]. For example, several groups have reported increased series resistances and reduced shunt resistances in the presence of interfacial barriers [26, 64, 77].
By assuming a large R_{par} and therefore ignoring the last term in the equation, Equ. 2.23 yields the short-circuit current density when $V = 0$ V, which then is $J_{SC} \sim J_{ph}$. The same consideration but with J = 0 mA/cm^2 results in the open circuit voltage (V_{OC}) of the cell:

$$V_{OC} = \frac{n_{id}kT}{q} \cdot ln(\frac{J_{ph}}{j_0} + 1) \tag{2.24}$$

With the help of Equ. 2.24 the solar cell's ideality factor can be determined from the slope of the resulting curve of different V_{OC}s measured at various light intensities, through the following simplified correlation:

$$V_{OC} = \frac{n_{id}kT}{q} \cdot ln(\frac{J_{ph}}{j_0}) \tag{2.25}$$

The ideality factor n_{id} can be used as an indicator of the type of recombination process which takes place, though the exact interpretation is not straightforward. An explanation was already given above in section 2.3.1.
According to Fig. 2.7(a), the fill factor is represented as the ratio of the gray square spanned by the vertices V_{MPP} and J_{MPP} to the area spanned by V_{OC} and J_{SC}. It is given by

$$FF = \frac{J_{MPP} \cdot V_{MPP}}{J_{SC} \cdot V_{OC}} \tag{2.26}$$

The power conversion efficiency (PCE) of a solar cell is calculated from the ratio of incident irradiation power density (P_{in}) to the electrical power at the operating point (P_{MPP}) of the solar cell, following the equation:

$$PCE = \frac{P_{MPP}}{P_{in}} = \frac{J_{MPP} \cdot V_{MPP}}{P_{in}} = \frac{J_{SC} \cdot V_{OC} \cdot FF}{P_{in}} \tag{2.27}$$

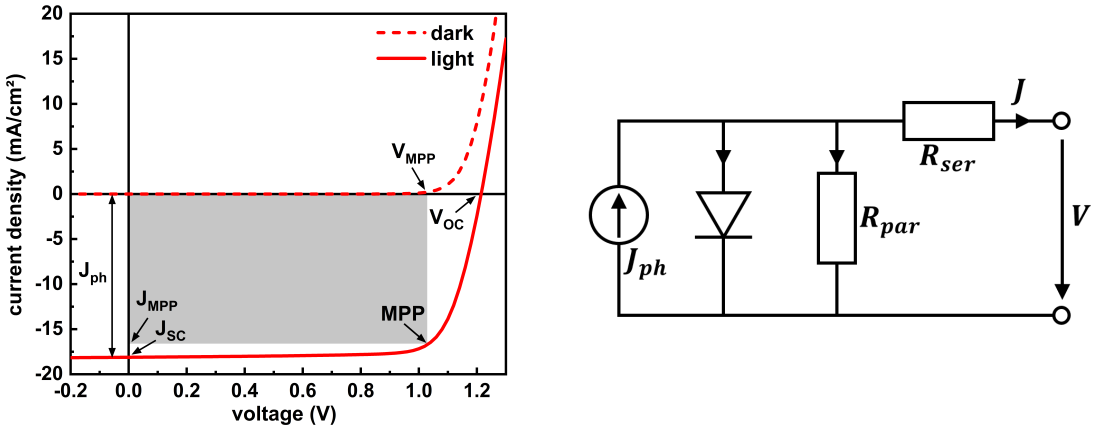

(a) (b)

Figure 2.7: (a) J-V characteristics of a solar cell including the most important values: The open-circuit voltage V_{OC}, short-circuit current density J_{SC}, photocurrent density J_{ph}, and the maximum power point MPP, J_{MPP}, and V_{MPP}, and (b) Equivalent circuit of the one-diode model of a solar cell.

2.3.3 Structure and functions of a perovskite solar cell layer stack

Perovskites are a relatively novel semiconductor compound that can be used as solar cell absorbers. A hybrid organic-inorganic lead or tin halide-based material is commonly used for solar cell applications. Perovskites offer the opportunity to engineer their optical band gap by varying their components [78, 79]. Therefore, they are extremely interesting for the application in both tandem architectures and high-efficiency single-junction devices [80–82]. The absorber is typically sandwiched between selective charge transport layers of opposing polarity. Depending on the sequence in which the layers are deposited, a distinction is made between p-i-n and n-i-p architectures. Here, n refers to n-type materials, p refers to p-type materials, and i refers to i-type (intrinsically undoped) materials. Both architectures are presented in Fig. 2.8. ETL stands for electron transport layer, an electron selective layer that blocks holes and extracts electrons. Often, titanium oxide (TiO_2), tin oxide (SnO_2), or fullerenes (f.e. PCBM, C_{60}, ...) are used as ETLs, which strongly depends on the deposition sequence, and thus, the architecture. Commonly used deposition techniques for metal oxide, and sometimes their need for high-temperature treatments, degrade the perovskite absorber. Therefore, they are mostly not applicable in the p-i-n structure. HTL stands for hole transport layer, which refers to a hole selective layer that blocks electrons. The most widely used HTL materials are poly[bis(4-phenyl)(2,4,6-trimethylphenyl)amine (PTAA), poly(3,4-ethylene dioxythiophene):polystyrene sulfonate (PEDOT:PSS), nickel oxide (NiO_x), 2,2',7,7'-tetrakis(N,N-di-p-methoxyphenylamine)-9,9'- spirobifluoren (Spiro-

OMeTAD), and the variety of self-assembling monolayers (for details on SAMs, we refer to [65, 83]). The electrode is either a TCO or a metal. Usually, the front-electrode (considering illumination through the glass substrate) is a TCO, f.e. SnO_2:F (FTO), ITO, or IZO. Whereas the rear electrode typically is an opaque metal consisting, for example, of copper, silver, gold, or aluminum, except for semitransparent perovskite solar cells, where both electrodes are TCOs. The built-in potential, originating from the work function difference of the electrodes, can impact the solar cell's efficiency. In perovskite solar cells with charge selective layers forming the p-i-n structure, charge extraction is expected to be diffusion controlled [84]. However, a sufficient work function fitting for the adjacent layers is desirable for photogenerated charge carrier extraction through the charge selective contacts, reducing interfacial recombination and transport losses. Under operating conditions, a lowered built-in potential may even cause a reversed electric field inside the active layer, which increases the recombination of the photogenerated charges, ultimately lowering the quasi Fermi-level splitting (QFLS) in the absorber [29, 30]. However, in order to guarantee a successful extraction of majority carriers through the charge transport layers in perovskite solar cells, a high enough electrode work function difference, hence built-in potential, is required [29, 70].

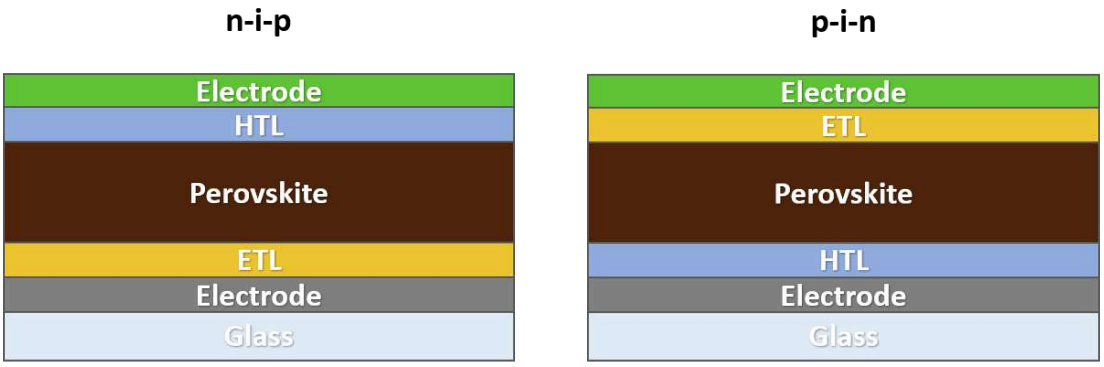

(a) (b)

Figure 2.8: Illustration of a planar a) p-i-n and b) n-i-p perovskite solar cells architecture.

Electrode / solar cell interface

When an electrode and an (n-type) semiconductor are connected, potential energy differences trigger electrons flowing over the interface to achieve charge equalization. Charge equalization continues until the Fermi energy of the semiconductor ($E_{F,SM}$) is in equilibrium with the Fermi energy of the electrode ($E_{F,E}$). As a result, this leads to a depletion of electrons/holes in the semiconductor, which causes the semiconductor bands to bend.

For efficient charge collection at the electrodes, it is necessary to have an ohmic contact between the electrode and the adjacent solar cell layer. In order to facilitate an ohmic contact with the CTL, an energetically matching electrode work function and a good energetic alignment are needed. Fig. 2.9(a) exemplarily shows the case of an ohmic contact between an electrode and an n-type semiconductor. Here, the n-type semiconductor bands bend downwards as the potential energy difference causes the electrons to flow from the electrode to the semiconductor, leading to a space charge region. The band bending at the interface describes a continuous change in the occupation probability of energy levels by electrons due to the additional electrons at the interface provided by the electrode. An ohmic contact facilitates a low series resistance contribution and a high shunt resistance contribution due to a decrease of interfacial recombination [64]. It has been observed that in severe cases of mismatch between the electrode's work function and the energy bands of the respective adjacent semiconductor, a Schottky barrier may be formed, which significantly impacts the charge collection [25–28]. The Schottky-Mott limit, which is applicable for weakly interacting materials, describes the height of barriers originating from electrodes' work function (WF or ϕ_E) located within the semiconductor band gap [85]. In Fig. 2.9(b), an example of the formation of an n-type Schottky-barrier is given. In the example, the high electrode work function led to a potential energy difference, which caused the electrons to flow from the semiconductor to the electrode. In other words, electrons accumulate on the electrode side of the interface, and a positive space charge region (or electron depletion layer) is formed in the semiconductor to maintain electrical neutrality at the interface. Due to that, the occupation probability level (Fermi level) shifts with respect to the energy bands in this area. Consequently, the semiconductor's energy bands bend upwards, resulting in a Schottky-barrier. The size of an ideal Schottky barrier can be predicted by considering the Schottky-Mott rule, using the superposition principle of the electrostatic potentials [86, 87]. The n-type Schottky-barrier height is expressed by $\phi_{B,n} = \phi_E - X_{SM}$, and the p-type by $\phi_{B,p} = \mathrm{I}_{SM} - \phi_E$ (I_{SM} is the ionization potential of the semiconductor). Electron injection and/or collection are significantly affected by Schottky-barriers. A Schottky-barrier results in large series and low shunt resistances, and sometimes even in s-shaped J-V curves [26, 27, 64].
While the Schottky-Mott limit describes the dependency of the barrier height on the electrode WF for non-(weakly-)interacting materials, moderate or strong chemical interaction leads to strain and interfacial states and may result in Fermi-level pinning [88–90]. The latter situation is complex, and estimating whether two materials will or will not form a Schottky-barrier when forming an interface and explaining the exact origin of the barrier is difficult. Surface states, for example, propagate barrier height pinning in the electrode/CTL interface, according to the Bardeen-limit [88–91]. A Schottky-barrier based on interface states is shown in Fig. 2.9(c). Here, The n-type Schottky-barrier height, or to be precise, the Bardeen limit, is calculated by $\phi_{B,n} \approx \mathrm{E}_{g,SM}$

– ϕ_0 [92], which is a description independent of the electrode's work function. Here, ϕ_0 describes the height of the charge neutrality level (CNL) originating from the interface states. Moderate interface interaction and the impact of sputter deposition of the electrode might also affect the interface formation through damage of the ETL surface, penetration of electrode atoms into the underlying layer, defects, strain between the materials, or chemical reaction between the electrode's atoms with the adjacent layer [25, 26, 85, 93].

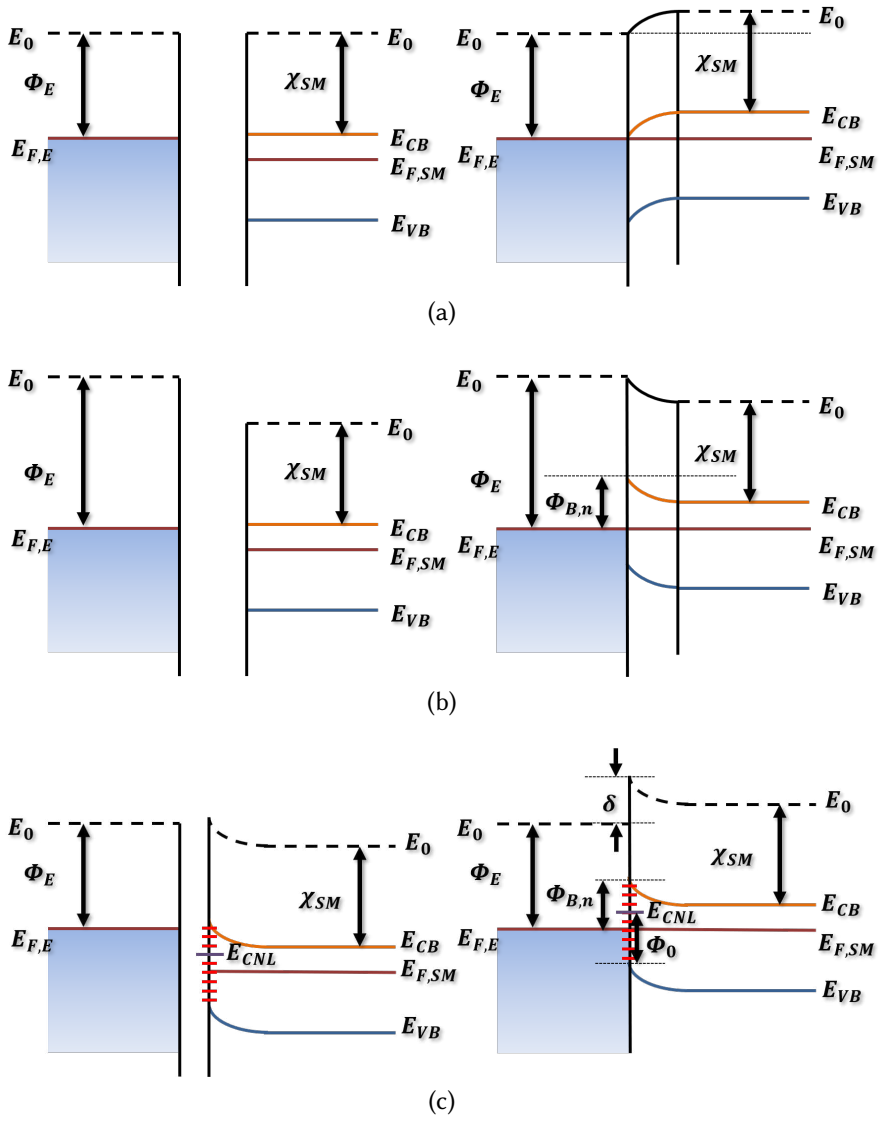

Figure 2.9: Illustration of metal and n-type semiconductor band diagrams before contact and after contact, for (a) an ohmic contact, (b) an ideal Schottky barrier, and (c) a non-ideal Schottky barrier as proposed by the Cowley and Sze [89].

2.4 Perovskite-based tandem solar cells

Multijunction solar cells are made from two or more absorbers of different band gaps. In this work, two-absorber tandem architectures are discussed. They have the potential to attain substantially higher efficiencies than single-junction solar cells if the bandgaps of the absorbers are wisely selected. As portrayed in Fig. 2.10(a), conventional silicon solar cells with band gaps around 1.1 eV have comparably high thermalization losses (thermalization losses were discussed in Chapt. 2.3.1), limiting their detailed balance limit efficiency to 32.23 % [74]. These losses can be decreased when paired with a solar cell of a higher band gap, for example, a perovskite solar cell with $E_g \approx 1.6$ eV (see Fig. 2.10(b)). Such multijunction solar cells, so-called tandem solar cells, exhibit a much higher detailed balance limit due to their lower thermalization losses.

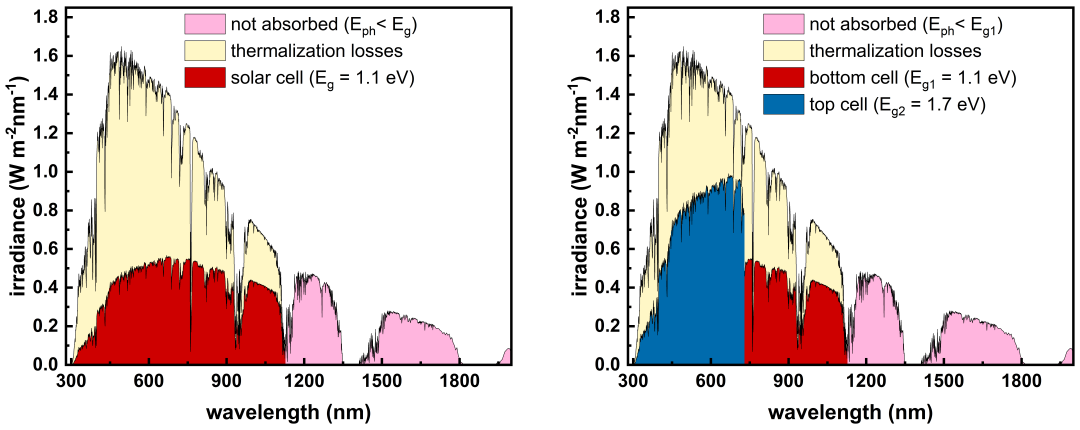

Figure 2.10: The effective spectral utilization in (a) a single junction solar cell with an absorber material's band gap of 1.1 eV and (b) a multi junction absorber consisting of silicon (E_{g1} = 1.1 eV) and perovskite (E_{g2} = 1.7 eV) absorbers with regard to the standard AM1.5g spectrum according to detailed balance considerations. The red and blue areas visualize the absorbed incident power, the yellow area visualizes thermalization losses, and the pink area visualizes incident photon energy that is not absorbed due to the photon energy being lower than the band gap energies.

The detailed-balance limit for perovskite/silicon tandem solar cells with, for example, band gaps of 1.73 eV and 1.12 eV was reported to be 45.1 % [5]. Recently, a certified PCE of 30.93% for a planar device and 31.25% for a fully textured perovskite/silicon tandem devices was shown [3, 4]. This achievement is partially attributable to continual improvements made to the front contact's optoelectrical characteristics.

2.4.1 Requirement and development of transparent front electrodes for tandem solar cells

There are four main requirements for a transparent metal oxide top electrode for efficient perovskite solar cells: 1. it should not react with the underlying perovskite layer and the charge transport layers; 2. The deposition process must not damage the underlying perovskite layer and charge transport layers; 3. It should have high transmittance in the relevant spectrum for incident sunlight; 4. It should have good conductivity for charge collection.
Points 1. to 4. vary slightly between the 2-terminal (2-T) and 4-terminal (4-T) tandem configurations, and therefore we will present the historical scientific developments in the following for each configuration separately.

4-T tandem solar cells

In 2014 Löper *et al.* manufactured a semi-transparent perovskite solar cell with a transparent electrode made of 100 nm indium tin oxide (ITO), which was deposited directly on the Spiro-MeOTAD hole selective layer by sputter deposition [94]. However, the resulting J-V property was significantly deteriorated compared to a metal contact reference solar cell. This was attributed to sputter damage, although their sputter deposition process was optimized for soft depositions. Therefore, a MoO_x buffer layer was evaporated onto the organic hole transport layer prior to the ITO sputter deposition. The introduction of the buffer layer led to a semi-transparent solar cell with a V_{OC} of 821 mV, a J_{SC} of 14.5 mA/cm^2, and a FF of 51.9 % (PCE = 6.2 %) on an active area of 0.2773 cm^2. The semi-transparent perovskite solar cell was then combined with a c-Si heterojunction bottom cell to a mechanically stacked tandem solar cell with four terminals, resulting in an efficiency of 13.4 %. The comparably low efficiency of the filtered bottom cell (7.2 %) in the mechanically stacked tandem design was attributed to the upper perovskite cell having a high non-convertible parasitic absorption below the perovskite absorber's band gap. Specifically, the combination of MoO_x buffer and ITO electrode was assigned to cause a significant increase in infrared parasitic absorption, leading to an average of ~55 % transmission of light through the semi-transparent top-cell between 800 nm and 1200 nm.
Instead of a TCO, Bailie et al. used a transparent silver nanowires (AgNWs) electrode on top of spiro-OMeTAD to create a semi-transparent perovskite solar cell device [95]. The silver nanowires electrode was mechanically transferred onto the spiro-OMeTAD-topped perovskite solar cell with caution to avoid damage. With the help of lithium fluoride (LiF) as an anti-reflective coating, the transmission through the semi-transparent perovskite solar cell peaked at 77% at around 800 nm and was still around 60 % at 1200 nm, which was overall significantly higher than previously achieved by Löper and colleagues. The resulting semi-transparent perovskite single junction solar

cell had a V_{OC} of 1025 mV, a J_{SC} of 17.5 mA/cm^2, and a FF of 71 % (PCE = 12.7 %). They combined the perovskite single junction solar cell with two kinds of bottom solar cells, a copper indium gallium diselenide solar cell (CIGS) and a low-quality multi-crystalline silicon solar cell, forming mechanically stacked tandem configurations. This resulted in a 4-terminal tandem solar cell efficiency of 18.6 % for the perovskite + CIGS tandem solar cell and 17.0 % for the perovskite + Si tandem solar cell. However, the complicated deposition procedure makes the silver nanowires electrode less reproducible, which is a drawback. Furthermore, the silver reacts with iodide, which migrates through the spiro-MeOTAD. The formation of AgI compounds decreases solar cell performance and reduces the cell's stability.
To increase the front electrode's optical properties, Werner and colleagues replaced the tin-doped indium oxide (ITO) with an indium zinc oxide (IZO) rear contact [96]. Compared to ITO, IZO exhibits lower absorption in the relevant wavelength range and allows for room-temperature fabrication. The IZO electrode was sputter deposited from a ceramic target in an RF magnetron process. The deposition process was optimized for sputter damage reduction by reducing the RF sputter power from 120 W to 60 W (0.76 W cm^{-2}), thereby reducing sputter damage-provoked s-shapes in the solar cells. In contrast to the results by Löper *et al.* [94], these circumstances enabled a direct deposition of the TCO onto the Spiro-OMeTAD layer with small acceptable losses assigned to sputter damage. A comparison was made between the parasitic losses caused by the MoO_x buffer layer and losses assigned to sputter damage. The average transmittance in the 800-1100 nm wavelength range could be improved from 58.8% with a 10 nm thick MoO_x buffer to 61.6% without buffer, which increases the silicon heterojunction (SHJ) bottom cell's short circuit current from 14.6 mA/cm^2 to 15.81 mA/cm^2. The semi-transparent solar cells of 0.25 cm^2 active area had a V_{OC} of 870 mV, a J_{SC} of 17.51 mA/cm^2, and a FF of 68 % (PCE = 10.36 %) with 10 nm MoO_x and a V_{OC} of 938 mV, a J_{SC} of 17.4 mA/cm^2, and a FF of 59.6 % (PCE = 9.71 %) without buffer. The resulting efficiencies of the 4-terminal tandem cells, with and without a damage buffer, were very similar (18.18% vs. 18.19%). The tandem efficiency was further increased to 19.6% due to the bottom cell's short circuit current improvement to 18.38 mA/cm^2 by replacing the heavily doped FTO substrate with an ITO substrate.
Hydrogenated indium oxide (IO:H) is a high mobility TCO that can be fabricated at comparably low temperatures. It has several optical advantages addressed in Chap. 2.1. In 2015 Fu and colleagues attempted to utilize the potential of IO:H as a transparent front electrode [53]. They used RF magnetron sputtering to deposit the IO:H directly on the Spiro-OMeTAD as well as on a 35 nm MoO_3 buffer, without post-annealing. Without the MoO_3 buffer layer, a semi-transparent perovskite solar cell with an efficiency of 10.1 % could be produced (the exact J-V parameters were not disclosed), whereas a solar cell with a 35 nm MoO_3 buffer had a V_{OC} of 1104 mV, a J_{SC} of 17.4 mA/cm^2, and a FF of 73.6 % (PCE = 14.1 %). Both had an active area of 0.517 cm^2. The latter had an average

transparency of 72 % in a wavelength range of 800 to 1150 nm and was mechanically on a CIGS bottom cell, resulting in a 4-terminal tandem efficiency of 20.5 % and a filtered short circuit current density of 12.7 mA/cm^2.
By replacing the MoOx buffer layer with solution-processed ITO nanoparticles, McMeekin et al. were able to further reduce parasitic absorption in the perovskite top-cell [97]. The thin, solution-processed ITO nanoparticle buffer layer was spin-coated on the hole transport layer (spiro-OMeTAD) for sputter damage protection. A 120 nm thick ITO electrode was then sputter-deposited onto the buffer layer. This resulted in a semi-transparent single junction solar cell with a V_{OC} of 1.1 V, a J_{SC} of 19.9 mA/cm^2, and a FF of 70.7 % (PCE = 15.1 %). Together with a silicon solar cell in a 4-terminal tandem configuration, a peak efficiency of 25.2 % and a stabilized power efficiency of 19.8 % could be achieved with a current density of the filtered bottom cell of 14.4 mA/cm^2.
In an inverted semi-transparent perovskite solar cell architecture, solution-processed nanoparticles were also demonstrated as a buffer. Bush et al. used spin-coated zinc-oxide nanoparticles on top of the electron selective layer PCBM [28]. Subsequently, 500 nm ITO was deposited by DC-magnetron sputtering (at 400 W) using a ceramic target. However, an extraction barrier was observed, which was attributed to the misaligned work functions of the nanoparticles and the ITO. Therefore, the group introduced aluminum doped (2 mol%) zinc oxide (AZO) nanoparticles to act as a buffer, thereby eliminating the extraction barrier. Anti-reflection coatings (MgF_2) were used on both sides of the semi-transparent cell. The resulting semi-transparent perovskite solar cell had an area of 0.66 cm^2 and a V_{OC} of 952 mV, a J_{SC} of 16.5 mA/cm^2, and a FF of 77 % (PCE = 12.3 %). The semi-transparent perovskite solar cell was then mechanically stacked onto a monocrystalline silicon bottom cell in a 4-terminal tandem configuration, resulting in a power conversion efficiency of 18.0% and a current density of 13.3 mA/cm^2.
Fu and colleagues demonstrated a similar approach [98]. They deposited an ZnO:Al front-electrode onto a ZnO nanoparticle buffer by radio frequency magnetron sputter deposition. The ZnO nanoparticle buffer protected the PCBM electron selective contact. Their resulting semi-transparent perovskite solar cell had an active area of 0.286 cm^2, an average transmittance of 80.4% between 800 and 1200 nm wavelength range, and a V_{OC} of 1.116 V, a J_{SC} of 19.1 mA/cm^2, and a FF of 75.4 %, resulting in a PCE of 16.1 %. Their mechanically stacked perovskite/CIGS 4-T tandem solar cell achieved a PCE of 22.1 % and filtered bottom cell current density of 12.1 mA/cm^2.

Table 2.2: List of discussed semi-transparent perovskite single junction solar cell parameter. The substrate-contact design is not shown. Illumination in all cases was carried out through the ETL. For the sake of space, we refer to Spiro-MeOTAD simply as Spiro in the following list.

PSC design	V_{OC} (mV)	J_{SC} (mA/cm^2)	FF (%)	PCE (%)	ref.
$MAPbI_3$/Spiro/MoO_x/ITO	821	14.5	51.9	6.2	[94]
$MAPbI_3$/Spiro/AgNWs	1025	17.5	71	12.7	[95]
$MAPbI_3$/Spiro/MoO_x/IZO	870	17.51	68	10.3	[96]
$MAPbI_3$/Spiro/IZO	938	17.4	59.6	9.7	[96]
$MAPbI_3$/Spiro/MoO_3/IO:H	1104	17.4	73.6	14.1	[53]
$MAPbI_3$/Spiro/IO:H				10.1	[53]
$FACsPb(I_{0.6}Br_{0.4})_3$/Spiro/$ITO_{np}$/ITO	1100	19.9	70.7	15.1	[97]
$MAPbI_3$/PCBM/AZO_{np}/ITO	952	16.5	77	12.3	[28]
$MAPbI_3$/PCBM/ZnO_{np}/ZnO:Al	1116	19.1	75.4	16.1	[98]

2-T tandem solar cells

Monolithic tandem solar cells with a 2-T connection require fewer layers than mechanically stacked tandem solar cells. Consequently, they exhibit significantly less parasitic absorption losses. However, in the monolithic 2-T tandem solar cells, both sub-cells are connected in series, and the smallest current of both cells limits the total current of the final 2-T tandem device. Therefore, it is necessary to adjust the current of both cells by optical design optimization.

The first monolithically connected perovskite/silicon tandem solar cell was designed in 2015 by Mailoa et al. [99]. However, it had silver nanowires as a transparent front contact, leading to similar stability issues described earlier in this chapter. Half a year later, Albrecht and colleagues demonstrated the first-ever monolithic 2-T tandem solar cell with TCO as the front contact, producing a stable efficiency of 18.1 % at an active area of 0.27 cm^2 [100]. This monolithic 2-T tandem solar cell had a perovskite top cell in normal structure. The front contact, an 80 nm thick amorphous ITO, was applied using RF magnetron sputter deposition at a power of 70 W from a ceramic target at room temperature onto a 27 nm thermally evaporated MoO_3-buffer layer, protecting the Spiro-OMeTAD. Consequently, illumination through the HTL interface led to significant parasitic absorption.

By the end of 2015, Werner et al. developed a monolithic perovskite/crystalline silicon tandem solar cell with an efficiency of 21.2 % at an active cell area of 0.17 cm^2 and 19.2 % at an active cell area of 1.22 cm^2, respectively [101]. The perovskite sub-cell in normal structure was deposited on a double-side mirror-polished silicon wafer, connected through an IZO recombination layer. The top contact, a 110 nm IO:H/ITO bilayer, was

sputter deposited on the Spiro-OMeTad, which was protected by a 10 nm thermally evaporated MoO_x buffer layer. Reflection losses were reduced by the application of microtextured anti-reflective foils (ARF) on the front side of the cells, improving the Jsc from 13.65 mA/cm^2 to 15.9 mA/cm^2. However, the cells still suffered from a current loss of ~1.5 mA/cm^2 within the perovskite sub-cell, reportedly caused by parasitic absorption in the Spiro-OMeTad and darkened MoO_x-buffer layer.
Bush *et al.* significantly reduced the parasitic losses in their 2-T tandem solar cell by combining an inverted perovskite stack with a single-side-textured silicon wafer [102]. By utilizing an inverted perovskite solar cell stack, they circumvented the earlier problems of parasitic absorption by Spiro-OMeTAD and darkened MoOx films. This novel approach resulted in a certified 23.6% tandem PCE. The front electrode was composed of a 150 nm thick ITO electrode and an ALD-deposited ZnO/SnO_2 bilayer (ZTO) that served as a buffer layer. The ITO was deposited using a DC magnetron sputtering process at room temperature and a ceramic target (90:10 In_2O_3:SnO_2 wt.%). The remaining current losses were assigned to front-surface reflection and parasitic absorption in the front electrode. The sub-cell currents for the perovskite and silicon parts were 18.9 and 18.5 mA/cm^2, respectively.
In 2018 Sahli and colleagues designed a fully textured perovskite/silicon tandem solar cell with a certified power conversion efficiency of 25.2%, thus setting a new world record [103]. Instead of using an ITO front electrode, they took advantage of the remarkable optoelectronic properties of room-temperature sputtered amorphous IZO, as previously reported by the same group. The ETL C_{60} was protected from sputter damage by a 10 nm ALD-deposited SnO_2 buffer layer. The 110 nm thick IZO electrode was sputter-deposited in an RF sputter process with a power of 70 W, using a 4-inch ceramic target (90% In_2O_3 + 10% ZnO). As a consequence of reduced reflection losses, the integrated current densities of the double-side-textured tandem solar cell were as high as 20.1 mA/cm^2 for the perovskite sub-cell and 20.3 mA/cm^2 for the silicon sub-cell.
As mentioned earlier, textured light management (LM) foils improve the tandem solar cell current. In combination with a back-side-textured silicon bottom cell, Jošt et al. were able to fabricate a monolithic perovskite/silicon tandem solar cell with a power conversion efficiency of 25.5%. The transparent top electrode consisted of room temperature deposited IZO, sputtered in an RF process with a power of 70 W from a 2-inch ceramic target (90 wt% In_2O_3 and 10 wt% ZnO). The C_{60} electron transport layer was protected by a 20 nm SnO_2 buffer layer, prepared by thermal ALD. The reflection losses were decreased by 3.65 mA/cm^2 thanks to the use of the LM foil, resulting in integrated current densities of 20.21 mA/cm^2 for the perovskite top cell and 18.88 mA/cm^2 for the silicon bottom cell. Optical simulations within the same report showed a theoretical PCE potential of this device design of 31.5%. The main losses were identified as parasitic absorption in IZO, in the C_{60} ETL, in the ITO recombination layer, the back contact,

the total reflection, and the non-optimized perovskite band gap and thickness. They suggested that using a less absorptive front TCO material such as the high mobility, low carrier density TCO IO:H, and replacing C_{60} with a less absorbing material can potentially reduce losses further. Later, the same group set a new efficiency world record for a monolithic perovskite/silicon tandem solar cell with a PCE of 29.1% [104]. This was accomplished by lowering nonradiative recombination by interface engineering, thereby boosting the FF and V_{OC}. In addition, they performed electrical simulations, which predicted a potential efficiency of 32.43% under current-matching conditions and decreased transport losses. In 2021, the group again set a new world record PCE of 29.80%, combining earlier efforts with reduced reflection losses [105]. The optical improvement resulted from tailor-made sinusoidal nanotextures at the perovskite/silicon interface.
As presented in Tab. 2.3, in recent years, the front electrode stack design did not change, despite reports claiming that there is potential for parasitic absorption reduction. This work addresses this topic, among other things.

Table 2.3: List of discussed monolithic perovskite-based tandem solar cell parameter. For the sake of space, only top-contact design is shown, thorugh which illumination was carried out. We refer to Spiro-MeOTAD simply as Spiro in the following list. *larger active area of 1.22 cm^2.

front electrode design	$J_{SC,EQE}$ (mA/cm^2)	V_{OC} (mV)	FF (%)	PCE (%)	ref.
Spiro/AgNWs/LiF	11.5/14.7	1580	75	13.7	[99]
Spiro/MoO_3/ITO/LiF	14.67/14.01	1785	79.5	19.9	[100]
Spiro/MoO_x/ITO+IO:H/ARF	16.4/15.6	1692	79.9	21.2	[101]
Spiro/MoO_x/ITO+IO:H/ARF	16.8/17.4	1703	70.9	19.2	[101]*
PCBM/ZTO/ITO/LiF	18.9/18.5	1650	79.0	23.6	[102]
C_{60}/SnO_2/IZO/MgF_2	20.1/20.3	1788	73.1	25.24	[103]
C_{60}/SnO_2/IZO/LM foil	20.21/18.81	1760	78.5	25.5	[106]
C_{60}/SnO_2/IZO/LiF	19.41/20.18	1900	79.52	29.15	[104]
C_{60}/SnO_2/IZO/LiF	20.03/19.88	1900	79.4	29.8	[105]

Chapter 3

Materials and methods

3.1 Sample and device preparation

3.1.1 Indium zinc oxide layer preparation

For optical and electrical analysis of the TCO, 100 nm thick IZO layers were sputter deposited via RF magnetron sputtering in a Roth&Rau MicroSys 200 PVD system on quartz glass substrates. The target used had a size of 2 inches and a composition of 90 wt.% In_2O_3 and 10 wt.% ZnO (purchased from FHR Anlagenbau GmbH). Two RF power densities were investigated for the sputter damage reduction experiments, 4.21 W/cm^2 and 2.41 W/cm^2. Both processes were dynamic, meaning the substrate oscillates at a 30° angle below the target surface at a distance of approximately 17 cm. The process pressures used were 6×10^{-3} mbar (which is the standard process pressure) and 1.2×10^{-2} mbar, and the base pressure prior to the sputter deposition was in the 10^{-7} mbar range. The argon/oxygen gas flow ratio in each case was in sum 40 sccm. The precise ratio is stated for the respective oxygen series experiments.
In Chapter 4.2 and 4.3 the IZO was mostly prepared via RF magnetron sputtering in a "Multifunktionssputteranlage" *FHR-MS150x4 S* by FHR Anlagenbau GmbH. In this work we refer to this sputter tool as *Vinci tool*. The target used had a size of 4 inches and a composition of 90 wt.% In_2O_3 and 10 wt.% ZnO (purchased from robeko GmbH & Co. KG). The process pressure used was 6×10^{-3} mbar, and the base pressure prior to the sputter deposition was in the 10^{-7} mbar range. The RF power was 150 W (1.85 W/cm^2) and the argon/oxygen gas flow ratio was 0.167%.

3.1.2 Single-junction solar cell preparation

The discussed semitransparent perovskite single-junction solar cells were in inverted structure (p-i-n). In Chapter they had the following design: commercial laser-patterned ITO coated glass substrates/2-PACz/perovskite/LiF/C_{60}/PEIE/IZO/Ag fingers, whereas the reference cells had an additional SnO_2-buffer layer between the PEIE and the IZO. And in Chapter they had the following design: commercial laser-patterned ITO coated glass substrates/2-PACz/perovskite/LiF/C_{60}/interlayer/IZO/Ag fingers, where the interlayer was either SnO_2, PEIE, or no interlayer. The Ag fingers are located outside the active area and shorten the charge transport path over the IZO. The ITO-coated glass substrates (25 x 25 mm, 15 Ω/sq, laser-patterned by Automatic Research GmbH) were cleaned in Mucasol (2%vol in water, substrate surfaces were rubbed with a glove), DI-water, acetone, and isopropanol subsequently, in an ultrasonic bath. Each step was carried out for 10 min, and after Mucasol, the samples were purged with DI-water. Prior to the 2-PACz ([2-(9H-carbazol-9-yl)ethyl]phosphonic acid) spin-coating step, the samples were treated in a UV-ozone cleaner (FHR UVOH 150 Lab) for 15 min. The HTL 2-PACz (TCI) was dissolved in ethanol (1 mmol/l ml solution) and spin-coated (5 s acceleration at 3000 rpm, 15 s duration at 3000 rpm) in a nitrogen atmosphere and annealed for 5 min at 100 °C. The 1.5 M perovskite precursor was prepared in a FAPbI3 to MAPbBr3 volume ratio of 77:23, with 5 vol% of 1.5 M nominal CsI. The precursor components FAI and MABr were purchased from Dyenamo, PbI2 and PbBr2 from TCI, and CsI from abcr GmbH. The precursor was then dissolved in DMF:DMSO = 4:1 volume and placed in a shaker for 90 min at 60°C. Subsequently, 100 μl of perovskite solution was spin-coated (5 s acceleration and 35 s duration at 3500 rpm) in a nitrogen atmosphere. After 25 s of the spin-coating process, 300 μl of the anti-solvent Anisole was dropped on the perovskite film. The resulting perovskite absorber has a thickness of ~550 nm and a band gap of 1.68 eV. Following the spin-coating step, the films were annealed at 100 °C for 20 min. The subsequent two layers were done in one vacuum run. 1 nm LiF (Sigma Aldrich) passivation layer was thermally evaporated at a rate of 0.05 Å s^{-1} onto the perovskite film, directly followed by the ETL, 18 nm C_{60} (CreaPhys GmbH) layer at a rate of 0.15 Å s^{-1}. Before IZO sputter deposition, a thin film (~ 2 nm) of polyethyleneimine ethoxylated (PEIE) with a concentration of 0.025 wt.% (original solution in water 37 wt.% diluted with IPA) was spin-coated (1 s acceleration at 5000 rpm, 15 s duration at 5000 rpm) onto the C_{60}. After the sputter deposition of 100 nm IZO (described above) through a 2-stripes shadow mask, 100 nm Ag was thermally evaporation through a specific mask that only contacts the IZO, without shading the active area, at a rate of 1 Å s^{-1}.

3.1.3 Monolithic 2-terminal tandem solar cell preparation

The silicon bottom-cells for the tandem devices were manufactured following a similar fabrication process as described by Cruz *et al.* [107], if not stated otherwise. The bulk silicon consisted of a 260 μm float zone (FZ) Wafer with a resistivity of ~1-3 Ωcm. The (n)nc-SiO:H layer in-between the 5 nm thick (i)a-Si and the TCO-recombination layer had a thickness of 100 nm. The backside (i)a-Si had a thickness of 5 nm. The front side electrode (recombination layer in a tandem device) was 20 nm of InO:H-based TCO film from newSCOT. The rear side electrode consisted of a 110 nm thick InO:H-based TCO film from newSCOT and 400 nm silver. No grid was used on either side. Instead, the active area had a size of 1.1 cm^2, defined by the silver and TCOs. The bottom cell was backside textured, and the front was polished. Also, no SiO_2 film was deposited on the recombination layer. The perovskite top-cells for the tandem devices were prepared similarly, if not stated otherwise, as described above and by Al-Ashouri et al. [65]. The silicon bottom cell was blow-cleaned with a nitrogen gun and washed with ethanol. Subsequently, the ITO surface of the bottom cells needs to be treated in a 15 min UV-ozone treatment step before spin-coating the HTL. The HTL used for the tandem device fabrication was Me-4PACz dissolved in ethanol (3 mmol solution), while the perovskite solution preparation is equal to the one described before. The anti-solvent used for tandem devices was ethyl acetate, which results in a thicker perovskite film of ~600 nm. For the devices with tin oxide (SnO_2) buffer, 20 nm SnO_2 was deposited onto the C_{60} via thermal atomic layer deposition (ALD, in an Arradiance GEMStar reactor) instead of PEIE prior to IZO sputter deposition. The Ag frame used to contact the IZO was evaporated through a rectangular-shaped mask around the edges and on top of the IZO electrode, forming the active area of 1 cm^2. Subsequently, 100 nm of LiF anti-reflective coating was thermally evaporated.

3.1.4 Perovskite samples preparation

Perovskite samples that were used for contact angle measurements or the in-situ GISAXS sputter deposition experiments in Chapter were prepared equivalent to the preparations described above in section 3.1.2 without depositing the front electrode stack (no IZO, Ag, or LiF anti-reflection). The IZO deposition was part of the in-situ experiment and will be detailed in Chap. 4.2.

3.2 Characterization techniques

In this section, information on the characterization techniques utilized is provided.

3.2.1 Material characterization

Spectrophotometry
Spectrophotometry or ultraviolet–visible-near infrared (UV-Vis-NIR) spectroscopy is a technique to measure reflection (R) and transmission (T) of thin films, stacks or devices. This technique is particularly convenient to measure key traits of TCOs. In this study, we used a Perkin Elmer *Lambda - 1050* spectrophotometer. The setup consists of a light source (halogen and deuterium lamps), a monochromator, and an integrating sphere. Depending on the sample, the measurement can be conducted in a spectral range of 250 nm to 2450 nm. The measured spectra are all given in relation to a calibration measurement. The calibration measurement is performed without a sample placed in the beam path. Calibrating the reflection measurement requires a white standard or mirror. The absorption (A) of a sample can be calculated with

$$A(\lambda) = 1 - R(\lambda) - T(\lambda) \tag{3.1}$$

Profilometry
The thicknesses of sputter-deposited thin films were evaluated by *DektakXT* profilometer by Bruker. Therefore, it is necessary to have "step" in the film profile on the substrate, which was achieved by applying kapton tape on the substrate.

4 point probe
A 4 point probe setup is conveniently used to determine a film's sheet resistance. The setup measures the electrical resistance with particularity to disregard the contact resistance between the metal needles and the measured film, which would falsify the results. This is achieved using four needles at an equidistant distance in a row. Two needles inject the current into the film while the other two measure the voltage drop. As a result, the current injection and voltage measurement happen in two different circuits. The sheet resistance is determined using

$$R_{sq} = \frac{\pi}{ln(2)} \frac{U}{I} = \frac{\rho}{d} \tag{3.2}$$

ρ is the specific resistivity, a material property independent of the layer's dimensions, which is obtained by multiplying the sheet resistance with the film thickness d. In this work, we measured the sheet resistance with a Jandel RM3-AR setup utilizing a probe head of 1 mm needle to needle spacing, a tip radii of 100 μm, and a load of 100 g.

Hall effect measurements
For quantifying (semi-)conducting thin films it is often important to know their resistivity (ρ), carrier concentration (N), and carrier mobility (μ). By using Hall measurements in the van der Pauw geometry [108], these values can be extracted. In this work, the

Hall measurements were performed with the system *HMS-3000* from Ecopia. On each corner of the sample surface, four contact needles are mounted. In relation to the sample size, the contacts must be small. Also, the film needs to be smooth, without holes or cracks, and homogeneous to get reliable results.

Spectral Ellipsometry
Ellipsometric spectra were recorded with a Sentech SE850 DUV variable angle spectroscopic ellipsometer. Optical spectra were fitted using the software RIG-VM [109]. From this method information on the film thickness was retrieved, as well as n,k data for optical simulations. Details on fits done in this theses can be found in the Supplementary section 6.3.

Scanning electron microscopy (SEM) and Energy Dispersive X-ray Spectroscopy (EDS) Measurements
Scanning electron microscopy (SEM) measurements were used to capture high-resolution pictures of sample surfaces or cross sections of layer stacks. The SEM measurement principle uses focused beams of electrons to image the surface/cross-section of a sample with nm-level resolution with kinetic energies in the keV range. More in-depth explanation can be found in [110]. The SEM measurements for this thesis were performed using the Zeiss Merlin Field Emission SEM with a Gemini 2 microscope equipped with an InLens detector for secondary electron (SE) detection along the optical axis. Additionally, energy dispersive X-ray spectroscopy (EDS) was carried out inside the microscope utilizing an accelerator voltage of 6 kV and a windowless silicon drift detector from Oxford Instruments called the Ultimate Extreme.

Contact angle measurements
Contact angle measurements were performed using the sessile drop method with a Krüss 100 drop shape analysis system in air. Two solutions were used, a dispersive (water) and a polar (diiodo-methane) solution. For both, averaged values from several measurements were used to determine the mean contact angles. The surface energy was calculated following the Owens-Wendt method (detailed information can be found in [111]), which is the sum of the dispersive and polar components calculated from the respective contact angles.

Grazing incidence small angle x-ray diffraction scattering
Grazing incidence small angle x-ray diffraction scattering (GISAXS) experiments are performed using the 2D Pilatus 2M detector at a sample-detector distance (SDD) of 3355 mm at the P03 beamline at DESY (Hamburg, Germany). The detector pixel size was 172 $\times$ 172 μm^2. The X-ray wavelength was λ = 0.1048 nm at an incident photon energy of 11.8 keV and an incidence angle of α_i = 0.4°. The detector is positioned in a large SDD of

a few meter to resolve small scattering angles and, consequently, nanoscale structural details. An evacuated flight tube between the sample (apparatus) and the detector is set up to minimize air scattering throughout the long X-ray path. Beamstops are positioned at the direct and specularly reflected beam positions to prevent the detector from oversaturation. The micro-focused X-ray beam is directed onto substrates at a defined grazing incidence angle. Any variation in the near-surface regime's roughness or electron density causes diffuse scattering of the signal with a certain intensity in horizontal direction (q_y-direction) as a function of the out-of-plane angle ($I(2\Theta_f)$) or in vertical direction (q_z-direction) as a function of the exit angle ($I(\alpha_f)$) [112]. In evaluating the 2D data, the key scattering features are analyzed using the DPDAK v1.5.0 software and fitted using a suitable model [113]. Therefore, the 2D data is translated into 1D cuts in either q_z- or q_y-direction. Extractable information on the cluster center-to-center distances (D) or cluster radii (R) can be found in the q_y-direction (out-of-plane at the substrate Yoneda peak position). At the same time, the height of nanoparticles, roughness, and layer thickness are visible in the q_z-direction (off-detector at $q_y \neq 0$ nm^{-1}). The Yoneda region is defined by a material's critical angle. The data modeling is based on a model assuming spherical form factors. More in-deph information can be found in [112, 114–116].

3.2.2 Device characterization

Current density-voltage measurements

Current density-voltage (J-V) measurements enable the essential characterization of solar cells, providing J_{SC}, V_{OC}, FF, and η. A solar cell's current output is extracted as a function of applied voltage in the dark or under light. The illumination is typically produced by lamps replicating an AM1.5G irradiation with a 1000 W/m^2 intensity.
The J-V measurements in chapters 4.1.2 and 4.2.1 (excluding the light intensity dependent measurements) were conducted with a custom setup inside a glovebox with an inert atmosphere. The illumination was provided by an ABB sun simulator of the Oriel class calibrated to the J_{SC} of a calibrated silicon solar cell (2×2) cm^2 in size (Fraunhofer ISE). With a scan rate of 0.4 V/s, the voltage was swept in 0.02 V steps from 1.4 to -0.2 V (in the "reverse" direction) and back (in the "forward" direction) using a digital source measure unit (SMU) (Keithley 2400) in a two-wire arrangement. The solar cells were maintained at a constant temperature of 25°C.
Tandem solar cell J-V and maximum power point (MPP) measurements in chapter 4.3 as well as the light intensity dependent J-V measurements of the single junction solar cells in chapters 4.1.2 and 4.2.1 were carried out on a Wavelabs LED-based Sinus 70 sun simulator (class AAA), at 25 °C, 0.25 V/s scan rate, and 0.02 V voltage step-size. Before the measurement, the spectrum was corrected using a calibrated silicon reference cell. A sample holder with a hole was used for the semitransparent single-junction solar cells

J-V measurements, allowing measurements from both sides by simply turning the holder around. Back-reflection from surfaces of or behind the holder was not intentionally suppressed.

External Quantum Efficiency

The spectral incident photon-to-electron conversion efficiency of a solar cell is acquired by external quantum efficiency (EQE) measurements. The EQE describes the percentage at which incident photons generate electron-hole pairs that contribute to extracted charges. Ideally, every incident photon of a particular wavelength generates an electron-hole pair. Theoretically, the EQE would be 1 (100 %) if all the generated charges were extracted at the electrodes due to an applied bias. In reality, the solar cell EQE spectrum is reduced by losses resulting from reflection, parasitic absorption, or inefficient charge collection [63]. The respective contributions can be revealed by comparing the EQE spectra with the spectrally resolved reflection of the samples.
The ratio between the extracted photo-generated charge carrier current ($J_{photo}(\lambda)$/q) and the spectral photon flux ($\Phi(\lambda)$) of the light source reaching the sample leads to the formula describing the EQE following [63] is:

$$EQE(\lambda) = \frac{J_{photo}(\lambda)}{q \cdot \Phi(\lambda)} \tag{3.3}$$

It is also possible to calculate an EQE-integrated short-circuit current density ($J_{SC,EQE}$) by integrating EQE spectra with the spectral photon flux of the AM1.5G spectrum ($\Phi_{AM1.5G}$):

$$J_{SC,EQE} = q \cdot \int EQE(\lambda) \cdot \Phi_{AM1.5G}(\lambda) d\lambda \tag{3.4}$$

In this work, the single-junctions EQE was measured with a QE-R apparatus from Enlitech, while the tandem devices EQE was measured by an in-house designed setup. A small illumination spot (2 x 5 mm2) was directed to the active area of the tandem device. The measurement was carried out as a function of wavelength in a range of 300 - 1200 nm (in 10 nm steps). By applying a bias light, the sub-cells are measured independently. Specifically, the top cell is measured applying a bias light of 850 nm wavelength and a voltage of 0.6 V, and the bottom cell is measured applying a bias light of 455 nm wavelength and 0.9 V bias voltage. While the single single-junctions EQE was used to extract the exact short circuit densities and correct the J-V measurements of respective devices, the tandem EQE measurements of each sub-cell are essential to perform spectral mismatch corrections during tandem J-V measurements (more detailed information can be found in [117]).

Transient optoelectrical measurements with the *Paios* (FLUXIM AG, Switzer-

land) characterization tool

The all-in-one characterization instrument *Paios* (FLUXIM AG, Switzerland) is a tool that uses several steady-state and transient optoelectronic characterization techniques. In this work, it has been used to investigate the impact of the ETL/TCO interface on device parameters by analyzing, for example, the charge carrier extraction mobility, the extracted charge carrier density, or the transient voltage behavior. These parameters can then further be correlated to phenomena such as traps, barriers, or interfacial charge-transfer resistivity.
The automated tool's light source is controlled by a function generator (a white LED). The specs of the light source are given in Tab. 3.1. The output is a current or a voltage of the measured solar cell, which is measured using a digitizer.

Table 3.1: FLUXIM *Paios* light source specs.

LED rise time	100 ns
Illumination area	1.7 cm^2
LED current	100 mA
Total optical power	60mW
Color	white

For the interpretation of the data measured by the all-in-one characterization instrument *Paios*, we make some considerations that are presented in the following.
A solar cell can be understood as a device with two electrodes and a dielectric in-between. Mathematically this is expressed by a geometric capacitance (C_{geom}). If the voltage applied to the capacitance is changed over time, the current in the capacitance changes proportionally to the voltage according to:

$$i(t) = C_{geom} \cdot \frac{dV}{dt} \tag{3.5}$$

For transient photocurrent (TPC) measurement, the current response of the solar cell device to a light pulse is measured. As the photogenerated charges leave the device they are collected in an external circuit. The time constant derived from the rise and decay time of the current response is linked to the carrier transport time (charge carrier mobilities) [61, 118]. Furthermore, trapping dynamics can be revealed. For the TPC measurement the solar cell devices were illuminated with light pulse of 200 ms and the transient current was measured. Two regions can then be identified, the TPC rise, and TPC decay region. The respective time constants are calculated from the current rise regime before a steady-state is reached, and from the decay region, before the current reaches zero. Each system can furthermore be described by a characteristic RC-time constant, which determines the smallest meaningful timescale that can be attributed to

a process. The RC-time constant is calculated from the solar cells series resistance and geometric capacitor. In a circuit with a resistance in series (R_s) and $\frac{d}{dt}$ expressed as a time constant τ, the RC-time constant can be calculated according to the equation:

$$\tau_{RC} = C_{geom} \cdot R_s \tag{3.6}$$

The geometric capacitance can be generally described by:

$$C_{geom} = \epsilon_0 \epsilon_r \cdot \frac{A}{d} \tag{3.7}$$

Where d is the active layer thickness, or the distance between the device's electrodes respectively. When inserting Equ. 3.7 in Equ. 3.5 and expressing the current by a current density instead, we get:

$$j(t) = \frac{1}{A} \cdot \frac{dV}{dt} \cdot C_{geom} = \frac{1}{A} \cdot \frac{dV}{dt} \cdot \frac{\epsilon_0 \epsilon_r \cdot A}{d} \tag{3.8}$$

In CELIV, the voltage is linearly increased by a defined ramp rate, and the change in voltage over time is constant (dV/dt = const.). Consequently, the displacement current (j(t), Equ. 3.8) will be also constant. We can replace the time-dependent voltage in Equ. 3.8 V(t) = R_{ramp}·t. Then the constant displacement current will be calculated according to:

$$j_d = \frac{R_{ramp} \cdot \epsilon_0 \epsilon_r}{d} \tag{3.9}$$

To understand the retrieved parameters, refer to Fig. 3.1, which shows an illustrated example of a photo-CELIV measurement. The term "photo-CELIV" refers to the process of using a light pulse to photogenerate charges in the device. In this work, dark and photo-CELIV measurements were both performed. The lower graph in Fig. 3.1 shows charge carriers being extracted from the photoactive layer, which is visible as a peak in the transient current response. The maximum extraction current is denoted as Δj, and the time corresponding to it is given as t_{max}.

From dark-CELIV measurements, the relative dielectric permittivity can be calculated, when the displacement current is measured:

$$\epsilon_r = \frac{d \cdot j_d}{R_{ramp} \cdot \epsilon_0} \tag{3.10}$$

The CELIV carrier mobility can be calculated from the time, where the measured current from the extracted (photogenerated) charges leads to a peak (J_{max} at the time of t_{max})[119]:

$$\mu = \frac{2d^2}{3R_{ramp} \cdot t_{max}^2 (1 + 0.36 \Delta j / j_d)} \tag{3.11}$$

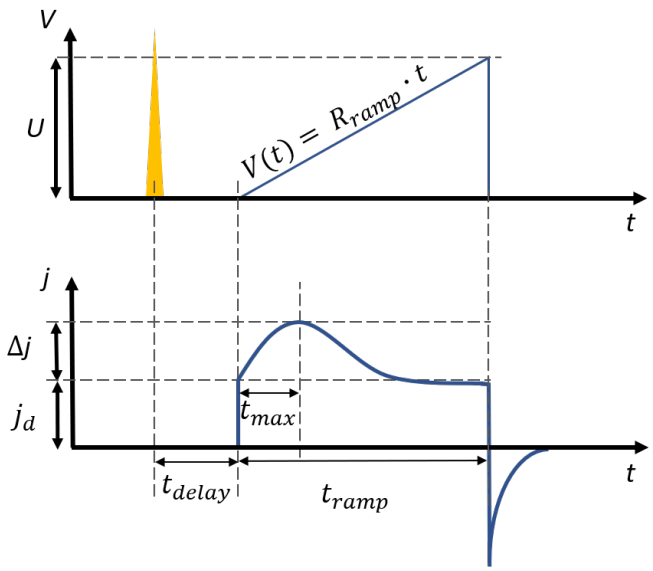

Figure 3.1: Illustration of a CELIV measurement depicting the voltage ramp and the device's current response. The drawing is based on [63].

where Δj is equal to j_{max} - j_d and the factor $1 + 0.36\Delta j/j_d$ takes into account an empirical correction, accounting for extraction length of photogeneration in the device's volume. We need to state here, that the calculated charge mobilities from CELIV are not necessarily bulk mobilities, as the signal (as exemplary shown in Fig. 3.1) is derived from charges that passed through the extraction layers of the solar cell device.

In the charge carrier extraction experiment, the solar cell is illuminated and maintained under predetermined conditions, which are open-circuit conditions (no charge extraction) in this work. Once in steady-state, the solar cell's light source is turned off, and the device is switched to short-circuit simultaneously (charges are extracted now). An extraction current ($j(t)$) is measured. The concentration of the extracted charge carrier density n_{CE} is then calculated by integrating the extraction current over time, according to the following equation:

$$n_{CE} = \frac{1}{d_{SC} \cdot q} \cdot \left(\int_0^{t_e} j(t) \cdot dt - (V_a - V_e) \cdot C_{geom} \right) \tag{3.12}$$

where d is the solar cell device thickness (or the distance between the electrodes that sandwich the dielectric medium), $0 - t_e$ is the time of charge extraction, $j(t)$ is the time-dependent diplacement current density (following Equ. 3.8), V_a is the initially applied voltage (here V_{OC}), V_e is the voltage during extraction, and C_{geom} is the geometric capacitance.

Open-circuit voltage decay (OCVD) and transient photovoltage (TPV) are related measurements based on similar considerations. In both cases, the recombination and trapping dynamics are being investigated due to probing the device under open-circuit

conditions. For OCVD, the voltage response of a solar cell kept in steady-state to a light pulse of 50 ms, with a light intensity of 90%, is measured. Then the normalized voltage decay over time is analyzed.
The TPV is a response to a light pulse in order to determine charge carrier lifetimes. Therefore, the measured device is kept at open-circuit conditions. A small light pulse (of 1 ms) leads to generation of charges, hence a transient voltage signal $\Delta V_{OC}(t)$. When these charges recombine, an exponential voltage decay is observed. This decay can give details about the recombination dynamics inside the device, as different recombination rates correspond to different free carrier concentrations within the voltage decay time [63], according to the correlation:

$$R(n_{e,h}) \propto (n_e n_h)^{\beta/2} \tag{3.13}$$

where β is the reaction order of a recombination process. β_{SRH} = 1, for SRH recombination, β_{SRH} = 2, for radiative recombination, and β_{SRH} = 3, for Auger recombination. Consequently, the transient voltage decay is dominated by different recombination processes at different timescales. Arguably, this work's observed timescales of charge carrier lifetimes are not considered bulk carrier lifetimes, which are much shorter (nanosecond-scale) [120]. In fact, the observed decay features are considered to be capacitive discharging events [121]. Therefore, the dynamics that can be resolved with the measurements are instead an interpretation of the much slower recombination of electrons accumulated at the contacts. The voltage decay in a TPV experiment is defined as:

$$V(t) = V_{OC} + \Delta V \cdot exp(-t/\tau) \tag{3.14}$$

ΔV is the differential voltage response to the laser pulse and τ is the minority carrier lifetime as defined in equation 2.19. The time constants that can be extracted originate from different decay components in the photovoltage decay curve and represent different recombination dynamics of charge carriers [122].

As opposed to the time-dependent transient measurement techniques discussed above, impedance spectroscopy is a frequency-domain method. The strength of this method lies in the assumption that different effects inside the solar cell respond to different frequencies. Therefore, impedance spectroscopy can help to distinguish between different charge carrier processes in the device. In the illustration in Fig. 3.3 the correlation between the resolution of impedance spectroscopy and the timescale of charge carrier dynamics is shown. For the measurements, an AC voltage $\Delta V_{AC} = \Delta V \cdot e^{i\omega t}$ is applied to the solar cell, kept under steady-state conditions [63]. The current response

is measured, while the frequency ω is varied over several orders of magnitude. The impedance is calculated via:

$$Z(\omega) = \frac{\Delta V \cdot e^{i\omega t}}{\Delta I \cdot e^{i\omega t}} = \frac{\Delta V}{\Delta I} \tag{3.15}$$

An equivalent circuit model is used to represent the device in impedance spectroscopy.

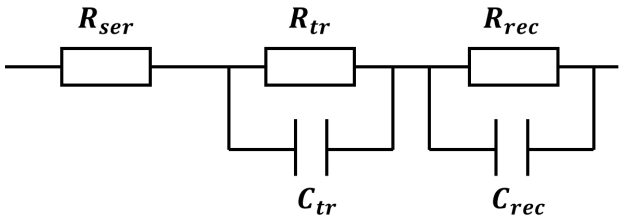

Figure 3.2: Illustration of a simple equivalent circuit model employing R_{ser}, R_{tr}, and R_{rec}.

The simplest model is a circuit with capacitors and various resistors, each representing a physical effect (a series resistance R_{ser}, a transport resistance R_{tr}, and a recombination resistance R_{rec}), such as shown in Fig. 3.2. A parallel circuit of a capacitor and resistor commonly represents the interface of two materials. The impedance of such circuit can be given as [63]:

$$Z(\omega) = \frac{R}{1 + (R\omega C)^2} - i \cdot \frac{R^2 \omega C}{1 + (R\omega C)^2} \tag{3.16}$$

At high frequencies (above 10^6 Hz) the capacitance is dominated by the RC-effect. Fast processes, like charge transport, or trapping/de-trapping, correspond to intermediate frequencies (10^3 Hz < x < 10^6 Hz) [123]. Whereas, in the low frequency region (below 10^3 Hz) slow processes like interaction of mobile ions (ion migration) and charge accumulation at the interfaces, and deep and slow traps can be traced [124].

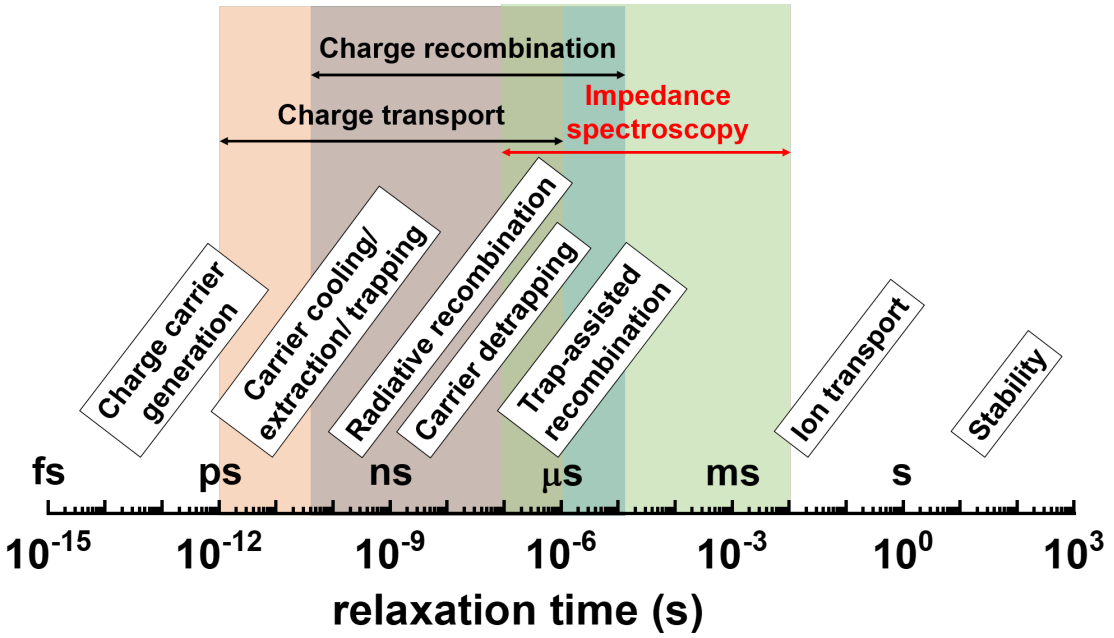

Figure 3.3: Timescale of charge carrier processes inside of a solar cell device, which highlights the range and phenomena covered by impedance spectroscopy.

3.3 Simulation

3.3.1 Electrical simulation

The electrical charge transport in solar cells may be simulated with a drift-diffusion model. As the name suggests, such a model can solve a semiconductor's drift and diffusion currents. This study uses the simulation program SCAPS [125] to examine the energy alignment between the C_{60} ETL and the transparent IZO electrode in a simplified HTL/perovskite/ETL stack, replicating a perovskite solar cells. The IZO electrode is represented by a variable work function in the left contact. For ease of analysis, the charge transport layers (CTL) are assumed to be transparent, and the optical absorption in the perovskite follows the Lambert-Beer law.

3.3.2 Optical simulation

Optical simulations were conducted using the MATLAB-based program GenPro4 [126]. Using a net-radiation method, GenPro4 estimated the absorption characteristics of the tandem layer stacks. The c-Si wafer was considered incoherent because, at 280 μm thickness, it greatly surpassed the coherence length of sunlight. The other layers, which had nanometer layer thicknesses, were treated as coherent. A random pyramid surface

texture was used to represent the back side of the c-Si wafer, and a ray-tracing model was used to simulate the adjacent interfaces. Every other layer on top was treated as optically flat. The J_{SC} loss analysis under AM1.5G illumination was computed using the absorption profiles of each layer. The source data for the simulation is presented in Tab. 6.2 in the appendix Chapter 6.3.

Chapter 4

Results and Discussion

4.1 Deposition of indium zinc oxide with focus on sputter damage reduction

Because of its remarkable optoelectrical properties and ability to be manufactured at ambient temperature without the need for post-deposition treatments, sputtered amorphous indium zinc oxide (IZO) is a promising electrode material [16, 17, 19, 127, 128]. However, the impact of sputter damage must be taken into account when sputtering TCOs onto sensitive materials, such as perovskite solar cells, without an adequate protective layer. Sputter damage is associated with highly energetic particles hitting the substrate (discussed in section 2.2.2), causing strain at the interfaces or damage to the crystal/atomic structure at or below the ETL/IZO interface, resulting in defects and deteriorated J-V characteristics [17, 48, 127–130]. Therefore, we modified the sputter deposition process to perform a soft (reduced energetic particle bombardment) IZO deposition. The soft sputter deposition process parameters were chosen with high energetic particle damage reduction in mind, based on the hypotheses in Chap. 2.2.2. Overall, the hypotheses declared that negatively charged oxygen ions are the primary causes of sputter damage, that they form at the target surface and accelerate away from it in a normal direction, and that their kinetic energy is in the range of the target potential.

The first approach that will be discussed in this chapter is the reduction of the sputter power. In this case, the sputter power density of the Roth&Rau MicroSys 200 PVD (the tool used for this work) which is usually set to 4.21 W/cm^2 for the standard process (1. line in Tab. 4.1), was almost halved to a power density of 2.41 W/cm^2 (2. line in Tab.

4.1). This leads to the target potential being reduced by ~25%. Since the flux and the energy of damaging particles are directly dependent on the target potential, the overall sputter damage must be reduced.
The second soft deposition approach (3. line in Tab. 4.1) investigated is an indirect coating process, where the substrate is laterally moved about 10cm away from its original position, which was under the target and at the edge of the substrate plate, to its center - away from the target. This leads to two beneficial effects: 1. the distance from the substrate to the target increases by about 3cm, which increases the possibility of collision between the damaging target particles and the sputtering gas, and 2. moving the substrate away from the area which is directly opposing the target. Hence, the sensitive substrate surface no longer directly faces the target erosion area (not at a 90° impact angle), where a high intensity of the damaging ion flux is expected [49, 50, 52]. As described before, the damaging ions leave the target perpendicular to its surface and are accelerated in normal direction, which depends on the depth of the race track erosion [49, 52, 131–133].
The third soft sputtering approach (4. line in Tab. 4.1) aims to reduce the effective mean free path length, which is inversely proportional to the process gas pressure, using the thermodynamic principles of the kinetic theory of ideal gases. By increasing the gas pressure from 0.6 to 1.2 Pa, the mean free path length of sputtered atoms is expected to be cut in half, thereby increasing the probability of kinetic energy-reducing collisions. However, certain sputtered particles need some energy when arriving at the substrate surface to diffuse and allow for dense thin film growth. Therefore, decreasing the particle energy, increasing the substrate to target distance, or decreasing the mean free path length may also impact the thin film growth.
The following examines how these soft IZO deposition techniques affect the optical and electrical film characteristics and how sputter damage and the suggested low-damage techniques impact the solar cell parameters of single junction perovskite solar cells.

Table 4.1: Process parameters of investigated sputter deposition techniques and the induced negative bias voltage, which depends on the electron and ion flux to the target.

Process	power density (W/cm^2)	process pressure (Pa)	substrate - target positioning	bias (V)
1. standard	4.21	0.6	direct	196
2. low power	2.41	0.6	direct	142
3. indirect	4.21	0.6	indirect	196
4. high pressure	4.21	1.2	direct	208

4.1.1 Impact of soft sputter deposition techniques on the optical and electrical film properties

In this section, we will compare the optical and electrical properties of IZO thin films deposited by soft sputtering deposition approaches to the standard sputtering procedure. First, however, all approaches are optimized based on the added oxygen during the deposition process. Subsequently, a direct comparison of thin films deposited by chosen parameter sets is made to investigate the impact of the soft deposition on the layer quality.

The free carrier concentration, electron mobility, and resistivity of a-IZO thin films sputter-deposited on glass substrates by applying the deposition approaches from Tab. 4.1 were determined by means of Hall effect measurements and are presented in Fig. 4.1 in dependence of the oxygen partial pressure. Oxygen is supplied during the deposition to achieve the desired film stoichiometry of the IZO thin films. We varied the oxygen partial pressure in five steps for each sputter deposition process. Because each deposition approach required a different amount of additional oxygen to achieve similar stoichiometry, we adjusted the oxygen partial pressure range covered by those five steps for each deposition approach. Different reasons are responsible for this: high sputter power leads to a higher target surface temperature and consequently more oxygen gassing out from the target surface, which is lost to the pump. Also a higher sputtering rate leads to more sputtered particles arriving at the substrate surface which requires more oxygen to achieve the required stoichiometry. A higher pressure results in more gas particles, and consequently the amount of additional oxygen increases compared to the sputtered particles.

In Fig. 4.1 a generally similar trend can be observed for each case. The free carrier concentration of the films was found to decrease as the oxygen supply increased, presumably because more oxygen atoms were incorporated into the films. As a result, the number of oxygen vacancies V_O^{++}, which are known to act as double-charged donors, drops. According to Ito *et al.*, oxygen vacancies or interstitial Zn^{2+} ions are the sources of the charge carriers in IZO [20]. While Leenheer *et al.* concluded that the carrier concentration is rather dependent on the oxygen content during sputtering and is less dependent on the metal ratio In:Zn [11], which is in line with observations proposed by others [19, 21, 22].

Differences can be observed in the trends in electron mobility. On the one hand, electron mobility rises steadily over the experimentally investigated oxygen range in both the standard (Fig. 4.1 in red) and low power processes (Fig. 4.1 in dark blue), from 32.69 cm2/Vs to 53.45 cm2/Vs and 37.31 cm2/Vs to 55.38 cm2/Vs, respectively. This is largely attributed to impurity scattering by doubly charged oxygen vacancies being reduced when oxygen is incorporated into the films. Leenheer and colleagues found that for a-IZO, the electron mobility depends primarily on the carrier concentration [11]. However, for carrier concentrations in the order of 10^{19} cm^{-3}, they suggest that

the charge carriers are trapped in localized states, again limiting the mobility, and the conductivity is dominated by a hopping or percolation mechanism. A maximum electron mobility of 54 cm^2/Vs was reported, at a free carrier concentration of 1.3×10^{20} cm^{-3}, where intrinsic lattice scattering is the main limitation for electron mobility, which is in good accordance with our results for both the standard and the low power process.

To better understand this relation, the electron mobility is plotted versus the free carrier concentration in Fig. 4.2. According to Equ. 2.1, the conductivity of the TCO thin film is directly proportional to the free carrier concentration N_e and the electron mobility μ. However, N_e and μ follow competing trends. As the electron mobility trend saturates, the free carrier concentration dominates the equation, and the resistivity eventually increases with increasing oxygen flow ratios ($r(O_2)$) for all films.

While for free carrier concentration greater than 3×10^{20} cm^{-3} the electron mobility follows a similar trend in all four cases (see Fig. 4.2), for both the indirect and high pressure processes μ saturates at carrier concentrations considerably higher than those predicted by Leenheer and colleagues (1.3×10^{20} cm^{-3}). Generally, disorder or defects (f.e. due to lower film density) in the material constrain the electron mobility. The curves in Fig. 4.2 imply that at carrier concentrations $<3 \times 10^{20}$ cm^{-3} different scattering mechanisms limit the mobility of the investigated films. A maximum electron mobility of 48.91 cm2/Vs at 1.99×10^{20} cm^{-3} was observed for the high pressure process, and 46.84 cm2/Vs at a carrier concentration of 2.41×10^{20} cm^{-3} for the indirect process. This can only be explained by the impact of the different film deposition methods. Because particle energies were deliberately reduced in order to achieve soft sputtering, this may have influenced the thin film formation and characteristics in different ways.

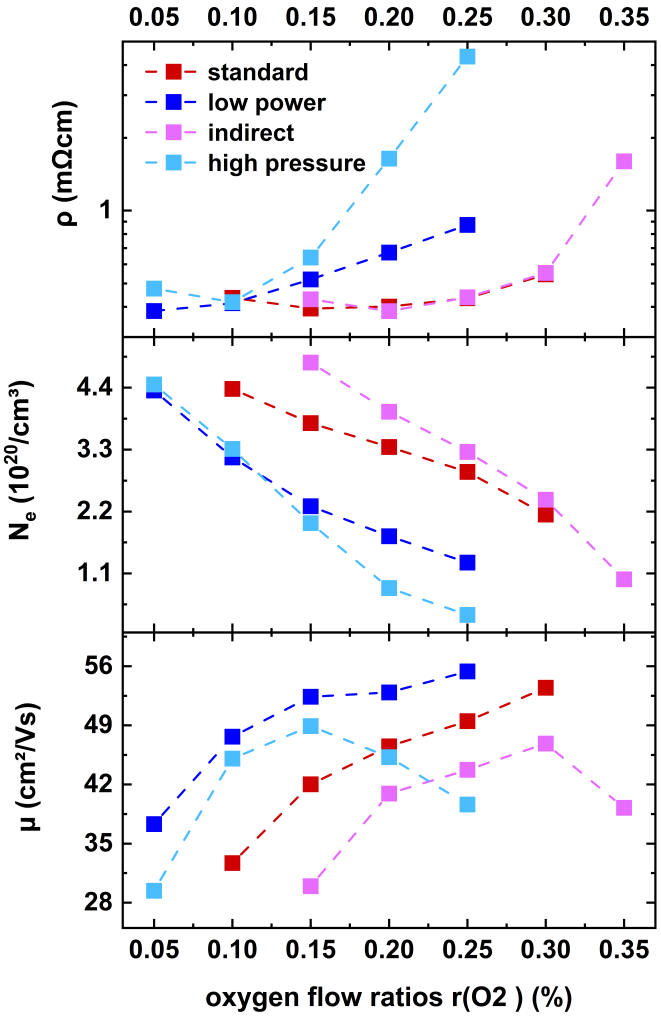

Figure 4.1: Electrical properties of IZO thin films deposited on glass with varying oxygen flow ratios r(O_2) using different sputtering deposition techniques. The carrier concentration, mobility, and resistivity obtained from hall measurements are shown.

Generally, the optical spectra of a-IZO thin films are divided into three regions: 1. the ultraviolet wavelength region (<500nm), where band gap absorption occurs. 2. the wavelength region above the band gap (>500nm). Here, absorption reaches a minimum, and only reflection limits the optical performance. In the 3. region, the near-infrared spectral region (NIR), free carrier absorption sets in - the higher the carrier concentration, the further red-shifted the free carrier absorption is.
Fig. 4.3(a), (c), (e), and (g) demonstrate the optical transmission and absorption spectra of the a-IZO thin films deposited at varying r(O_2) using different sputtering deposition techniques, while Fig. 4.3(b), (d), (f), and (h) show the dependence between the

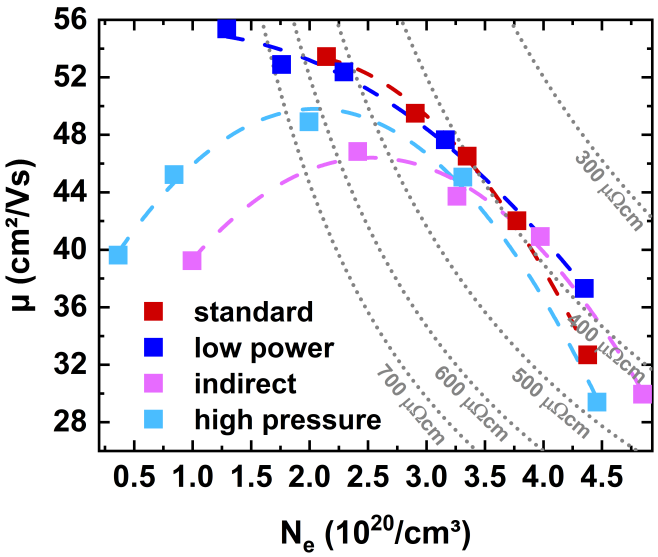

Figure 4.2: Electron mobility versus carrier concentration for IZO thin films deposited on glass with varying oxygen flow ratios r(O_2) using the standard, low power, indirect and high pressure method, respectively. The dashed lines included serve as guide for the eye. The gray dotted lines represent iso-ρ lines for different resistivities.

absorption coefficient (α^2) and the photon energy $h\nu$ of the same films. For details on the calculation of α^2, we refer to Chap. 2.1 and Equ. 2.12. We need to mention that the optical data is slightly incorrect, probably due to a calibration issue during the spectrophotometry measurement. This leads f.e. to values below zero for the absorption. At the point of writing, the problems with the spectrophotometer were not yet solved. We observe that with increasing r(O_2), the impact of free carrier absorption on the film optics is reduced within the observed spectral range. However, the carrier concentration, which is controlled by r(O_2), also affects the band gap. The band gap scales with the carrier concentration, which is known as the Burstein–Moss shift [14, 15]. This effect is visible in the respective plots on the right of Fig. 4.3 for all the films of different sputtering deposition techniques. The band gap is estimated by the intersection of the linear fits to linear parts of the respective α^2 versus $h\nu$ curves and the x-axis. The shift of the linear fits towards lower photon energies indicates narrowing of the optical band gaps with increasing r(O_2), i.e., the reduction of the carrier concentration. As a result, while additional oxygen makes the film more transparent in the longer wavelength region, the light of shorter wavelengths is lost due to band-gap absorption as the band gap narrows.

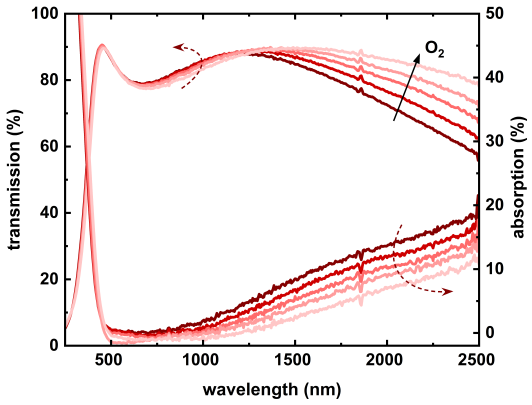
transmission (%)
absorption (%)
wavelength (nm)
O2

(a)

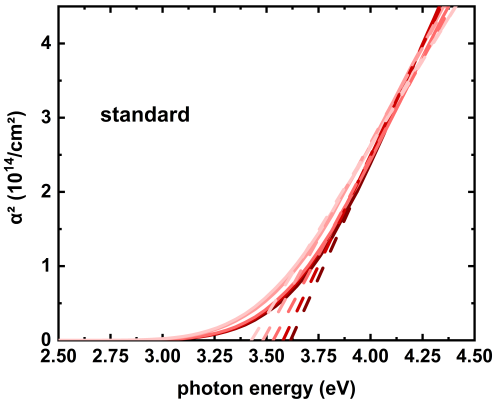
standard
α² (10¹⁴/cm²)
photon energy (eV)

(b)

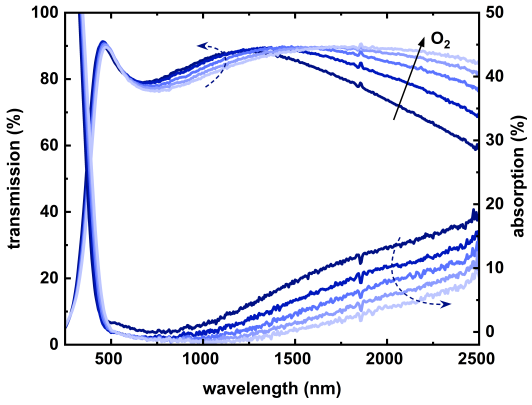
transmission (%)
absorption (%)
wavelength (nm)
O2

(c)

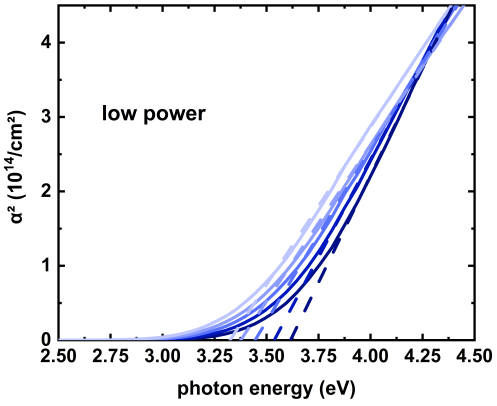
low power
α² (10¹⁴/cm²)
photon energy (eV)

(d)

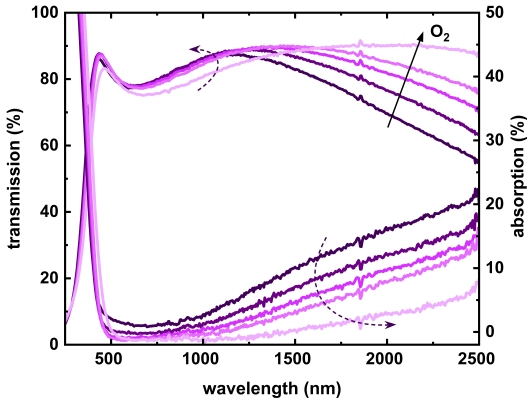
transmission (%)
absorption (%)
wavelength (nm)
O2

(e)

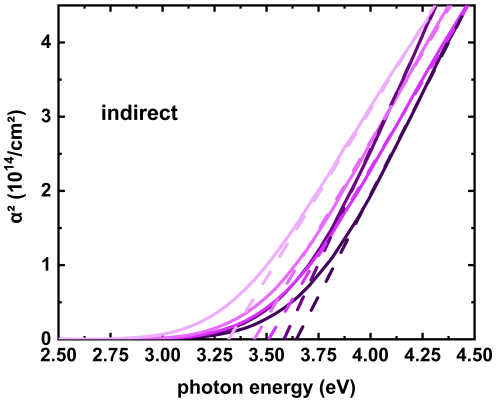
indirect
α² (10¹⁴/cm²)
photon energy (eV)

(f)

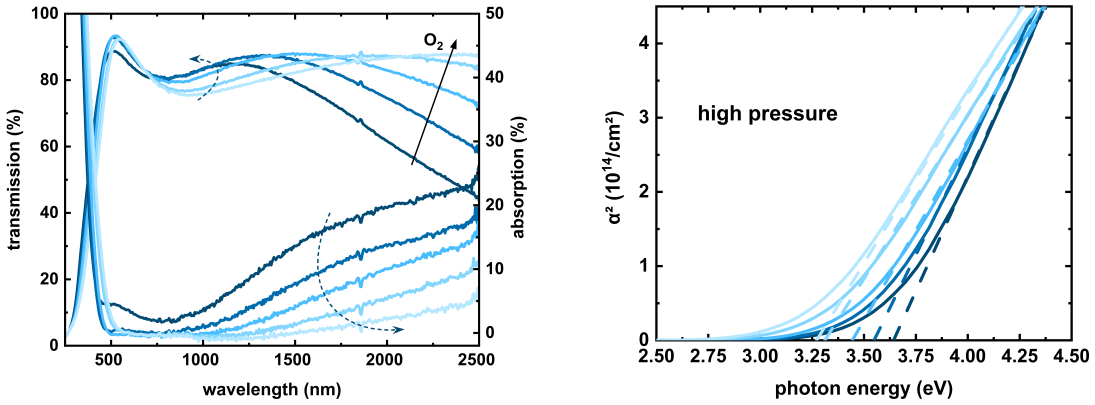

(g) (h)

Figure 4.3: (a), (c), (e), and (g) Optical transmittance and absorptance spectra, and (b), (d), (f), and (h) α^2 versus $h\nu$ plots with linear fits of a-IZO thin films deposited at varying oxygen flow ratios r(O_2) for the standard (ref), low power (blue), indirect (purple), and high pressure (cyan) process. The intersection of the linear fits and the x-axis is used to estimate the band gap.

The figure of merit (FOM) can be used as a criterion for deciding on a film based on a compromise between optical and electrical properties from a set of varying parameters. The weighted FOM, which Haacke suggested, is given by T_{avg}^{10}/R_{sq}, where T_{avg} is the average transmittance between 250 and 2500 nm, and R_{sq} the sheet resistance measured by 4 point probe of the film [134]. In Fig. 4.4 the FOM of the standard (red), low power (dark blue), indirect (magenta), and high pressure (light blue) processes are displayed. For the standard and the indirect process, an r(O_2)=0.25% was found to be a good compromise of conductivity and transparency, while for the low power and the high pressure process, an r(O_2)=0.10% was chosen, according to the FOM.

The characteristics of the chosen thin films of each sputter deposition method are presented and compared in Tab. 4.2. However the goal was to fabricate films with layer thicknesses of 100nm, but due to a lack of in-situ deposition rate tracking, the deposition time had to be estimated based on previously deposited films. This explains the unintended differences in film thicknesses for each method. The optical performance is expressed by the refractive index (n) and the extinction coefficient (k) in Fig. 4.5 (a). n and k were simulated by a Drude model based on the optical data obtained by UV-vis-NIR spectrophotometry and ellipsometry measurements. All the presented films have a refractive index of ~1.90 at 850 nm that matches well with the adjacent layers (n_{SnO2}≈1.90 and n_{C60}≈1.95 at 850 nm as seen in Fig. 6.16 in the Supplementary Information), leading to low reflection losses. For good light in-coupling into the solar cell device with such a front electrode, an anti-reflective layer with a refractive index of $\sqrt{n_{air} \cdot n_{IZO}} = \sqrt{1 \cdot 1.90} = 1.38$ (according to the optimum minimal Fresnel reflection)

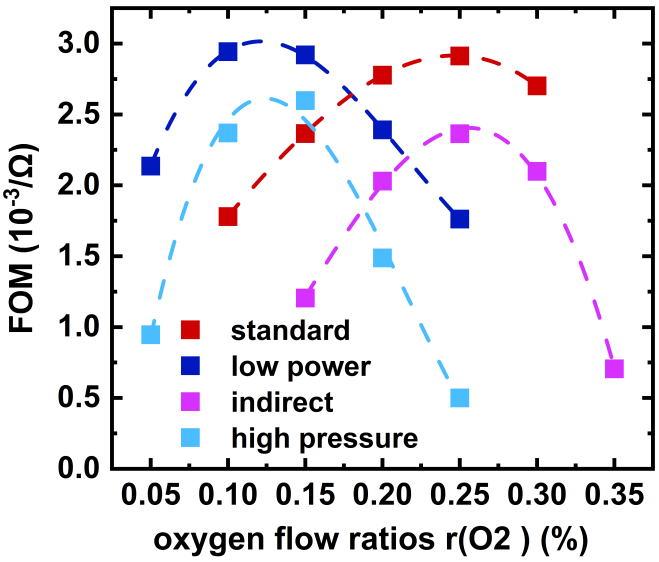

Figure 4.4: Weighted figure of merit (FOM) according to Haacke [134] in dependence of r(O_2) for the standard, low power, indirect and high pressure method, respectively. The dashed lines included serve as guide for the eye.

is needed, as, for example, lithium fluoride (LiF) with n_{LiF}=1.39 [135]. The minor discrepancies for the IZO films in n are likely due to the free carrier concentrations of the films being slightly different.

We furthermore extracted the Urbach energy (E_U) for the set of selected films following the Urbach relation $\alpha(h\nu) = \alpha_0 \exp(-h\nu/E_U)$, where α_0 and E_U are constants. The α used for this calculation was extracted from spectrophotometer measurements, which is explained in Chap. 2.1. E_U can be calculated from the slope of a linear region below the band gap energy when α is plotted over $h\nu$ in a semi-logarithmic plot (shown in Fig. 4.5 (b)). E_U then represents the width of the tail states, representing disorder or defects in the film. We adapted this approach from [16]. We found the largest Urbach energies for films deposited by the indirect (288 meV), and the high pressure (286 meV) process. This correlates with the overall lower hall mobility of those soft deposition approaches, as defects limit the carrier mobility due to electron scattering. The lowest values were found for low power process (244 meV), and the standard process (257 meV). The estimated values for the Urbach energies are reasonable values for TCOs and in a similar range as observed by others [16, 41].

The morphological properties of sputtered thin films depend on the energy of the atoms arriving on the substrate surface during the sputter deposition. The sputtered target atoms need sufficient kinetic energy to diffuse to an energetically favorable position on the substrate surface to generate a high-quality TCO film [9, 136]. When process parameters are modified to favor a soft sputter deposition, the kinetic energy of film-forming atoms can be significantly impacted, resulting in a considerable reduction in film quality if the energy required for sufficient surface diffusion is not provided.

We believe that the increased Urbach energies of the indirect and high pressure processes

correlate with reduced film quality due to insufficient diffusion energies of the atoms on the substrate surface.

Table 4.2: Electrical parameters and film properties of selected thin films, which were chosen based a good compromise of conductivity and transparency, and their corresponding r(O_2).

Process (r(O_2))	μ (cm^2/Vs)	N_e (10^{20}/cm^3)	ρ (mΩcm)	d (nm)	E_g (eV)	E_U (meV)
standard (0.25%)	49.50	2.90	0.43	97.15	3.48	257
low power (0.1%)	47.66	3.16	0.41	102.27	3.54	244
indirect (0.25%)	43.73	3.26	0.44	89.4	3.51	288
high pressure (0.1%)	45.06	3.31	0.42	121.73	3.55	286

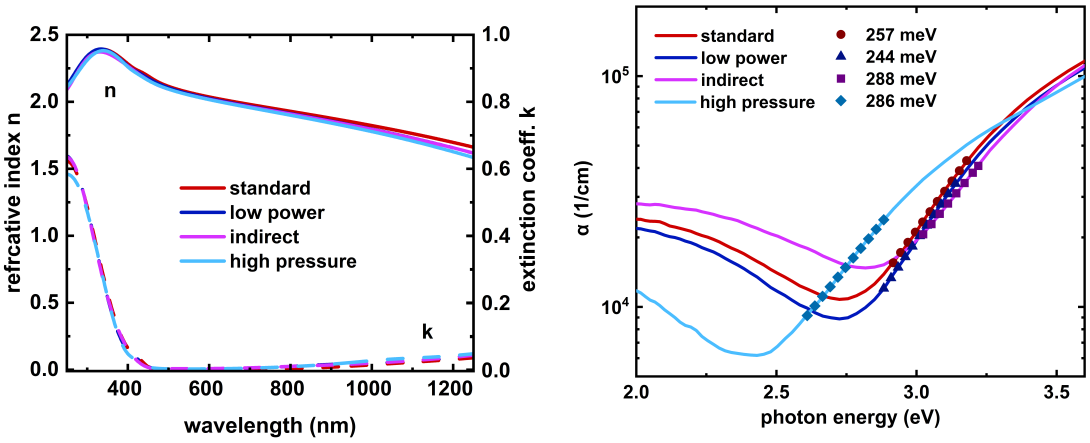

(a) (b)

Figure 4.5: (a) n,k data, and (b) absorption coefficient over photon energy of selected IZO thin films. The region is selected with focus on the Urbach energy approximation. The symbols show the area of the slope of a linear region used to calculate the width of the tail states.

Summary of the main findings

- At free carrier concentrations <3 × 10^{20} cm^{-3} different scattering mechanisms limit the mobility of the investigated films deposited by different sputter approaches, presumably due to the intentionally reduced sputtered IZO particle energies.
- Adequate oxygen flow ratios were selected for each film deposition methods, based on the evaluation by the figure of merit, which takes into account both, optical and electrical performance.

- All of the selected films exhibit similar optical performances based on the refractive index and extinction coefficient, while minor discrepancies can be attributed to slightly different free carrier concentrations.
- The refractive indices match well with those of the adjacent solar cell layers.
- Evaluation of the Urbach energies of the selected films gives reason to believe, that the lower particle kinetic energy during film formation leads to an increase of defects for both the indirect and the high pressure processes, while the the low power and the standard process exhibit comparably low Urbach energies.

4.1.2 Impact of sputter damage on the solar cell parameters of single junction perovskite solar cells

In the previous section, the TCO quality of IZO thin films deposited under various sputter conditions, including three proposed soft deposition approaches, were optimized regarding their optoelectrical properties for the application as front electrodes in perovskite solar cells. Therefore, this section investigates the application of the selected abovementioned IZO sputter depositions on perovskite single junction solar cells.
Firstly, we want to test the effectiveness of our low-damage IZO sputter depositions on solar cells without a protective buffer layer. Usually, the sensitive layers of the perovskite solar cells are protected from sputter damage by a SnO_2 buffer layer prepared by thermal ALD. In this experiment, we remove the SnO_2 buffer layer and deposit the IZO directly on the C_{60} electron transport layer (ETL) by standard and low-damage sputter deposition methods, as shown in Fig.4.6(c) "various IZO". A single junction solar cell layer stack with an electron contact comprised of a stack of C_{60}/Bathocuproine (BCP)/Cu, without sputtered IZO, served as a reference (see Fig.4.6(c) layer stack named "reference"). The other reference device (denoted as "with buffer" in Fig.4.6(c)) features an IZO layer deposited using the standard deposition method on a conventional SnO_2-buffer layer ETL design. In this experiment, the IZO layers of the different sputter deposition techniques are not optimized with respect to their optoelectronic properties. Unfortunately, the IZO layer optimizations based on additional oxygen during the sputter deposition for the different processes were carried out at a later point. Here, the oxygen ratio was kept at 0.25% for each process, which is the optimized value for the standard IZO deposition conditions. We investigate the electrical properties of these single junction solar cells and evaluate their performance in comparison to reference cells. We provide the J-V analysis findings of multiple experiments, which produced large amounts of data points for some combinations (minimum was 12 for "with buffer" and maximum was 122 for "reference"), in Fig. 4.6(a), (b), and (d). The corresponding schematic device designs are depicted in Fig. 4.6(c). The illumination in these experiments occurs from the ITO glass substrate side (indicated by the colorful arrow in Fig. 4.6(c)). A 100 nm thick copper stripe was deposited onto the 100 nm

thick IZO to increase the lateral charge conductivity. Consequently, the solar cells were opaque. This enables us to separate the impacts of lateral conductivity on solar cells' series resistance from any potential consequences of sputtering damage. Furthermore, the non-optimized IZO layers result in significantly different sheet resistances. The J-V measurements were conducted using an active-area defining shadow mask, and the current was not corrected according to EQE measurements.
The J-V curves in Fig. 4.6(a) were selected to represent the statistical results. As can be seen, the standard IZO deposited directly onto the C_{60} leads to an overall reduction in FF and hysteresis compared to the standard IZO deposited onto the SnO_2 buffer layer devices. With a clear tendency for s-shape formations, the low-damage IZO deposition approaches result in even lower FFs. The IZO-free reference exhibits the highest FF and V_{OC}.
The statistical evaluation in Fig. 4.6(b) and (d) shows the V_{OC}s and FFs. While the IZO-free reference solar cells have the highest average V_{OC}, the devices with buffer exhibit the lowest average V_{OC}. The average V_{OC} is higher in the buffer layer-free solar cells with differently deposited IZOs. With ~1.09 V, the V_{OC} of the devices with standard IZO is the lowest of all SnO_2-free solar cells, while the low-damage approaches lead to ~1.10 V on average. Surprisingly, devices with standard IZO have the highest average FF of 65% of all SnO_2-free solar cells with sputtered IZO. Though, admittedly they also exhibit the highest spread in results. The observed s-shape formation tendency is likely the cause of the low-damage IZO methods' substantially reduced FFs, which average less than 60%. The reference and the devices with buffer resulted on average in FFs of ~77% and ~73%, respectively.
The comparably low V_{OC} of the devices with SnO_2 buffer could originate from the ALD deposition process, especially if the precursor is aged. We observed a correlation between the age of the precursor and the V_{OC}, which is not shown in this work. Additionally, adding an interlayer, namely polyethyleneimine ethoxylated (PEIE), between SnO_2 and C_{60} significantly improves the electrical performance of the corresponding devices, suggesting that the interfaces between these materials are not ideal. This observation was also reported by others [137, 138]. This may also possibly be the reason for the on average higher V_{OC}s of the devices where the SnO_2-buffer was skipped and IZO was sputter-deposited directly onto the C_{60}.
The slightly higher V_{OC}s of the low-damage IZO devices indicate that fewer losses caused by sputter damage are expected. On the other hand, this trend is not reflected in the FF. No low-damage approach resulted in higher FFs than the standard IZO deposition. We speculate that this interface is subjected to other limitation than sputter damage. The s-shape tendency suggests an energetic barrier, possibly due to an energetic mismatch. The non-optimized deposition methods may potentially have an impact on the IZO's work function. As we observed in the previous chapter, each process requires a correction of the oxygen ratio to adjust the carrier concentration.

The electrical performance of the low-damage IZO devices deteriorated even more than the standard IZO devices (where we would predict the highest sputter damage) as we attempted to reduce the impact of sputter damage. We, therefore, conclude that the C_{60}/IZO interface might not be appropriate for examining the effects of sputter damage because it appears to be affected by issues unrelated to sputter damage.

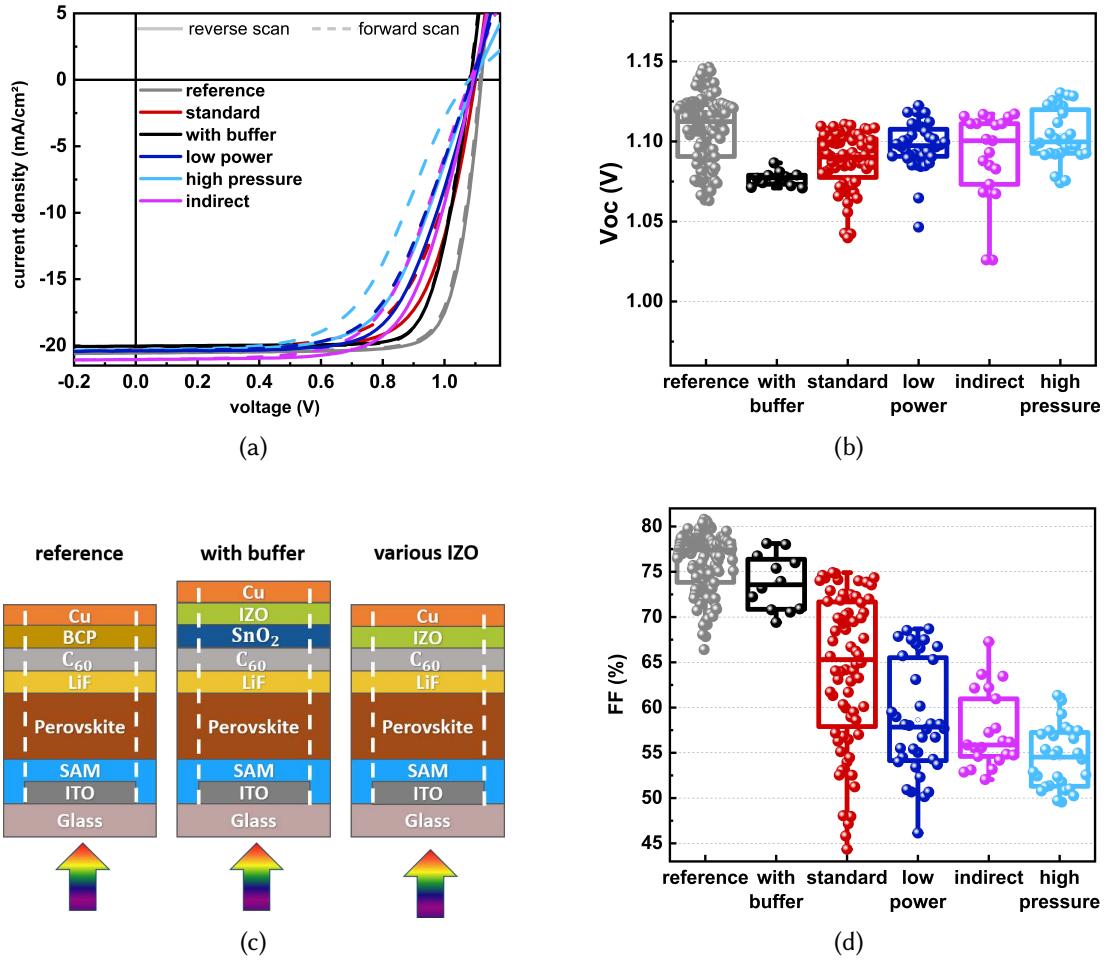

Figure 4.6: (a) J-V characteristics, (b) box plots of open circuit voltage of reverse J-V measurement, (c) schematic solar cells design (opaque devices) and illumination direction, and (d) box plots of fill factor of reverse J-V measurement of opaque perovskite single junction solar cells. Compared are solar cells where IZO was deposited directly onto C_{60} in a standard, low power, indirect, and high pressure deposition process. The solar cells called "reference" (no IZO) and "with buffer" (IZO deposited in a standard deposition process on solar cells containing an SnO_2-buffer layer) serve as references for comparison. The statistic's different pixel count is caused by the fact that the shown data is a summary of numerous experiments that not always included all investigated sputter parameters. An active-area defining shadow mask was used to conduct the J-V measurements. The colored arrows indicate the illumination through the ITO back electrode and the glass substrate. The copper electrode completely covered the IZO and helped to increase lateral conductivity across the electrode. The IZO was not optimizes prior to the device implementation and r(O_2) was kept at 0.25%.

In the following, we introduce the polymer polyethyleneimine ethoxylated (PEIE)

to bypass the poor C_{60}/IZO interface properties. PEIE is known to operate as a work function shifter [27]. With IZO front electrodes deposited directly on the cell's ETL by conventional and soft sputter deposition methods without a protective SnO_2-buffer layer, we investigate the impact on the electrical performance of semi-transparent single junction solar cells. These devices are compared with references that consist of a standard deposited IZO front electrode and a conventional SnO_2-buffer layer design. As shown in Fig. 4.7, the ETL of SnO_2-free solar cells was composed of a stack of C_{60}/PEIE on which IZO was deposited using different techniques. The reference's ETL, on the other hand, was composed of C_{60}/PEIE/SnO_2. Additionally, we conduct a light intensity-dependent analysis of the J-V characteristics to investigate the losses and correlate them with sputter damage.

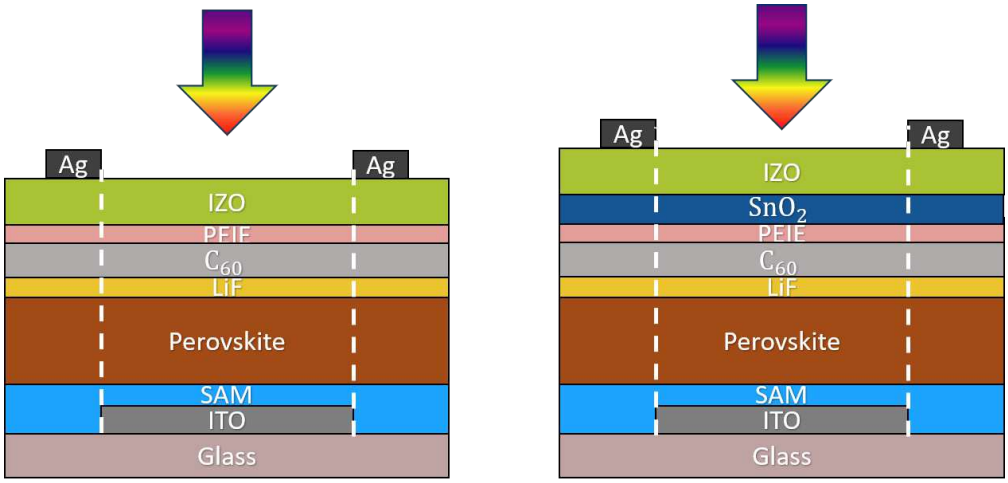

Figure 4.7: Schematic device layout of semi-transparent perovskite single junction (SJ) solar cells used in this work. Shown is one solar cell pixel of each configuration of a substrate, which consists of six individual pixels. On the left the SnO_2-free design is depicted, which served as basis for the sputter-damage analysis. On the right the state-of-the-art SnO_2-buffer design is depicted, which served as reference for the experiment. The overlap of the segmented ITO area and the IZO front electrode stripe defines the active area.

As already discussed in Chap. 2.2.2 sputter damage can result in various limitations in a solar cell. It can cause defects in the ETL/TCO interface and below, which results in transport losses due to damaged material (f.e. breaking of chemical bonds) and recombination losses in the interfaces or even in the perovskite bulk. This may lead to deteriorated J-V characteristics, reflected in lower fill factors and open-circuit voltages. In Fig. 4.8 the results of current-corrected J-V measurements (the current was corrected according EQE measurements due to misaligned shadowing masks during silver evaporation, leading to errors in the area estimation), including box plots of the open circuit voltage (V_{OC}) and the fill factor (FF), and external quantum efficiency (EQE)

measurements are shown.
For all samples, the IZO thickness was approximately 100nm. The IZO deposition process conditions are identical to the ones presented in section 4.1.1 and summarized in Tab. 4.2. The solar cells described as 'with buffer' (Fig. 4.8 in black) and 'standard' (Fig. 4.8 in red) were both coated with the same IZO deposition process (in this work referred to as standard deposition), which is considered to be the most harmful process, as no measures were taken to reduce sputter damage during this deposition.
Moreover, as expected, the solar cells that have been coated with the standard deposition process without a SnO_2-buffer layer exhibit both reduced V_{OC} (Fig. 4.8 (b)) and FF (Fig. 4.8 (d)) compared to the reference with buffer. The series resistance (R_{ser}) is likewise increased, although the same IZO deposition process was performed in both cases. Interestingly, the shunt resistance (R_{par}) is higher in the case of the standard IZO deposition process. The resistance values for all samples can be found in Tab. 4.3. Furthermore, differences in the short circuit current (J_{SC}) can be seen in Fig. 4.8 (c), which can mainly be associated with a different interference pattern of the reflection and reduced parasitic absorption, caused by the omitting of the 20nm SnO_2.
When solar cells with IZO front electrodes deposited by the low power process (Fig. 4.8 in dark blue) are compared to those with the standard process, both V_{OC} and FF reveal a positive trend. The average V_{OC} increases from ~1.166 V to ~1.179 V and the average FF increases from 71.18% to 73.86%. In the case of the indirect process (Fig. 4.8 in magenta), the mean V_{OC} is higher than the standard process IZO solar cell's mean V_{OC} as well (~1.173 V vs. ~1.166 V), and lower than the mean V_{OC} of the low power process. However, the FF is significantly lower for the indirect process, which correlates with a lower R_{par} and a lower R_{ser}. The high pressure IZO solar cells exhibit similar values in both V_{OC} and FF as the standard IZO solar cells. However, R_{par} is much lower, while R_{ser} is also slightly lower. The overall higher series resistances of the SnO_2 buffer layer free solar cells indicate that the ETL/TCO interface is significantly affected by omitting the SnO_2 layer.
The J_{SC} of both the indirect and the high pressure IZO solar cells is higher than for the standard and the low power IZO solar cells, likely due to either slightly different IZO thicknesses or due to lower free carrier densities. As discussed in the previous section, the free carrier density impacts the TCO's band gap. Higher free carrier densities lead to larger band gaps, shifting the absorption onset of the TCO to a lower wavelength, which can be observed in Fig. 4.8 (c) at around 350nm.

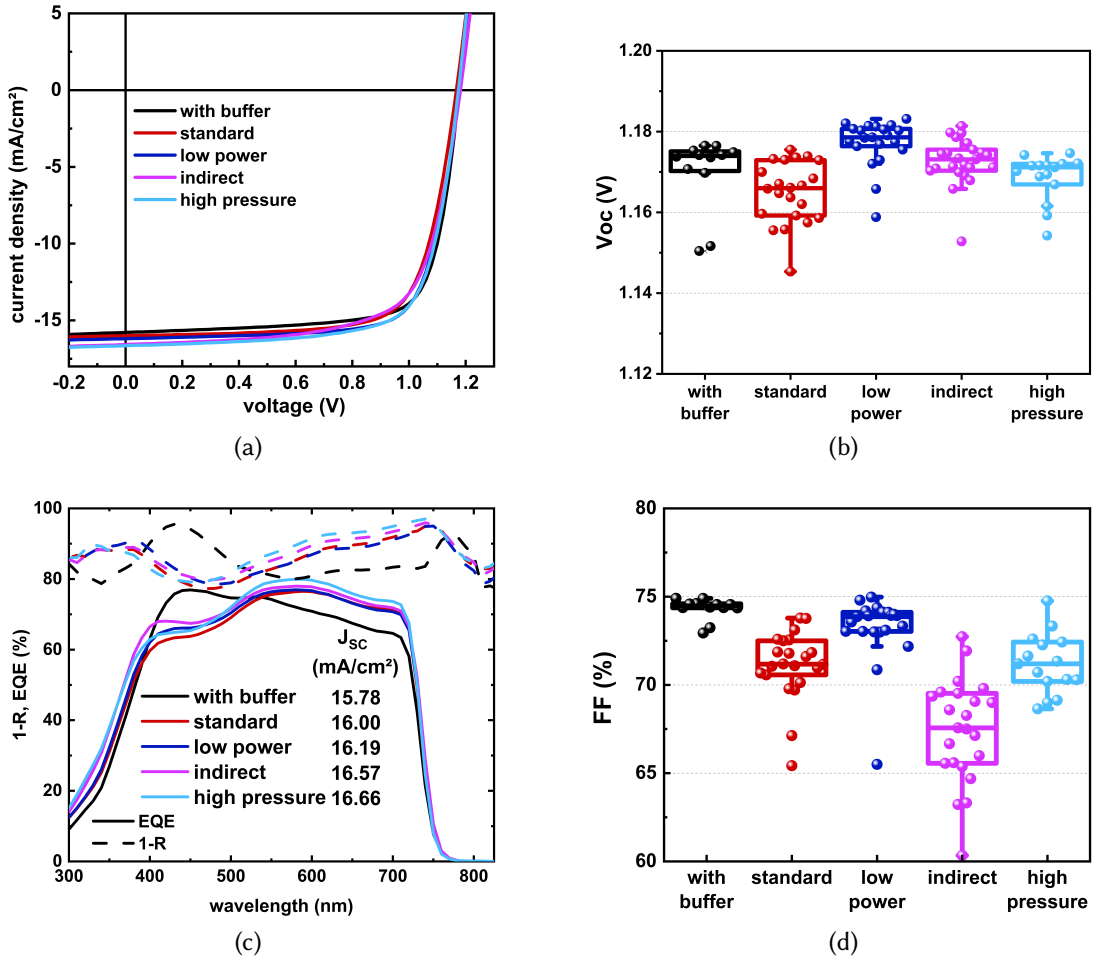

Figure 4.8: (a) J-V characteristics, (b) box plots of open circuit voltage, and (d) fill factor of semi-transparent perovskite single junction solar cells (24 pixels each) with standard IZO-front contact deposited on a buffer layer, and standard and different soft sputtered IZO front electrode, deposited onto the ETL without a protective buffer layer, measured through the IZO front electrode; (c) External quantum efficiency (EQE) spectra and reflection (denoted as 1-R) of selected semi-transparent solar cells measured through the IZO front electrode.

Table 4.3: Solar cell parameters of semi-transparent perovskite single junction solar with IZO front electrodes deposited by different deposition techniques and the reference with buffer with standard IZO deposition.

IZO process	PCE (%)	J_{SC} (mA/cm²)	V_{OC} (V)	FF (%)	R_{ser} ($m\Omega cm^2$)	R_{par} (Ωcm^2)
with buffer	13.91	15.78	1.176	74.90	5.52	1563
standard	13.55	16.00	1.167	72.55	7.14	2815
low power	14.17	16.19	1.180	74.11	7.06	2620
indirect	13.43	16.57	1.181	68.59	6.73	1435
high pressure	14.14	16.66	1.174	72.27	6.60	1937

To summarize, according to the results, the best performing sputter deposition process without a protective SnO_2-buffer is the low power process. The results of the high pressure and the indirect process solar cells do not show promising improvements compared to the standard process. We observed that the different processes impacted the solar cells series and shunt resistance differently. As explained in Chap. 2.3.2, the solar cell series resistance depends on the device's overall conductivity, which is related to the transport resistance through individual layers and interfaces of the solar cell stack as well as the electrodes' sheet resistance. The lowest R_{ser} was achieved for solar cells with a SnO_2-buffer. We therefore speculate, that the SnO_2 leads to a better ohmic contact. We did not observe a strong correlation between R_{ser} and sputter damage reduction. On the other hand, the shunt resistance is linked to losses due to photogenerated charge carrier recombination within the device [76]. The lowest R_{par} was observed for solar cells with a SnO_2-buffer and with an indirect IZO deposition process, indicating charges recombining through shunts instead of being collected. The highest statistical R_{par} was achieved by the low power process (see Chap. 6 Fig. 6.3), indicating reduced recombination losses.
Furthermore, we want to investigate the correlation between sputter damage and the various losses we observe in V_{OC}, FF, and resistances, especially since several soft deposition methods were not as promising. In particular, the FF of the indirect and the high pressure processes was even worse than of the standard process, which correlates with lower shunt resistances in both cases. Generally speaking, a solar cell's fill factor is determined by recombination losses in the bulk and the interfaces and by transport losses, including charge carrier transport over the interfaces and contact materials and the sheet resistance of the TCOs. In order to quantify the nature of the observed losses, a deeper understanding is necessary. Therefore, a light intensity dependent J-V analysis was performed, allowing for a separation of transport and recombination losses.

Light intensity analysis of the impact of sputter damage on the photovoltaic parameters

So far, it is unclear how sputter damage affects the V_{OC} and the FF, whether charge extraction is compromised, or whether the damage induces traps or defects that facilitate non-radiative recombination losses. Usually, the V_{OC} is directly dependent on energy alignment and recombination processes in solar cell devices, while FF losses are somewhat more difficult to interpret. The device FF is affected by charge transport, series and shunt resistance, and recombination processes. The ideality factor n_{id} can be used as an indicator of the type of recombination process which takes place, though the exact interpretation is not straightforward. While an ideality factor of n_{id} = 1 points to bimolecular recombination (radiative recombination), n_{id} = 2 indicates that trap-assisted recombination (non-radiative recombination) is dominant. We determined the ideality factor by measuring V_{OC} at different intensities. V_{OC} is then plotted against the light intensity on a semi-logarithmic scale. Then, n_{id} is calculated from the slope. The following measurements were conducted several days after the previous measurements. After a few days of rest, we have noticed that solar cells with PEIE operate better and recover a little bit. This explains some discrepancies between the following measurements and the previous ones.

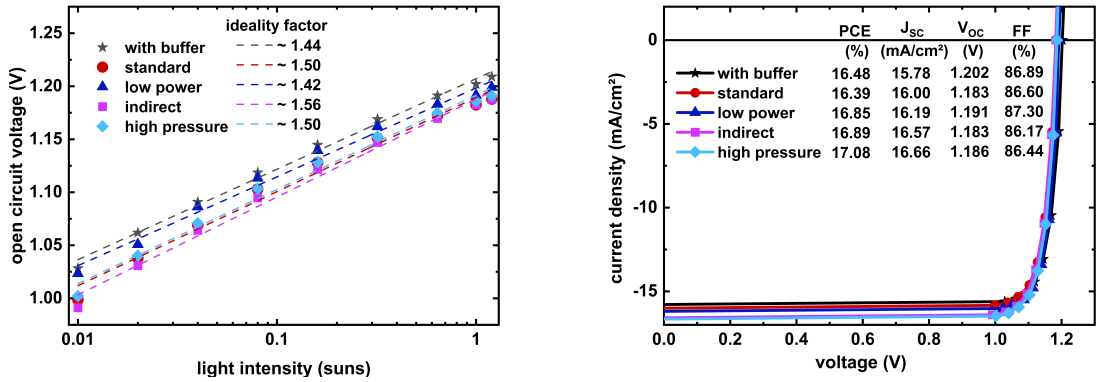

(a) (b)

Figure 4.9: (a) Light intensity-dependent open-circuit voltage with linear fits (dashed lines) and extracted ideality factors (n_{id}); (b) Pseudo-J-V curves reconstructed from the light intensity measurements from panel (a).

In Fig. 4.9(a), the V_{OC} over light intensity for the reference solar cell with buffer and the solar cells with different IZO sputter deposition techniques without buffer is displayed. The light intensity is given in "suns". For the light source that means that 1 sun equals 100% illumination intensity. This value was set according to the current of a reference solar cell. Then, 0.1 suns equals 10% illumination intensity of the original intensity, which could be adjusted through the software "Wavelabs". The calculated

ideality factors are shown in the inset of Fig. 4.9(a). The solar cells with buffer exhibit an n_{id} of 1.44, while the solar cells with standard IZO deposition, without buffer, show an increased n_{id} of 1.50, pointing to increased trap-assisted non-radiative recombination, most likely due to sputter damage. Consistent with the measured V_{OC} in Fig. 4.8 (b), where the low power IZO solar cells achieved the highest values, they also exhibit the lowest n_{id} of 1.42, implying that by the low power process trap-assisted recombination could successfully be reduced. In comparison to the standard IZO deposition processed solar cells, the soft sputter approaches of indirect and high pressure IZO deposition, on the other hand, could not yield a reduced n_{id} in the solar cell devices.
Furthermore, we calculated the solar cells' maximum possible FF (the pseudo FF, pFF) by constructing pseudo J-V curves from the light intensity dependent measurements, which allows for an interpretation in the absence of transport losses. Therefore, the V_{OC} is plotted as a function of short-circuit current density since light intensity is proportional to generated current density. The x- and the y-axes are then switched and the J_{SC} is subtracted, creating an exponential current-voltage curve. The results are given in Fig. 4.9 (b).

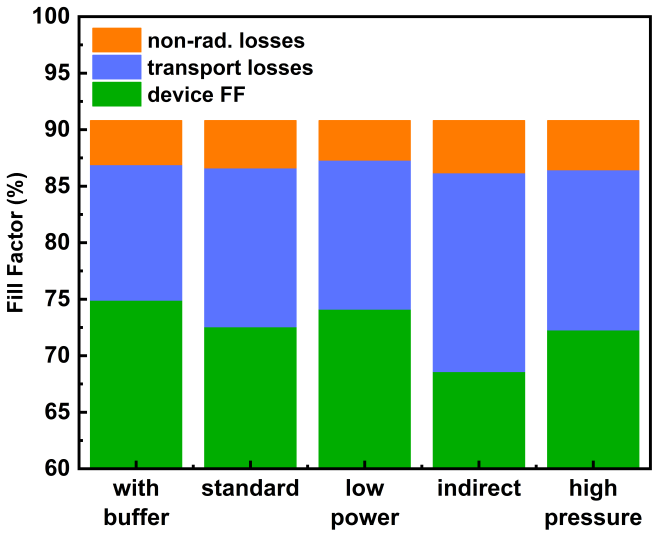

Figure 4.10: A comparison of the device FF derived from J-V measurements and the FF from pseudo J-V curves, as well as the FF in the radiative limit [74], for the device with buffer and devices with various IZO deposition processes.

Table 4.4: Comparison of ideality factors, device open-circuit voltages, device fill factors, impact of transport losses on the FF and impact of non-radiative recombination losses on the FF.

Process	n_{id}	V_{OC} (V)	FF (%)	transport loss (%)	non-rad. loss (%)
with buffer	1.44	1.202	74.9	11.99	3.91
standard	1.50	1.183	72.55	14.05	4.20
low power	1.42	1.191	74.11	13.19	3.50
indirect	1.56	1.183	68.59	17.58	4.63
high pressure	1.50	1.186	72.27	14.17	4.36

The different loss mechanisms related to the FF of the reference solar cell with buffer and the standard, low power, indirect, and high pressure process IZO solar cells without buffer, are reviewed in Fig. 4.10 by correlating the electrical FF to the pFF, and the FF in the radiative limit for each - a method adapted from Stolterfoht *et al.* [69]. The FF of solar cells with SnO_2-buffer is reduced by 11.99% due to losses assigned to charge transport over the interfaces and by another 3.91% due to losses assigned to non-radiative recombination in the bulk. Overall, these samples have the lowest transport losses of all investigated solar cells. The standard IZO process solar cells exhibit increased transport and non-radiative recombination losses, compared to the solar cells with a SnO_2-buffer, of 14.05% and 4.20%.
In line with the lowest n_{id}, the low power process IZO solar cells exhibit the lowest non-radiative recombination-related FF-losses of 3.50%. This is most likely due to fewer defects, which is in line with the notion that high energetic particles induce defects in the underlying layers, which are reduced in this case. The transport losses, which make up 13.19% of the FF losses, are also lower than they would be with standard IZO deposition. On the other hand, the other soft sputter approach, the indirect process that exhibits the highest n_{id} of 1.56, also has the highest overall FF losses due to both comparably higher transport losses of 17.58% and higher non-radiative recombination losses of 4.63%.
Like the indirect IZO sputter technique, the high pressure IZO sputter approach does not yield the expected reduced losses compared to the standard IZO deposition. Specifically, n_{id} was found to be 1.50, the same value as for the standard deposition IZO solar cell's n_{id}. Also, transport and non-radiative recombination losses are similar in both cases (14.17% and 4.36%), indicating no reduced impact of sputter damage.
At this point, we would like to highlight two conclusions: 1. The low transport losses of the solar cells with SnO_2-buffer indicate that the SnO_2 leads to a lower interfacial resistivity for charges that are transported to the electrode; 2. the most effective low-damage IZO sputter deposition approach according to the J-V measurement evaluation was the low power process. It exhibits lower transport and non-radiative recombination losses than the standard IZO deposition, indicating that sputter damage impacts both loss mechanisms. It appears that neither of the other two low damage deposition techniques

reduced the effects of sputter damage.
Here, the indirect process, which exhibits the highest n_{id}, the highest transport and the highest non-radiative recombination losses, performed even worse than the standard IZO deposition. This raises the question of whether the interface may not have been well formed due to inefficient particle surface diffusion and whether damaging particles with high kinetic energy were effectively prevented from impinging on the substrate surface. As earlier explained, oxygen ions are believed to leave the target perpendicular to its surface. If the target is not entirely flat anymore, due to race tracks forming, the damaging oxygen ions might spread into more directions. As for the high transport losses, high contact resistance between IZO and ETL may reduce charge extraction and increase interfacial recombination. Another reason for high transport losses could be a higher than expected sheet resistance due to a different formation of the IZO thin film when deposited on an organic substrate instead of glass. Unfortunately, the measurement does not differentiate between the kind of transport losses.
As for the high pressure IZO deposition solar cells, the collision cross section of the damaging negatively charged oxygen ions with the sputtering gas is comparably small due to their high energy, preventing the collision-driven thermalization, even when the gas pressure is increased [131]. Moreover, an increased bias voltage was observed for the high pressure process (see Tab. 4.1), indicating even higher potential kinetic energies of the damaging ions.
In summary, the most effective approach to reducing sputter damage appears to be the reduction of the bias voltage by decreasing the sputter power and thereby reducing the kinetic energy of the damaging ions. However, further investigations are necessary to understand and quantify the elevated transport losses for all SnO_2-free devices. They could be linked to either the IZO sheet resistance due to different film formations on an organic substrate layer, contact resistance, or damage-related isolating interfaces. Hence, we suggest contact resistance measurements following the Cox and Strack method [139], or using the spatial dependence of electroluminescence (EL) intensity across the active area, in order to determine the sheet resistance of the IZO front electrode of the solar cell stack [140].

Summary of the main findings

- When coating solar cells with an IZO deposition process that is not optimized in terms of sputter damage reduction (here the standard deposition process), solar cells without a protective SnO_2-buffer layer exhibit considerable V_{OC} and FF losses, compared to solar cells with SnO_2-buffer.
- The n_{id} and FF-loss analysis confirms that to some extent, the losses in V_{OC} and FF originate from increased trap-assisted non-radiative recombination, while transport losses are also increased.

- The low power IZO deposition process effectively reduces the impact of sputter damage, which is reflected in a higher V_{OC} and FF, and lower n_{id} and non-radiative recombination losses, compared to the standard deposition process.
- Although the V_{OC} for the indirect IZO deposition process improved compared to the standard IZO deposition, the FF was the lowest in this case, even lower than for the standard IZO deposition, most likely due to the increased transport losses. The origin of these transport losses remains unclear so far.
- The high pressure IZO solar cells show no noticeable improvement compared to the standard IZO solar cells, indicating that the measures taken to reduce sputter damage by reducing the mean free path length (due to a higher process pressure) were ineffective.

4.1.3 Conclusion

IZO sputter deposition processes based on reducing the damage due to high kinetic energy particles (sputter damage) have been implemented and optimized based on the oxygen ratio during the sputter process according to IZO film quality. We found that reducing the sputtered IZO particle energy by two of the investigated low-damage approaches (namely the indirect and the high pressure process) also reduces the IZO film quality. Based on Urbach tail investigations, we believe that due to insufficient diffusion energies of the atoms on the substrate surface, certain approaches lead to increased defects and a considerable reduction in film quality. This needs to be taken into consideration, when investigating low-damage sputter deposition methods.
We tested the optimized IZO deposition techniques on different solar cell devices. In our first approach, we removed the SnO_2-buffer layer, and directly sputter-deposited the IZO onto the C_{60} electron contact layer of perovskite single junction solar cells. Non of the low-damage sputter deposition approaches resulted in improved electrical performance in this case, therefore we assume, that the C_{60}/IZO interface might be subjected to other limitations than sputter damage. By using PEIE as an interlayer between C_{60} and IZO, we were able to examine the effects of sputter damage. We tested the various optimized IZO deposition techniques by fabricating semi-transparent SnO_2-free solar cell devices and compared the results to a semi-transparent solar cell device with a typical SnO_2-buffer. As for the standard IZO deposition process on SnO_2 and directly onto the C_{60}/PEIE interface, the V_{OC} and the FF are reduced when omitting the SnO_2-buffer, indicating sputter damage. Interestingly, not all our proposed soft sputter deposition processes lead to improved solar cell performances. While the low power process seems to effectively reduce sputter damage, which is reflected in improved J-V characteristics, a lower n_{id} and lower transport and non-radiative recombination losses, the indirect and the high power process approaches were not as successful. We

believe that poor IZO film growth conditions due to reduced atom surface diffusion and insufficient suppression of damaging particle bombardment might be responsible.

4.2 Interactions between the substrate and the growing thin film

In the previous chapter, we discussed the dependence of the TCO layer quality and the single junction solar cell performance on the sputter deposition process parameters. However, the ETL/TCO interface dynamics and the growth of the TCO may also be influenced by the choice of substrate layer (f.e. due to its topography, surface chemistry, and surface energy) on which the TCO is deposited. In this chapter, we will first discuss the impact of different ETL designs on the solar cell performance. Therefore, in the first part of this chapter, presented in section 4.2.1, we will sputter deposit the IZO layer by the same soft deposition method (using the Vinci tool as presented in Chap. 3.1.1) on different layers of perovskite single junction solar cells and investigate the impact of the ETL-design on the solar cell performance by applying adequate characterization techniques. In the second section of this chapter, we will present an in-situ investigation, where the early stages of IZO growth on selected layers of the perovskite solar cell are monitored by time-resolved microbeam grazing incidence small-angle X-ray scattering (μGISAXS), a method that is introduced in Chap. 3.2.1 . This technique allows for studying the growth kinetics of the transparent conductive oxides on the substrate on atomistic, nano-, and mesoscale.

4.2.1 Sputtering on different layers of the single junction perovskite solar cells

The current state-of-the-art perovskite top-cell designs with p-i-n polarity and competitive efficiencies make use of a thermal atomic layer deposited (ALD) SnO_2 buffer layer, which is considered necessary in order to protect against sputter damage. However, because ALD is a time-consuming process, it is desirable to omit this step in an industry-relevant mass fabrication process. In the previous chapter (Chap. 4.1.2), we presented our results on sputter damage reduction. We showed that simply omitting the SnO_2 buffer layer and performing various soft IZO sputter deposition attempts directly onto the ETL layer C_{60} does not lead to the desired solar cell performance. By adding an ultra-thin ($\leq$2 nm) PEIE interlayer in-between the C_{60} and the IZO, we were able to circumvent some interfacial limitations, which we assumed to be connected to an interfacial barrier. So far, it is unclear how PEIE or SnO_2 improve the ETL/IZO interface and how the ETL materials interact with the IZO growing on top. The following results differ from the results in the first part of Chap. 4.1.2, even though similar sample designs were used (the SnO_2/C_{60} design is similar to samples referred to as "with buffer" and for the C_{60} only ETL design IZO was deposited directly onto C_{60}, like for samples referred

to as "various IZO"). However, previously the electrode design included copper resulting in opaque single junction solar cells. The first experiment's perovskite composition was also different, leading to a smaller band gap (1.6 eV), and the IZO was deposited with a different tool and recipe (using the Roth&Rau). Nevertheless, significant differences in the J-V curve's shape and the J-V measurements' results originating from the ETL/IZO interface were observed. We now want to discuss the differences originating from the ETL design in more depth. Therefore, we fabricated all the samples in this chapter in one batch and under similar conditions for a better direct comparison. In the following, we will focus on the influence of the ETL design on the interface dynamics, the interactions between the substrate material and the initial IZO growth, and the solar cell performance.

For the investigation, semitransparent single junction solar cells with three different ETL-designs were analyzed. In Fig. 4.11(a) a schematic illustration of the investigated solar cells with the different ETL-design is shown. The illumination direction for the following measurements is indicated by the sun-symbol. If not stated otherwise, the devices were illuminated through the IZO. The semitransparent single junction solar cells were fabricated according to preparation steps detailed in Chap. 3.1.2. Each device received a transparent IZO front electrode, which was sputter deposited through a shadow mask with the sputter tool, which we refer to as the Vinci tool (deposition method described in Chap. 3.1.1), and the same standard recipe. The process parameters and film properties are presented in Tab. 4.5. The RF power density of 1.85 W/cm^2 that was applied in this sputter deposition is significantly lower than the RF power density of the low power process presented in Chap. 4.1.1 (2.41 W/cm^2). Therefore, it can be assumed that the sputter deposition used here is possibly even less damaging. The additional oxygen content in the argon gas was 1.67%. The thin film properties were determined from an IZO film on a glass substrate by 4 point measurements and profilometry.

The solar cell stacks were capped with a silver electrode that was deposited through a shadow mask, in order to contact the IZO. The silver stripes were located outside of the active area, to avoid shading. An illustration of the top-view of the design can be found in Chap. 3.1.2.

Table 4.5: Process parameters and film properties of the sputter deposited IZO front electrode for this section's experiment.

	P_d (W/cm^2)	p (Pa)	bias (V)	r(O_2) (%)	d (nm)	R_{sq} (Ω/sq)	μ (cm^2/Vs)	N_e (10^{20}/cm^3)
Vinci tool IZO	1.85	0.6	69	0.16	100	45.2	49.76	2.84

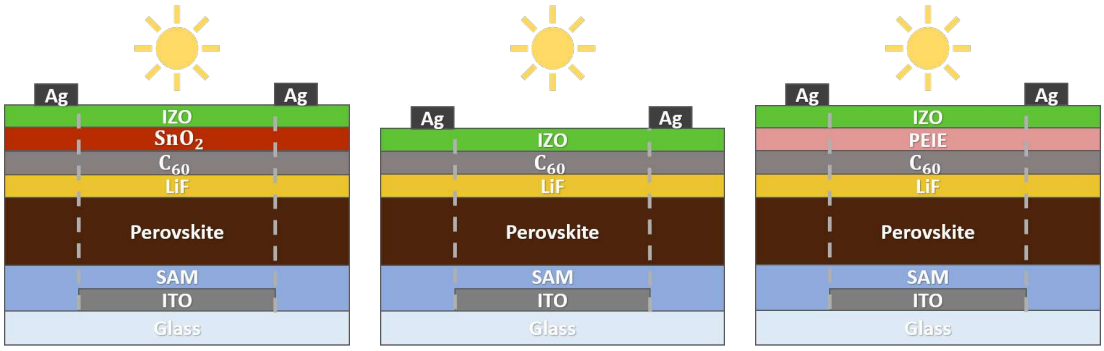

Figure 4.11: Schematic device layout of semi-transparent perovskite single junction (SJ) solar cells with various ETL designs: (a) C_{60}/SnO_2-design; (b) C_{60}-only design; (c) C_{60}/PEIE-design.

First, the electrical properties of perovskite solar cells are investigated to assess the influence of the ETL-design on device parameters. The results of J-V and EQE scans of the devices with three different ETL-design under illumination are displayed in Fig. 4.12. Each configuration in the box plots includes data of at least 12 pixels. This experiment has been repeated several times with similar outcome, so the displayed results are considered meaningful.

Fig. 4.12(a) shows J-V characteristics under illumination with corrected J_{SC}'s (J_{SC}'s were calculated from the EQE scans) for devices based on a C_{60}-only ETL (in red), as well as C_{60}/SnO_2 (in cyan), and C_{60}/PEIE (in dark blue) double-layer ETL. The dark J-V scans can be found in Fig. 6.4 in the Supplementaries (6.1). We chose devices that are representative of the ETL design based on their J-V parameters being close to the average values. A significantly higher FF and V_{OC} can be observed for the two double-layer ETL designs, while the C_{60}-only ETL design exhibits an s-shape behavior. The highest average FF of ~75.82% and V_{OC} of ~1.180 V was observed for the C_{60}/PEIE ETL design. These trends are also statistically represented as box plots in Fig. 4.12(b) and (d). Both average values are slightly higher than in Chap. 4.1, which is probably a result of the even lower target bias of ~70 V (resulting from the lower RF power density) compared to the low power process. The solar cells with the C_{60}-only ETL structure had overall lower average V_{OC} of ~1.124 V and lower FF of ~44.35%. The solar cell devices with the conventional C_{60}/SnO_2 ETL design reach on average 43 mV higher V_{OC}'s and 23% higher FF's than the C_{60}-only ETL design. And the solar cell devices with the C_{60}/PEIE double-layer ETL reach on average 56 mV higher V_{OC}'s and 31.47% higher FF's than the C_{60}-only ETL design. Interestingly, the C_{60}/PEIE double-layer ETL design shows both higher average V_{OC}'s and FF's compared to the conventional C_{60}/SnO_2 ETL design.

Fig. 4.12(c) shows EQE and 1-R scans of the devices with the three different ETL designs.

Due to the PEIE thickness being probably ≤2 nm, the EQE and 1-R scans and the resulting integrated current density of the C_{60}-only and the C_{60}/PEIE double-layer ETL are nearly identical. Both designs show J_{SC}'s of 16.89 mA/cm^2. The C_{60}/SnO_2 ETL design lead to slightly higher J_{SC}'s of 16.92 mA/cm^2. The 1-R spectra appears to be shifted towards higher wavelengths for the C_{60}/SnO_2 ETL design, probably due to the 20 nm SnO_2, which together with 100 nm IZO leads to total metal oxide thickness of 120 nm. We assume that this results in a shift of the interference fringes.

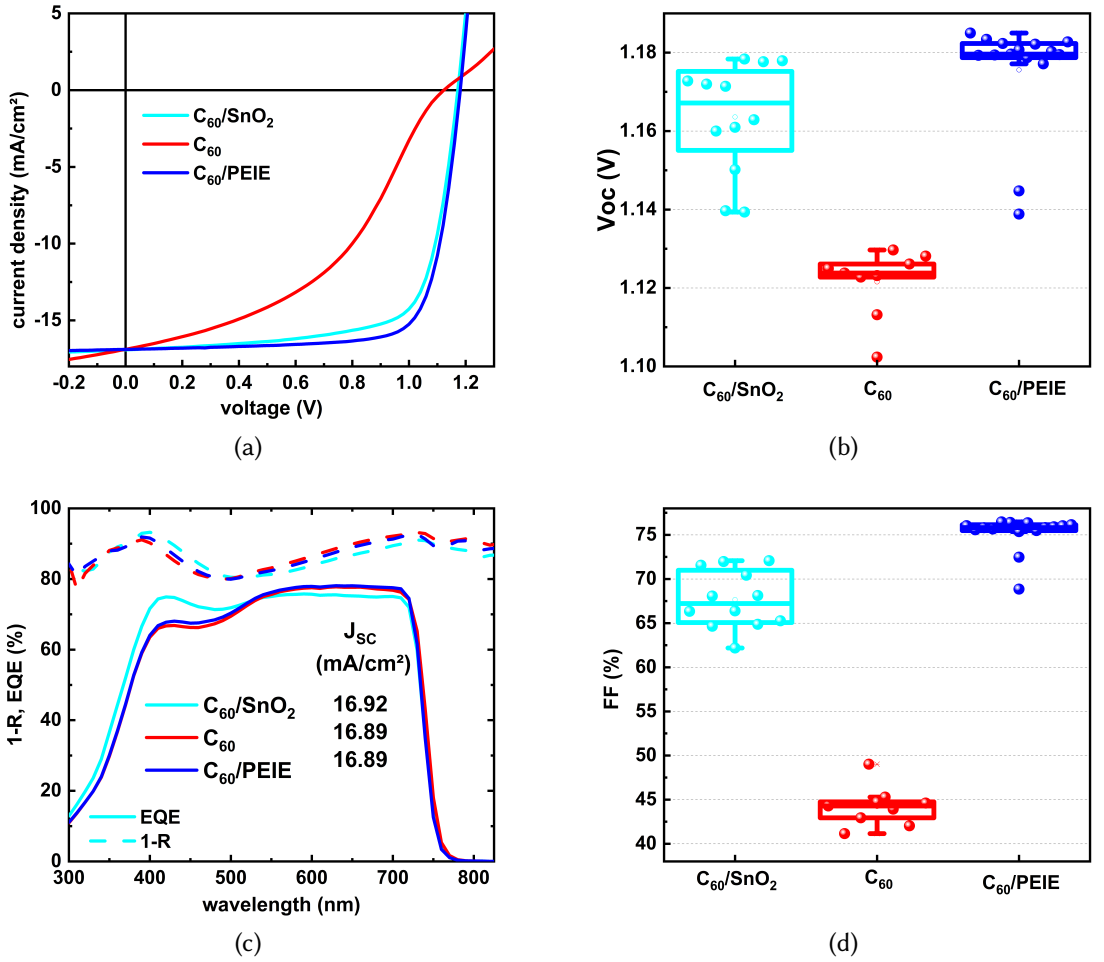

Figure 4.12: (a) J-V characteristics, (b) box plots of open circuit voltage, and (d) fill factor of semi-transparent perovskite single junction solar cells (~ 12 pixels each) with a standard IZO-front contact deposited directly onto the C_{60}-only ETL, as well as onto the C_{60}/SnO_2, and C_{60}/PEIE double-layer ETLs; (c) External quantum efficiency (EQE) spectra and reflection (denoted as 1-R) of selected semi-transparent solar cells measured through the IZO front electrode.

As was also shown in the previous chapter (Chap. 4.1.2), we observe an s-shaped J-V characteristic when omitting the SnO_2 buffer layer and depositing the IZO directly onto the C_{60} electron selective layer. An s-shaped behavior in the J-V characteristics can appear due to various reasons: imbalanced charge transportation [141], insulating interfaces [142], unfavorable energetic alignment [26, 27], or Fermi-level pinning by interface states resulting in Schottky barriers [89, 143]. In Chap. 2.3.3 we discuss the origin and impact interfacial barriers in the electrode/solar cell interface more in detail. Ideally, the nature of the ETL/TCO interface should be an ohmic contact with low interface resistance. Besides the s-shape, reduced FF and reduced V_{OC}, we observe a comparably high series resistance (R_{ser}) of 69.90 $m\Omega cm^2$ for the C_{60}-only ETL device versus 5.76 $m\Omega cm^2$ for the standard C_{60}/SnO_2-buffer layer ETL design and a lowered shunt resistance (R_{par}) of 305 Ωcm^2 for the C_{60}-only ETL device and 1236 Ωcm^2 for the standard C_{60}/SnO_2-buffer layer ETL design, which is listed in Tab. 4.6. For example, interfacial barriers can cause an increased series resistance and reduced shunt resistance [26, 64, 77].
Interestingly, by inserting an ultra-thin ($\leq$2 nm) layer of PEIE, the s-shape vanishes, R_{ser} decreases to 5.07 $m\Omega cm^2$, R_{par} increases to 2731 Ωcm^2, which is even more than twice as high as for the standard C_{60}/SnO_2-buffer layer ETL design, suggesting the lowest recombination losses of the three designs. Consequently, the single junction device PCE dramatically increases from 8.33% to 15.25% (see Tab. 4.6). A similar phenomenom has been observed for bathocuproine (BCP) in perovskite single-junction solar cells, which was inserted between the fullerene PCBM and Ag (the PCBM/Ag interface formed a Schottky contact), resulting in the formation of an ohmic contact, thereby reducing interface recombination [64]. We observe that devices with the C_{60}/PEIE double-layer ETL even outperform the conventional C_{60}/SnO_2-buffer layer design (15.25% PCE vs. 14.29% PCE, see Tab. 4.6), which raises the question, how exactly the PEIE improves the interface. Kim *et al.* claimed that PEIE can act as a "*buffer layer to minimize sputter-damage*" [144]. PEIE is also known to work as a TCO work function modifier [27, 145, 146], and as nucleation layer for metal oxide growth on the non-polar surface of C_{60}, due to its hydroxyl functional groups [137, 138]. As discussed in the previous chapter, the device's V_{OC} is directly dependent on energy alignment and recombination processes, and the FF is dependent on charge transport, series and shunt resistance, and recombination processes. In order to understand the significant differences between C_{60}-only ETL device, and the C_{60}/SnO_2, and C_{60}/PEIE double-layer ETL devices, further, more profound analysis is necessary.

Table 4.6: Solar cell parameters of semi-transparent perovskite single junction solar with IZO front electrodes deposited directly on the C_{60}-only ETL, as well as on the C_{60}/SnO_2, and C_{60}/PEIE double-layer ETL.

ETL configuration	PCE (%)	J_{SC} (mA/cm²)	V_{OC} (V)	FF (%)	R_{ser} ($m\Omega cm^2$)	R_{par} (Ωcm^2)
C_{60}/SnO_2	14.29	16.92	1.172	72.08	5.76	1236
C_{60}	8.33	16.89	1.123	43.93	69.90	305
C_{60}/PEIE	15.25	16.89	1.181	76.46	5.07	2731

In the following, the interface formation between the IZO and the layers beneath, namely SnO_2, C_{60} and PEIE will be further analyzed by electrical light intensity dependent measurements, surface photovoltage analysis, and opto-electronic characterization with the FLUXIM *Paios* technique.

Impact of the ETL-design on the interface formation to the transparent electrode - a light intensity analysis of the the photovoltaic parameters

As explained in the previous Chap. 4.1.2, light intensity dependent J-V measurements may help to understand performance-limiting factors and the significant discrepancies in V_{OC} and FF for the three different ETL design solar cells. Fig. 4.13(a) shows the V_{OC} as a function of light intensity in a semi-logarithmic scale, for the C_{60}-only ETL device (in red), as well as the C_{60}/SnO_2 (in cyan), and C_{60}/PEIE (in dark blue) double-layer ETL devices. The light intensity was varied from 1% (0.01 suns) to 120% (1.2 suns) in 25 steps. The respective ideality factors (n_{id}) were extracted through linear fits (dashed lines). For the C_{60}/SnO_2, and C_{60}/PEIE double-layer ETL devices, similar ideality factors of $\leq$1.54 and $\leq$1.50 were calculated from the slope of the linear fit. Interestingly, we observe the lowest ideality factor of $\leq$1.36 for the C_{60}-only ETL device. The ideality factor describes the dominant recombination processes in the devices and usually exhibits a value between n_{id} = 1 and n_{id} = 2. n_{id} = 1 describes bimolecular recombination (radiative band-to-band) and n_{id} = 2 describes trap-assisted recombination (non-radiative, also called Shockley-Reed-Hall SRH recombination) processes. The value is usually insignificantly influenced by transport losses in the solar cell. Usually, we would expect that a lower n_{id} for the, in principle, same perovskite absorber would result in a higher V_{OC} of the respected devices. Surprisingly, here we observe a low n_{id}, despite a comparably low V_{OC}. This suggests that non-radiative losses inside the perovskite bulk are likely not the primary origin of the V_{OC} reduction in the case of the C_{60}-only ETL device.
Fig. 4.13(b) shows the pseudo-J-V curves for the C_{60}-only ETL, and the C_{60}/SnO_2, and C_{60}/PEIE double-layer ETL devices.

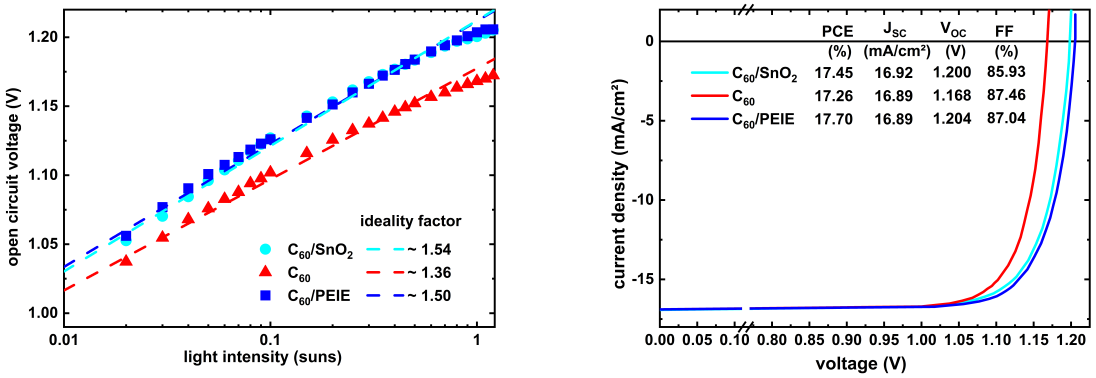

(a) (b)

Figure 4.13: (a) Light intensity-dependent open-circuit voltage with linear fits (dashed lines) and extracted ideality factors (n_{id}); (b) Pseudo-J-V curves reconstructed from the light intensity measurements.

The inset in 4.13(b) shows theoretical solar cell parameters that were extracted from the pseudo-J-V curves. Noticeably, the highest pseudo-FF (pFF) of 87.46% is achieved by the C_{60}-only device, suggesting that the real device's FF was primarily limited by charge transport losses. The same device also shows the lowest V_{OC} = 1.168 V. The highest V_{OC} of 1.204 V and the second highest pFF of 87.04% was achieved by the C_{60}/PEIE device. A similar V_{OC} = 1.2 V, but lower pFF of 85.93% was observed for the C_{60}/SnO_2-buffer layer device.
Comparing the values from Fig. 4.13 to the n_{id}s and pseudo-J-V curves in Fig. 4.9 from Chap. 4.1.2 we see a higher n_{id} and lower V_{OC} and FF for the solar cell with a C_{60}/SnO_2 ETL design than for the solar cell, which also contains a SnO_2-buffer layer, referred to as "with buffer" (n_{id} = 1.44, V_{OC} = 1.202 V, and FF = 86.89%). The difference between those two devices is that the latter contains a C_{60}/PEIE/SnO_2 triple-layer ETL design. It has been reported that PEIE significantly improves the C_{60}/SnO_2 interface [137, 138], which may explain the difference in n_{id}, V_{OC}, and FF. The device with a C_{60}/PEIE ETL design exhibits a higher n_{id}, but also a higher V_{OC} and a similar FF to the "low power" device from Chap. 4.1.2 (n_{id} = 1.42, V_{OC} = 1.191 V, and FF = 87.30%), despite a similar device design. The difference in V_{OC} might originate from the possible lower target potential leading to less sputter damage during the IZO deposition with the Vinci tool compared to the "low power" deposition of Chap. 4.1.2. Furthermore, it needs to be noted that differences between both experiments may also stem from batch-to-batch variations.
In order to visualize the different loss mechanism contributions to the FF, we compared the device's FF from the J-V measurements to the pFF from the pseudo-J-V curves and the theoretical FF in the detailed balance limit of a perovskite absorber with a band gap

of 1.675 eV [74] in Fig. 4.14, a methodology already mentioned and described in Chap. 4.1.2. From this, it becomes clear that the C_{60}/SnO_2-buffer layer design leads to the highest non-radiative recombination losses in the perovskite bulk, reducing the FF by 4.9%. In contrast, the C_{60}-only design exhibits the lowest non-radiative recombination loss contribution to the FF of 3.37%, which suggests that the s-shape and reduced solar cell performance, in this case, do not originate from higher trap-assisted recombination in the perovskite bulk. Instead, the C_{60}-only design suffers from the highest transport loss contribution. The increased transport losses in the case of an IZO electrode sputter deposited on the C_{60} substrate could possibly be attributable to an IZO layer with a higher sheet resistance due to a different film growth on the C_{60} substrate. Therefore, we measured the sheet resistance of the IZO via 4 point probe on glass and on the three different ETL configurations. The sheet resistance of the IZO films were 43.36 Ω, 46.51 Ω, 46.06 Ω and 45.58 Ω for IZO sputter deposited on glass, glass/C_{60}/SnO_2, glass/C_{60} and glass/C_{60}/PEIE respectively. The values are all very similar and follow no obvious trend. Thus, the lateral conductivity within the IZO film is unaffected by the substrate, and cannot explain the difference in transport losses. Therefore, we conclude that the transport losses originate from reduced internal carrier mobility, likely resulting from an interfacial barrier.

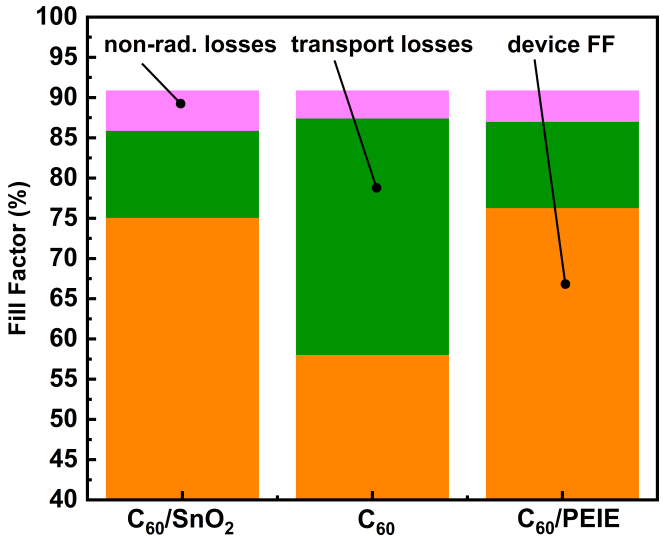

Figure 4.14: A comparison of the device FF derived from J-V measurements and the FF from pseudo J-V curves, as well as the FF in the radiative limit [74], for the C_{60}-only ETL, as well as the C_{60}/SnO_2, and C_{60}/PEIE double-layer ETL devices.

Tress *et al.* described an approach to identify the type of barrier for s-shaped solar cells - extraction or injection [142]. Here, a qualitative analysis based on normalized light intensity dependent J-V measurements provides information about the nature of the barrier. Correspondingly, we normalized the s-shaped J-V curves of the C_{60}-only device, obtained from the light intensity measurements in a range of 1% (0.01 suns) to 120% (1.2 suns), at a reverse bias of -0.2 V. The resulting plot is shown in Fig. 4.15. This technique enables a comparison of s-shapes, which are most prominent at high light

intensities and less prominent for lower light intensities. In case of an extraction barrier, the normalization of the curves would lead to a point of intersection. This can be explained as follows: When electrons accumulate at the corresponding interface due to an extraction barrier, this affects the spatial charge density and electric field distribution. When no external voltage is applied, such accumulations of charges screen the device's built-in field. When an external voltage is applied, the potentials overlap, and a large part of the applied voltage drops across the extraction barrier where the charges are accumulated, consequently reducing the field in the bulk. As a result, charge carriers are extracted less efficiently from the perovskite, and the photocurrent is lower compared to a barrier-free solar cell at the same voltage. This behavior causes the s-shape of the J-V curve in case of an extraction barrier. The field-screening effect is lessened at low light intensities because fewer charges build up at the barrier. Therefore, normalization of the J-V curves of different light intensities results in points of intersection.
We, however, do not observe such a crossing of the normalized curves, suggesting that the origin of our s-shape might rather be an injection barrier. The shape of the dark J-V characteristics (Fig. 6.3 in the supplementary Chap. 6.1) at high forward bias supports this assumption. An injection barrier appears, for example, for a misalignment of the electrode's work function to the adjacent charge transport layer. This can be triggered by interfacial dipoles or an energetic mismatch [25–27].

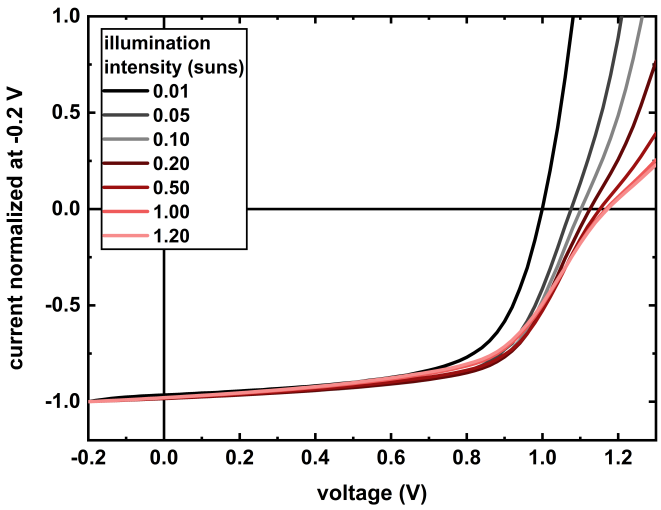

Figure 4.15: At -0.2V reverse bias normalized J-V curves for several light intensities (as shown in the inset). The analysis shown is for the s-shaped C_{60}-only device J-V characteristics.

A quantitative summary of the main findings of the light intensity analysis can be found in Tab. 4.7. By calculating the ideality factor and the percent contribution of non-radiative recombination losses, we were able to extract a measure of charge recombination processes for the three ETL-designs. While at the same time exhibiting the lowest V_{OC} = 1.168 V, the C_{60}-only device also displays the lowest n_{id} = 1.36 and a reduction of the FF due to non-radiative recombination losses by 3.37%, suggesting that the V_{OC} limitation is not a result of SRH recombination in the perovskite bulk. Instead,

the loss analysis revealed that the FF of the C_{60}-only device is dominantly limited by transport losses (29.39%). However, we found no correlation between the IZO sheet resistance and the increased transport losses. Our findings of the normalization of the s-shaped under light intensity variation measured J-V curves support the perception that an injection or Schottky barrier is the source of the observed s-shape. Possible explanations may be sputter damage, which can result in interface states and unfavorable Fermi-level pinning, or a misalignment of the electrode work function to the adjacent charge transport layer [85, 147]. Inserting a SnO_2 or PEIE interlayer between the C_{60} and the IZO significantly improves the J-V characteristics. According to our conjecture, the interlayers either improve energy alignment or lessen the impact of sputtering damage. Both the C_{60}/SnO_2, and C_{60}/PEIE double-layer ETL devices exhibit similar ideality factors (n_{id} = 1.54 and n_{id} = 1.5), while the C_{60}/SnO_2-buffer layer design shows a higher percent contribution of non-radiative recombination losses to the FF reduction (4.9% versus 3.78 %). Therefore, we speculate that the SnO_2 ALD process may induce some degree of degradation to the perovskite bulk.
Finally, we want to point out that the C_{60}/ITO interface has already been the subject of discussions in literature due to a possible energetic mismatch between the ITO work function and the electron affinity of C_{60} [27]. Given that PEIE can operate as a work function modifier, we consider it possible that PEIE in our design also results in a more favorable band alignment, resulting in an ohmic contact between the C_{60} and the IZO.

Table 4.7: Comparison of ideality factors, device open-circuit voltages, device fill factors, impact of transport losses on the FF and impact of non-radiative recombination losses on the FF.

ETL configuration	n_{id}	V_{OC} (V)	FF (%)	transport loss (%)	non-rad. loss (%)
C_{60}/SnO_2	1.54	1.200	75.11	10.81	4.90
C_{60}	1.36	1.168	58.07	29.39	3.37
C_{60}/PEIE	1.50	1.204	76.33	10.72	3.78

Revealing charge carrier dynamics by transient opto-electrical characterization - FLUXIM *Paios* measurements

As it is so far unclear how to understand the above discussed interfaces, more advanced interface-analysis is necessary. In the following an analysis was performed with the characterization instrument *Paios*, which is a tool that uses several opto-electronic characterization techniques in order to investigate the impact of the ETL/TCO interface on device parameters, such as the charge carrier extraction mobility, or the extracted charge carrier density. These parameters can then further be correlated to phenomena such as traps, barriers or interfacial charge-transfer resistivity. The following experiments were carried out with the *Paios* set-up, which includes a white

LED. The maximum intensity of the light source is ~475 W/m^2 and the scan voltage range is ±12 V. The illumination of the devices occurred through the ITO-glass substrate. The density of extracted photo-induced charge carriers was measured by illuminating the solar cell at open-circuit voltage (no charges are collected in a circuit), and then the light is switched off and the device is switched to short-circuit simultaneously (charges are extracted). An extraction current is measured, which, by integrating over time, returns the extracted charge carrier density according to Equ. 3.12. We calculated the charge carrier density for various light intensities. The results are displayed in Fig. 4.16. The devices with an ETL/TCO design of C_{60}/SnO_2/IZO and C_{60}/PEIE/IZO show similar total extracted charge carrier densities, between ~$1.8{\cdot}10^{15}$ 1/cm^3 for the lowest light intensity and ~$5{\cdot}10^{15}$ 1/cm^3 for the highest light intensity. The C_{60}/PEIE device reaches slightly higher values than the C_{60}/SnO_2. The device with an ETL/TCO design of C_{60}/IZO on the other hand has an overall lower extracted charge density of ~$4{\cdot}10^{14}$ 1/cm^3 for the lowest light intensity and ~$1.7{\cdot}10^{15}$ 1/cm^3 for the highest light intensity. That means, overall less photo-generated charges reach the electrodes in case of the pure C_{60} ETL. The increased recombination in this case, as indicated by the lower suns-V_{OC}, causes this.

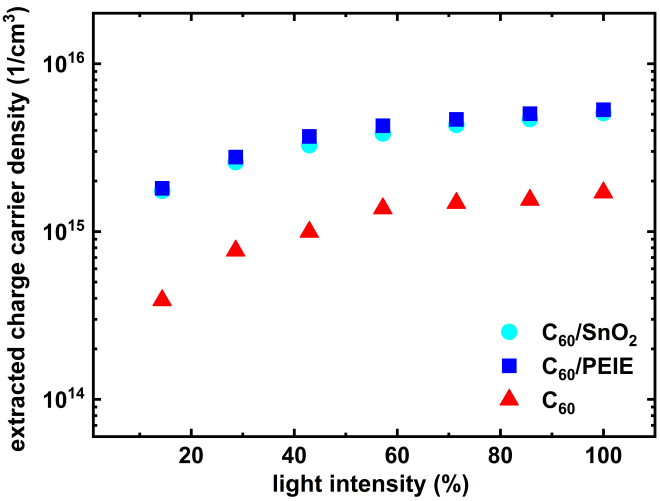

Figure 4.16: The density of extracted photo-induced charge carriers for the C_{60}-only ETL (red triangle) device, and the C_{60}/SnO_2 (cyan circle) and C_{60}/PEIE (blue square) double-layer devices.

By studying the open-circuit voltage decay (OCVD) recombination processes and charge trapping dynamics can be determined. We measured the voltage response to a light pulse of 50 ms, with a light intensity of 90%. In Fig. 4.17 the normalized voltage decay over time is shown for the three ETL configurations. It is noteworthy to mention, that the observed time-scales of charge carrier lifetimes are not considered bulk carrier lifetimes, which are much shorter (< microsecond-scale) [120]. In fact, the observed decay features are considered to be capacitive discharging events [121].
While the second kink at lower voltages in Fig. 4.17 at around 10^{-2} s is considered to be determined by leakage current, by the device's shunt resistance, the first decay

region between 10^{-6} and 10^{-3} s, which is observed for the C_{60}/SnO_2 and the C_{60}/PEIE device, can be described as a discharging of spatially separated mobile charge carriers, with an initially logarithmic time-dependence. However, since the charges are not homogeneously distributed throughout the device layer stack, the trend deviates from this logarithmic dependance. Initially, the photo-generated charges diffuse to the selective contacts, and most accumulate at the electrodes, as no external circuit is connected to collect the charges. These charges diffuse back slowly into the bulk where they recombine. Here, a faster decay (dark blue curve) can be understood as a smoother transition over the interfaces, meaning less defects. Interestingly, the C_{60} device shows a very different behavior in this region. Instead of a logarithmic decay over time, the voltage rises above its initial value at first, before it starts to decrease. Li and colleagues also discovered an overshoot in V_{OC} for transient open-circuit voltage measurements, which they attributed to barrier-induced band bending at the interfaces [148].

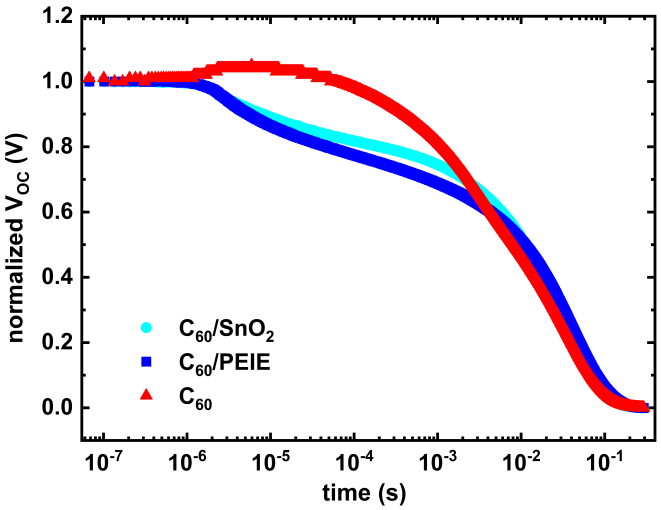

Figure 4.17: Open circuit voltage decay (OCVD) over time (s) for the C_{60}-only ETL (red) device, and the C_{60}/SnO_2 (cyan) and C_{60}/PEIE (blue) double-layer devices.

Similar to the OCVD, the transient photovoltage is a response to a light pulse in order to determine charge carrier lifetimes. Therefore, the measured device is kept at open-circuit conditions. A small light pulse (of 1 ms) leads to generation of charges. When these charges recombine, an exponential voltage decay is observed, following the Equ. 3.14. The time constants shown in Fig. 4.18 are determined by the decay rate of the transient photovoltage and represent averaged values of three time constants that were fitted (the three time constants are shown in Fig. 6.5 in the supplementary section 6.2). The three time constants originate from three different decay components in the photovoltage decay curve and represent different recombination dynamics of charge carriers [122]. It is worth repeating that the described carrier lifetimes are not perovskite layer carrier lifetimes, but rather an interpretation of the much slower recombination of electrons accumulated at the contacts. Similar to the OCVD measurement, the charges that were generated by the light pulse, diffuse towards the selective contacts, where

they accumulate. This leads to a geometric capacitance. When the light pulse is turned off and the capacitor discharges, the electrons will slowly move towards the bulk of the device, in order to recombine. This process can be described as a discharge over a resistor. The larger the resistor, the slower the observed decay and the higher the time constants. This is linked to defect states, in which electrons get trapped for a period of time before being released and able to recombine. A faster voltage decay, is associated with fewer defect states. The highest time constants for all light pulse intensities above 3% was observed for the C_{60} device. For a light pulse intensity of 90% the time constants of the C_{60}/SnO_2 and the C_{60}/PEIE devices are an order of magnitude smaller than the time constant of the C_{60} device (τ_{avg} is ~ 16 μs and ~ 27 μs for C_{60}/SnO_2 and C_{60}/PEIE and ~ 150 μs the C_{60} device).

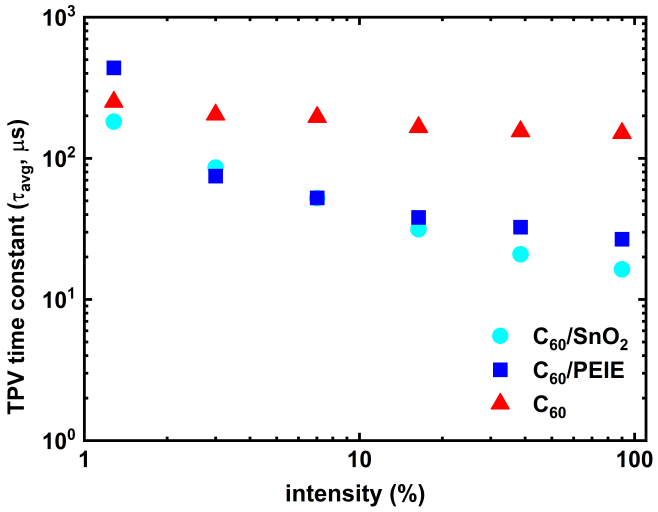

Figure 4.18: The time constants of an exponential voltage decay (the transient photo-voltage) at different light intensities for the C_{60}-only ETL (red triangle) device, and the C_{60}/SnO_2 (cyan circle) and C_{60}/PEIE (blue square) double-layer devices. The shown time constants represent averaged values of three time constants.

For transient photocurrent (TPC) measurement, the current response of the solar cell device to a light pulse is measured. In contrast to TPV, the photogenerated charges leave the device and are collected in an external circuit. The time constant derived from the rise and decay time of the current response is linked to the carrier transport time (charge carrier mobilities) [61, 118]. Furthermore, trapping dynamics can be revealed. For the TPC measurement the solar cell devices were illuminated with light pulse of 200 ms and the transient current was measured. The result of the normalized TPC rise and TPC decay are presented in Fig. 4.19 in (a) and (b), respectively. The respective time constants were calculated from the current rise regime before a steady-state is reached, and from the decay region, before the current reaches zero. A steeper current rise and decay is expressed by lower time constants and correlated to faster charge carrier transport time. In both cases the C_{60} device exhibits the lowest time constants of $\tau_{TPC,rise}$ = 3.77 μs and $\tau_{TPC,decay}$ = 0.61 μs, followed by the C_{60}/PEIE device with time constants of $\tau_{TPC,rise}$ = 6.65 μs and $\tau_{TPC,decay}$ = 0.66 μs. By far the highest time constants

were reached by the C_{60}/SnO_2 device. The $\tau_{TPC,rise}$ of the C_{60}/SnO_2 device is around three times larger than the C_{60} device at 11.72 μs.

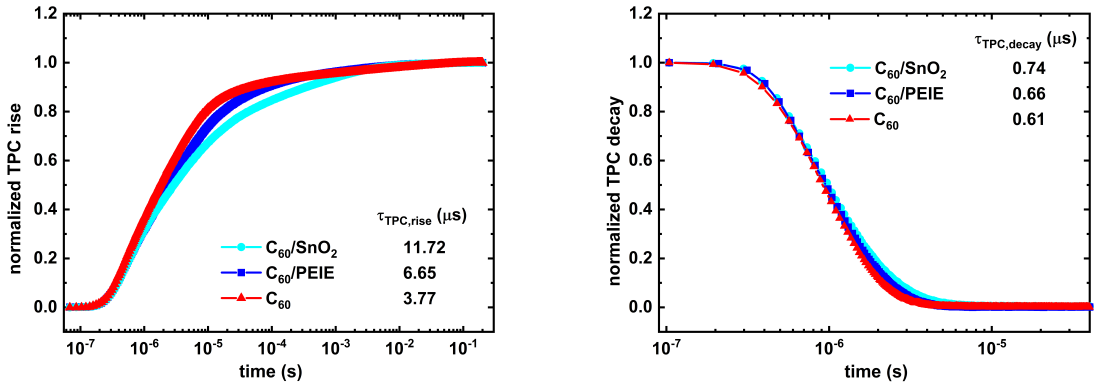

(a) (b)

Figure 4.19: (a) Transient photocurrent rise, and (b) transient photocurrent decay for the C_{60}-only ETL (red) device, and the C_{60}/SnO_2 (cyan) and C_{60}/PEIE (blue) double-layer devices. The respective time constants calculated from the rise, and the decay region are also given.

The respective time constant values are compared to the device specific RC-time constant in Tab. 4.8. The RC-time constant is calculated from the solar cells series resistance and geometric capacitor (according to Equ. 3.6), which determines the smallest meaningful time scale that can be attributed to a process. The series resistance is caused by the TCO sheet resistance, and the geometric capacitance is calculated from the dielectric constants of the layers (see Equ. 3.6). In all three cases the time constants derived from TPC measurement are higher than the RC-time constant and can therefore be considered valid. It appears that the time constants scale with the overall ETL layer stack thickness. The thickest ETL is represented by the C_{60}/SnO_2 device, with an ETL stack consisting of 18 nm C_{60} and 20 nm SnO_2. The thinnest ETL is obviously the pure C_{60}-ETL device, with an ETL thickness of only 18 nm. This is in line with observations done by Shi *et al.*, where although the introduction of a low-mobility organic HTM layer between the perovskite absorber and the electrode slows down the charge transport, leading to longer photocurrent decay times, the charge extraction dynamics are improved [118]. In light of this, the results should be taken with caution because the displayed curves are normalized values rather than absolute numbers. As a consequence, no conclusion concerning the amount of charges extracted can be drawn from this measurement.

Table 4.8: The time constants calculated from the TPC rise and the TPC decay region, and the device specific RC-time constants.

ETL configuration	τ_{RC} (μs)	$\tau_{TPC,rise}$ (μs)	$\tau_{TPC,decay}$ (μs)
C_{60}/SnO_2	0.476	11.72	0.74
C_{60}	0.156	3.77	0.61
C_{60}/PEIE	0.364	6.65	0.66

Another method to investigate the charge carrier transport and mobility and a popular technique for perovskite solar cells is charge extraction by linearly increasing voltage (CELIV) [149–151]. As the name already suggests, a voltage ramp is applied to the devices and equilibrium (dark-CELIV) or photogenerated (photo-CELIV) charge carriers are extracted. Photo-CELIV describes the response to a light pulse, in addition to the applied voltage ramp. As a consequence to the linearly increasing voltage ramp, the extracted charges will lead to a measurable current density, which is described by the Equ. 3.9. This transient current density will have a peak value and a constant displacement current. The charge carrier mobility can be estimated according to the time of the appearance of that current peak [119]. We calculated the CELIV mobility for both, dark- and photo-CELIV. The results for the three different ETL-designs are presented in Fig. 4.20 and Tab. 4.9.

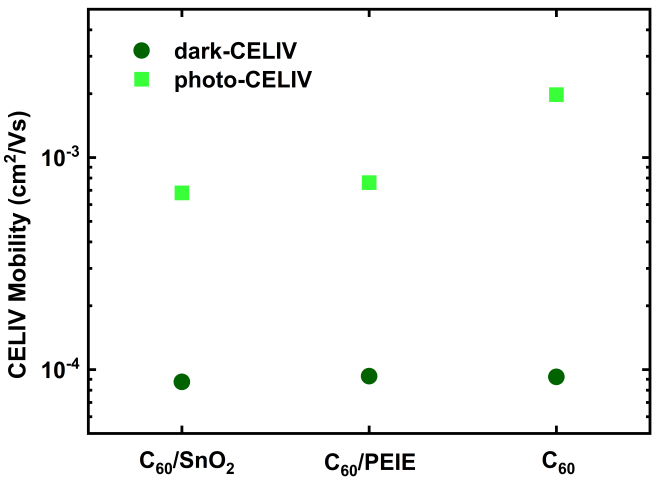

Figure 4.20: The calculated the CELIV mobilities for both, dark- (dark green circles) and photo-CELIV (light green squares) for the C_{60}-only ETL device, and the C_{60}/SnO_2 and C_{60}/PEIE double-layer devices.

Thermally generated/intrinsic carriers in case of dark-CELIV have all very similar CELIV-mobilities, of $8.75{\cdot}10^{-5}$ cm^2/Vs, $9.24{\cdot}10^{-5}$ cm^2/Vs, and $9.31{\cdot}10^{-5}$ cm^2/Vs for C_{60}/SnO_2, C_{60}, and C_{60}/PEIE respectively. In case of the photo-CELIV measurement, where the extracted photogenerated charges lead to a current overshoot, that enabled the calculation of the CELIV-mobility, lead to distictive difference in values. While

the C_{60}/SnO_2 and the and C_{60}/PEIE devices showed similar photo-CELIV mobilities of $6.81 \cdot 10^{-4}$ cm^2/Vs and $7.61 \cdot 10^{-4}$ cm^2/Vs, the C_{60} device reached the highest photo-CELIV mobility of $19.8 \cdot 10^{-4}$ cm^2/Vs, which is consistent with the previous results of the TPC measurement, where the C_{60} device had the lowest time constants, and thus the highest estimated charge mobility.
Nevertheless, the interpretation of the photo-CELIV mobilities is not trivial. The electron mobility of the perovskite absorber is reported to be in the range of 1 - 10 cm^2/Vs [30, 70], which is much higher than the measured photo-CELIV mobilities. On the other hand, the charge carrier mobility in the CTLs can be much lower. For C_{60} several different mobilities have been reported: 1.6×10^{-4}, 8×10^{-2}, 1×10^{-2}, 0.5 cm^2/Vs [30, 70, 152–155]. As a result, the device's multilayer structure may have a lower total carrier mobility. Also, due to disorder or grain boundaries that scatter carriers or the interfaces between the perovskite absorber and the charge collecting electrodes, the observed values of charge carrier mobility are often substantially lower in reality.

However, these results need to be taken with care. According to Stephen et *al.* the calculated mobility rather reflects the mobility of the faster carrier type, which becomes relevant, when the electron and hole mobilities are highly unbalanced [119]. Meaning, if the slower carriers are subjected to traps, the faster carriers might screen the influence of the slower carriers.

Table 4.9: The calculated the CELIV mobilities for both, dark- and photo-CELIV for the C_{60}-only ETL device, and the C_{60}/SnO_2 and C_{60}/PEIE double-layer devices.

ETL configuration	dark-CELIV (10^{-5} cm^2/Vs)	photo-CELIV (10^{-4} cm^2/Vs)
C_{60}/SnO_2	8.75	6.81
C_{60}	9.24	19.8
C_{60}/PEIE	9.31	7.61

The previously presented methods track the response-time of the devices. Impedance spectroscopy (IS) on the other hand is a frequency-domain method. For the measurement, an external voltage of 0.7 V was applied to the devices with a superimposed alternating voltage pulse of 20 mV, and a current was measured for a range of frequencies. This was done under dark conditions (see Fig. 4.21(a)) and for several illumination intensities (see Fig. 4.21(b)). The strength of this methods lies in the assumption, that different effects inside the solar cell respond to different frequencies. The light impedance spectroscopy measurement allows for a qualitative analysis. In the low frequency region (below 10^3 Hz) slow processes like interaction of mobile ions (ion migration) and charge accumulation at the interfaces, and deep and slow traps can be traced [124]. At intermediate excitation frequencies (10^3 Hz < x < 10^6 Hz), slow traps cannot catch and release the charges fast enough to contribute to the capacitive

response, so only fast shallow traps and charge transport in the absorber and CTL can be probed [123]. Above 10^6 Hz the capacitance is dominated by the RC-effect. A higher series resistance shifts the decay to lower frequencies [156]. In Fig 4.21(b) the earliest decay in capacitance at the lowest frequency occurs for the C_{60}/SnO_2-device at around 10^6 Hz (in cyan), directly followed by the C_{60}/PEIE-device and the C_{60}-device shows a capacitance-decay onset at a much higher frequency of around $3x10^6$ Hz. Thus, according to the light impedance spectra, it appears that the C_{60}/SnO_2 configuration leads to the highest series resistance. As a consequence of this, and according to Equ. 3.6 the C_{60}/SnO_2 configuration also has the highest RC time constant τ_{RC} (see Tab. 4.8). The C_{60}/SnO_2 configuration counts one more layer and one more interface than the simple C_{60} configuration, and the SnO_2 is much thicker than the PEIE layer in the C_{60}/PEIE configuration. At intermediate, as well as at low frequencies, an overall higher capacitance response can be seen for the simple C_{60} devices, which is related to trapped [123], slow or accumulated charges [124, 157] in the perovskite layer or the interfaces of the solar cell.

The dark impedance spectroscopy allows for a quantitative analysis, by equivalent circuit fitting. The measurement was performend in dark conditions at a bias of 0.7 V. The data is plotted in a Nyquist (or Cole-Cole) plot (see Fig. 4.21(a)), which was then fitted with a simple equivalent circuit (see Fig. 3.2 in Chap. 3.2.2), to obtain the series resistance, transport resistance and recombination resistance (see Tab. 4.10).

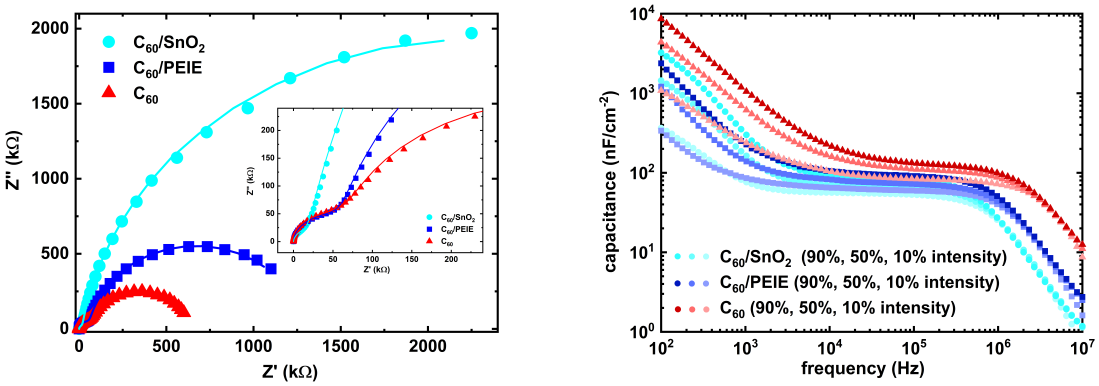

(a) (b)

Figure 4.21: (a) Nyquist (or Cole-Cole) plot of dark impedance spectroscopy (at 0.7 V bias), and (b) frequency resolved impedance Spectroscopy at various light intensities (at 0.7 V bias) for the C_{60}-only ETL (red triangle) device, and the C_{60}/SnO_2 (cyan circle) and C_{60}/PEIE (blue square) double-layer devices.

The series resistance (R_{ser}) is determined by the contact materials, which leads to significant values, when the electrodes consist of TCOs. The transport resistance (R_{tr}) stands for charge transport through bulk material and transfer over interfaces and

may be subjected to charge recombination dynamics. The recombination resistance (R_{rec}) is a measure of charge trapping (in bulk defects or in surface/interface states). Increased charge recombination processes, which decreases the collected charge carrier density, lead to a decrease in R_{rec} and increase in R_{tr}, at the same time, which makes it challenging to determine their individual values [156]. However, the values we found by fitting the Nyquist plot are rather consistent to our previous observations, and therefore we assume them to be meaningful. According to our fits, the C_{60}-only device results in the lowest R_{rec} = 0.56 MΩ and highest R_{tr} = 61.18 kΩ, which stands for a higher recombination and lower extracted charge carrier density. This is in line with the previously discussed charge extraction measurement, where the lowest extracted charge carrier density was observed for the C_{60}-only device. The same device also has the lowest R_{ser} = 15.96 Ω. The highest R_{rec} = 4.43 MΩ and lowest R_{tr} = 15.48 kΩ was calculated for the C_{60}/SnO_2-device, which also has the highest R_{ser} = 38.41 Ω. It seems that R_{ser} scales with the type and number of layers and interfaces that the charges have to pass before being transfered to the circuit. The values of R_{ser} for each ETL design correlate with the previously measured charge extraction mobilities, where the C_{60}-only device has the highest photo-CELIV mobility of $19.8 \cdot 10^{-4}$ cm^2/Vs and the lowest R_{ser} of 15.96 Ω, followed by the C_{60}/PEIE device, with a photo-CELIV mobility of $7.61 \cdot 10^{-4}$ cm^2/Vs and an R_{ser} of 34.67 Ω, and the lowest photo-CELIV mobility and highest R_{ser} was observed for the C_{60}/SnO_2-device with values of $6.81 \cdot 10^{-4}$ cm^2/Vs and 38.48 Ω, respectively.

Table 4.10: Parameters obtained by fitting Nyquist plot with an equivalent circuit.

ETL configuration	R_{ser} (Ω)	R_{tr} (kΩ)	R_{rec} (MΩ)
C_{60}/SnO_2	38.41	15.48	4.43
C_{60}	15.96	61.18	0.56
C_{60}/PEIE	34.67	57.36	1.22

To summarize, we were able to qualitatively and quantitatively evaluate the three different ETL-design devices with the *Paios* (FLUXIM AG, Switzerland) characterization instrument. Overall, very significant differences could be observed for the C_{60}-only device and the devices with interlayers (SnO_2 and PEIE) in between the C_{60} and the IZO-electrode. While we found that the C_{60}-only device exhibits the fastest charge carrier transport time, highest photo-CELIV mobility, and lowest series resistance compared to the C_{60}/SnO_2 and C_{60}/PEIE devices, we could also observe the overall lowest charge extraction density, highest TPV time constants, highest transport resistance and lowest recombination resistance for the C_{60}-only device (see Tab. 4.11). We conclude that while fewer layers in the ETL may lead to faster charge extraction and a lower series resistance (according to TPC, CELIV, and IS), the C_{60}/IZO interface is negatively

affected by defect states and recombination (according to CE, TPV and IS measurements). Furthermore, an overshoot in the OCVD signal was observed for the C_{60}-only device, which has been attributed to unfavorable band bending due to an interfacial barrier in literature. An interlayer, such as SnO_2 or PEIE, seems to improve charge extraction by reducing defect states and reduced recombination losses, leading to a better electrical contact between the ETL and the IZO. Additionally, we observed that the PEIE-interlayer showed less defects (according to OCVD and TPV) and faster charge extraction (according to TPC and CELIV) than the SnO_2-interlayer in the device. The considerable disparities in FF and V_{OC} that we observed for the J-V measurements of the three ETL-designs may be explained by these results. In accordance to our findings described above, we observed the lowest FF and the lowest V_{OC} for the C_{60}-only device (see Fig. 4.12). Furthermore, it is possible that the s-shape behavior of that device originates from defect states that cause unfavorable Fermi-level pinning and lead to an energetic barrier [88, 89]. Interestingly, the C_{60}-only device has the lowest ideality factor according to the light intensity dependent J-V analysis, despite being predicted to have the highest recombination losses given its low recombination resistance. However, we need to state here that the ideality factor represents recombination dynamics in the perovskite bulk rather than interfacial recombination losses, which may explain this discrepancy. The highest FF and V_{OC} was measured for the C_{60}/PEIE device, which might be connected to the low transient voltage time constants (fewest defect states).

Table 4.11: Paios results summarized and collected in one table.

	C_{60}/SnO_2	C_{60}	C_{60}/PEIE
CE at 100% ($1/cm^3$)	$5.08{\cdot}10^{15}$	$1.71{\cdot}10^{15}$	$5.32{\cdot}10^{15}$
OCVD response	fast decay	overshoot	slower decay
$\tau_{avg,TPV}$ at 100% (μs)	27	16	150
$\tau_{TPC,rise}$ (μs)	11.72	3.77	6.65
$\tau_{TPC,decay}$ (μs)	0.74	0.61	0.66
dark-CELIV mobility (10^{-5} cm^2/Vs)	8.75	9.24	9.31
photo-CELIV mobility (10^{-4} cm^2/Vs)	6.81	19.8	7.61
R_{ser} (Ω)	38.41	15.96	34.67
R_{tr} (kΩ)	15.48	61.18	57.36
R_{rec} (MΩ)	4.43	0.56	1.22

The results from this section show the impact of the ETL/IZO interface formation on the electrical characteristics of the solar cell. We observe a pronounced s-shaped J-V curve, when the IZO electrode is directly deposited onto the C_{60} ETL. This s-shape can be linked to an interfacial barrier, which reduces the FF of the respective devices through substantially increased transport losses. We found no evidence for also in-

creased non-radiative bulk recombination. A conventional SnO_2 buffer layer prevents such an s-shape formation, but according to our experiments, an ultra-thin PEIE interlayer, which is known as a dipole rather than for its buffer layer properties, is also able to prevent s-shape formation. We even speculate, that the SnO_2 buffer layer deposition leads to additional defects, thus resulting in a lower V_{OC} compared to C_{60}/PEIE devices, where the PEIE is spin-coated. We therefore raise the questions whether the C_{60}/IZO interface is limited by effects beyond sputter damage, whether the SnO_2 interlayer may not primarily protect against sputtering damage at all, and how PEIE helps the structural and electrical interface formation. The following two sections (4.2.2 and 4.2.3) will address the question of the impact of the ETL design on the IZO film formation and the energetic energy band alignment in the interface.

Summary of the main findings

- When the IZO electrode is directly deposited onto the C_{60} ETL in a semitransparent single junction solar cell, the J-V curves feature a pronounced s-shape.
- Both SnO_2 and the ultra-thin PEIE prevent s-shape formation when introduced as an interlayer between C_{60} and IZO.
- The V_{OC} is significantly lower for C_{60}-only ETL devices compared to C_{60}/SnO_2 and C_{60}/PEIE double-layer ETL devices.
- The highest FF and V_{OC} was measured for the C_{60}/PEIE device.
- According to light intensity dependent J-V measurements, the FF of C_{60}-only devices is mainly reduced by transport losses, which do not originate from different IZO sheet resistances.
- Increased non-radiative recombination losses in the perovskite bulk were not observed for C_{60}-only devices.
- A barrier analysis based on the light intensity dependent J-V measurements resulted in the qualitative statement, that the C_{60}/IZO interface is defined by an injection barrier.
- Transient opto-electrical measurements showed increased defect states and recombination for the C_{60}-only ETL device, and also revealed signs of unfavorable band bending due to an interfacial barrier.
- Devices with either SnO_2 or PEIE interlayer exhibited fewer defect states and reduced recombination losses.

- We suspect that the SnO_2 ALD process also leads to defects and consequently recombination losses.
- We believe that PEIE modifies the energetic band alignment between C_{60} and IZO rather than protecting against sputter damage.

4.2.2 Real-time in-situ investigations of the growth kinetics of sputtered indium zinc oxide on different layers of the electron selective contact

Investigation of the surface energy of the different ETL-designs by contact angle measurements

The surface energy of a substrate can have a significant impact on the formation of an interface and consequently the film growth. The nature of the thin film growth mode (Volmer–Weber, Frank–van der Merwe, or Stranski–Krastanov growth) depends on the interaction strength between adatom and surface [46]. A more detailed explanation of thin film formation processes are given in Chapt. 2.2.1. Furthermore, we can estimate the nature of an interfacial barrier based on the interaction strength of the involved materials. While the Schottky-Mott limit describes the dependency of the barrier height on the electrode WF for non-(weakly-)interacting materials, moderate or strong chemical interaction lead to strain and interfacial states and may result in Fermi-level pinning [88, 90]. The latter situation is complex, and estimating whether two materials will or will not form a Schottky-barrier when forming an interface and explaining the exact origin of the barrier is difficult. In the previous chapter we observed a significant s-shape when IZO is directly deposited on the C_{60}-ETL, suggesting an interfacial barrier, while the s-shape vanishes when SnO_2 or PEIE is inserted in-between the C_{60} and the IZO electrode. Now, we want to understand how the interface between C_{60} and IZO is formed, how the substrate surface energy correlates with the interface formation and whether surface properties are changed when an interlayer is introduced. Contact angle (CA) measurements can be used to identify the polarity and thus interaction strength of a material and quantify its surface energy.
First, we present our results on contact angle measurements. We analyzed the contact angle of water as a polar liquid and diiodo-methane - a dispersive liquid of a non-polar organic molecule - on solar cell-like stacks of HTL/perovskite/LiF/ETL, with the three different ETL configurations: only C_{60}, C_{60}/SnO_2, and C_{60}/PEIE. Polar materials typically interact strongly with polar surfaces, leading to small contact angles. A non-polar material usually tends to be hydrophobic. A water droplet will result in a large contact angle on such a surface. Digital photographs of the sessile droplets on the thin films were used to estimate the contact angle values for two tested liquids. In Fig. 4.22 we show selected photographs of the contact angle measurement for water (top row) and diiodo-methane (bottom row) on C_{60}/SnO_2, C_{60}, and C_{60}/PEIE (from

left to right). And in Tab. 4.12 we summarize the measured average contact angles of several measurements, as well as the calculated surface free energies, which is the sum of the dispersive and polar components, calculated from the respective contact angles. The C_{60}-only ETL stack shows a high mean contact angle of around ~85° with water (see Fig. 4.22(b) and Tab. 4.12), and a small mean contact angle of around ~12° with diiodo-methane (Fig. 4.22(e) and Tab. 4.12). In comparison, the C_{60}/SnO_2-double layer ETL stack has a much smaller mean contact angle with water of ~22° (Fig. 4.22(a) and Tab. 4.12), and a much higher mean contact angle with diiodo-methane of ~29° (Fig. 4.22(d) and Tab. 4.12). This results in significantly different surface free energies. The C_{60}/SnO_2-double layer surface free energy is 74.46 mN/m, a much higher surface free energy than the C_{60}-only stack surface with 50.51 mN/m. Therefore, we predict that, on top of both ETL designs, the IZO thin film growth mode will be considerably different. Furthermore, the ~2 nm thick PEIE layer on the C_{60} lowers the mean contact angle with water to ~57° and increases the mean contact angle with diiodo-methane to ~17°, compared to the pristine C_{60} surface. The resulting surface free energy of the C_{60}/PEIE-double layer surface is 59.45 mN/m, which is higher than the surface free energy of the pristine C_{60} surface, but significantly lower than the surface free energy of the C_{60}/SnO_2-double layer surface. According to this value, we tentatively expect a similar growth mode of IZO on the C_{60}/PEIE-double layer surface as on the pristine C_{60} surface.

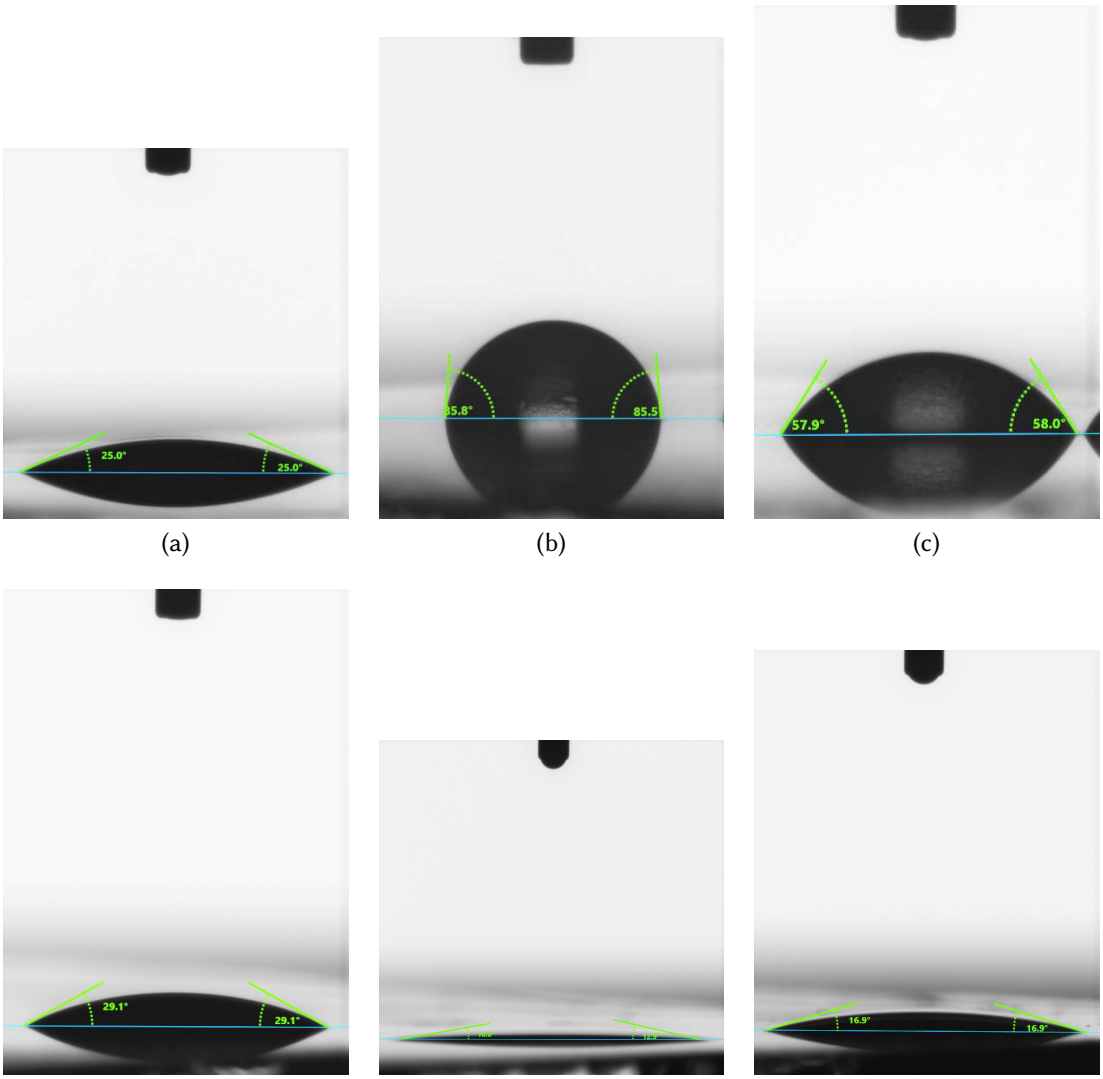

(a) (b) (c)

(d) (e) (f)

Figure 4.22: (a) - (c) images of water droplet contact angle; (d) - (f) images of diiodo-methane droplet contact angle. Images of droplets on the substrates with ETL configuration of (from left to right): C_{60}/SnO_2, C_{60}, C_{60}/PEIE. Corresponsing wetting envelopes are shown in Fig. 6.7 in Chap. 6.2 of the Supplementaries.

Table 4.12: Overview of measured contact angles (CA) of water and diiodo-methane and calculated surface free energy on perovskite solar cell-like stacks with different ETL designs.

	C_{60}/SnO_2	C_{60}	C_{60}/PEIE
mean CA water (°)	21.73 (±2.13)	85.11 (±2.85)	57.34 (±1.03)
mean CA diiodomethane (°)	29.15 (±0.34)	12.19 (±2.67)	16.86 (±0.58)
surface free energy (mN/m)	74.46	50.51	59.45

In-situ study of sputtering IZO on different ETL configurations of the perovskite solar cell

Although it is challenging to analyze buried interfaces, it is crucial to comprehend how interfacial features affect the electrical properties of solar cells. As mentioned earlier, the interface formation can significantly impact the solar cell performance, specifically the interaction of the two interface forming materials and the impact of the deposition process on the substrate, namely sputter damage. Therefore, we have utilized an in-situ analysis technique to investigate the interface formation during the IZO thin film sputter deposition. So far, little is known about the early stages of TCO growth, the interaction between the substrate material and the growing TCO layer, the formation of this critical interface, as well as the impact of the sputter process on the sensitive substrate. We used In-situ grazing-incidence small-angle X-ray scattering (GISAXS) to monitor the nanoscale nucleation, coalescence, and layer growth processes of the sputtered layer on the surface. This allows us to study the growth kinetics of the transparent conductive oxides influenced by the different substrate top-layers of the perovskite solar cell ETL. IZO was deposited by RF sputter deposition on the three different ETL configurations of perovskite solar-cell stacks, specifically directly on C_{60}, and on the ETL double layers SnO_2/C_{60}, and PEIE/C_{60} (note that in this section, the materials stack order definition is reversed; the material through which the signal beam passes first is written first - in all other sections/chapters, we usually start the sequence of writing a material stack with the substrate and the layers that are deposited first). Sample details in the order they were analyzed for the experiments are shown in Tab. 4.13. We used a ceramic IZO (90%wt. In_2O_3 und 10%wt. ZnO) target. The sputter power density was 9.03 W/cm^2 and the working pressure was set to 3.5×10^{-2} mbar (due to technical limitation it was not possible to go to lower pressures). The sputter gas was pure argon, and no additional oxygen was added during the deposition. The sputter rate was estimated to be $3.01\cdot10^{-3}$ nm/s. The whole deposition time for each sample was 75 min, except for IZO on silicon, which was 610 min. The final IZO thickness after 75 min of IZO deposition was calculated to be ~13.54 nm. Later in this section we will discuss the accuracy of this value.
We performed real-time monitoring of the early stages of IZO growth on the selected layers of the perovskite solar cell using time-resolved micro-beam GISAXS (μGISAXS).

We chose to sputter at certain time intervals (5 min, 10 min, 20 min, and 40 min), and in between the time intervals, we made GISAXS "beauty" shots and damage scans (not shown here). The "beauty" shots are detector images used to track the evolution of the growth after each deposition step. They served more as a guide during the experiments. The damage scans serve as evidence that the observed effects are not related to beam damage due to irradiation of the sample. After the samples were exposed to the beam for a significant time, no change was observed, so we can conclude that the samples remained stable to the method.
The following detector was used: PILATUS 2M for μGISAXS in 2.5m distance. The beam was micro-focused at an energy of 11.8 keV. Images were taken at 10 Hz. The abovementioned analysis was carried out in one setup, including the in-situ RF sputter deposition at the P03 beamline of the facilities of Deutsches Elektronen-Synchrotron (DESY).

Table 4.13: Sample details in the order they were used for the in-situ GISAXS experiments.

nr.	sample
1.	silicon
2.	SnO_2/C_{60}/silicon
3.	C_{60}/silicon
4.	PEIE/C_{60}/silicon

The setup and the basic principle of this method in explained in Chap. 3.2.1. In Fig. 4.23 resulting 2D GISAXS detector images of the IZO sputter deposition on SnO_2/C_{60}/Si, C_{60}/Si, and PEIE/C_{60}/Si samples (left to right column) is presented in 6 images each at different IZO thicknesses. Each image is a sum of in total 100 images, improving the resolution of the images and measurement statistics. The respective approximated IZO thickness at the point of the 100th image is shown as an inset in the right column. The first row represents the initial substrate situation for each case, when little to no IZO particle arrived at the surface.
Key scattering features belonging to the structure of IZO particles forming on the surface of each substrate type can be observed in the horizontal and the vertical direction of the the 2D reciprocal space data in Fig. 4.23. The initial shape of the signal for the three substrates is significantly different, mostly in the q_z-direction, which indicates different surface structure, morphology, layer thickness or roughness for the pristine C_{60} layer, the PEIE/C_{60} double layer and the SnO_2/C_{60} double layer. The most pronounced difference is observed for the SnO_2/C_{60} double layer compared to the pristine C_{60} layer, which originates from the 20 nm thick SnO_2 on top of the C_{60}. We observe pronounced fringes of the signal intensity in q_z-direction and some out-of-plane scattering features in the q_y-direction, suggesting that the ALD-deposited SnO_2 layer is not a homogeneous film on the C_{60}, but formed large grains. This is supported by observations made by

Raiford *et al.* [137]. After approximately 1 nm of IZO deposition pronounced out-of-plane scattering features in the q_y-direction can be observed for the C_{60}/Si samples, and similar but overall weaker signal intensities are observed for the PEIE/C_{60}/Si samples. From the out-of-plane maxima the IZO cluster size and distribution can be extracted. Interestingly, no out-of-plane scattering features appear for the SnO_2/C_{60}/Si sample at ~ 1 nm, while the signal shape clearly changes in q_z-direction, indicating indeed a change in layer thickness. We assume that the IZO particles do not form particle clusters, suggesting either a Frank–van der Merwe or Stranski–Krastanov growth mode. At ~ 3.18 nm, weak out-of-plane scattering features appear for the SnO_2/C_{60}/Si samples, while the out-of-plane scattering side maxima of the C_{60}/Si and PEIE/C_{60}/Si samples move inwards towards smaller q_y's. We correlate this with increasing cluster sizes. At ~ 5.28 nm, the onset of additional out-of-plane scattering features appear at large q_y's for the C_{60}/Si and PEIE/C_{60}/Si samples indicating new clusters of smaller sizes forming on top of the initial IZO film, while the out-of-plane scattering features for the SnO_2/C_{60}/Si sample grows in intensity but shows no pronounced maxima, suggesting the formation of clusters in a broad range of sizes. Furthermore, we observe additional out-of-plane peaks parallel to the detector, for the C_{60}/Si sample and even stronger pronounced for the PEIE/C_{60}/Si samples. We assume these peaks appear due to either higher orders of the C_{60} buckyball structure, restructuring due to the sputtering, or increased scatter contrast due to the decoration (accumulation of deposited atoms creating surface structures). For ~ 9.48 nm and ~ 12.63 nm the intensity of the out-of-plane scattering features for the SnO_2/C_{60}/Si sample increases, while for the C_{60}/Si and PEIE/C_{60}/Si samples the second order side maxima grow inwards, resulting in further out-of-plane peaks parallel to the detector.

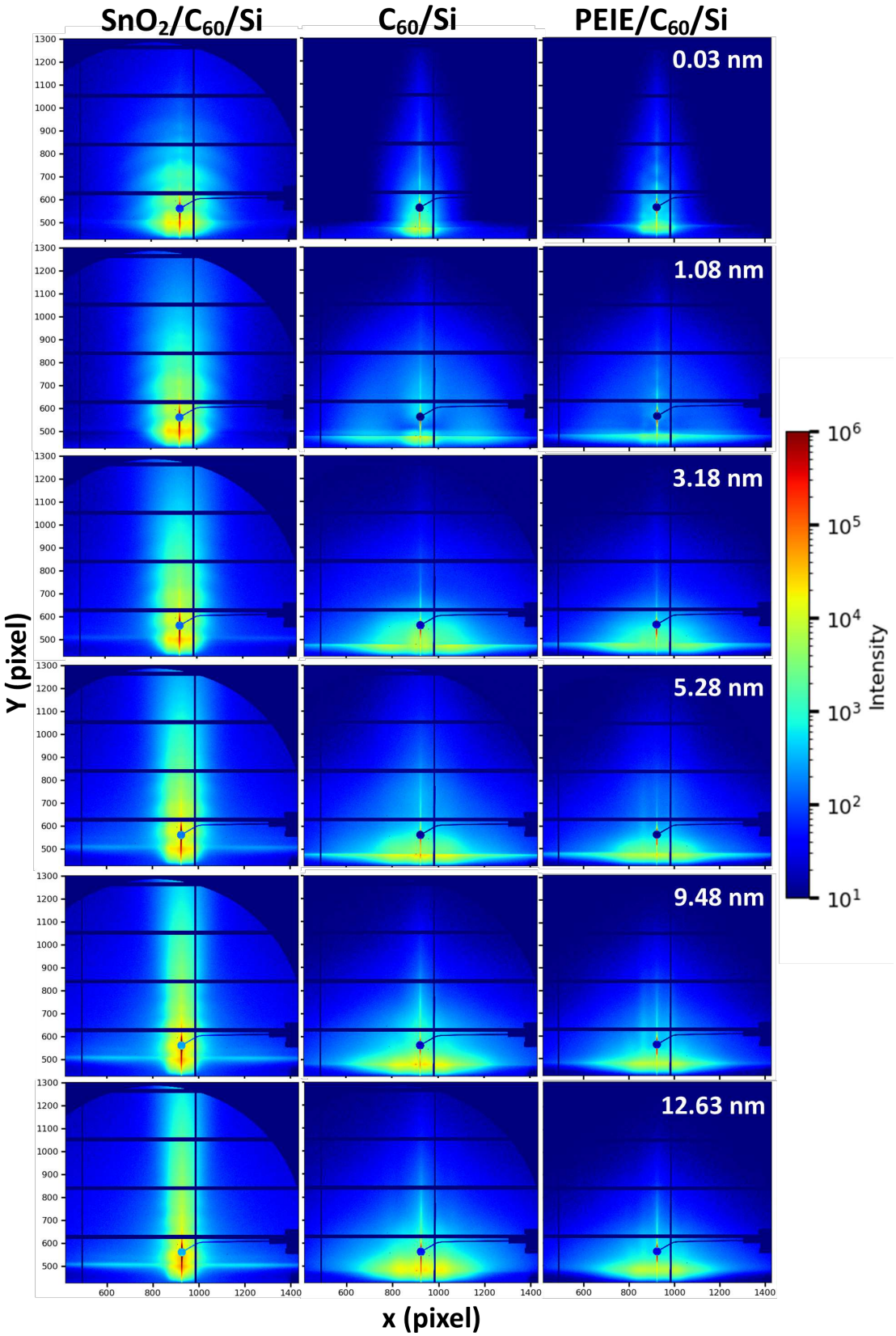

102

Figure 4.23: Selected 2D GISAXS detector images taken in-situ during the sputter deposition of IZO. The evolution of the scattering features with increasing IZO film thickness can be seen (from top to bottom). The effective IZO film thickness was estimated and is given in an inset on the right row. From left to right, the detector images are assigned to: $SnO_2/C_{60}/Si$, C_{60}/Si, and $PEIE/C_{60}/Si$ (the materials are given in the order of beam passing). The gap between the modules appears as black stripes, and the beam stop that shades the specularly reflected beam appears as a black circle.

Morphological evolution of IZO growth on different substrate designs

Horizontal line cuts (also referred to as out-of-plane cuts) along q_y at constant q_z give information on the horizontal intensity distribution. Usually, a section along the critical angle is selected for this purpose. In Fig. 4.24 we present the horizontal line cut evolutions for each substrate configuration. On the left side, the horizontal line cut evolutions are depicted as a 2D intensity map, and on the right side, the 1D data in a double logarithmic scale. In Fig. 4.24(a) and (b) we present the SnO_2/C_{60}/Si sample data, in Fig. 4.24(c) and (d) the C_{60}/Si sample data, and in Fig. 4.24(e) and (f) the PEIE/C_{60}/Si sample data.
In the horizontal line cuts we can observe some ob the above discussed features. In Fig. 4.24(a) the 2D map, showing the intensity evolution of the horizontal cuts, reveals weak of out-of-plane scattering features, with slightly increasing intensity at higher calculated IZO thicknesses. The data suggests a Stranski-Krastanov growth mode for IZO on SnO_2/C_{60}, meaning an initial layered growth of up to several monolayers thickness is followed by an island-like growth of IZO particles after a critical thickness is reached. In Fig. 4.24(b), we can observe the initial out-of-plane scattering features at small q_y values, which probably are connected to big SnO_2 grains (indicated by the small opaque red arrow). These features vanish after some nanometers of IZO deposition. The evolution of the weak out-of-plane IZO cluster scattering features is indicated by a big transparent red arrow. We notice a very subtle tendency of the side maxima moving inward.
In Fig. 4.24(c) we present 2D intensity evolution map of IZO sputter-deposited on the C_{60}/Si sample. Here, we observe the appearance of various new side maxima originating from out-of-plane scattering features, up to several orders, and a dynamic influence from the substrate, indicated by a change of side maxima intensity below 3 nm IZO film thickness (pointed at by the small opaque red arrow). The latter, we suspect to originate from gaps between the C_{60} buckyballs being filled up with IZO clusters so that the scattering length density (SLD) is adjusted or from a kind of refractive index matching. In Fig. 4.24(d) the 1D data of the horizontal cuts evoluation reveals that the sidemaxima consist of a first, second, and third order of clusters forming on the surface for increasing IZO thickness (indicated by big transparent red arrows). Also a clear tendency of these side maxima moving inward can be observed, which correlates with a growth in size of these clusters. In Fig. 4.24(e), for IZO sputter-deposited on the PEIE/C_{60}/Si sample, we likewise observe a dynamic influence from the substrate as indicated by a change in the intensity of the side maxima at small q_y values below 3 nm of IZO thickness. The initial side maxima, probably a feature of the C_{60} surface exhibits an overall lower intensity than in Fig. 4.24(c) for the pristine C_{60}, which may indicate that the PEIE layer smoothed the C_{60} surface. Furthermore additional side maxima appear at higher q_y values (~ 0.2 nm^{-1}), which may be a contribution of PEIE clusters

at the surface, as they are not present in the case of the pristine C_{60}.
Fig. 4.24(f) depicts the 2D intensity evolution map of IZO sputter-deposited on the PEIE/C_{60}/Si sample. Here, we see a similar overall trend as in Fig. 4.24(d) for IZO sputter-deposited on the C_{60}/Si sample, as first, second, and third-order clusters forming on the surface for increasing IZO thickness can be observed, too. However, the intensity maxima belonging to the clusters appear to be wider or stretched along q_y, indicating much less preferred cluster sizes. To be precise, the intensity maximum can be understood as a statistical distribution of cluster sizes. A wider peak appears due to more different cluster sizes. Moreover, the IZO cluster peaks move to lower q_y values, compared to the C_{60}/Si case, ~ 0.2 nm^{-1} for the PEIE/C_{60} double-layer substrate and ~ 0.3 nm^{-1} for the pristine C_{60} substrate. We interpret lower q_y values of IZO cluster peaks as, on average, bigger IZO clusters.

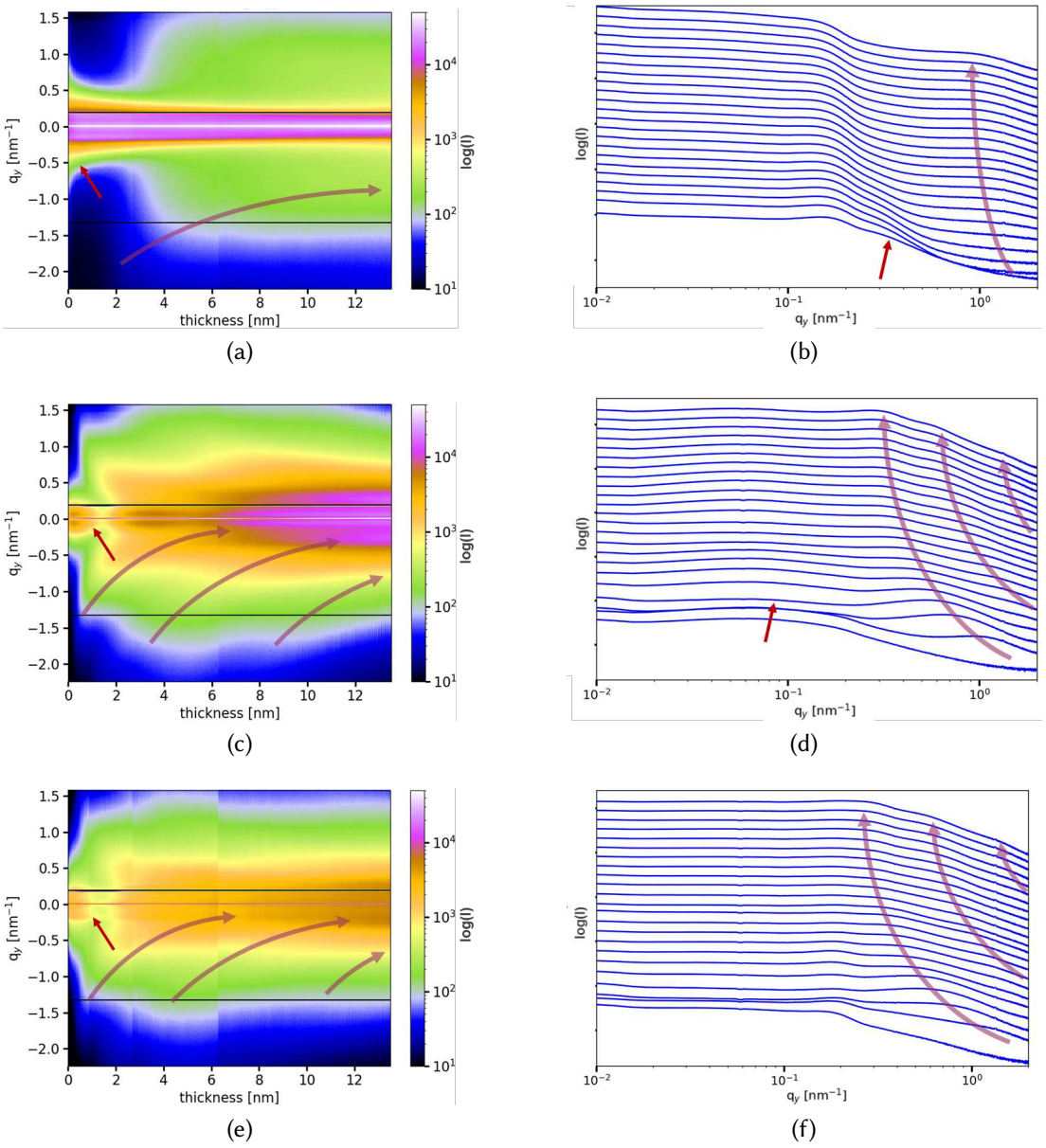

Figure 4.24: Contour mapping plots of the horizontal line cut evolution for summed images (100 images are summarized to one, improving the resolution) on the left, and 1D data of the horizontal cuts evolution for every 20th image of the 450 summed images on the right. The presented data depicts the growth of IZO from 0 nm to 13.5 nm. (a) and (b) show IZO growth on $SnO_2/C_{60}/Si$, (c) and (d) show IZO growth on C_{60}/Si, and (e) and (f) show IZO growth on $PEIE/C_{60}/Si$. The transparent red arrows indicate the occurrence and growth of IZO clusters. The red opaque arrow points at phenomena discussed in the text.

Next, the 1D horizontal line cuts data for each case is fitted using a combination of different fit-functions. We used a Lorentzian function for the intensity at $q_y = 0$ in each case. In the case of the pristine C_{60} and the PEIE/C_{60} double layer we used double symmetric Lorentzian functions for the stationary side maxima (probably of the C_{60}), while additional double symmetric Gaussian functions were used to fit the second side maxima at ~ 0.2 nm^{-1}, and in case of the SnO_2/C_{60} double layer we used a Gaussian function at $q_y = 0$ and double symmetric Lorentzian functions in order to fit the substrate. The evolving lateral IZO cluster peaks of first order were fitted using double symmetric Gaussian functions, while higher orders of IZO cluster peaks were fitted with two symmetric double Lorentzian functions. The fits for each case at 13.5 nm IZO film thickness are presented in Fig.6.11 and at 6 nm for the C_{60}/Si substrate and the PEIE/C_{60}/Si substrate in Fig.6.12 (highlighting the additional peak of the substrate at ~ 0.2 nm^{-1}) in the supplementary section 6.2.
The position of the IZO cluster peaks is used to evaluate the cluster growth behavior. The average cluster center-to-center distance can be calculated as follows [116]:

$$D \approx 2 \cdot \pi / q_{y,1,IZO} \tag{4.1}$$

where $q_{y,1,IZO}$ is the first order IZO cluster peak position. A geometrical model described by Schwartzkopf *et al.* which was applied for gold deposition on polymer substrates furthermore suggests a calculation of the IZO film thickness-dependent cluster radius, assuming a uniform and hemispherical growth [114, 116]:

$$R(\delta) = \sqrt[3]{\frac{3^{3/2}}{4\pi} D^2 \delta} \approx \left[3^{3/2} \pi \frac{\delta}{q_{y,1,IZO}^2} \right]^{1/3} \tag{4.2}$$

where D is the above-mentioned average cluster center-to-center distance, and δ is the IZO film thickness. The ratio of average cluster diameter (2R) to cluster center-to-center distance, or 2R/D, provides information on the various processes that predominate during certain growth regimes. Additionally, it provides the crucial percolation threshold at which clusters merge and form the initial percolated IZO layer, defined by 2R/D=1.
In Fig. 4.25, we demonstrate the dynamic changes that occurred as the IZO layer forms on the C_{60}/Si substrate, providing a thorough understanding of the growth mechanism. Fig. 4.25(a) shows the average first order cluster radius (blue), center-to-center distance (red), and 2R/D (green) calculated from fits. Furthermore, we present measurements from ex-situ SEM to highlight the surface morphology. The SEM pictures were taken at estimated IZO film thicknesses of 1.5 nm (Fig. 4.25(b) and (d)) and 13.5 nm (Fig. 4.25(c) and (e)), showing the nanoscale size evolution of the IZO clusters on the C_{60}/Si substrate. The white bar in the upper right corner in each image shows the size scale. According to each stage's most prominent process, the structure evolution can be

classified into distinct regimes (classification is based on the work of Schwartzkopf *et al.* [112, 114]):

- I. beyond our resolution, the nucleation of IZO clusters takes place (grey region).
- II. then D increases fast, which indicates diffusion-mediated coalescence of mobile clusters (yellow region).
- III. the increase of D slows down, suggesting an adsorption-dominated growth of immobile clusters; while the expansion of clusters continues, it becomes increasingly time-consuming; at the end of this growth regime (at ~6 nm), we observe that the Yoneda peak shifts to slightly higher q_z-values (see also Fig. 6.8(b) in the supplementary section 6.2), indicating an increasing IZO coverage of the C_{60} surface (orange region).
- IV. when the percolation threshold is reached at $\delta_{1,IZO}$ = 6.41 nm (2R/D = 1, grey dashed line), D continues to increase linearly, implying vertical IZO layer growth (grey-blue region).

In Fig. 4.25(b) and (d), we see small structures that we conclude to be initial IZO clusters forming on top of the C_{60}/Si substrate, while we exclude these structures to be the C_{60} surface itself (compare to Fig. 6.10 in the supplementary section 6.2). At ~1.5 nm IZO layer thickness, the clusters exhibit an average radius of ~4 nm and a center-to-center distance of ~10 nm, according to our fits. We can conclude from the horizontal line cut evolution in Fig. 4.24(c) and (d) that higher order clusters begin forming on top of the initial layer. Before the percolation threshold of 6.41 nm is reached, the second order cluster side maxima develop at an IZO layer thickness greater than 2 nm. The structures that we observe at estimated 13.5 nm IZO layer thickness in Fig. 4.25(c) and (e) are therefore likely clusters of higher order, forming on top of already existing structures underneath.

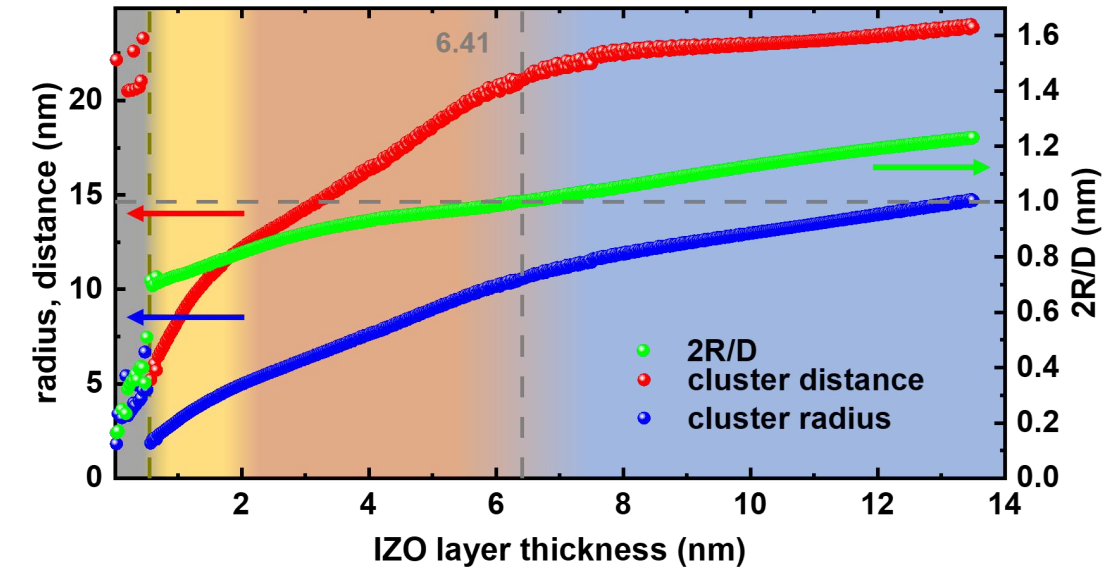

(a)

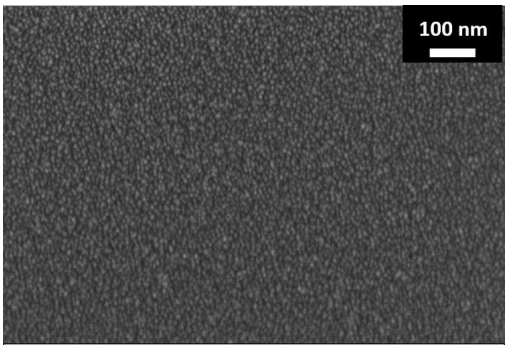

(b)

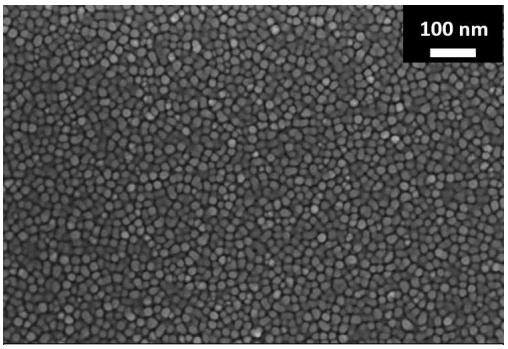

(c)

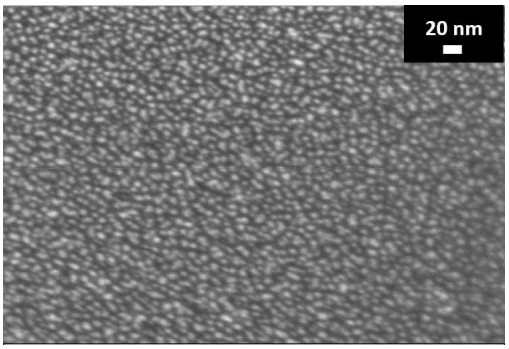

(d)

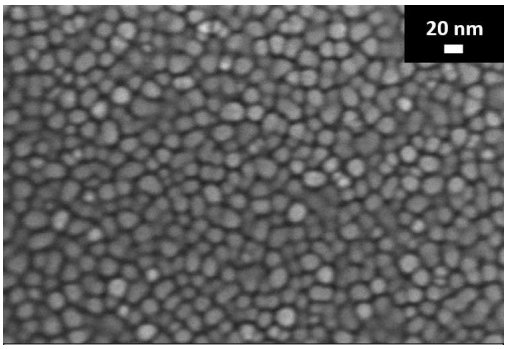

(e)

Figure 4.25: (a) Model-based structure evolution over effective film thickness represented by the average cluster distance D (red), the cluster radius R (blue), and the relation 2R/D (green) for the IZO film growing on C_{60}/Si. The structure evolution is divided into different stages, as defined by the respective most dominant process, highlighted by the background color. The gray dotted vertical line represents the percolation threshold 2R/D=1. (b) to (e) show SEM images of the IZO at different effective film thicknesses and image resolution. (b) and (d) show IZO at ~1.5 nm layer thickness, (c) and (de) show IZO at ~13.5 nm layer thickness. The inset shows the SEM image resolution.

In Fig. 4.27 we present the IZO layer growth on the SnO_2/C_{60}/Si substrate. Below 2 nm (indicated by the gray area in Fig. 4.27(a)), there was no detectable scattering in the horizontal direction leading to side maxima. Therefore, this area is below our resolution. According to the 2D intensity map (see horizontal line cut evolution in Fig. 4.24(a) or Fig. 6.9 of the supplementary section 6.2, which is depicted with a different contrast) we observe initial out-of-plane scattering features from IZO clusters between 1.5 and 2 nm of estimated IZO layer thickness. Interestingly, we do not observe a point of the percolation threshold (where 2R/D = 1), as the cluster diameter (2R) is bigger than the center-to-center distance from the moment they are detectable. Still, we observe a dynamic change in the cluster distance and radius slopes. At first, the slopes are steeper, possibly due to a slight expansion of IZO surface clusters (orange background), which becomes increasingly time-consuming. Then the slope becomes flatter (blue background).
Overall, the cluster growth dynamic is fundamentally different from the IZO growth dynamic on the C_{60}/Si substrate as mentioned above, which might underline our earlier idea that the IZO growth follows the Stranski-Krastanov growth mode - a layered growth followed by an island growth.
Additionally, we estimated the average particle density based on the triangular unit cell of the model clusters' covered area, in order to better understand the differences in case of both substrate designs, according to the following formula [116]:

$$\rho = \frac{2}{\sqrt{3} \cdot D^2} \tag{4.3}$$

In Fig. 4.26 we compare the average estimated particle density of the IZO model clusters ($\rho_{IZOcluster}$) on the C_{60}/Si substrate with $\rho_{IZOcluster}$ for the SnO_2/C_{60}/Si substrate in dependence of the estimated IZO film thickness. The value of $\rho_{IZOcluster}$ for the SnO_2/C_{60}/Si substrate is over ten times higher than $\rho_{IZOcluster}$ for the C_{60}/Si substrate at all times of the deposition. At ~ 2 nm of estimated IZO layer thickness the average particle density of the IZO model clusters is $\rho_{IZOcluster} \approx 10^{13}$ cm^{-2} for the SnO_2/C_{60}/Si substrate, and $\rho_{IZOcluster} \approx 8{\times}10^{11}$ cm^{-2} for the C_{60}/Si substrate, and at ~ 13.5 nm of estimated IZO layer thickness the average particle density of the IZO model clusters decreases to $\rho_{IZOcluster} \approx 2{\times}10^{12}$ cm^{-2} for the SnO_2/C_{60}/Si substrate, and to $\rho_{IZOcluster} \approx 2{\times}10^{11}$ cm^{-2} for the C_{60}/Si substrate. The overall decrease of $\rho_{IZOcluster}$ in both cases is linked to merging IZO clusters, leading to fewer but bigger structures. The difference of the average particle density of the IZO model clusters in both cases can only partly be explained by the IZO model clusters sizes. At ~ 13.5 nm of estimated IZO layer thickness the average IZO model cluster radius is R ≈ 7 nm in case of the SnO_2/C_{60}/Si substrate and R ≈ 15 nm in case of the C_{60}/Si substrate.
Therefore, we assume that the much higher IZO cluster density in the case of the SnO_2/C_{60}/Si substrate can be understood as smaller and also much more densely packed

IZO clusters compared to the case of IZO clusters forming on the C_{60}/Si substrate, which correlates with the difference in center-to-center distance is both cases.

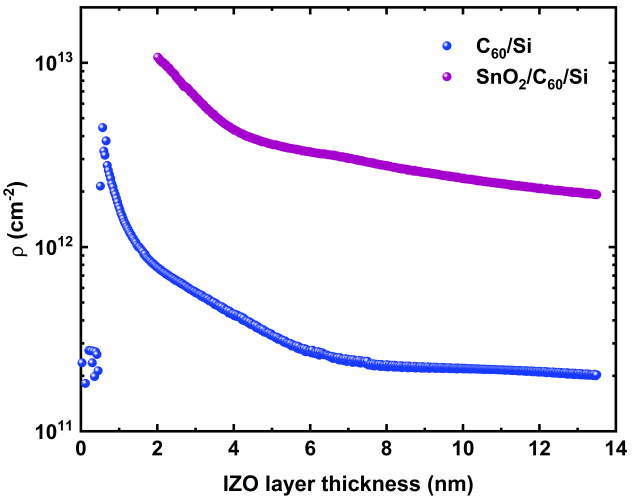

Figure 4.26: Comparison of the average estimated particle density of the IZO model clusters ($\rho_{IZOcluster}$) on the C_{60}/Si substrate and the SnO_2/C_{60}/Si substrate in dependence of the estimated IZO film thickness.

The SEM images in Fig. 4.27(b) - (e) confirm the lack of individually pronounced cluster formation. While in Fig. 4.27(b) and (d) the substrate morphology is still clearly visible (compare with the bare C_{60} surface in Fig. 6.10 of the supplementary section 6.2), in Fig. 4.27(c) and (e) the structure becomes less distinctive and blurry. However, it seems like no domains belonging to IZO clusters become visible as opposed to the case of the C_{60}/Si substrate.

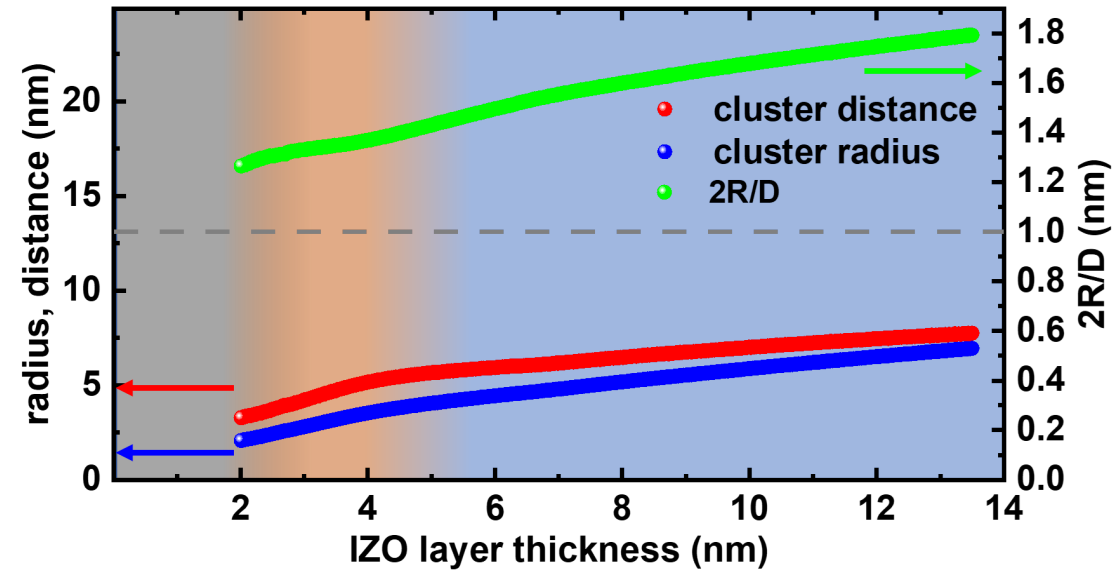

(a)

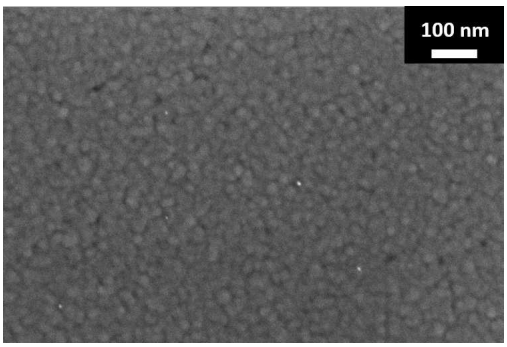

(b)

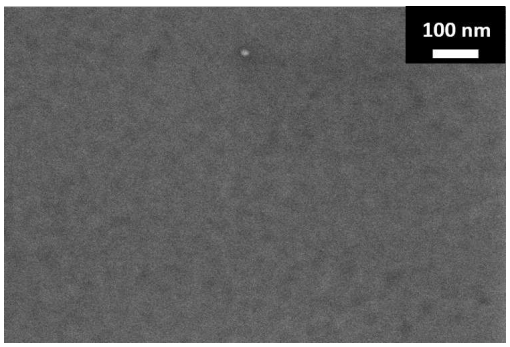

(c)

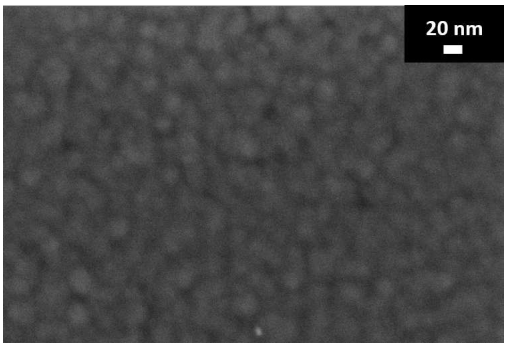

(d)

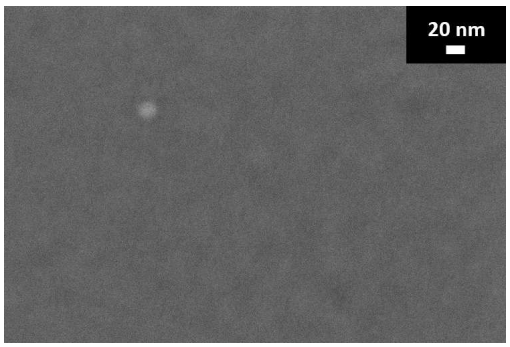

(e)

Figure 4.27: (a) Model-based structure evolution over effective film thickness represented by the average cluster distance D (red), the cluster radius R (blue), and the relation 2R/D (green) for the IZO film growing on SnO_2/C_{60}/Si. The structure evolution is divided into different stages, as defined by the respective most dominant process, highlighted by the background color. The gray dotted vertical line represents the percolation threshold 2R/D=1. (b) to (e) show SEM images of the IZO at different effective film thicknesses and image resolution. (b) and (d) show IZO at ~1.5 nm layer thickness, (c) and (de) show IZO at ~13.5 nm layer thickness. The inset shows the SEM image resolution.

Lastly, we present the IZO layer growth on the PEIE/C_{60}/Si substrate in Fig. 4.28. Fitting the IZO formation process on the PEIE/C_{60}/Si substrate was comparably more difficult. For once, the detected signal evaluated throughout the sputter deposition was not continuously changing with the IZO growth and exhibits interruptions (f.e. at around 6.3 nm in Fig. 4.28 (a)). As can also be seen in the horizontal cut evolution in Fig. 4.24(e), we observe these interruptions at certain points of the experiment. Since these interruptions correlate with the stop-sputter times, we assume that the IZO experiences some sort of reorganization or rearrangement when resting. The maxima appear to be shifted towards the center after each break, hinting at a continuation of dynamic surface processes, even in the absence of an active sputter deposition process.
Furthermore, the substrate showed maxima that were overlapping with the IZO cluster maxima, which complicated the fitting (see additional maxima at ~0.18 nm^{-1} in Fig. 6.12(b) compared with (a) in the supplementary section 6.2). This resulted in the fits shown in Fig. 4.28(a) being bumpy and discontinuous. A general trend is recognizable, nonetheless. The sputtered IZO shows a similar behavior as on the C_{60}/Si substrate, therefore the growth stages can be categorized in a similar manner. The the percolation threshold is reached at $\delta_{1,IZO} \approx 7$ nm (2R/D = 1, grey dashed line), which is similar as for the C_{60}/Si substrate, which was 6.41 nm. Moreover, Fig. 4.28(b) - (e) expectedly resembles Fig. 4.25(b) - (e). We see initially small clusters in Fig. 4.25(b) and (d) at $\delta_{1,IZO} \approx 1.5$ nm and the substrate structure beneath is also conceivable from the images, while in Fig. 4.25(c) and (e) we see bigger IZO clusters at $\delta_{1,IZO} \approx 13.5$ nm, likely of second or higher order.
In conclusion, we observed a clear dependency between the initial IZO growth behavior and the substrate material/configuration. Based on our fits of the horizontal line cuts, we assume a Volmer-Weber-type growth mode for IZO on C_{60} and PEIE/C_{60} and a Stranski-Krastanov-type growth mode for IZO on SnO_2/C_{60}. It should be highlighted that it seemed as if the PEIE/C_{60} substrate triggered dynamic surface processes, resulting in reorganization or rearrangement of the surface IZO even in the absence of an active sputter deposition process. Furthermore, while being able to evaluate scattering patterns for the SnO_2/C_{60} sample where distinct side maxima formed, we could not identify any clusters in the SEM pictures visually.

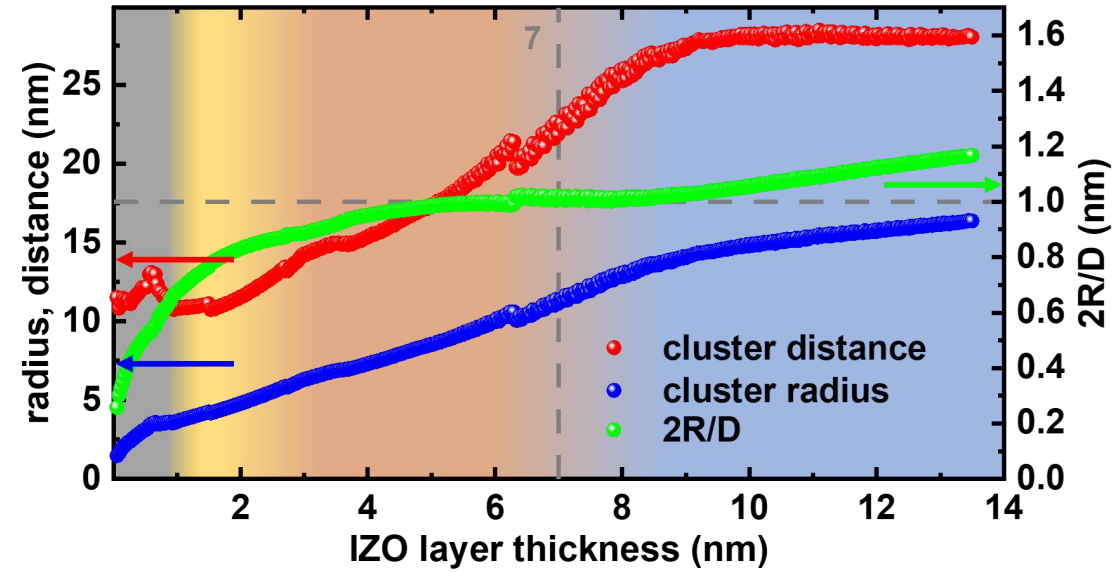

(a)

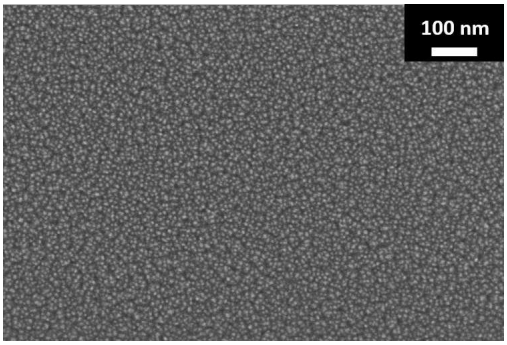

(b)

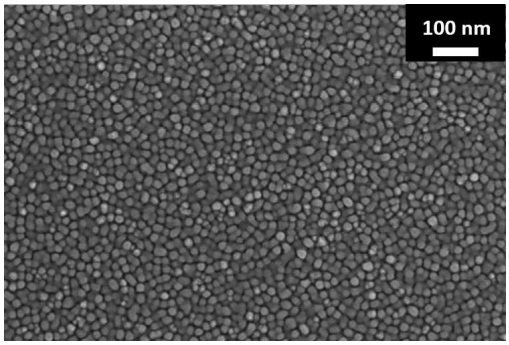

(c)

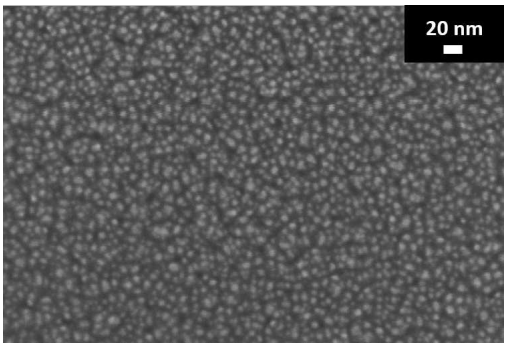

(d)

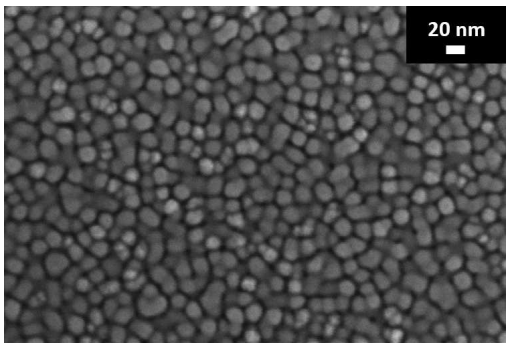

(e)

Figure 4.28: (a) Model-based structure evolution over effective film thickness represented by the average cluster distance D (red), the cluster radius R (blue), and the relation 2R/D (green) for the IZO film growing on PEIE/C_{60}/Si. The structure evolution is divided into different stages, as defined by the respective most dominant process, highlighted by the background color. The discontinuities occured during the sputter deposition-breaks, and may originate from continuous IZO paticle dynamics on PEIE. The gray dotted vertical line represents the percolation threshold 2R/D=1. (b) to (e) show SEM images of the IZO at different effective film thicknesses and image resolution. (b) and (d) show IZO at ~1.5 nm layer thickness, (c) and (de) show IZO at ~13.5 nm layer thickness. The inset shows the SEM image resolution.

Comparison of the DESY IZO with standard top-electrode IZO

Prior to the experiment, the DESY IZO deposition was not optimized regarding TCO electrode quality for use in solar cells. Now we want to evaluate how transferable the results are to our solar cells. Therefore, we examined the sputtered IZO used in the experiment at DESY and compared it with our standard IZO, which we typically use as transparent top-contact. We deposited DESY IZO on silicon and on quartz glass substrates to conduct a series of measurements.
In Fig. 4.29 we show the SEM images of (a) a top-view of our standard electrode IZO of 100 nm film thickness, (b) a top-view of the DESY IZO that we deposited during the beam-time experiment on a silicon substrate, and (c) a cross-section of the same DESY IZO. We can clearly see a fundamentally different micro-structure of the DESY IZO compared to our standard IZO. While the amorphous standard IZO exhibits a smooth surface in the SEM image, the DESY IZO surface and bulk appear to be rough and porous. We consider at least three possible reasons, 1. the comparably high working pressure (3.5×10^{-2} mbar) can lead to low sputter particle energies, which consequently leads to reduced density of the deposited films, 2. the extremely low sputter rate and probably low temperature at the substrate surface (the temperature adds to the surface energy of arriving atoms), and 3. the impact of impurities on the micro-structure. Samatov *et al.* sputter-deposited indium oxide films in an room-temperature rf-magnetron process and analyzed the influence of oxygen on the film properties [158]. They showed that high oxygen concentrations lead to the formation of amorphous grains and consequently rough films, originating from the segregation of the impurities (here oxygen) at grain boundaries. Impurities in the sputter-deposited films may originate from the atmosphere or the target itself. Ideally, the target is kept in high vacuum ($<10^{-6}$ mbar) to avoid target contamination and target poisoning when not in use. However, since we had to open the sputter chamber in order to exchange samples, the target was exposed to air each time. Usually, sputter targets are conditioned after air exposure by removing the first few layers to avoid impurities in the sputter-deposited film. Unfortunately, we did not have the time during the experiment to do that or avoid the target being exposed to air. Therefore, we consider it possible that the observed film structure originates from a high concentration of impurities. The SEM cross-section revealed an IZO film thickness of ~73 nm, while profilometer measurements on the sample revealed a thickness of ~94 nm. The difference might be due to some measurement inaccuracy or film inhomogeneity. We also attempted to measure a sheet resistance with the 4 point probe, but no value could be retrieved, suggesting a too high resistance of the film.

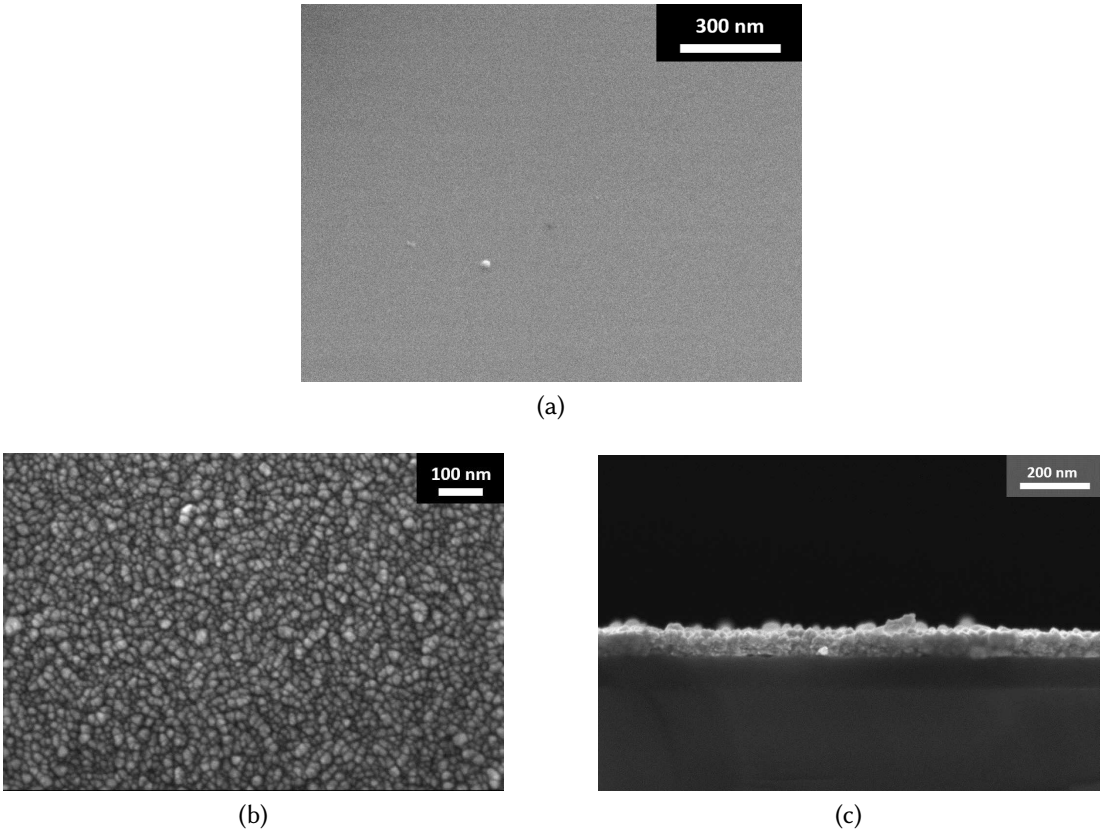

Figure 4.29: (a) SEM top-view of an IZO film deposited with the standard deposition tools at HZB, (b) top-view and (b) cross-section of SEM images of the DESY IZO deposited during the in-situ GISAXS experiments. The inset shows the SEM image resolution.

We performed spectrophotometry measurements in order to optically compare the DESY IZO (in blue) with our standard IZO (in red), which are shown in Fig. 4.30. The film thicknesses are not identical. Therefore, a detailed comparison is difficult. However, in contrast to the standard IZO, we observe almost no impact of free charge carrier absorption in the NIR-region of the spectra, which suggests inefficient doping of the DESY IZO films and consequently the lack of free charge carriers. Furthermore, we see a shift of the reflection maximum of the DESY IZO towards smaller wavelength (~450 nm), compared to the standard IZO (~680 nm), which is probably connected to a different film density and thickness, and maybe different composition.

A comparison of an EDS analysis of the standard IZO and the DESY IZO is shown in Fig. 4.31. DESY IZO on both silicon (in orange) and quartz glass substrates (in red) was analyzed. The standard IZO is presented in blue. All three curves were normalized to an indium peak at 3.3 keV, which reveals that the In/Zn ratio is similar for all three samples. The high silicon peak (at 1.75 keV) of the DESY IZO on the silicon substrate is due to the signal probing the substrate. Interestingly, the oxygen peak (at 0.5 keV) is much

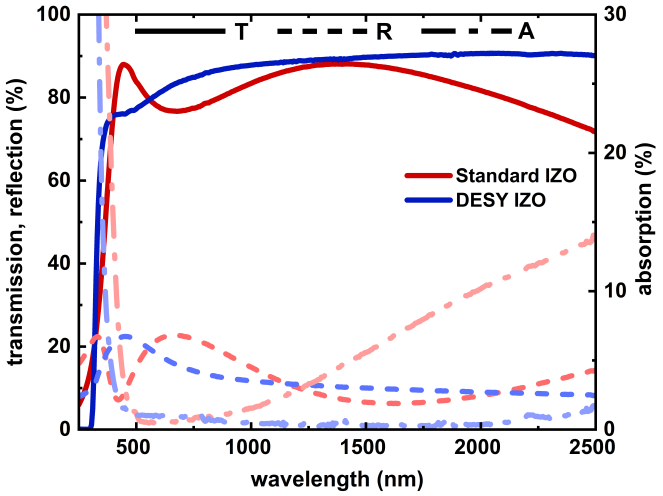

Figure 4.30: Reflection (R), transmittance (T) and absorption (A) spectra of the HZB standard IZO (red), and the DESY IZO (blue).

higher for both DESY samples compared with the standard IZO. Above, we formulated the theory that the difference observed in the DESY IZO compared with our standard IZO might originate from unintentional impurities. The high oxygen concentration can be the origin of such impurities and explain the observed film structure. Furthermore, oxygen vacancies contribute charge carriers in IZO films, while overstoichiometric films may result in neutralized oxygen vacancies.

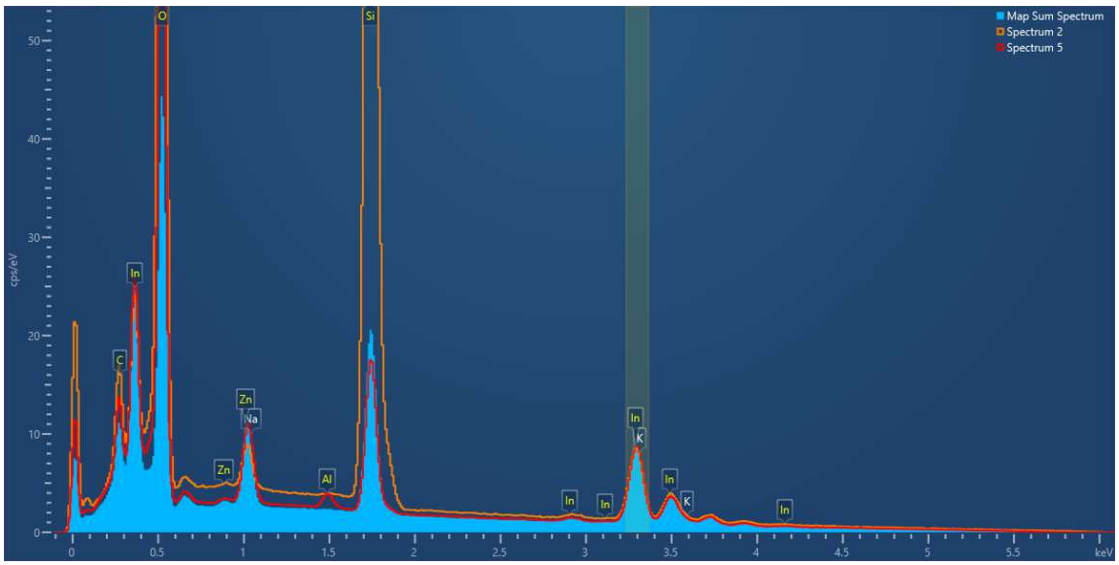

Figure 4.31: Comparison of an EDS analysis of the standard IZO on glass (blue area) and the DESY IZO on a silicon (orange) and a glass substrate (red). The Spectra are normalized to the indium peak at ~3.3 keV for better comparison.

Further an XRD analysis may be interesting in order to understand the nature of the DESY IZO films (whether the structures are indeed amorphous), and correlate the obtained film structure with observations by Samatov *et al.* [158].
We conclude that the results from the in-situ GISAXS study need to be taken with care when trying to transfer the results to the ETL/IZO interface of our solar cells, as the IZO that was sputter-deposited in this study is subjected to particular dynamics that were not observed in the sputter systems that were used for the IZO front-electrode deposition. The pronounced clustering of IZO particles might be far less severe, if present at all, in our standard process. Therefore, the results of the in-situ GISAXS study might not explain the differences in electrical interface properties for different ETL configurations. However, we wish to state that the substrate design severely impacted the IZO film formation as revealed by the GISAXS measurements, which may be an essential general finding. Interestingly though, while the IZO film formation was not strikingly different in the case of direct deposition on a C_{60} ETL substrate film compared to the PEIE/C_{60} double layer ETL substrate configuration, the insertion of PEIE in between C_{60} and IZO in a solar cell leads to huge electrical performance improvements. With caution, we would like to state that this could hint that the IZO formation itself is not the reason for the observed differences in electrical properties of the solar cells.

Summary of the main findings

- The surface free energy of the three different ETL designs was calculated from contact angle measurements by the sum of the dispersive and polar components.
- The highest surface free energy of 74.46 mN/m was found for the C_{60}/SnO_2 double layer ETL, followed by a significantly lower surface free energy of 59.45 mN/m for the C_{60}/PEIE double layer ETL, and the lowest surface free energy of 50.51 mN/m was found for the C_{60}-only ETL solar cell stack.
- Based on the surface free energy calculation, which resulted in similar values for the C_{60}-only ETL surface and the C_{60}/PEIE double layer ETL surface, a similar growth mode behavior of IZO is predicted.
- In-situ GISAXS measurements were performed during the IZO sputter deposition, to monitor the early stages of IZO growth on the C_{60}-only ETL surface, and the C_{60}/PEIE and C_{60}/SnO_2 double layer ETL surfaces.
- The GISAXS analysis reveals a Volmer–Weber growth mode for both, the C_{60}-only ETL and the C_{60}/PEIE double layer ETL surfaces, while IZO on the C_{60}/SnO_2 double layer ETL surface seems to rather follow a Stranski–Krastanov growth mode.

- Because the IZO sputter conditions during the in-situ GISAXS experiment were not optimal and led to quite different IZO film properties than in the usually used sputter systems, the analysis suggests a trend and is not entirely transferable to IZO front electrode deposition in actual solar cell devices.
- The sputter deposition process for the in-situ experiment needs to be optimized to get closer to real IZO sputter conditions.

4.2.3 Electrical simulation of solar cell performance influenced by the interface formation between electron selective contact and transparent electrode

In the following, we simulate the impact of the C_{60}/IZO interface conditions on the perovskite solar cell performance in order to better understand the previous experimental results on the impact of the interface on the solar cell parameters. To do this, we investigate a simple three-layer stack approach consisting of an HTL layer, perovskite, and ETL layer, similar to the layers we used in the experiments. We use the drift-diffusion simulation software SCAPS-1D [125]. The simulation parameters for each layer, including the interfacial recombination velocities from perovskite to the CTL and the electrode work functions are listed in Tab. 4.14. We note that the chosen parameters aim to replicate experimental trends rather than being a perfect replica of the actual layer properties. First, we study how changes in the front electrode work function (WF) affect the device's J-V characteristic, especially concerning the curve's shape, the open-circuit voltage (V_{OC}), and the fill factor (FF). Therefore, we simulate a perovskite solar cell using the values from Tab. 4.14, and modify the front electrode's work function between 3.7 eV and 4.7 eV in increments of 0.1 eV. The resulting J-V curves and open circuit voltage and fill factor dependency are shown in Fig. 4.32.

Table 4.14: SCAPS simulation parameters.

Parameter	C_{60}	perovskite	HTL
d (nm)	18	550	10
E_g (eV)	2[70]	1.680	3.0[70]
EA (eV)	3.9[70, 153]	3.9[70]	2.5[70]
ϵ_r	5[70]	22[70]	3.5[70]
N_C ($1/cm^3$)	1×10^{20}[30, 70]	2.2×10^{18}[70]	1×10^{20}[70]
N_V ($1/cm^3$)	1×10^{20}[30, 70]	2.2×10^{18}[70]	1×10^{20}[70]
μ_n (cm^2/Vs)	1×10^{-2}[30, 70]	10[30]	1.5×10^{-4}[70]
μ_p (cm^2/Vs)	3.5×10^{-3}[152]	10[30]	1.5×10^{-4}[70]
N_D ($1/cm^3$)	1×10^{5}[30]	1×10^{13}[70]	0
N_A ($1/cm^3$)	0	1×10^{13}[70]	1×10^{5}[30]
N_t ($1/cm^3$)	1×10^{14}[152]	1×10^{15}	1×10^{14}
τ (ns)	1[30, 70]	500[70]	1[30, 70]
S_{min} (cm/s)	2000[70]	-	200[30, 70]
S_{maj} (cm/s)	1×10^{7}[70]	-	1×10^{7}[70]
k (cm^3/s)	-	3×10^{-11}[120]	-
adjacent electrode WF (eV)	variable	-	5.5
R_{ser} (Ωcm^2)	5	-	-

We observe an explicit dependency of the J-V shape and characteristics on the front electrode's WF. A variation of the IZO work function values below the electron affinity of C_{60} ($WF_{IZO} \leq EA_{C60}$) has no impact on the solar cell J-V shape and characteristics. While the V_{OC} stays at around 1.22 V, the FF stays at around 79% in the observed range. For values of $WF_{IZO} > EA_{C60}$, the V_{OC} decreases rapidly by 100 mV, and the FF decreases slightly by 2% for WF_{IZO}s of up to 4.2 eV. Then, for values of $WF_{IZO} \gg EA_{C60}$ (WF_{IZO}-$EA_{C60} \geq 0.4$ eV), the J-V curves start to form an s-shape, and the V_{OC} and FF decrease rapidly, from 1.09 to 0.79 V and from 71 to 51% respectively. The increasing mismatch that causes the s-shape to develop may indicate that charge collection is increasingly inefficient and that electrons are piling up at the IZO/C_{60} interface. We explain this by the formation of a Schottky-barrier [86, 87]. While a too high work function may result in an energetic barrier, an energetically matching work function will facilitate an ohmic contact with the ETL. The Schottky-Mott limit, which is applicable for weakly interacting materials, describes the height of barriers originating from electrodes' WF located within the semiconductor band gap [85]. The Schottky-barrier height is then expressed by $\phi_B = WF_{electrode} - EA_{ETL}$. Electron injection and/or collection are significantly affected by Schottky barriers.

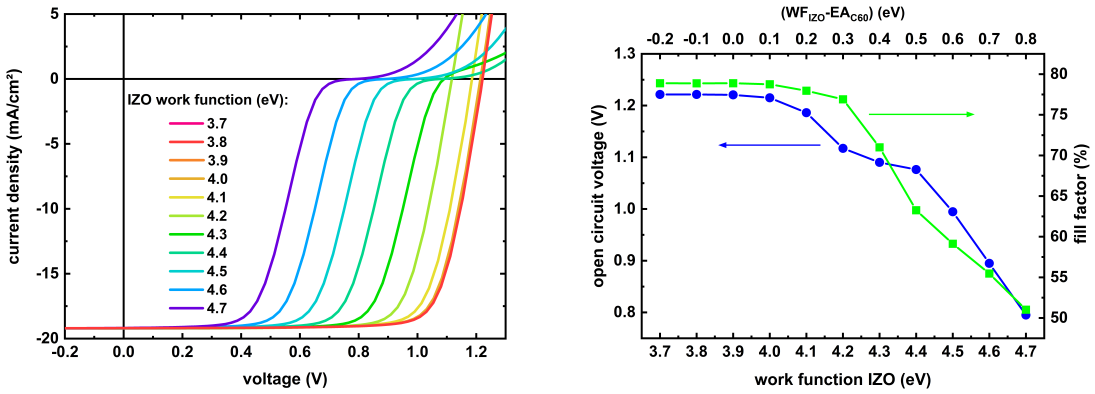

(a) (b)

Figure 4.32: (a) Evolution of the simulated J-V curve with IZO work function variation from 3.7 eV to 4.7 eV in increments of 0.1 eV, (b) evolution of V_{OC} and FF as a function of the WF_{IZO} (bottom axes) and the WF_{IZO} - EA_{C60} difference (top axes).

Next, we examine the energy bands of the simulated perovskite solar cells to get a general grasp of how differently high WF affect device properties. In Fig. 4.33(a) and (b) we display the band lineup at V_{OC} conditions (at AM1.5G) for WF_{IZO} values of 3.9 eV and 4.5 eV, respectively. We chose those values from the set of simulated WF_{IZO}s, as they are representative of different regimes - an energetically well-aligned interface leading to an ohmic contact with the C_{60} and a significant mismatch between WF_{IZO} and EA_{C60} leading to an s-shaped J-V curve.
For the well-aligned C_{60}/IZO interface, where $WF_{IZO} \leq EA_{C60}$ representing an ohmic contact, the band alignment at open circuit conditions happens as follows: In order to achieve charge equilibrium charges diffuse from the electrode to the C_{60} due to the difference in potential energy. As a result, a depletion region of holes close to the interface in the C_{60} occurs, which causes the energy bands of C_{60} to bend downwards (This is not a physical bending, but a difference in the electrochemical potential of the free charge carriers at the interface - see also explanation given in Chap. 2.3.3). The energy bands are shown in Fig. 4.33(a) and represent this behavior. Here, the simulated quasi-Fermi level splitting of 1.221 eV (QFLS) is identical to eV_{OC} (e is the elemental charge).

In Fig. 4.33(b) we show the case of $WF_{IZO} \gg EA_{C60}$ (WF_{IZO} - EA_{C60} = 0.6 eV). Here, it seems the energy-level band alignment leads to an energetic barrier, resulting in an s-shape of the J-V curve (turquoise line in Fig. 4.32). When an n-type semiconductor and an electrode with comparably high WF form an interface, intrinsic electrons flow preferentially from the semiconductor to the high WF electrode due to the difference in potential energy. The charge equalization continues until equilibrium is reached. As a consequence, a depletion of electrons (or in other words a positive space charge

region) in the semiconductor is formed, forcing the conduction bands to bend upwards in order to preserve equilibrium with the WF_{IZO} (see "Electrode / solar cell interface" in Chap. 2.3.3). This deformation of the band structure is the cause of a potential barrier. Furthermore, we observe that the electron QFL (red dashed line) bends downwards at the electrode/C_{60} interface. In other words, the electron QFL near the IZO electrode experiences a significant gradient, causing a QFLS–V_{OC} mismatch, which lowers the V_{OC} to 0.995. This may be explained by accumulating charge carriers at the potential barrier in the electrode/C_{60} interface, resulting in increased recombination [142]. At the same time, the QFLS inside the bulk remains at higher values of 1.182 eV, but lower compared to the lower IZO WF case. This can be explained by understanding the impact of the built-in potential on the charge transport dynamics. The higher IZO WF results in a lowered built-in potential, originating from the work function difference of the electrodes (in the described case it is $\Delta WF = 1$ eV). The built-in potential and its impact on the solar cell is discussed in detail in section 2.3.3. As the charge carrier lifetimes in the bulk and recombination velocities C_{60}/perovskite interface remained unchanged in the simulations, we explain the origin of the lowered electrochemical potential of the photogenerated charges within the bulk perovskite with an increase of recombination losses resulting from the effect of the WF_{IZO} height (i.e. the built-in potential) on the charge separation.

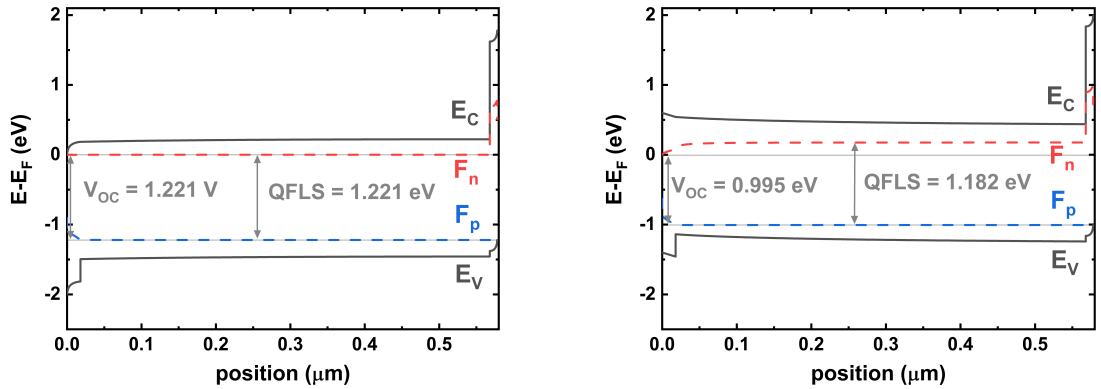

Figure 4.33: The energy bands of selected simulated perovskite solar cells. In both cases, the ETL is on the left, and the HTL is on the right of the diagram. (a) shows a well-aligned C_{60}/IZO interface (WF_{IZO} = EA_{C60} = 3.9 eV), and (b) shows a case where $WF_{IZO} \gg EA_{C60}$ (WF_{IZO} - EA_{C60} = 0.6 eV).

In the following the simulated WF_{IZO} development in relation to light intensity is investigated, in order to understand and compare with the light intensity dependent J-V measurements from section 4.2.1. In Fig. 4.34(a), (b), and (c), we show the light intensity-dependent V_{OC}, the pseudo J-V curves, and the FF loss mechanism analysis

for WF_{IZO} values from 3.7 to 4.7 eV, respectively.
Fig. 4.34(a) shows the light intensity dependence of the open-circuit voltage over four orders of magnitude. From the slope of the linear traces of the light intensity-dependent V_{OC}, the evolution of the ideality factor n_{id} can be qualitatively interpreted (indicated by the gray arrow). We observe a reduction in slope with increasing WF_{IZO}, which translates to a decreasing ideality factor. Generally, a lower ideality factor correlates with a higher V_{OC}, due to decreased trap-assisted non-radiative (Shockley-Read-Hall) recombination in the bulk [71]. Interestingly, in our simulation a decreasing n_{id} occurs for simultaneously decreasing V_{OC} (see Fig. 4.34(b)). A low V_{OC} despite low n_{id} can have several reason. Significant non-radiative second-order surface/interface recombination is one aspect that is quite likely the cause of our situation. Surface or interface recombination, for example because of non-selective contacts, can result in a n_{id} of <2 or even <1 despite significant SRH recombination, especially if the built-in potential restricts the V_{OC} [159]. This implies that a lower n_{id} (as for the C_{60} only ETL solar cells from Chap. 4.2.1) does not necessarily lead to a high V_{OC} or improved solar cell performance. Then, the V_{OC} is limited by non-radiative second-order surface/interface recombination instead of SRH recombination in the bulk [72].
According to our FF loss mechanism analysis in Fig. 4.34(c), the percentage contribution of non-radiative recombination losses that lower the FF, derived from comparing pFF of the pseudo J-V curves (Fig. 4.34(b)) with the detailed balance limit of the absorber band gap [74], even decrease after the onset of an s-shape in the J-V curves (for $WF_{IZO} \geq 4.3$ eV), reaching a minimum at $WF_{IZO} = 4.5$ eV, which correlates to a built-in potential of 1 V. For higher values of WF_{IZO}, the non-radiative recombination loss contribution to the device's FF increases again. According to Stolterfoht *et al.* and Diekmann *et al.*, a built-in potential below 1 V can lead to inefficient charge extraction in perovskite solar cells, which in turn increases the influence of SRH recombination in the bulk [30, 69, 70]. This may explain the increase of non-radiative recombination loss contribution to the device's FF for even higher WF_{IZO} values.
As the illumination intensity dependent analysis of the n_{id} and pseudo J-V curves are analyzed at V_{OC} the influence of the series resistance is irrelevant because the net current is zero. However, the device FF is strongly dependent on the series resistance, hence the huge differences between the simulated device FF (in organge in Fig. 4.34(c)) and the pFF (the difference is marked by the green field in Fig. 4.34(c)). The series resistance is composed of the ohmic resistance of the electrodes and the transport resistance originating from the resistance of each layer and interface resistance [64, 160]. It contributes to the transport losses in Fig. 4.34(c). A Schottky-barrier in the C_{60}/IZO interface, for example, affects the charge collection and results in large series resistances [64], which is one possible explanation for the large transport losses that we observe for $WF_{IZO} \geq 4.3$ eV.

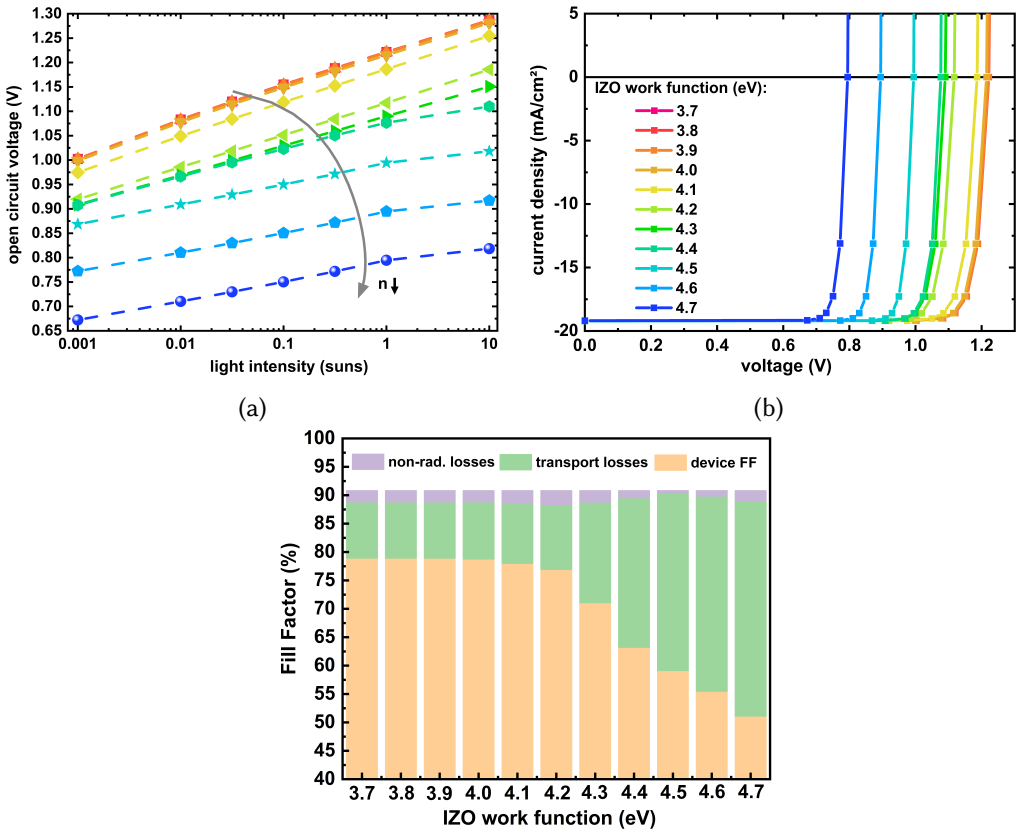

Figure 4.34: (a) Light intensity-dependent open-circuit voltage with linear fits (dashed lines) end extracted ideality factors (n_{id}); (b) Pseudo-J-V curves reconstructed from the light intensity measurements; (c) A comparison of the device's FF extracted from simulated J-V measurements and simulated pseudo J-V curves, as well as the FF in the radiative limit of the respected perovskite band gap [74], as a function of the IZO work function.

Finally, we aim to generate a similar behavior with our simulation, as for our experimental results. Thus, we compare an energetically well-aligned solar cell stack, composed of an IZO/C_{60} interface with WF_{IZO}=3.9 eV, with a scenario where the WF_{IZO} is much higher than the EA_{C60} (WF_{IZO}=4.4 eV). Moreover, we consider a WF_{IZO} of 4.4 eV as realistic, as we measured WF_{IZO}=4.47 eV by Kelvin Probe measurements on the surface of an IZO film, sputtered with the Roth&Rau system (see Tab. 6.1). However, we want to note that bulk properties might differ from surface properties, and Kelvin Probe measurements are surface sensitive.
We present the resulting simulated J-V curves in Fig. 4.35(a). The blue line represents the case of WF_{IZO}=3.9 eV, and the red line represents the case of WF_{IZO}=4.4 eV. The simulation results are numerical predictions, and deviate from the experimental results from Chap. 4.2.1, but we can identify similar key features. For the experimental results,

where we deposited IZO onto the C_{60}/SnO_2, or C_{60}/PEIE double-layer ETL, a comparably high FF and a high V_{OC} as for the blue curve was achieved, while depositing IZO directly onto the C_{60} ETL leads to a distinctive s-shaped J-V curve, lower FF and a lower V_{OC}, similar to the case of the red curve. Thus, according to our simulations, a variation in the WF_{IZO} is sufficient to evoke a reduction in the FF as well as the V_{OC}. Therefore, misaligned contacts resulting in a Schottky-barrier can be one explanation for the observations in Chap. 4.2.1.
In the following we try to understand the recombination dynamics resulting from such a Schottky-barrier. Therefore, in Fig. 4.35(b) we compare the recombination currents for the simulated solar cells with WF_{IZO} = 3.9 eV (solid line) and WF_{IZO} = 4.4 eV (dashed line). In both cases, the total bulk recombination current (green) is dominated by Shockley-Reed-Hall (SRH) recombination (dark red). While the total recombination current (grey) is limited by the interfacial recombination in both cases (pink), defining the height of V_{OC} [30, 161]. Radiative recombination and recombination losses at the contacts play only minor roles in small forward bias. For WF_{IZO} = 4.4 eV, we observe increased recombination currents for forward voltages greater than 0.5 V due to the WF shift, which correlates with the onset of the s-shape. At around 0.9 V (indicated by the black pointed line), the total recombination loss is around 47 times higher for the simulated solar cell with WF_{IZO} = 4.4 eV than for the simulated solar cell with WF_{IZO} = 3.9 eV, which originates from interface recombination. As previously stated, high interface recombination can lead to a significant reduction in V_{OC} for simultaneously low n_{id}. We therefore state, that the significantly higher observed interface recombination in case of the high WF_{IZO} values is the origin of the lowered V_{OC} and s-shape behavior. In addition, we observe that the total bulk recombination current is almost five times higher at 0.9 V for WF_{IZO} = 4.4 eV due to the increased SRH recombination. The fact that recombination losses in the bulk are increased despite no parameters in the bulk being changed in the simulation points to a lowered charge extraction efficiency through the charge selective contacts, resulting from the lower built-in potential. However, beyond 1 V, the bulk recombination losses are again similar in both cases, which is where the ideality factors were determined (V_{OC} vs. light intensity). Furthermore, contact recombination losses and radiative recombination negligibly impact the total recombination losses.
This simulation shows a case of misaligned contacts leading to a Schottky barrier. In reality, this barrier can also originate, for example, from interfacial states. Nevertheless, the simulation showed that significant (interfacial) recombination losses and thus s-shapes J-V curves result from non-ideal electrode/ETL conditions.

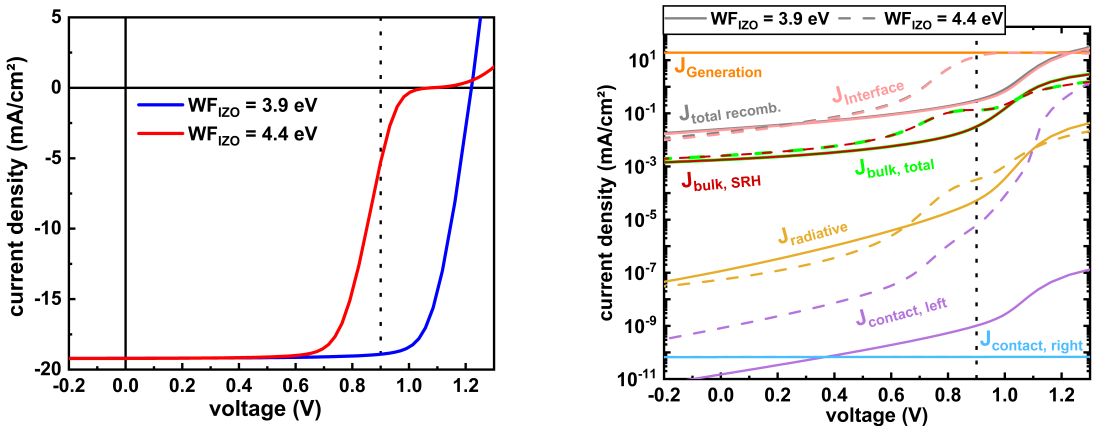

(a) (b)

Figure 4.35: (a) Simulated J-V curves of selected model-devices with an IZO work function of 3.9 eV (blue) and 4.4 eV (red); (b) simulated generation and recombination currents for the same model-devices as a function of bias voltage. The black dotted line at 0.9 V serves as a reference point in order to compare and explain FF losses in the J-V characteristic curve at the same forward voltage.

The simulation shows a general trend and may not replicate the experiments entirely. The Schottky-Mott model, which predicts the interfacial Schottky barrier height, only holds for weakly interacting materials and ignores the impact of chemical interactions. Predicting the impact of the real interfacial barrier is complex. Surface states, for example, propagate Fermi-level pinning in the C_{60}/IZO interface, according to the Bardeen-limit [88, 90, 91, 147]. Moderate interface interaction and the impact of sputter deposition of the IZO might also affect the interface formation through damage of the C_{60} surface, penetration of IZO material into the C_{60}, strain between the materials, or chemical reaction between IZO atoms with the C_{60} [25, 26, 85, 93]. For example, it is suggested that physisorbed oxygen can create defects, electron traps and impurity gap states in the C_{60} [154, 155, 162, 163]. A chemical reaction between C_{60} and oxygen may even occur when C_{60} is exposed to oxygen and light [154]. Consequently, this alters the energy bands close to the surface/interface and the band structures or cause defect-induced gap states, and may lead to decreased charge collection or electron injection efficiency. All of the abovementioned effects may impact the interfacial barrier height. While we do not know the exact origin of the interfacial barrier in the C_{60}/IZO interface, we do observe a correlation with the IZO WF hight-induced misalignment in simulations.

Summary of the main findings

- According to SCAPS-1D simulations, when the $WF_{IZO} \leq EA_{C60}$ no impact on the solar cell characteristics is observed, while $WF_{IZO} > EA_{C60}$ leads to notable V_{OC} reductions, and WF_{IZO} - $EA_{C60} \geq 0.4$ eV leads to s-shaped J-V curves.
- Energy band diagrams revealed a well-aligned C_{60}/IZO interface for $WF_{IZO} = EA_{C60}$, and unfavorable band bending due to an interfacial barrier for $WF_{IZO} \gg EA_{C60}$.
- Simulated light intensity dependent measurements revealed a decreasing ideality factor and simultaneously decreasing V_{OC} with increasing WF_{IZO}.
- We explain this with increasing non-radiative second-order surface/interface recombination (which is not reflected in the n_{id}) limiting the V_{OC}, instead of SRH recombination in the bulk (which impacts the n_{id}).
- The FF loss analysis showed that the FF is increasingly reduced by transport losses, with increasing WF_{IZO}.
- We assume that the transport losses are related to a Schottky-barrier forming the in the C_{60}/IZO interface.
- Simulated generation and recombination currents confirmed substantially increased interfacial recombination for a high WF_{IZO} - EA_{C60} difference, which lower the photocurrent compared to a barrier-free solar cell at the same voltage, hence the s-shape.

4.2.4 Conclusion

This chapter analyzed the interactions between the substrate and the growing thin film. We sputter depositing IZO on different layers of the semitransparent single junction perovskite solar cells, to be precise, on the C_{60}/SnO_2 and C_{60}/PEIE double layer ETLs and directly onto the C_{60} ETL. The solar cells were analyzed by measuring their electrical properties (J-V and EQE scans). While the C_{60}/SnO_2 and C_{60}/PEIE double layer ETL solar cells exhibited FFs > 70%, which were probably mainly limited through the lateral conductivity of the IZO, the C_{60} single layer ETL devices (IZO is directly deposited onto the C_{60}) were s-shaped, leading to low FFs ~ 45%. The V_{OC} was also significantly lower in the case of the C_{60}-only ETL devices. Light intensity-dependent analysis of the photovoltaic parameters revealed that the primary FF loss of the C_{60}-only ETL devices could be attributed to transport losses. We assume an injection or Schottky-barrier in the C_{60}/IZO interface is responsible. Interestingly, the solar cell with a conventional buffer design, the C_{60}/SnO_2 double layer ETL device, exhibited the highest FF reduction by non-radiative recombination losses.
Our interpretation of the results obtained by the all-in-one characterization instrument

Paios are increased defect states/traps and interfacial recombination losses for the C_{60}-only ETL device compared to the other two designs. The results furthermore hinted at unfavorable band bending due to an interfacial barrier. On the other hand, the double layer ETL devices exhibited fewer defects or trap states.
We tried to correlate our observations from electrical measurements with structural differences during the interface formation. Therefore, we performed contact angle (CA) measurements to predict the interaction strength between the ETL layers and the IZO and in-situ GISAXS measurements during IZO sputter deposition. The in-situ GISAXS measurements monitored the early stages of IZO growth on the different ETL designs. Our prediction based on the contact angle measurements and the results obtained by the in-situ GISAXS measurements were in good agreement. While we observed similar results for the C_{60}-only ETL and the C_{60}/PEIE double layer ETL samples in terms of surface free energy (by CA measurements) and initial IZO growth (by in-situ GISAXS), samples with a C_{60}/SnO_2 double layer ETL showed very different results. As the growth behavior of IZO does not correlate with the results obtained from electrical device measurements, we tentatively assume that the IZO growth behavior does not affect the device performance much. We note that the IZO deposited during the in-situ GISAXS experiments is not comparable to the IZO used as an electrode in the devices. Therefore the results might not be transferable.
Finally, we performed electrical simulations focusing on the ETL/TCO interface dynamics. We investigated the dependence of the J-V characteristics and the energy bands on the electrode's work function (WF). We observed a clear dependency between the electrode's WF and the J-V curve's characteristics and shape. We found that for WF_{IZO} - $EA_{C60} \geq 0.4$ eV, the J-V curve starts to form an s-shape. The analysis of the energy bands revealed the formation of a potential barrier in such an s-shape case. We also simulated the J-V characteristics' light intensity-dependence to better understand the results obtained from the experiments. Similar to the experimental results, we saw a lower n_{id} for simulated devices with $WF_{IZO} \gg EA_{C60}$, that also had a reduced V_{OC}. At the same time, visualizing the overall recombination currents revealed that non-radiative second-order surface/interface recombination was strongly increased for simulated devices with $WF_{IZO} \gg EA_{C60}$, compared to devices with $WF_{IZO} \sim EA_{C60}$. Such interface recombination limits the V_{OC} but might not be revealed by the n_{id}. We even observed a reduction in non-radiative recombination losses from the bulk with increasing WF_{IZO}. The simulation seems to be in good agreement with our electrical measurements. Therefore, we conclude that the s-shaped J-V curve of the C_{60}-only ETL device originates from an interfacial barrier, which might either stem from the IZO WF (Schottky-Mott limit) or interfacial defect states (Bardeen limit). The interlayer SnO_2 and PEIE are important in order to obtain a good band alignment. Their function is not completely clear at this point, but they seem to reduce the interfacial defect density.

4.3 Application of soft deposition methods in monolithic perovskite/silicon tandem solar cells

In the following chapter we will discuss the application of soft sputter deposited IZO into monolithic perovskite/silicon tandem solar cells. Firstly, we will discuss optical advantages of omitting/replacing the SnO_2-buffer. Therefore, we perform optical simulations on tandem stacks with and without a SnO_2-buffer layer. We will then assign the improvements to the respective optical loss phenomena. Furthermore, we will fabricate perovskite/silicon tandem devices in the conventional design including a protective SnO_2-buffer layer, which will be compared to tandem devices with C_{60}/PEIE double-layer ETL, where the ultra-thin PEIE layer replaces the 20 nm thick SnO_2-buffer. For a fair comparison, the IZO was deposited by the same sputter deposition conditions for both designs in each case. We will show that the C_{60}/PEIE double-layer ETL design leads to a superior solar cell performance in our experiments, which we will correlate to optical improvements, but also to an improved V_{OC}. Finally, we perform a long-term stability analysis on C_{60}/SnO_2- and C_{60}/PEIE-based tandem solar cells.

4.3.1 Basic requirements for the transparent front contact and optical optimization

In a tandem device, the front electrode must meet specific requirements. The front optical layers determine how much light enters the device and are a limiting factor for the sub-cells short circuit current density. Thus, it is detrimental to minimize reflection and parasitic optical absorption losses. The reflectivity is primarily determined by the material's refractive index and the thickness of the anti-reflection coating. According to Fresnel, a refractive index matching between a material and the adjacent optical media leads to better light in-coupling, whereas a low extinction coefficient leads to less optical absorption losses (more in-depth explanation can be found in Chap. 2.1). The parasitic absorption in the front layers is dependent on the respective material's layer thickness and extinction coefficient. We claim that due to our soft sputter approach, we can omit the protective SnO_2 buffer layer, thereby reducing the optical losses in the tandem solar cell. The refractive index (n) and extinction coefficient (k) of an SnO_2 film fabricated via ALD at 80°C on a silicon substrate, obtained from spectroscopic ellipsometry measurements, and modeled using Tauc–Lorentz oscillators, are shown in Fig. 4.36. We expect an unprecedented increase in short circuit current for the perovskite sub-cell due to the decrease in parasitic absorption in its relevant wavelength range (~ 350 to 700 nm) by omitting the SnO_2 buffer layer.

We used the MATLAB-based tool GenPro4 to perform optical simulations of conventional and SnO_2 buffer layer free monolithic perovskite/silicon tandem layer stacks to confirm the notion as mentioned above [126, 164]. Besides the SnO_2, which was only

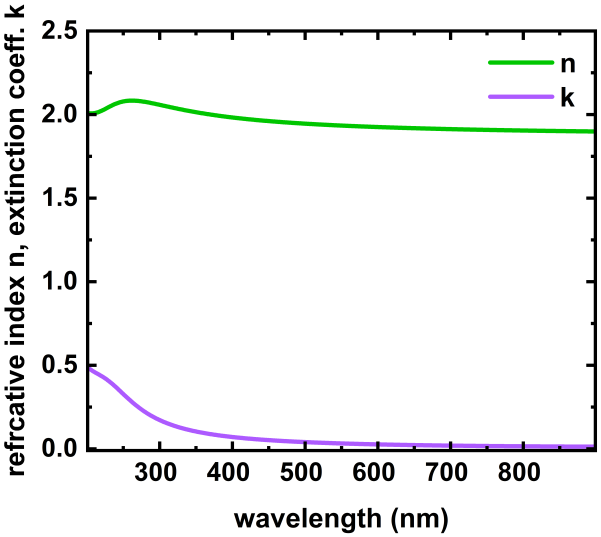

Figure 4.36: Optical properties of ALD-deposited SnO_2. Depicted are the refractive index (n) and extinction coefficient (k) obtained from spectroscopic ellipsometry measurements.

included in one stack, the optical data of each layer in the stacks were the same in both examples.

In Fig. 4.37(a) and (b), an illustration of the simulated solar cell stacks, including the layer thickness for the top-cell, are displayed. The layer stacks of the perovskite top-cells are similar to the semitransparent single junction solar cells investigated in Chap. 4.1.2. The bottom cell is a front-side polished, back-side textured silicon heterojunction (SHJ) solar cell (details can be found in Chap. 3.1.2). The whole tandem stack is similar in design to the simulated tandem stack described by Köhnen *et al.* [165]. We listed the layers used in the simulation, their source, and their thicknesses in Tab. 6.2 in the supplementary section (6.3). The n,k-data which we extracted from optical measurements for the simulation in this work is shown in Fig. 6.16 in the supplementary section. The respective fits for the n,k-data are presented in Fig. 6.13 (for 100 nm IZO), Fig. 6.14 (for 20 nm SnO_2), and Fig. 6.15 (23 nm C_{60}).

In Fig. 4.37(c) and (d), we present the results of the simulations. Fig. 4.37(c) shows the simulated 1-R and absorption profiles of the two tandem solar cell devices, including the sub-cell short circuit densities and the reflection loss profiles and losses for the respective cases. We should point out that the short circuit current densities in the simulation are calculated from modeled absorption profiles, which are translated into currents by assuming an IQE of 100%. Therefore, the simulated short circuit current densities are unaffected by collection losses and reflect idealized values. A shift in the 1-R fringe from ~410 nm to ~390 nm can be observed when omitting the 20 nm thick SnO_2 buffer layer. We correlate this to a shift of interference fringes in the reflection spectra due to the overall oxide layer thickness reduction. The reflection losses are reduced by 0.1% by removing the SnO_2 buffer layer.

The absorption profiles of both tandem solar cell stacks show distinctive differences,

which can also be seen in the respective short circuit current densities. For the silicon bottom-cell, the short circuit current density increases from 19.8 mA/cm^2 for the SnO_2 buffer layer design to 20.0 mA/cm^2 for the SnO_2 buffer layer free tandem stack, and the perovskite top-cell the short circuit current density increases from 19.6 mA/cm^2 to 20.0 mA/cm^2 when removing the SnO_2 layer, respectively. In Fig. 4.37(d), the short circuit current densities and current density losses due to reflection and parasitic absorption of each sub-cell are visualized. It is assumed that light that is not reflected nor absorbed is lost to parasite absorption. Hence the parasitic absorption is calculated by 100-R-EQE. Removing the SnO_2 buffer layer decreases the parasitic absorption loss from 3.9% to 3.4%, which accounts for most of the short circuit current density improvements, according to our simulation. The sum of both sub-cell currents was increased from 39.4 mA/cm^2 to 40.0 mA/cm^2, attributing to an overall 0.6 mA/cm^2 current density loss to the 20 nm thick SnO_2 buffer layer. We conclude that the SnO_2 buffer layer is responsible for the significant parasitic absorption losses at wavelengths below 750 nm, which is consistent with our findings of its refractive index in that spectral range (compare with Fig. 4.36).

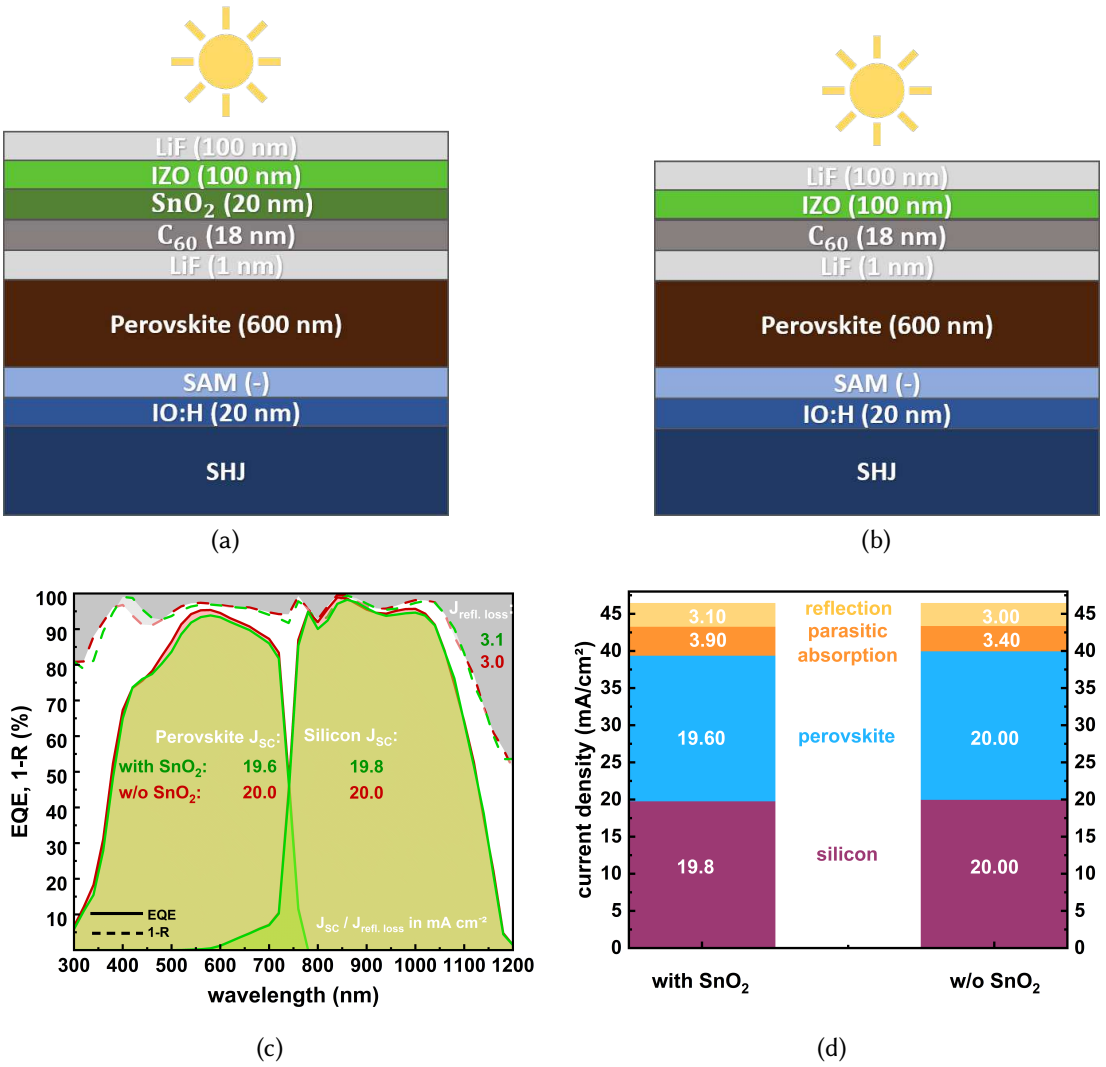

Figure 4.37: Schematic device layout of monolithic perovskite/silicon tandem solar cells, including the layer thicknesses as used for the optical simulation (a) with SnO_2 buffer layer and (b) without; (c) Simulated EQE and 1-R spectra of tandem devices with (green) and without (red) a 20 nm thick SnO_2 buffer layer using GenPro4. (d) The simulation's current density loss analysis showing each sub-cell's current densities and current density losses due to reflection and parasitic absorption for tandem devices with and without SnO_2.

Our simulation shows that omitting the SnO_2 buffer layer offers an excellent potential for optical loss reduction and consequently higher short circuit current densities in both sub-cells, especially in the perovskite sub-cell, where the SnO_2 layer induces parasitic absorption losses. Furthermore, we implemented the approaches mentioned above into tandem solar cells. Further optical improvements can be achieved by thinning the top-contact layer stack, increasing UV- and NIR transparency of the transparent

front-electrode, by using a TCO with a higher optical band gap, and with less free charge carrier absorption.

Summary of the main findings

- Our optical simulations demonstrate that eliminating the SnO_2 buffer layer leads to higher short circuit current densities in both sub-cells by reducing optical losses.
- An overall 0.6 mA/cm^2 current density loss could be assigned to the SnO_2, mostly originating from parasitic absorption in the relevant wavelength range of perovskite absorption ($\sim$ 350 to 700 nm).

4.3.2 Buffer-layer-free tandem solar cell

We built monolithic two-terminal tandem devices based on a C_{60}/SnO_2 and a C_{60}/PEIE double layer ETL to implement the soft sputter deposited IZO electrode. The fabrication of the monolithic two-terminal tandem solar cells is described in Chap. 3.1.3. It is necessary to point out, that for the following experiments the LiF anti-reflective coating thickness differs from the optimal thickness of 100 nm, due to a calibration issue during the LiF evaporation in this experiment. This leads to a non-ideal reflection profiles and increased reflection losses. The IZO front electrode sputter deposition was carried out for both tandem designs, in the same way, using the Vinci tool as described in Chap. 3.1.1. We evaluated J-V curves and EQE spectra to confirm the hypothesis that we can enhance the short circuit current density by minimizing parasitic optical losses while avoiding sputter damage to the perovskite top-cell. We present a schematic illustration of the tandem devices in Fig. 4.38(a) and (b). Dashed lines mark the active cell area, which is 1 cm^2. In Fig. 4.38(c) and (d), we present the results of the J-V and EQE measurements, respectively. Except for the layer between C_{60} and IZO, the tandem devices are equal. In green, we show the tandem device with a thermal atomic layer (ALD) deposited SnO_2 buffer layer in-between the C_{60} and the IZO, and in red, we show the tandem device without (w/o) SnO_2, with a PEIE interlayer. The power conversion efficiency (PCE) of the tandem device with SnO_2 was 27.4%, and the device PEIE replacing the SnO_2 layer reached a PCE of 28.4%. The higher PCE of the device without SnO_2 mainly originates from the device's short circuit current density and V_{OC}, which were 0.34 mA/cm^2 and 30 mV higher for the PEIE device, respectively. We assign the difference in V_{OC} to the SnO_2 ALD deposition process, which requires water as oxidants and may contribute to the degradation of the perovskite absorber [166, 167]. The device's higher short circuit density originates from improved sub-cells integrated current densities (see Fig. 4.38(d)). We record a gain of 0.48 mA/cm^2, from 18.92 mA/cm^2 to 19.40 mA/cm^2, in the perovskite top-cell when replacing the SnO_2 buffer layer with

the thin PEIE, and a gain of 0.12 mA/cm^2, from 19.23 mA/cm^2 to 19.35 mA/cm^2, in the silicon bottom-cell. In sum the short circuit density of the SnO_2-based device reaches 38.15 mA/cm^2 and the PEIE-based device reaches 38.75 mA/cm^2, resulting in a difference of 0.6 mA/cm^2, which was predicted by the simulation mentioned above.

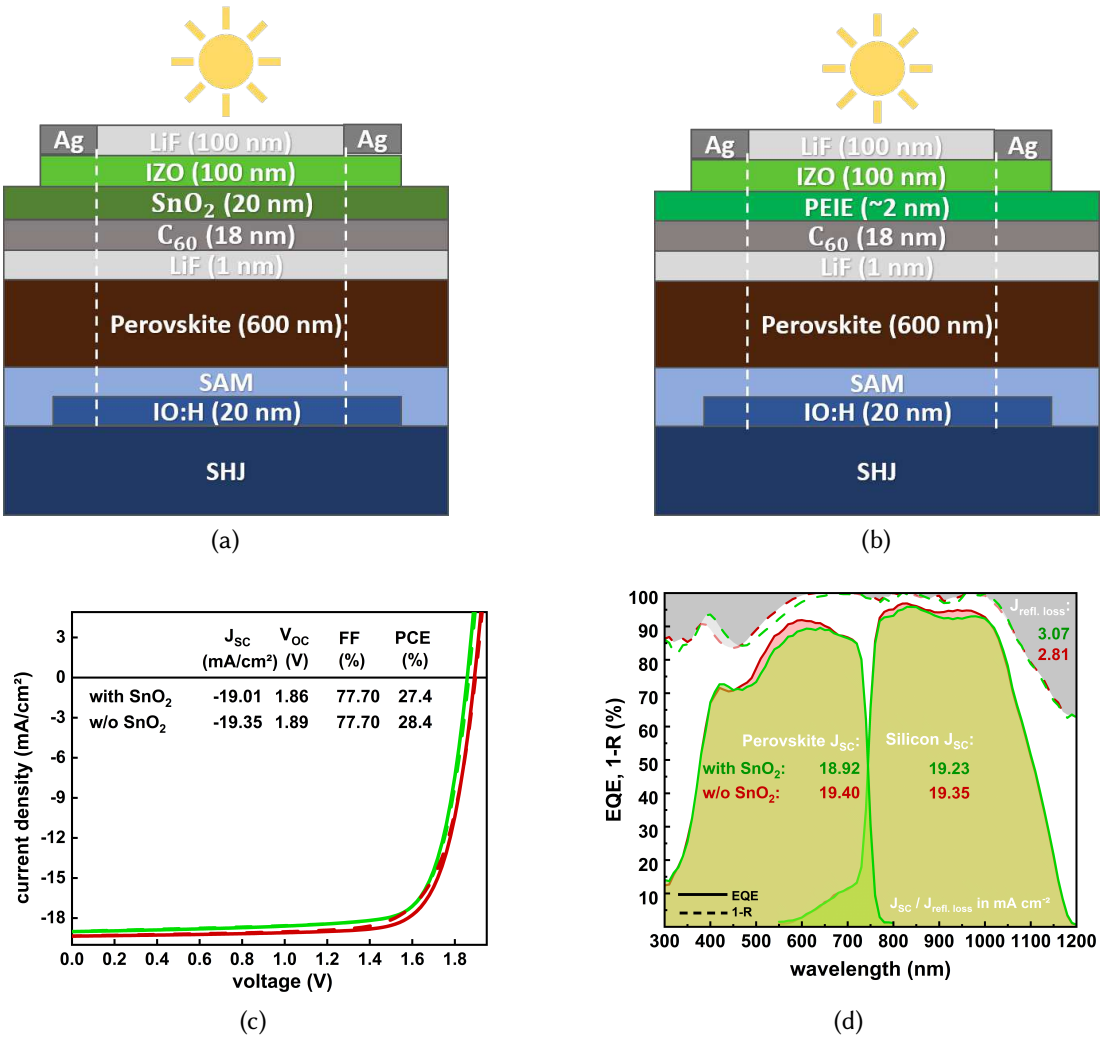

Figure 4.38: Schematic device layout of monolithic perovskite/silicon tandem solar cells, including estimated layer thicknesses for (a) a device with conventional SnO_2 buffer layer and (b) an ultra-thin PEIE interlayer; (c) Comparison of the tandem J-V characteristic after spectral matching (straight lines are forward scan direction and dashed reverse), and (d) the measured EQE and 1-R spectra of tandem devices with (green) and without (red) a 20 nm thick SnO_2 buffer layer (w/o SnO_2 refers to devices where PEIE was used instead of SnO_2).

In Fig. 4.39 we present a comparison of the sub-cells current densities, parasitic

absorption losses, and reflection losses based on the EQE and the 1-R measurements of the same devices. This comparison allows us to understand the origin of the improved sub-cells integrated current densities (from Fig. 4.38(d)) in detail. While the reflection losses dropped by 0.26 mA/cm^2 from 3.07 mA/cm^2 to 2.81 mA/cm^2, the parasitic absorption was decreased by 0.32 mA/cm^2, from 5.24 mA/cm^2 to 4.92 mA/cm^2. The optical simulations predicted a difference in reflection losses of 0.1 mA/cm^2 and a difference in parasitic absorption of 0.5 mA/cm^2, which is close to our experimental results. The biggest difference between the optical simulation and experimental results we observed was in the parasitic absorption losses, which are overall higher in the experiments, accounting for lower integrated current densities of the sub-cells. Because of the assumption that all light is either absorbed, reflected or contributes to parasitic absorption, no further distinction is made as to which loss mechanisms are involved in parasitic absorption. The simulation assumes only optical losses in the parasitic absorption. On the other hand, real tandem devices are also subjected to collection losses, for example. Overall, we found a good agreement between optical simulations and experimental results.

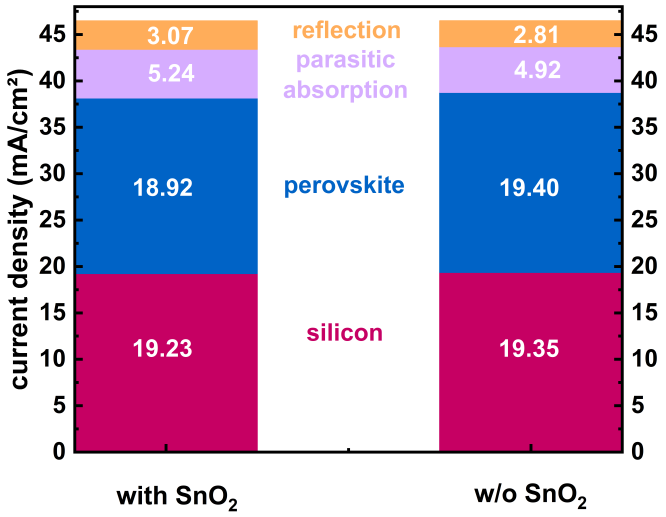

Figure 4.39: Comparison of the tandem's current density and current density losses, based on the EQE and the 1-R measurements of tandem devices with and without a 20 nm thick SnO_2 buffer layer (w/o SnO_2 refers to devices where PEIE was used instead of SnO_2).

Summary of the main findings

- The PCE of monolithic two-terminal tandem devices was increased from 27.4% to 28.4% when replacing the SnO_2-buffer with an ultra-thin PEIE interlayer, which originates from improved J_{SC} and V_{OC}.
- While the improvement of J_{SC} was already predicted by the optical simulation, we assign the difference in V_{OC} to the SnO_2 ALD deposition process, which can degrade the perovskite.

- Overall, the current density loss was decreased by 0.58 mA/cm^2 for the SnO_2-buffer layer free tandem device, which is close to the value predicted by optical simulations.

4.3.3 Stability of tin oxide-free perovskite/silicon tandem solar cells

As mentioned above, we were able to remove the SnO_2 buffer layer in the tandem stack, by applying a sputter damage free IZO deposition and deposited IZO on the C_{60}/PEIE double-layer ETL instead. However, the SnO_2 layer does not only act as a protective buffer against sputter damage, but also as a diffusion barrier, increasing the solar cell stability by preventing penetration of oxygen and moisture and stopping inter-diffusion of perovskite degradation products [168, 169]. Therefore, we raise the question whether removing the SnO_2 buffer layer solar cell leads to poor tandem device stability.
We tracked the maximum power of a C_{60}/SnO_2 and a C_{60}/PEIE double-layer ETL tandem device measured under continuous 1 sun illumination at 25 °C temperature for over 3 minutes. The devices were fabricated following the method described in Chap. 3.1.3, and the IZO was, contrary to the IZO electrode of the tandem devices in the previous section, deposited by the low power deposition process of the Roth&Rau sputter tool (more information can be found in Chap. 3.1.1). The tandem devices for the experiment in this section were not prepared in the same batch as the previously presented tandem solar cells. Unidentified issues during the fabrication led to overall lower efficiencies here. However, since the following samples were produced in the same batch and are subject to similar limitations, we believe a comparison of the results is still meaningful. In Fig. 4.40 we present the J-V curves of both devices, together with the MPP track in the inset, 8 days after device fabrication. While for the C_{60}/SnO_2 double-layer ETL tandem device a stabilized PCE of ~24.7% is achieved, confirmed by a 180 s MPP-track as shown in the inset of Fig. 4.40 (in green), the C_{60}/PEIE double-layer ETL tandem device (in red) shows an initial increase in MPP from ~25.3 to ~25.7% in the first 25 s, followed by a continuous decline, from ~25.7% to ~25.2% after 180 s. In the observed time range, we do not see a stabilized MPP value for the C_{60}/PEIE double-layer ETL tandem device. We assume the initial increase in MPP could be linked to light-soaking dynamics. The presented J-V curves were measured after the 180 s MPP tracking.

We encapsulated two tandem solar cells that had been fabricated 22 days prior. We measured them at 25 °C, ambient humidity (not actively controlled) for a long-term stability test in an in-house built aging setup. Details about the setup used for the analysis can be found in the publication by Jošt *et al.* [170]. For the encapsulation, the devices are placed between two glasses and sealed around the edges with UV-curable resin. The front and rear contacts are connected by two copper stripes, respectively. The cells were measured for about 935 h. After 172 h, we lost contact to the C_{60}/PEIE double-layer ETL tandem device, and the signal dropped to zero.
The results of the long-term stability analysis are shown in Fig. 4.41. The current

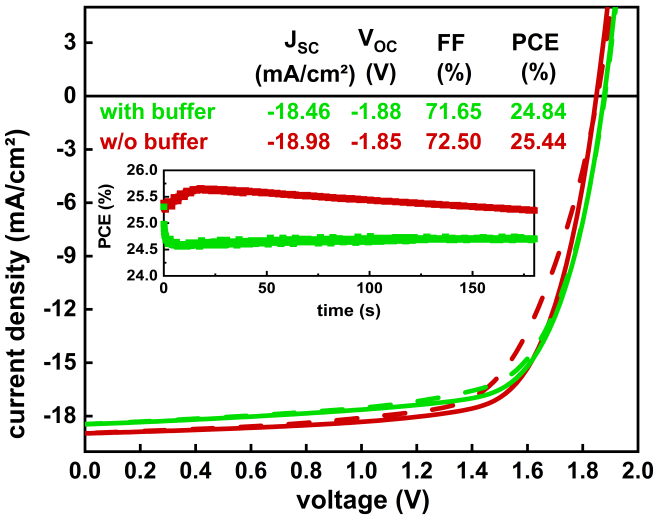

Figure 4.40: Forward (dashed lines) and reverse (solid lines) J-V scans of tandem devices with (green) and without (red) a 20 nm thick SnO_2 buffer layer (w/o SnO_2 refers to devices where PEIE was used instead of SnO_2), together with the respective MPP tracks shown in the inset, eight days after device fabrication. The displayed values belong to the reverse J-V scans.

and voltage of both cells at MPP were tracked periodically every 5 minutes for 935 h, resulting in 10324 data points for each parameter (the PCE of the whole analysis time is shown in Fig. 6.17 in the supplementary section). Fig. 4.41 displays the tracked time-dependent data of V_{MPP}, J_{MPP} and PCE from top to bottom for an analysis time of 367 h. After 367 h, we observed an unexpected jump in the signal that seems to be related to technical issues as it matches a jump in the blue light LED intensity (see Fig. 6.17 in the supplementary section). Therefore, we do not discuss the data beyond 367 h here. In Fig. 4.41 we present the results of the C_{60}/SnO_2 double-layer ETL device in green, labeled as "with SnO_2", and the results of the C_{60}/PEIE double-layer ETL device in red, labeled as "w/o SnO_2" for the analysis time of 367 h. We observe an initial drop from ~24.3% to ~21.2% in the first 0-22 h for the C_{60}/SnO_2 device PCE (the so-called "burn-in" effect [171]), and then a slower steady decrease at t > 22 h. The main reason for both decline regions is the decrease in J_{MPP}, while the C_{60}/SnO_2 device V_{MPP} stays rather constant over the whole measurement time. At t > 22 h the C_{60}/SnO_2 device J_{MPP} decreases faster than the blue LED light intensity for the same time (see Fig. 6.18 in supplementary). Due to degradation a continuous decline in J_{MPP} and PCE of the C_{60}/SnO_2 device can be observed.

In the following we will evaluate the stability of both tandem devices individually, starting with the C_{60}/SnO_2-based tandem device. In Fig. 4.42 we show the normalized PCE values for the C_{60}/SnO_2 and the C_{60}/PEIE double-layer ETL tandem device. A common way to evaluate the stability of a device is by giving the time during which the PCE drops to a certain percentage of its initial efficiency. Usually, this value is 80% of the initial efficiency (denoted as T_{80}). However, evaluating the device stability based on a "stabilized" trend after the rapid initial degradation (the burn-in) makes more sense. A detailed discussion on how to evaluate the stability of perovskite devices was done

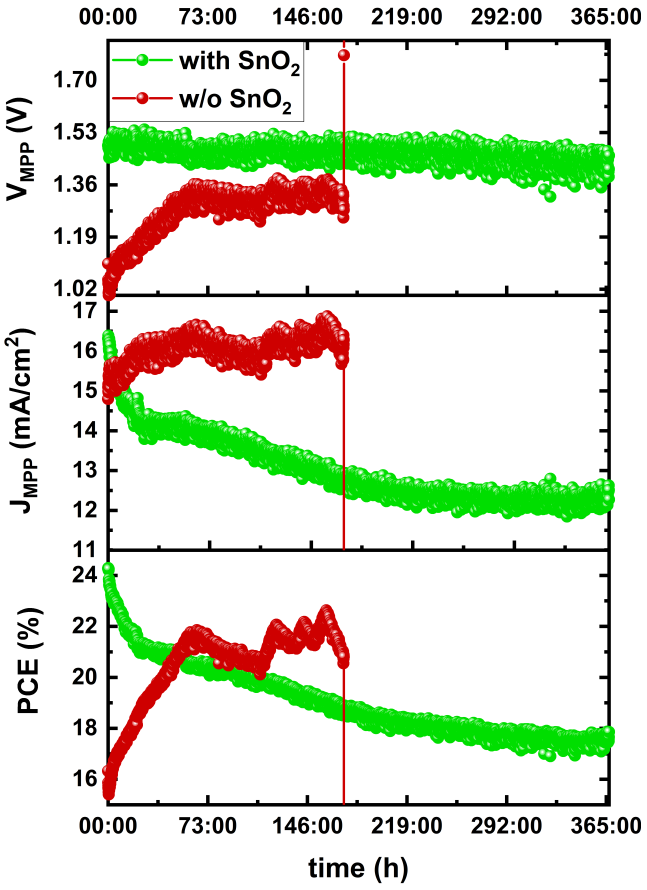

Figure 4.41: The voltage and current at MPP (V_{MPP} and J_{MPP}), and the PCE of the long-term stability analysis as a function of the time (h) of tandem devices with (green) and without (red) a 20 nm thick SnO_2 buffer layer (w/o SnO_2 refers to devices where PEIE was used instead of SnO_2).

by Khenkin *et al.* [171]. Here, we utilized the three suggested approaches to calculate the figure of merit as proposed by Khenkin:

1. Normalization of the PCE data at t=0.
2. Normalization of the PCE data after the burn-in time (at $t_{burn-in}$, blue vertical line in the graphs).
3. Normalization of the PCE data at t=0 for back-extrapolated data of PCE(t $t_{burn-in}$). We chose the extrapolation time for a linear region of the decay, between 21-172 h.

As can be seen in Fig. 4.42(a) for the C_{60}/SnO_2-based tandem device PCE, the first approach leads to a figure of merit of $T_{1,80}$ = 140 h. For the second approach, the PCE data does not reach 80% of its initial value, and the third approach leads to $T_{3,80}$ = 340 h. The latter value is in the same range as observations that were done by Köhnen *et al.* for a similar experiment, and devices [165].
Rainford and colleagues claim they could even increase the device stability of SnO_2 buffer layer-based perovskite solar cells by inserting PEIE as an interlayer in-between the C_{60} and the SnO_2 [137]. They tested the solar cell stability in a custom-built maximum power tracking setup at 60 °C in ambient air under ~0.77 sun illumination. The devices were not encapsulated prior to the stability test. While their SnO_2-free devices fully degraded in less than 25 h of continuous MPP tracking, their C_{60}/SnO_2-based devices were more stable, exhibiting on average over 60% of their initial PCE after 250 h of testing. Their C_{60}/PEIE/SnO_2 devices maintained 81.5% of their initial PCE on average after 250 h of operation. They assign the improved stability to enhanced SnO_2 nucleation on the C_{60}/PEIE interface, leading to better barrier properties of the ALD film. However, they have not tested a SnO_2-free device that includes a PEIE interlayer. Like Rainford *et al.* we exposed our samples (perovskite/C_{60}/IZO, perovskite/C_{60}/PEIE/IZO, and perovskite/C_{60}/SnO_2/IZO, the IZO was each 100 nm thick) to a drop of water on the IZO surface, in order to test their water diffusion stability (see Fig. 6.6 in the Supplementary Chap. 6.2). Surprisingly, in case of the conventional perovskite/C_{60}/SnO_2/IZO-stack, the water penetrated through the electron contact immediately (within seconds) and started to react with the perovskite, which was recognizable by a yellow phase forming. As time progressed, the degradation effect extended further and further. For the perovskite/C_{60}/IZO and Perovskite/C_{60}/PEIE/IZO, we did not observe significant degradation of the underlying perovskite layer. In a few places, small defects resulted in yellow dots, but no spreading degradation effect was evident. According to this experiment, the electron contact with 100 nm IZO provides a better water barrier without the SnO_2 buffer layer. Therefore, we are interested in whether maybe PEIE itself, without SnO_2, can improve the device stability, too.
For the C_{60}/PEIE double-layer ETL tandem device (in red), we observe a boost in the

PCE for in first 0-60 h (see Fig. 4.42), which is promoted by an increase in V_{MPP} and J_{MPP}. This indicates an improvement in V_{OC} and J_{SC} and/or FF. Such an initial boost has been observed by others and is also often referred to as the "burn-in" period [137, 171]. However, the initial PCE is unexpectedly low. It exhibits a value of only 15.5%. It is therefore much lower than the device PCE of ~25% extracted from J-V measurements prior to the long-term stability analysis (compare to Fig. 4.40). The reason for this is currently unclear. However, at t > 60 h, the PCE, V_{MPP}, and J_{MPP} reach average values similar to those recorded on day 8 (see Fig. 4.40). At 172 h, the contact to the C_{60}/PEIE device was lost due to either technical issues or the solar cell died. Interestingly, before that, no continuous decline region in PCE was observed. However, the values fluctuated much more than for the C_{60}/SnO_2 device. We assume this might originate from a contacting and/or equipment issue since the ripples in the C_{60}/PEIE device PCE curve match with ripples observed for the LED light intensity, which we show in Fig. 6.19 in the supplementary section. Therefore, we recommend validating the data by repeating the analysis for this device structure. Overall, the C_{60}/PEIE double-layer device PCE increased from initially ~15.5% at 0 h to an average of ~21.5% at 60-172 h, due to the increase of V_{MPP} from ~1.0 V to an average of ~1.3 V, and an increase of J_{MPP} from ~15.4 mA/cm^2 to an average of ~16.3 mA/cm^2. As seen in Fig. 4.42(b), we were not able to calculate a stability figure of merit for any of the three suggested approaches for the C_{60}/PEIE double-layer device PCE, as the measurement was interrupted due to the device dying before we were able to observe a degradation regime, making conclusions about the real device stability difficult.

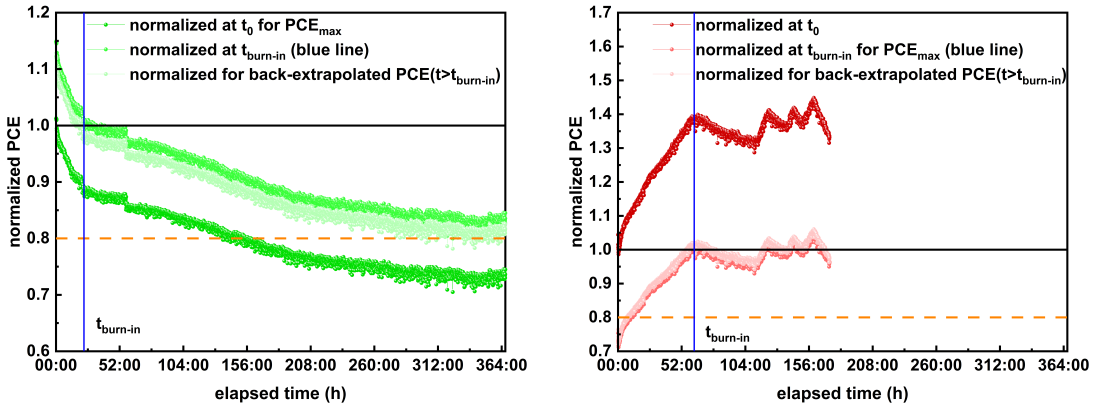

(a) (b)

Figure 4.42: Calculated stability figure of merit for (a) tandem devices with (green) and (b) without (red) a 20 nm thick SnO_2 according to the three approaches suggested by [171]: 1. Normalizing the PCE data at t=0, 2. Normalizing the PCE data after the burn-in time (at $t_{burn-in}$, blue vertical line) and 3. Normalizing the PCE data at t=0 for back-extrapolated data of PCE(t $t_{burn-in}$), at an extrapolation time for a linear region of the decay, between 21-172 h.

Summary of the main findings

- Stability tests revealed, that the C_{60}/SnO_2-based device PCE drops fast at first and then follows a steady degradation dynamic, while we observe an initial boost in PCE for the C_{60}/PEIE-based device.
- We were not able to quantify the stability of the C_{60}/PEIE-based tandem device by a figure of merit as proposed by Khenkin *et al.* [171], due to issues during the measurement.
- Therefore, we were ultimately not able to directly compare the long-term stability of both device designs.

4.3.4 Conclusion

We performed optical simulations on perovskite/silicon tandem solar cells with and without a 20 nm thick SnO_2 buffer layer to investigate the optical losses assigned to the buffer layer. Overall 0.6 mA/cm^2 current density loss could be assigned to the SnO_2, mainly originating from parasitic absorption below 700 nm. We built tandem solar cells with a similar design to the simulated devices. In the case of the SnO_2 buffer layer free tandem devices, an ultra-thin (~2 nm) thick PEIE interlayer was inserted between the C_{60} and the IZO electrode. The IZO for both designs was deposited in a low-damage sputter deposition process. Electrical measurements (J-V and EQE scans) of the devices revealed that we could increase the PCE from 27.4% to 28.4% when replacing the SnO_2-buffer with the ultra-thin PEIE interlayer. The improvement originated from a higher J_{SC} (as predicted by the optical simulations) and a higher V_{OC}. We believe that the V_{OC} difference stems from degradations during the SnO_2 ALD deposition. A current density loss analysis revealed a reduction of 0.58 mA/cm^2 when replacing SnO_2 with PEIE, which originated from reduced reflection and parasitic absorption. This is in good agreement with the optical simulations.
We performed a long-term stability test on both tandem device designs, which revealed opposing initial trends. While the PCE initially drops fast, for the C_{60}/SnO_2-based tandem device, we observe an initial boost in efficiency for the C_{60}/PEIE-based tandem device. After 172 h, the C_{60}/PEIE-based tandem device broke, and the long-term stability test was interrupted. We suggest repeating this experiment to get a more conclusive result.

Chapter 5

Conclusion and Outlook

5.1 General conclusion

The scope of the thesis was to optimize IZO for the application as a front-electrode in tandem solar cells and to investigate sputter damage during the sputter deposition of IZO onto the perovskite (sub-)cell. The experimental part of this work has focused on investigating how sputter damage impacts the perovskite solar cell characteristics and developing and optimizing low-damage IZO sputter deposition methods. A major goal was to enable the electrode's sputter deposition directly onto the sensitive layer of the perovskite solar cell without the need for an ALD SnO_2 sputter protection buffer layer. Omitting the buffer layer has several advantages: 1) it results in reduced optical parasitic absorption losses, and 2) it circumvents thermal ALD-induced degradation of the perovskite solar cell. However, the approach of simply omitting the SnO_2 buffer was not as straightforward as initially believed. When we first deposited IZO directly onto the C_{60} ETL, we were faced with a significantly reduced device performance, originating from a lower FF, precisely an s-shape, and lower V_{OC}. Even our low-damage sputtering methods did not improve the performance. From this, we concluded that the C_{60}/IZO is subject to other limitations that are not directly attributable to sputtering damage. Our investigations based on targeted measurements and electrical simulations have shown that a potential barrier in the C_{60}/IZO interface triggers the deformation of the J-V characteristic, leading to substantial interfacial recombination losses. On the other hand, we found no direct correlation between the s-shape and sputter damage. The s-shape formation was avoided by inserting an ultra-thin (~2 nm) PEIE interlayer. In combination with a low-damage IZO sputter deposition, the solar cell performance was significantly improved. The average performance of our low-damage, buffer-layer-free

semi-transparent single solar cells was higher than that of equivalent devices with an ALD processed SnO_2 buffer layer. We also addressed the question of how the PEIE interlayer improves the interfacial properties. Using in-situ GISAXS measurements during the IZO sputter deposition process on ETLs consisting of only C_{60}, C_{60}/PEIE, and C_{60}/SnO_2, we investigated whether the surface properties of these designs have an impact on initial IZO growth. While we found fundamentally different growth behaviors, we could not find any correlation with the solar cell characteristics.
We see a huge potential for our low-damage, SnO_2 buffer-free solar cells as an application in monolithic tandem devices. Based on optical simulations and measurements, we were able to show that higher short-circuit currents can be achieved in both subcells of a tandem solar cell by omitting the SnO_2 buffer layer. In our experiment, our low-damage, SnO_2 buffer layer-free tandem solar cell with a PCE of 28.4 % even outperformed our reference cell with 27.4 %, which had a conventional electron contact stack, including SnO_2. These extraordinary results can be explained primarily by reduced parasitic absorption but also by a higher V_{OC}, presumably due to circumventing degradation by the thermal ALD process.
We expect that our findings will considerably improve the perovskite/silicon tandem efficiency and enable less complex manufacturing of this solar cell technology, accelerating its commercialization.

5.2 Outlook for further research

This work identifies several aspects for future research. The potential for efficiency improvements in perovskite/silicon tandem solar cells is not yet exhausted. As shown in this work, interface engineering still offers much room for optimization, including recombination loss reduction, band alignment optimization, or materials research. While we found that a PEIE interlayer could significantly improve the C_{60}/IZO interface properties, it is interesting to further test other materials with certain features, such as materials with known dipole properties.
One key finding of this work was that the perovskite/silicon tandem PCE could be improved by reducing optical parasitic losses by omitting the SnO2 buffer layer. Nevertheless, parasitic absorption losses of approximately 5 mA/cm2 were still found. We believe that we can further reduce the parasitic losses by two approaches:

1. Reducing the C_{60} thickness or replacing it with an ultra-thin material. We believe that our low-damage sputter deposition approach offers the opportunity to deposit front-electrode TCOs on very thin ETLs without inducing sputter damage to the perovskite solar cell.

2. Replacing the IZO with a TCO of a higher band gap and lower free carrier absorption. We believe that high-mobility TCOs are an emerging trend, offering a huge potential for front-electrode application in tandem devices. we collected

a few possible candidates in Tab. 2.1 in Chapter 2.1. However, temperature-dependent degradation of the perovskite must be considered during the annealing of TCOs.

In order to prevent long-term annealing at degrading temperatures and reduce thermal stress, flash lamp annealing (FLA) might be an intriguing approach for crystallizing transparent front electrodes for perovskite-based tandem solar cells. In Chap. 2.1 we already briefly discussed FLA. So far, it has only been shown that FLA is capable of producing high mobility IO:H films on silicon wafers, with an annealing time of only 2.7 ms. These IO:H films were comparable to IO:H films annealed at 180°C for 30 min. Investigating whether this procedure can be applied to perovskite devices would be really intriguing.
As we have shown, the possibilities for soft deposition of transparent electrodes using conventional RF magnetron sputtering techniques are limited from the process side. Nevertheless, soft and especially industry-relevant deposition processes are highly relevant for the perovskite solar cell research field. One potential low-damage technique was presented in Chap. 2.2.3, the hollow cathode gas flow sputter deposition. As discussed, sputter damage can be reduced by decreasing damaging kinetic particle energies using a lower power during sputtering. The principle of hollow cathode gas flow sputtering promises very low particle energies due to its special sputtering process method. Furthermore, it is a fast and scalable technology. An alternative method to reduce the energy of sputtered TCO particles proposed in the literature is a biased mesh between target and substrate [172]. It has been shown that by applying a negative bias voltage to a grid with defined hole diameters, the kinetic energy of negative oxygen ions can be reduced. This principle has not yet been used for front electrode deposition in perovskite solar cells, although it is a promising method for low-damage sputter deposition.
We would also like to stress that novel measurement technique approaches can help identify previously unsolved problems. One such novel approach was discussed in Chap. 4.2.2, and we would like to emphasize that this measurement method's full potential has not yet been utilized. In the future, monitoring the growth behavior of crystalline high-mobility, low-temperature TCOs during sputter deposition dependent on substrate materials could be of great importance because many crystalline TCOs benefit from optimal initial growth conditions. Combined with simultaneous GIWAXS measurements, which are also available in-situ at the same facility, it is possible to detect possible degradation processes during the sputter deposition process. Therefore, it is important to optimize the TCO sputter deposition process at the DESY facilities in order to get closer to real TCO sputter conditions.
Finally, we would like to emphasize that the long-term stability studies from Chap. 4.3 need to be repeated with higher statistical relevance. While we gave several strong arguments to exclude the SnO_2 deposited by thermal ALD, it is entirely unclear so

far how stable a perovskite/silicon tandem solar cell would be in the absence of SnO_2. Long-term stable solar cells are of immense importance for the commercialization of this technology.
Numerous novel approaches have been investigated in this study. Their findings present a variety of new opportunities for future scientific work.

Chapter 6

Supplementary Information

6.1 Supplementary Information to Chapter 4.1

The absorption coefficient is a film thickness-independent thin film material property that provides information about the electronic band structure or band tails. Typically, it is calculated using optical data obtained from spectrophotometry or ultraviolet–visible-near infrared (UV-Vis-NIR) spectroscopy. In the following, two methods will be presented to calculate α. The first method follows the general Lambert-Beer law, neglecting any reflection. The second method takes reflection at the incident interface into account. By rearranging Equ. 2.9 in Chap. 2.1.2 we obtain a simple relation between the absorption coefficient α_1 and the transmittance (T) (neglecting interference), where T = $I(\lambda, x)/I_0$ (the light intensity $I(\lambda, x)$ reduced by absorption in a medium), and x = d (the layer thickness):

$$\alpha_1 = -\frac{1}{d}\ln(T) \tag{6.1}$$

Realistically, reflection occurs at the light impinging interface of conventional thin film materials, which is why the method above leads to significant errors. Such reflection can be accounted for in the absorption coefficient as follows:

$$\alpha_2 = -\frac{1}{d}\ln(\frac{T}{1-R}) \tag{6.2}$$

However, this method can result in implausible negative absorption coefficients, for example, when transmittance (T) and reflectance (R) measurements exhibit errors due to insufficient calibration of the measuring unit.

We believe that there is a calibration error affecting the reflectance measurement in our experiment. Unfortunately, when the absorption coefficient was calculated using the second method, several negative values were obtained. In Fig. 6.1, we show the absorption coefficients for the selected IZO thin film according to both methods described above. The negative values for the absorption coefficient close to the Urbach tail energies affect their accurate determination. In Fig. 6.2(a) we show the Urbach energy determination according to α_1 and in Fig. 6.2(b) the determination according to α_2. It is obvious from Fig. 6.2(b) that it is difficult to identify a linear region to fit a slope for Urbach energy calculations. Therefore, for this work, we decided to use the first method (α_1) for Urbach energy estimations.

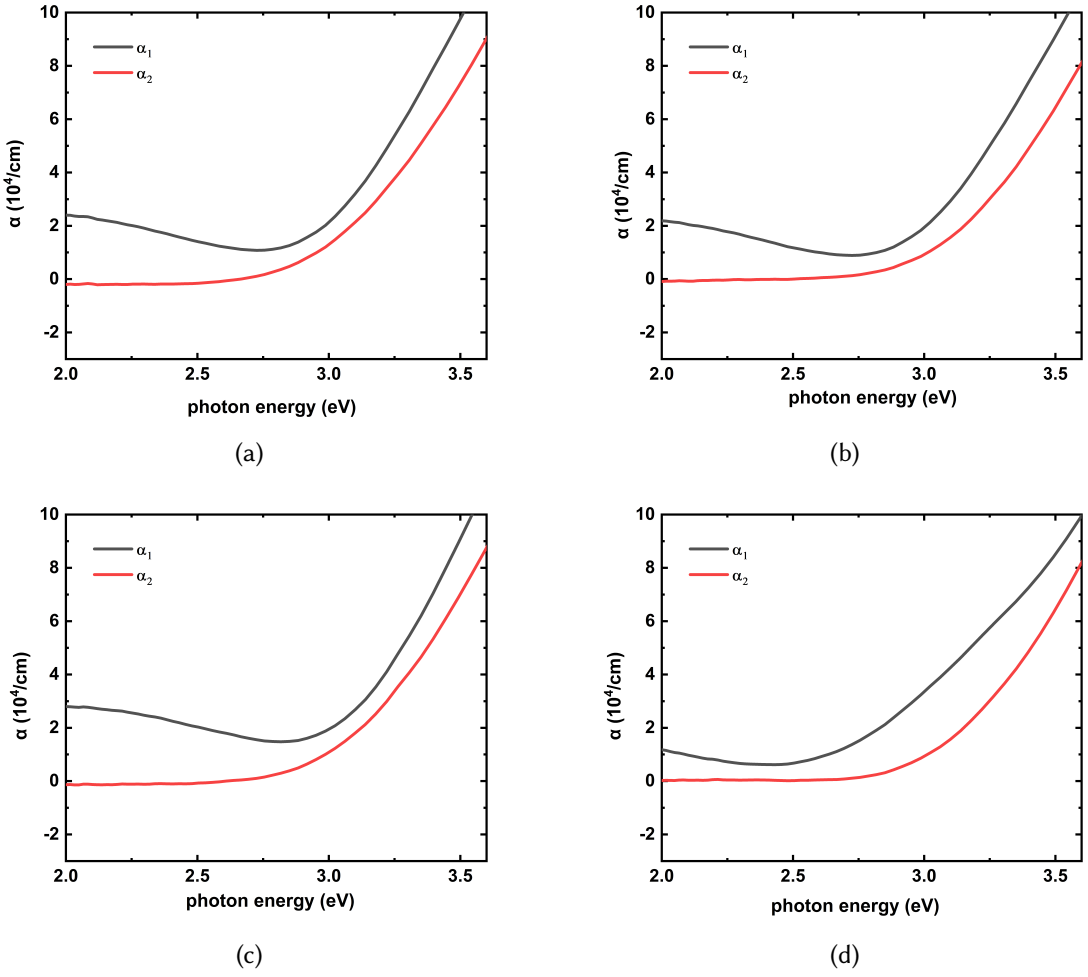

Figure 6.1: Absorption coefficient according to α_1, and α_2 for (a) the standard IZO process, (b) the low power IZO process, (c) the indirect IZO process, and (d) the high pressure IZO process.

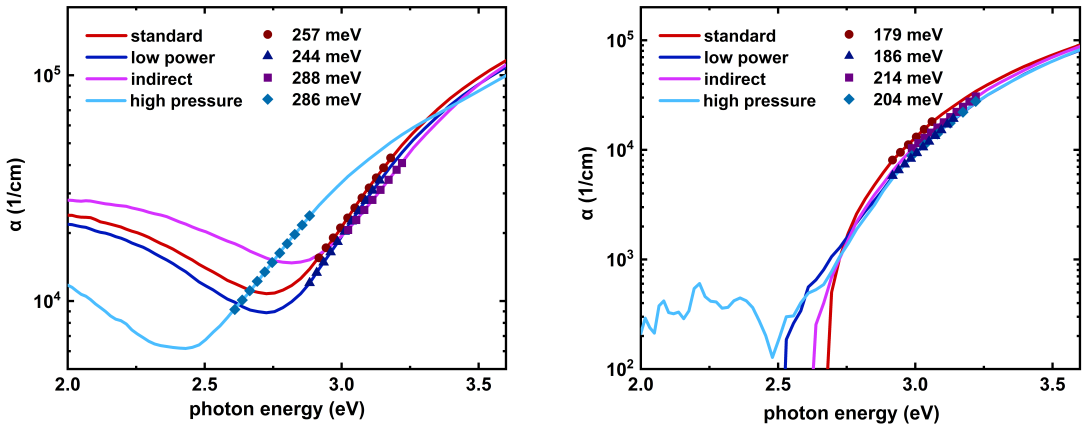

(a) (b)

Figure 6.2: Absorption coefficient in semi-logarithmic scale of the standard, low power, indirect, and high pressure IZO process for (a) α_1, and (b) α_2. Where it seemed possible, a linear fit was applied to calculate Urbach energies.

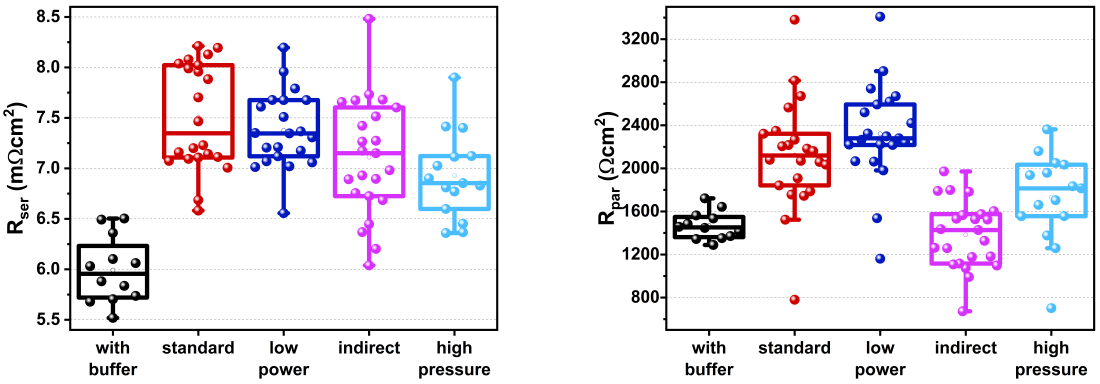

(a) (b)

Figure 6.3: (a) Statistical evaluation of the series resistance and (b) the parallel resistance extracted from the light J-V measurements of semi-transparent perovskite single junction solar cells with standard IZO-front contact deposited on a buffer layer, and standard and different soft sputtered IZO front electrode, deposited onto the ETL without a protective buffer layer, measured through the IZO front electrode.

6.2 Supplementary Information to Chapter 4.2

The dark J-V characteristics of devices with IZO films sputtered on different ETL configurations is shown in Fig. 6.4.

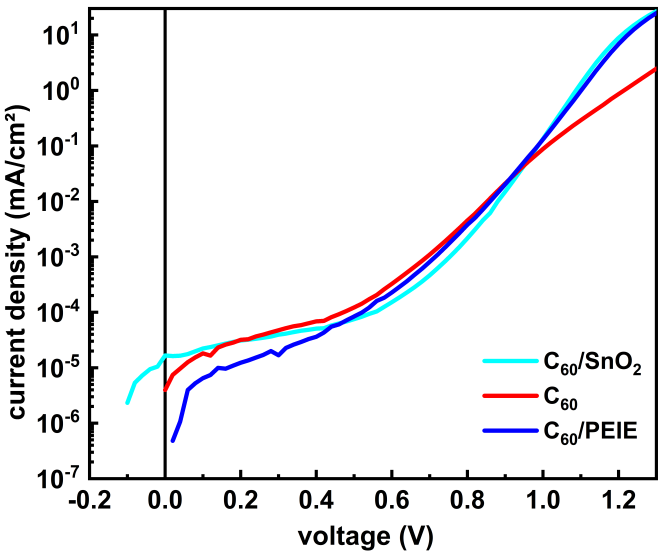

Figure 6.4: Dark J-V characteristics for solar cells with the different ETL configurations - C_{60}/SnO_2, C_{60}, and C_{60}/PEIE.

In Fig. 6.5, the time constants from the measured light intensity-dependent TPV decay signal and their averaged values are shown. Each time constant was derived from a different time scale of the decay signal and represents a different recombination mechanism.

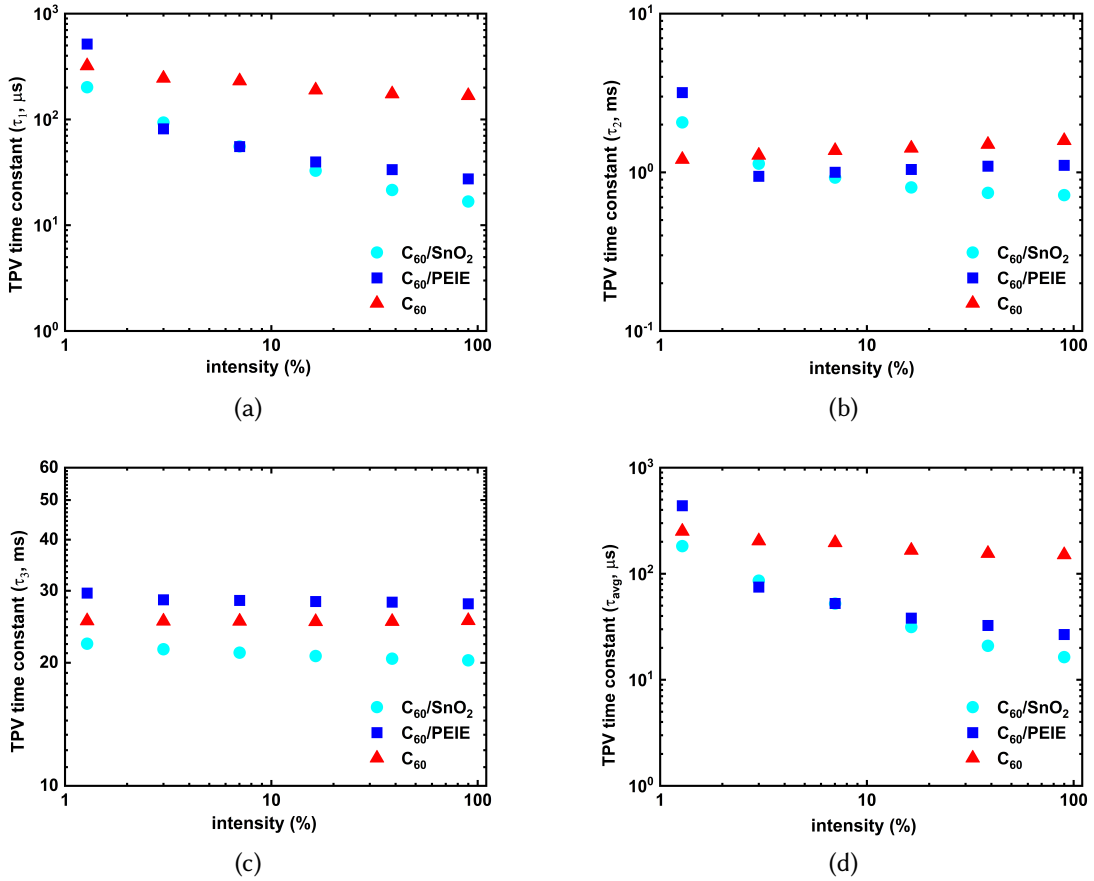

Figure 6.5: Light intensity-dependent TPV decay measurements leading to different time constants of different time scales - (a) in the microsecond-scale, (b) in the ~millisecond-scale, and (c) for several tenths of milliseconds, while (d) represents an average of all three time constants, which was calculated by $\tau_{avg} = \tau_1 \cdot \tau_2 \cdot \tau_3 / (\tau_1\tau_2 + \tau_2\tau_3 + \tau_1\tau_3)$ [173]. Each time constant represents an independent recombination phenomenon and was obtained from the decay of TPV. τ_1 or τ_2 possibly represent recombination processes in the ETL interfaces.

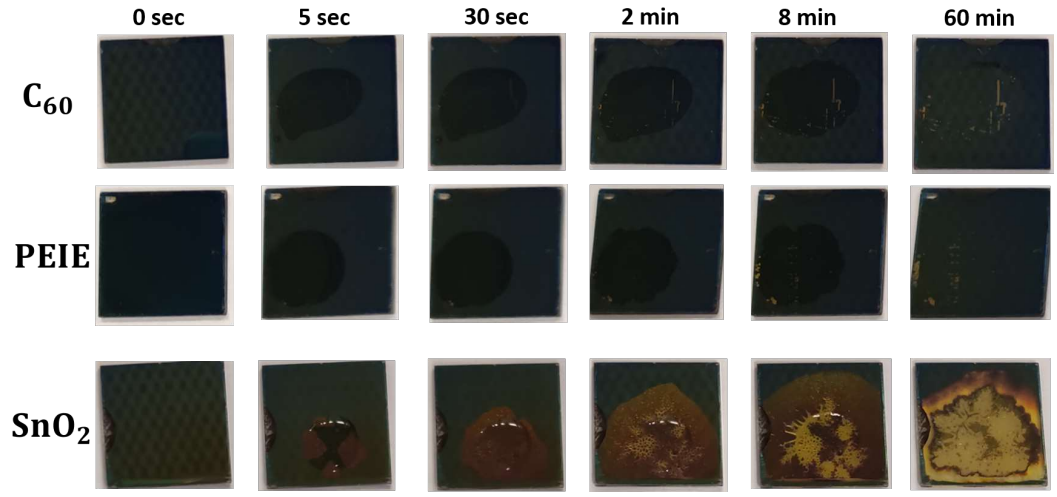

(a)

perovskite/C_{60}/IZO **perovskite/C_{60}/PEIE/IZO** **perovskite/C_{60}/SnO_2/IZO**

(b)

Figure 6.6: (a) Water drop interaction with stacks of perovskite/C_{60}/IZO (denoted as C_{60} in graphic (a)), perovskite/C_{60}/PEIE/IZO (denoted as PEIE in graphic (a)), and perovskite/C_{60}/SnO_2/IZO (denoted as SnO_2 in graphic (a)) as a function of time, and (b) side views after a few minutes.

Real-time in-situ investigation of IZO sputter deposited on different layers of the ETL of perovskite solar cells

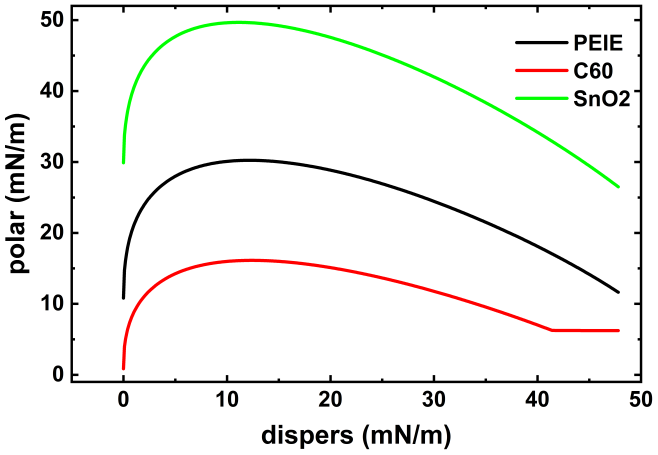

Figure 6.7: Wetting envelope of the Perovskite/C_{60}/SnO_2 (green), Perovskite/C_{60} (red), and Perovskite/C_{60}/PEIE (black) ETL stacks.

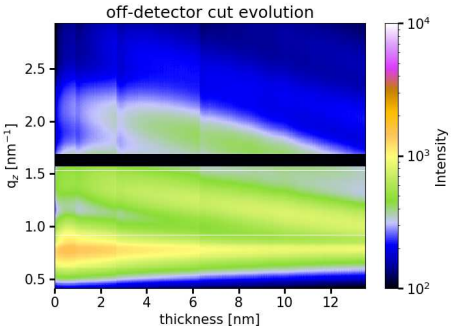

(a)

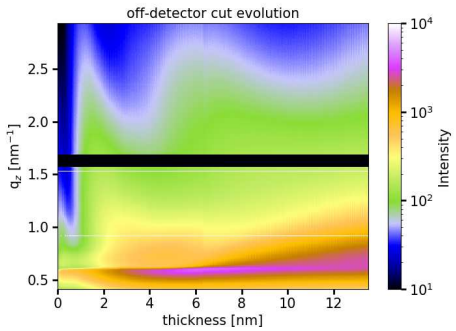

(b)

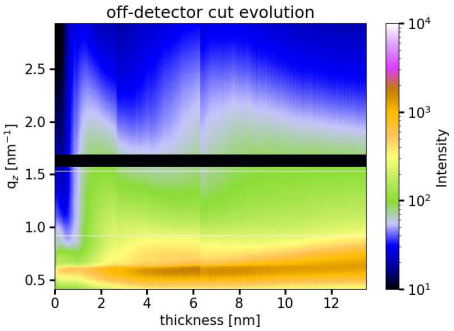

(c)

Figure 6.8: Contour mapping plots of the vertical off-detector line cut evolution for summed images (100 images are summarized to one, improving the resolution) as a function of IZO thickness, for (a) SnO_2/C_{60}/Si, (b) $_{60}$/Si, and (c) PEIE/C_{60}/Si substrates.

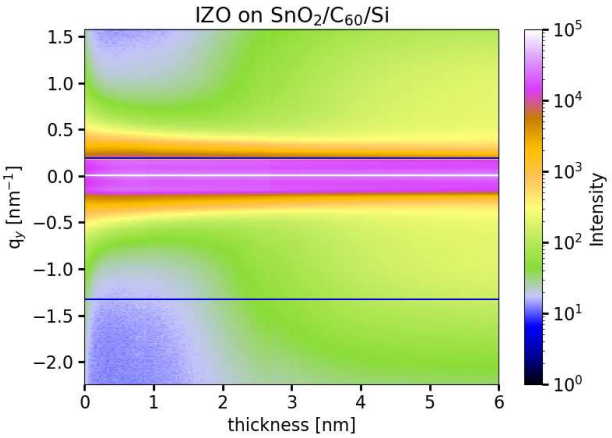

Figure 6.9: Contour mapping plots of the horizontal line cut evolution for summed images (100 images are summarized to one, improving the resolution) as a function of IZO thickness, for $SnO_2/C_{60}/Si$.

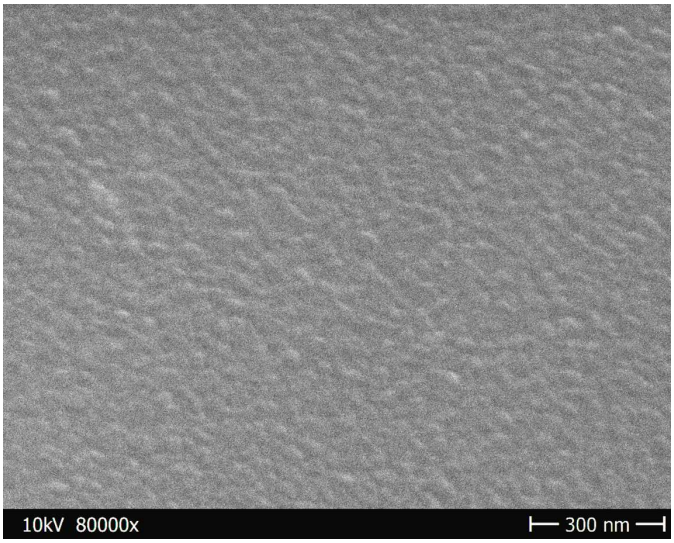

Figure 6.10: SEM top-view of a C_{60} surface.

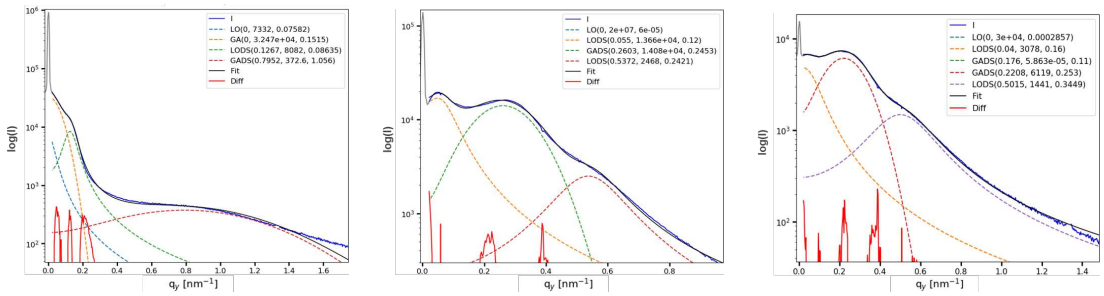

(a) (b) (c)

Figure 6.11: Fits of the horizontal line cut in the area of the cluster scattering signal for (a) SnO_2/C_{60}/Si, (b) $_{60}$/Si, and (c) PEIE/C_{60}/Si substrates at an IZO thickness of 13.5 nm.

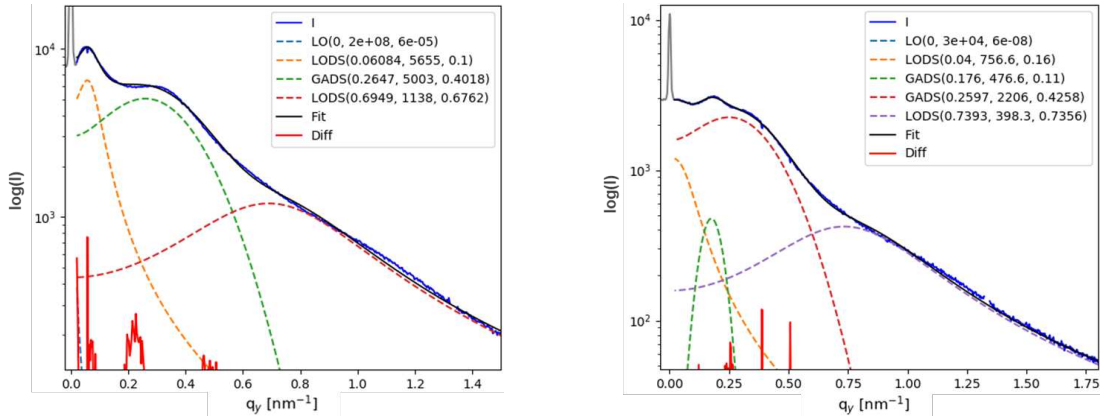

(a) (b)

Figure 6.12: Every 20th image from 450 summed-images .

Electrical simulations using SCAPS

Table 6.1: Parameters obtained by Kelvin Probe (KP) and Photoelectron Yield Spectroscopy (PYS) for samples of 23 nm C_{60} deposited on ITO substrates transferred in nitrogen, exposed to air, and with sputter deposited IZO of different thicknesses on top, and an IZO reference sample of 90 nm thickness deposited on quartz glass. Illumination for light measurements was at 2.75 eV. SPV: surface photovoltage, WF: work function, E_i: ionization potential, E_{DOS}: onset energy of an impurity band. Ionization potential of IZO very uncertain, as resolution of PYS only up to 7.4 eV, resulting in inaccurate fits.

sample sample	SPV (±3 mV)	dark WF (±0.04 eV)	light WF (±0.04 eV)	E_i (±0.05 eV)	E_{DOS} (±0.03 eV)
C_{60}	0	5.09	5.09	6.07	
C_{60} exp.	0	4.84	4.84	6.11	
$IZO_{<1nm}/C_{60}$	-206	4.45	4.25	6.62	5.00
IZO_{1nm}/C_{60}	-223	4.33	4.11	6.55	4.80
IZO_{2nm}/C_{60}	-147	4.40	4.25	6.63	4.64
IZO_{5nm}/C_{60}	-4	4.42	4.41		
IZO_{10nm}/C_{60}	0	4.47	4.47		
IZO_{20nm}/C_{60}	0	4.47	4.47		
IZO_{90nm}	0	4.47	4.47	6.75	4.55

6.3 Supplementary Information to Chapter 4.3

Table 6.2: Materials used for optical simulation, their thicknesses, and their source references.

material (layer)	thickness	source
LiF	100 nm	[135]
IZO	100 nm	this work
SnO_2	20 nm	this work
C_{60}	18 nm	this work
LiF	1 nm	[135]
perovskite	600 nm	[165]
InO:H	20 nm	[107]
nc-SiOx:H(n)	100 nm	[107]
a-Si:H(i)	5 nm	[107]
c-Si(n)	280 μm	[165]
a-Si:H(i)	5 nm	[107]
a-Si:H(p)	10 nm	[107]
InO:H	10 nm	[107]
Ag	400 nm	[107]

We fitted ellipsometric spectra for angles of 50°, 60°, and 70° from 220 nm to 2400 nm and reflection data from 260 nm to 2400 nm for IZO, which we show in Fig. 6.13. Due to the small spot size, corresponding low light intensity, and an unintentionally applied smoothening during data collection, ellipsometric data acquired in the NIR displayed increased noise. Based on [109, 174], we used a triple Tauc-Lorentz oscillator (two for the bandgap, one for tailing) and an extended Drude oscillator to represent the dielectric function of the IZO.

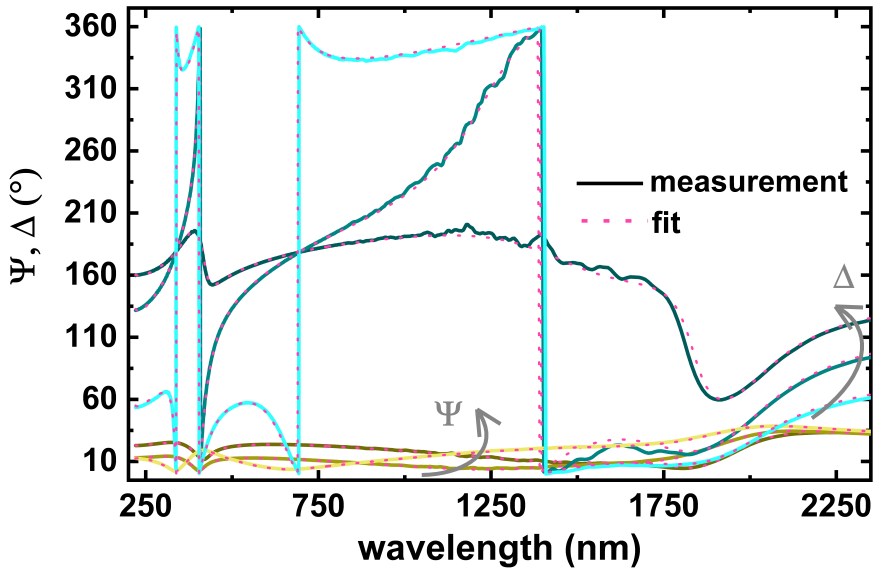

Figure 6.13: Graph showing measured ellipsometry data (solid lines) and respected fits (dashed red lines) for 100 nm IZO on quartz glass, where the colors from dark to light represent the increasing angle of the measurement of 50°, 60°, and 70°.

We deposited a 20 nm SnO_2 layer onto a single-sided polished Si wafer to determine the dielectric function of the film. Data and fits are shown in Fig. 6.14. By measuring a sample cut from the same Si wafer without the SnO_2 layer, we calculated a thickness of 2.6 nm of native oxide on the Si wafer using the dielectric function for SiO_2 from the Sopra database. The sample coated with SnO_2 on top of the native oxide was analyzed by including the native oxide. We modeled the dielectric function of SnO_2 using two Tauc-Lorentz oscillators [175]. Ellipsometric spectra were captured for both specimens (the Si wafer with and without SnO_2 layer) at 40°, 50°, 60°, and 70°. We fitted the acquired data in the 200–940 nm wavelength range.

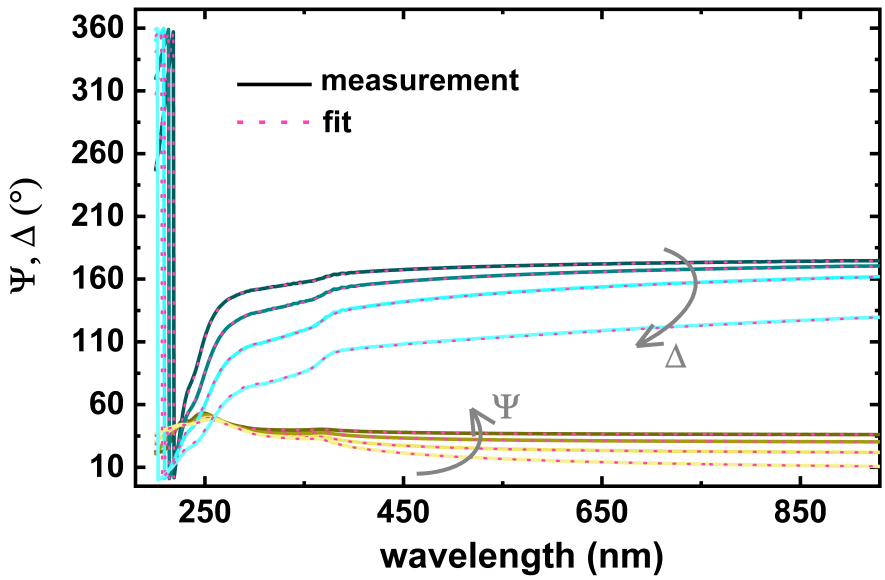

Figure 6.14: Graph showing measured ellipsometry data (solid lines) and respected fits (dashed red lines) for 20 nm SnO_2 on a polished silicon substrate, where the colors from dark to light represent the increasing angle of the measurement of 40° to 70° with a 10° increment.

For C_{60}, we calculated the dielectric function from a 22.5 nm thick film on quartz glass. Therefore, we fitted ellipsometric data for five different angles ranging from 50° to 70° in increments of 5° in the spectral range from 220 nm to 940 nm and transmission and reflection data in the spectral range from 260 to 2400 nm. Both graphs, including the fits, are presented in Fig. 6.15. We applied six Tauc-Lorentz oscillators to mimic the numerous optical transitions above the band gap since the dielectric function of C_{60} is quite complex. In order to decrease the number of fitting parameters, all oscillators had the band gap E_0. This method gave a fair description of the spectra produced for our relatively thin film, and we consider it sufficient for our objectives.

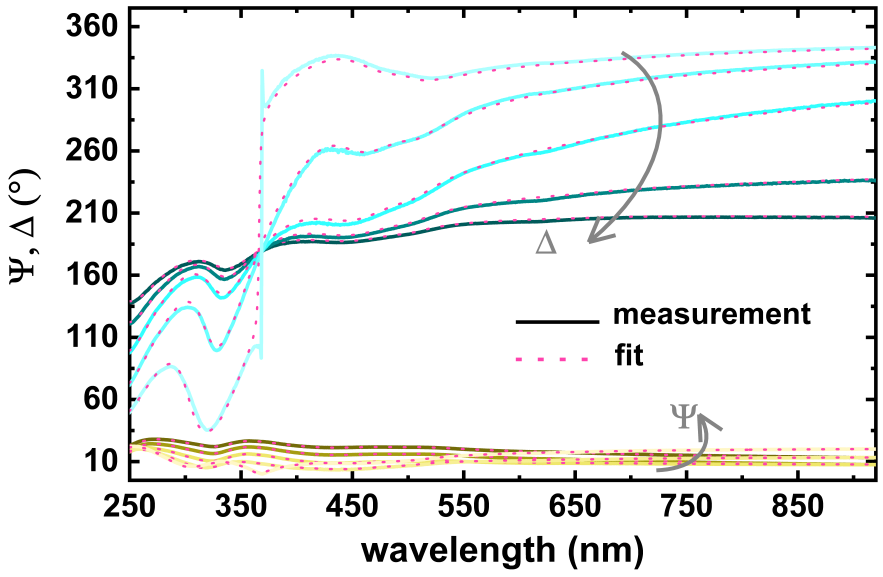

(a)

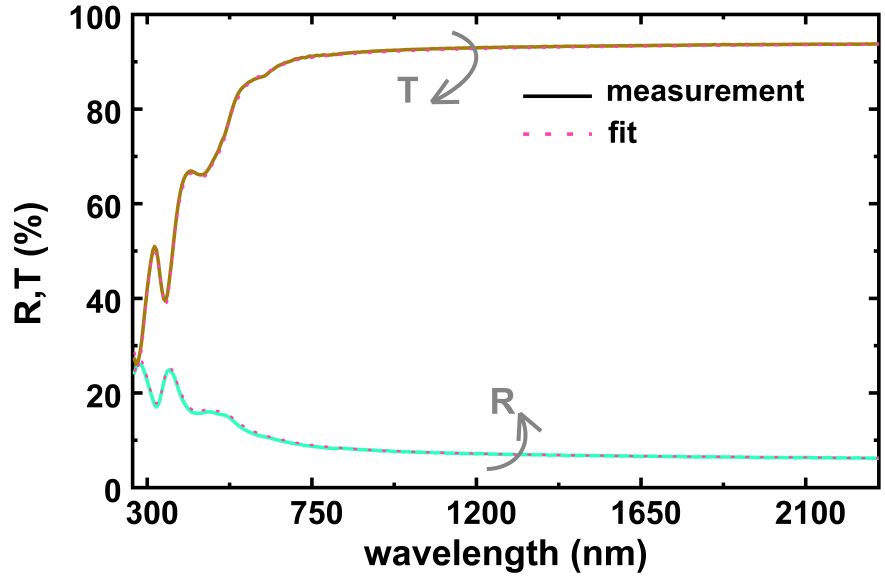

(b)

Figure 6.15: Graphs showing measured data (solid lines) and respected fits (dashed red lines) for 23 nm C_{60} on quartz glass from (a) ellipsometry measurements, where the colors from dark to light represent the increasing angle of the measurement for five different angles ranging from 50° to 70° with a 5° increment, and (b) spectrophotometry measurements, where brown represents the transmission and cyan the reflection data.

The n,k data used for optical simulations resulting from the abovementioned fits are presented in Fig. 6.16.

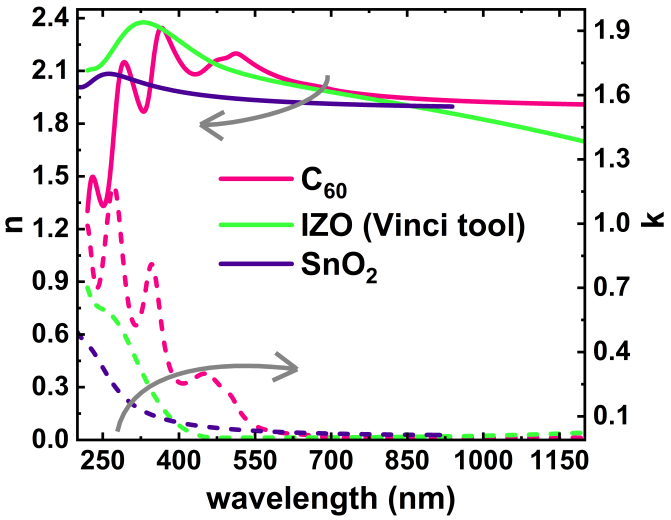

Figure 6.16: The n,k-data for C_{60} (orange), IZO (cyan) and SnO_2 (purple) measured by ellipsometry and spectrophotometry and fitted to a Drude-Tauc-Lorentz model for this work.

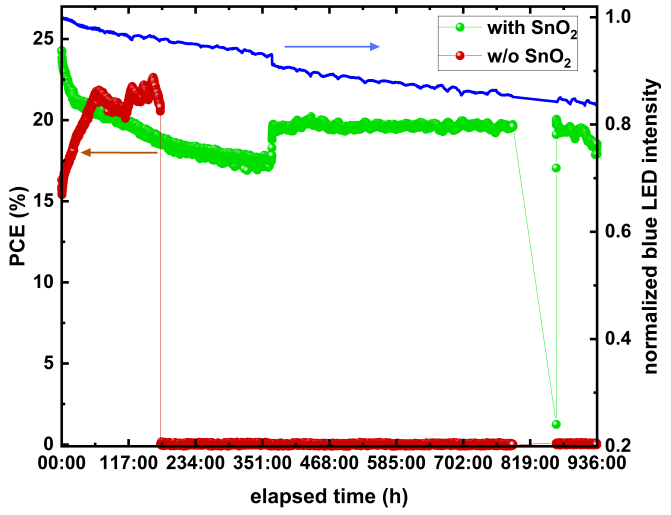

Figure 6.17: Blue LED light intensity and PCE of both tandem devices for the long-term stability analysis time at 0-935 h.

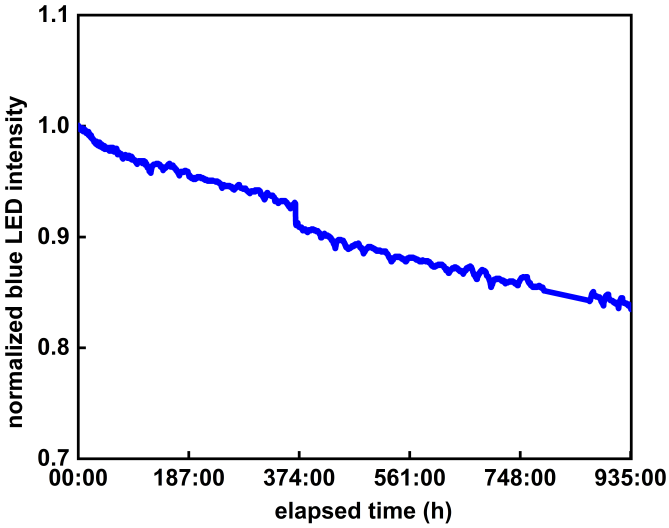

Figure 6.18: Blue LED light intensity over long-term stability analysis time at 0-935 h.

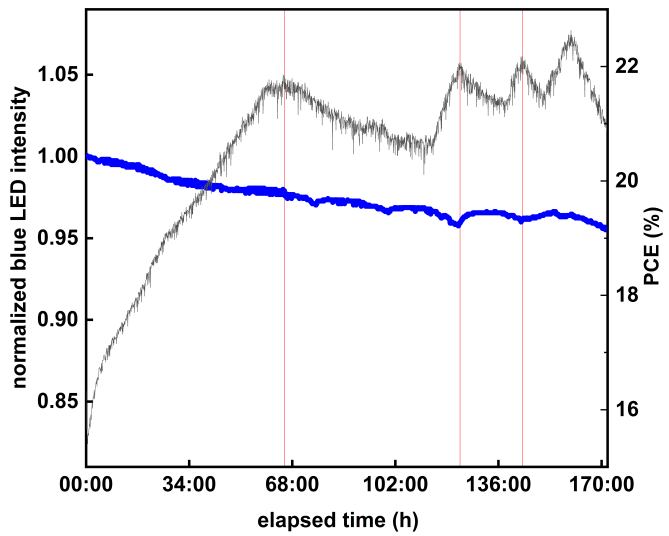

Figure 6.19: Blue LED light intensity and the long-term stability analysis of PEIE interlayer-based tandem PCE for a time of 0-172 h. The comparison shows some correlations between LED light intensity fringes and fringes in the PCE.

Bibliography

[1] *Daten zur Energiepreisentwicklung - Lange Reihen bis Juli 2022*. 2022. URL: https://www.destatis.de/DE/Themen/Wirtschaft/Preise/Publikationen/Energiepreise/energiepreisentwicklung-pdf-5619001.html (visited on 09/02/2022).

[2] *Energieverbrauch nach Energieträgern und Sektoren*. 2022. URL: https://www.umweltbundesamt.de/daten/energie/energieverbrauch-nach-energietraegern-sektoren (visited on 08/15/2022).

[3] *CSEM, EPFL achieve 31.25% efficiency for tandem perovskite-silicon solar cell*. 2022. URL: https://www.pv-magazine.com/2022/07/07/csem-epfl-achieve-31-25-efficiency-for-tandem-perovskite-silicon-solar-cell/ (visited on 08/15/2022).

[4] *NREL Solar Spectra, 2022*. 2022. URL: https://www.nrel.gov/grid/solar-resource/spectra-am1.5.html (visited on 08/08/2022).

[5] M. H. Futscher and B. Ehrler. "Efficiency Limit of Perovskite/Si Tandem Solar Cells". In: *ACS Energy Letters* 1.4 (2016), pp. 863–868. DOI: 10.1021/acsenergylett.6b00405.

[6] N. F. Mott. "Metal Insulator Transitions". In: *Physics and Chemistry of Electrons and Ions in Condensed Matter* (1984), pp. 287–296. DOI: 10.1007/978-94-009-6440-2_28.

[7] P. Würfel. *Physics of Solar Cells*. Wiley-VCH Verlag GmbH & Co, Weinheim, 2005.

[8] I. Hamberg and C. G. Granqvist. "Evaporated Sn-doped In2O3 films: Basic optical properties and applications to energy-efficient windows". In: *Journal of Applied Physics* 123 (11 June 1986), R123. DOI: 10.1063/1.337534.

[9] D. S. Ginley, H. Hosono, and D. C. Paine. *Handbook of Transparent Conductors*. 2010, p. 547.

[10] R. Martins et al. "Transport in high mobility amorphous wide band gap indium zinc oxide films". In: *Physica Status Solidi (A) Applications and Materials Science* 202 (9 2005), pp. 95–97. DOI: 10.1002/pssa.200521020.

[11] A. J. Leenheer et al. "General mobility and carrier concentration relationship in transparent amorphous indium zinc oxide films". In: *Physical Review B - Condensed Matter and Materials Physics* 77 (11 Mar. 2008), p. 115215. DOI: 10.1103/PHYSREVB.77.115215/FIGURES/5/MEDIUM.

[12] K. Ellmer and R. Mientus. "Carrier transport in polycrystalline transparent conductive oxides: A comparative study of zinc oxide and indium oxide". In: *Thin Solid Films* 516 (14 May 2008), pp. 4620–4627. DOI: 10.1016/J.TSF.2007.05.084.

[13] S. Calnan and A. N. Tiwari. "High mobility transparent conducting oxides for thin film solar cells". In: *Thin Solid Films* 518 (7 2010), pp. 1839–1849. DOI: 10.1016/j.tsf.2009.09.044.

[14] E. Burstein. "Anomalous Optical Absorption Limit in InSb". In: *Physical Review* 93 (3 Feb. 1954), p. 632. DOI: 10.1103/PhysRev.93.632.

[15] T. S. Moss. "The Interpretation of the Properties of Indium Antimonide". In: *Proceedings of the Physical Society. Section B* 67 (10 Oct. 1954), p. 775. DOI: 10.1088/0370-1301/67/10/306.

[16] M. Morales-Masis et al. "Low-Temperature High-Mobility Amorphous IZO for Silicon Heterojunction Solar Cells". In: *IEEE Journal of Photovoltaics* 5 (5 Sept. 2015), pp. 1340–1347. DOI: 10.1109/JPHOTOV.2015.2450993.

[17] M. Schultes et al. "Sputtered Transparent Electrodes (IO:H and IZO) with Low Parasitic Near-Infrared Absorption for Perovskite-Cu(In,Ga)Se2 Tandem Solar Cells". In: *ACS Applied Energy Materials* 2 (11 Nov. 2019), pp. 7823–7831. DOI: 10.1021/ACSAEM.9B01224/SUPPL_FILE/AE9B01224_SI_001.PDF.

[18] P. Barquinha et al. "Effect of annealing temperature on the properties of IZO films and IZO based transparent TFTs". In: *Thin Solid Films* 515 (24 SPEC. ISS. 2007), pp. 8450–8454. DOI: 10.1016/j.tsf.2007.03.176.

[19] E. Fortunato et al. "High mobility amorphous/nanocrystalline indium zinc oxide deposited at room temperature". In: *Thin Solid Films* 502 (1-2 Apr. 2006), pp. 104–107. DOI: 10.1016/J.TSF.2005.07.311.

[20] N. Ito et al. "Electrical and optical properties of amorphous indium zinc oxide films". In: *Thin Solid Films* 496 (1 Feb. 2006), pp. 99–103. DOI: 10.1016/J.TSF.2005.08.257.

[21] Y. S. Rim, S. M. Kim, and K. H. Kim. "Properties of Indium-Zinc-Oxide Thin Films Prepared by Facing Targets Sputtering at Room Temperature". In: *Journal of the Korean Physical Society* 54 (3 Mar. 2009), pp. 1267–1272. DOI: 10.3938/JKPS.54.1267.

[22] J. Jia, N. Oka, and Y. Shigesato. "Direct observation of the band gap shrinkage in amorphous In2O3–ZnO thin films". In: *Journal of Applied Physics* 113 (16 Apr. 2013), p. 163702. DOI: 10.1063/1.4802441.

[23] A. Walsh et al. "Nature of the band gap of In2O3 revealed by first-principles calculations and X-ray spectroscopy". In: *Physical Review Letters* 100 (16 Apr. 2008), p. 167402. DOI: 10.1103/PHYSREVLETT.100.167402/FIGURES/3/MEDIUM.

[24] A. Walsh, J. L. D. Silva, and S. H. Wei. "Multi-component transparent conducting oxides: Progress in materials modelling". In: *Journal of Physics Condensed Matter* 23 (33 2011). DOI: 10.1088/0953-8984/23/33/334210.

[25] S. Braun, W. R. Salaneck, and M. Fahlman. "Energy-level alignment at organic/metal and organic/organic interfaces". In: *Advanced Materials* 21.14-15 (2009), pp. 1450–1472. DOI: 10.1002/adma.200802893.

[26] J. Wagner et al. "Identification of different origins for s-shaped current voltage characteristics in planar heterojunction organic solar cells". In: *Journal of Applied Physics* 111 (5 Mar. 2012), p. 054509. DOI: 10.1063/1.3692050.

[27] Y. Zhou et al. "Direct correlation between work function of indium-tin-oxide electrodes and solar cell performance influenced by ultraviolet irradiation and air exposure". In: *Physical Chemistry Chemical Physics* 14 (34 Aug. 2012), pp. 12014–12021. DOI: 10.1039/C2CP42448G.

[28] K. A. Bush et al. "Thermal and Environmental Stability of Semi-Transparent Perovskite Solar Cells for Tandems Enabled by a Solution-Processed Nanoparticle Buffer Layer and Sputtered ITO Electrode". In: *Advanced Materials* 28 (20 2016), pp. 3937–3943. DOI: 10.1002/adma.201505279.

[29] O. J. Sandberg et al. "On the Question of the Need for a Built-In Potential in Perovskite Solar Cells". In: *Advanced Materials Interfaces* 7.10 (2020), p. 2000041. DOI: 10.1002/admi.202000041.

[30] M. Stolterfoht et al. "The impact of energy alignment and interfacial recombination on the internal and external open-circuit voltage of perovskite solar cells". In: *Energy & Environmental Science* 12.9 (2019), pp. 2778–2788. DOI: 10.1039/C9EE02020A.

[31] J. W. Kang et al. "High-performance flexible organic light-emitting diodes using amorphous indium zinc oxide anode". In: *Electrochemical and Solid-State Letters* 10 (6 2007), pp. 75–78. DOI: 10.1149/1.2720635.

[32] H. Cheun et al. "Inverted polymer solar cells with amorphous indium zinc oxide as the electron-collecting electrode". In: *Optics Express, Vol. 18, Issue S4, pp. A506-A512* 18 (104 Nov. 2010), A506–A512. DOI: 10.1364/OE.18.00A506.

[33] J. A. Jeong et al. "Electrical, optical, and structural properties of ITO co-sputtered IZO films by dual target magnetron sputtering". In: *Journal of Electroceramics* 23 (2-4 Oct. 2009), pp. 361–366. DOI: 10.1007/S10832-008-9468-4/FIGURES/9.

[34] H. J. Kim et al. "Work function and interface control of amorphous IZO electrodes by MoO3 layer grading for organic solar cells". In: *Solar Energy Materials and Solar Cells* 141 (Oct. 2015), pp. 194–202. DOI: 10.1016/J.SOLMAT.2015.05.036.

[35] M. Liu et al. "Carrier Density-Tunable Work Function Buffer at the Channel/Metallization Interface for Amorphous Oxide Thin-Film Transistors". In: *ACS Applied Electronic Materials* 3 (6 June 2021), pp. 2703–2711. DOI: 10.1021/ACSAELM.1C00284/SUPPL_FILE/EL1C00284_SI_001.PDF.

[36] G. H. Wang et al. "Transparent conductive Hf-doped In2O3 thin films by RF sputtering technique at low temperature annealing". In: *Applied Surface Science* 399 (Mar. 2017), pp. 716–720. DOI: 10.1016/J.APSUSC.2016.11.239.

[37] M. Jošt et al. "Monolithic Perovskite Tandem Solar Cells: A Review of the Present Status and Advanced Characterization Methods Toward 30% Efficiency". In: *Advanced Energy Materials* 10.26 (2020), p. 1904102. DOI: 10.1002/aenm.201904102.

[38] C. Battaglia, A. Cuevas, and S. D. Wolf. "High-efficiency crystalline silicon solar cells:status and perspectives". In: *Energy & Environmental Science* (2016), pp. 1552–1576. DOI: 10.1039/c5ee03380b.

[39] H. Scherg-Kurmes et al. "Optimization of the post-deposition annealing process of high-mobility In2O3:H for photovoltaic applications". In: *Thin Solid Films* 599 (Jan. 2016), pp. 78–83. DOI: 10.1016/J.TSF.2015.12.054.

[40] E. Aydin et al. "Zr-Doped Indium Oxide (IZRO) Transparent Electrodes for Perovskite-Based Tandem Solar Cells". In: *Advanced Functional Materials* 29 (25 June 2019), p. 1901741. DOI: 10.1002/ADFM.201901741.

[41] C. Han et al. "High-Mobility Hydrogenated Fluorine-Doped Indium Oxide Film for Passivating Contacts c-Si Solar Cells". In: *ACS Applied Materials and Interfaces* 11 (49 Dec. 2019), pp. 45586–45595. DOI: 10.1021/ACSAMI.9B14709/ASSET/IMAGES/LARGE/AM9B14709_0003.JPEG.

[42] F. Meng et al. "High mobility transparent conductive W-doped In2O3 thin films prepared at low substrate temperature and its application to solar cells". In: *Solar Energy Materials and Solar Cells* 122 (Mar. 2014), pp. 70–74. DOI: 10.1016/J.SOLMAT.2013.11.030.

[43] Y. Smirnov et al. "Scalable Pulsed Laser Deposition of Transparent Rear Electrode for Perovskite Solar Cells". In: *Advanced Materials Technologies* 6 (2 Feb. 2021), p. 2000856. DOI: 10.1002/ADMT.202000856.

[44] T. Koida, Y. Ueno, and H. Shibata. "In2O3-Based Transparent Conducting Oxide Films with High Electron Mobility Fabricated at Low Process Temperatures". In: *physica status solidi (a)* 215 (7 Apr. 2018), p. 1700506. DOI: 10.1002/PSSA.201700506.

[45] Y. Liu et al. "High mobility Ti, Zr and Ga-codoping In2O3 transparent conductive oxide films prepared at low temperatures". In: *Journal of Materials Science: Materials in Electronics* 32 (3 Feb. 2021), pp. 3201–3210. DOI: 10.1007/S10854-020-05068-X/TABLES/3.

[46] K. Wasa et al. *Handbook of Sputter Deposition Technology: Fundamentals and Applications for Functional Thin Films, Nano-Materials and MEMS: Second Edition.* 2012.

[47] J. A. Thornton. "High Rate Thick Film Growth". In: *http://dx.doi.org/10.1146/annurev.ms.07.080177.001323* 7 (Nov. 1977), pp. 239–260. DOI: 10.1146/ANNUREV.MS.07.080177.001323.

[48] B. Demaurex et al. "Damage at hydrogenated amorphous/crystalline silicon interfaces by indium tin oxide overlayer sputtering". In: *Appl. Phys. Lett.* 101.17 (2012), pp. 1–5. DOI: 10.1063/1.4764529.

[49] K. Tominaga, M. Chong, and Y. Shintani. "Energetic particles in the sputtering of an indium–tin oxide target". In: *J. Vac. Sci. Technol. A Vacuum, Surfaces, Film.* 12.4 (1994), pp. 1435–1438. DOI: 10.1116/1.579333.

[50] J. Jia, Y. Torigoshi, and Y. Shigesato. "In situ analyses on negative ions in the indium-gallium-zinc oxide sputtering process". In: *Applied Physics Letters* 103 (1 July 2013), p. 013501. DOI: 10.1063/1.4812668.

[51] K. Tominaga et al. "Mean Free Path of Energetic Oxygen Atoms in the Sputtering of ZnO". In: *Japanese Journal of Applied Physics* 23 (7R July 1984), pp. 936–937. DOI: 10.1143/JJAP.23.936/XML.

[52] W. Dewald et al. "Optimization of process parameters for sputtering of ceramic ZnO:Al2O3 targets for a-Si:H/μc-Si:H solar cells". In: *Thin Solid Films* 518.4 (2009), pp. 1085–1090. DOI: 10.1016/j.tsf.2009.04.068.

[53] F. Fu et al. "Low-temperature-processed efficient semi-transparent planar perovskite solar cells for bifacial and tandem applications". In: *Nature Communications* 6 (2015), pp. 1–9. DOI: 10.1038/ncomms9932.

[54] J. A. Jeong and H. K. Kim. "Al2O3/Ag/Al2O3 multilayer thin film passivation prepared by plasma damage-free linear facing target sputtering for organic light emitting diodes". In: *Thin Solid Films* 547 (Nov. 2013), pp. 63–67. DOI: 10.1016/J.TSF.2013.05.003.

[55] H. K. Kim, K. S. Lee, and J. H. Kwon. "Transparent indium zinc oxide top cathode prepared by plasma damage-free sputtering for top-emitting organic light-emitting diodes". In: *Applied Physics Letters* 88 (1 Jan. 2006), p. 012103. DOI: 10.1063/1.2159577.

[56] T. Jung, T. Kälber, and V. V. Heide. "Gas flow sputtering of oxide coatings: practical aspects of the process". In: *Surface and Coatings Technology* 86-87 (PART 1 Dec. 1996), pp. 218–224. DOI: 10.1016/S0257-8972(96)03043-5.

[57] S. Muhl and A. Pérez. "The use of hollow cathodes in deposition processes: A critical review". In: *Thin Solid Films* 579 (Mar. 2015), pp. 174–198. DOI: 10.1016/J.TSF.2015.02.066.

[58] M Höfer et al. "New DC Sputter Sources for the Large Scale Deposition of Oxide Films". In: (2000), pp. 287–292.

[59] J. Mahrholz et al. "Deposition of Amorphous Silicon Films by Gas Flow Sputtering (GFS)". In: (September 2009), p. 38108.

[60] A.-E. Becquerel. "On Electron Effects under the Influence of Solar Radiation". In: *Comptes Rendus de l'Academie Sciences Paris* 9 (1839), pp. 561–567.

[61] J. Shi et al. "From Ultrafast to Ultraslow: Charge-Carrier Dynamics of Perovskite Solar Cells". In: *Joule* 2 (5 May 2018), pp. 879–901. DOI: 10.1016/J.JOULE.2018.04.010.

[62] G. Xing et al. "Long-range balanced electron-and hole-transport lengths in organic-inorganic CH3NH3PbI3". In: *Science* 342 (6156 Oct. 2013), pp. 344–347. DOI: 10.1126/SCIENCE.1243167/SUPPL_FILE/XING.SM.PDF.

[63] P. Würfel and U. Würfel. *Physics of solar cells: from basic principles to advanced concepts*. John Wiley & Sons, 2016.

[64] C. Chen et al. "Effect of BCP buffer layer on eliminating charge accumulation for high performance of inverted perovskite solar cells". In: *RSC Advances* 7 (57 July 2017), pp. 35819–35826. DOI: 10.1039/C7RA06365B.

[65] A. Al-Ashouri et al. "Conformal monolayer contacts with lossless interfaces for perovskite single junction and monolithic tandem solar cells". In: *Energy & Environmental Science* 12.11 (2019), pp. 3356–3369. DOI: 10.1039/C9EE02268F.

[66] M. Stolterfoht et al. "Visualization and suppression of interfacial recombination for high-efficiency large-area pin perovskite solar cells". In: *Nature Energy* 3.10 (2018), pp. 847–854. DOI: 10.1038/s41560-018-0219-8.

[67] H. Zhou et al. "Interface engineering of highly efficient perovskite solar cells". In: *Science* 345.6196 (2014), pp. 542–546. DOI: 10.1126/science.1254050.

[68] J. H. Kim et al. "Transparent Sn-doped In2O3 electrodes with a nanoporous surface for enhancing the performance of perovskite solar cells". In: *Journal of Power Sources* 418 (2019), pp. 152–161. DOI: 10.1016/j.jpowsour.2019.02.018.

[69] M. Stolterfoht et al. "How To Quantify the Efficiency Potential of Neat Perovskite Films: Perovskite Semiconductors with an Implied Efficiency Exceeding 28%". In: *Advanced Materials* 32.17 (2020), p. 2000080. DOI: 10.1002/adma.202000080.

[70] J. Diekmann et al. "Pathways toWards 30% Efficient Single-Junction Perovskite Solar Cells and the Role of Mobile Ions". In: *Solar RRL* (2021). DOI: 10.1002/solr.202100219.

[71] W. Shockley and W. T. Read. "Statistics of the Recombinations of Holes and Electrons". In: *Physical Review* 87.5 (1952), pp. 835–842. DOI: 10.1103/PhysRev.87.835.

[72] W. Tress. "Perovskite Solar Cells on the Way to Their Radiative Efficiency Limit - Insights Into a Success Story of High Open-Circuit Voltage and Low Recombination". In: *Advanced Energy Materials* 7.14 (2017), p. 1602358. DOI: 10.1002/aenm.201602358.

[73] J. Bisquert. *The Physics of Solar Cells: Perovskites, Organics, and Photovoltaic Fundamentals*. CRC Press, Taylor & Francis Group, 2018.

[74] S. Rühle. "Tabulated values of the Shockley–Queisser limit for single junction solar cells". In: *Solar Energy* 130 (June 2016), pp. 139–147. DOI: 10.1016/J.SOLENER.2016.02.015.

[75] W. Shockley and H. J. Queisser. "Detailed Balance Limit of Efficiency of p-n Junction Solar Cells". In: *Journal of Applied Physics* 32.3 (1961), pp. 510–519. DOI: 10.1063/1.1736034.

[76] C.-G. Wu et al. "High efficiency stable inverted perovskite solar cells without current hysteresis". In: *Energy Environ. Sci.* 8.9 (2015), pp. 2725–2733. DOI: 10.1039/C5EE00645G.

[77] H. Kanda et al. "Analysis of Sputtering Damage on I-V Curves for Perovskite Solar Cells and Simulation with Reversed Diode Model". In: *Journal of Physical Chemistry C* 120 (50 Dec. 2016), pp. 28441–28447. DOI: 10.1021/ACS.JPCC.6B09219/ASSET/IMAGES/MEDIUM/JP-2016-09219H_0009.GIF.

[78] T. Jesper Jacobsson et al. "Exploration of the compositional space for mixed lead halogen perovskites for high efficiency solar cells". In: *Energy and Environmental Science* 9.5 (2016), pp. 1706–1724. DOI: 10.1039/c6ee00030d.

[79] K. A. Bush et al. "Compositional Engineering for Efficient Wide Band Gap Perovskites with Improved Stability to Photoinduced Phase Segregation". In: *ACS Energy Letters* 3.2 (2018), pp. 428–435. DOI: 10.1021/acsenergylett.7b01255.

[80] M. A. Green, A. Ho-Baillie, and H. J. Snaith. "The emergence of perovskite solar cells". In: *Nature Photonics* 8.7 (2014), pp. 506–514. DOI: 10.1038/nphoton.2014.134.

[81] D. P. McMeekin et al. "A mixed-cation lead mixed-halide perovskite absorber for tandem solar cells". In: *Science* 351.6269 (2016), pp. 151–155. DOI: 10.1126/science.aad5845.

[82] G. E. Eperon et al. "Perovskite-perovskite tandem photovoltaics with optimized band gaps". In: *Science* 354.6314 (2016), pp. 861–865. DOI: 10.1126/science.aaf9717.

[83] A. Magomedov et al. "Cover picture: Hole Transporting Monolayers: Self-Assembled Hole Transporting Monolayer for Highly Efficient Perovskite Solar Cells (Adv. Energy Mater. 32/2018)". In: *Advanced Energy Materials* 8.32 (2018), p. 1870139. DOI: 10.1002/aenm.201870139.

[84] T. Kirchartz et al. "Classification of solar cells according to mechanisms of charge separation and charge collection". In: *Physical Chemistry Chemical Physics* 17 (6 Jan. 2015), pp. 4007–4014. DOI: 10.1039/C4CP05174B.

[85] Y. Liu et al. "Approaching the Schottky–Mott limit in van der Waals metal–semiconductor junctions". In: *Nature 2018 557:7707* 557 (7707 May 2018), pp. 696–700. DOI: 10.1038/s41586-018-0129-8.

[86] W. Schottky. "Zur Halbleitertheorie der Sperrschicht- und Spitzengleichrichter". In: *Zeitschrift für Physik 1939 113:5* 113 (5 May 1939), pp. 367–414. DOI: 10.1007/BF01340116.

[87] N. F. Mott and F. R. S. H. H. W. Physical. "The theory of crystal rectifiers". In: *Proceedings of the Royal Society of London. Series A. Mathematical and Physical Sciences* 171 (944 May 1939), pp. 27–38. DOI: 10.1098/RSPA.1939.0051.

[88] J. Bardeen. "Surface States and Rectification at a Metal Semi-Conductor Contact". In: *Physical Review* 71 (10 May 1947), p. 717. DOI: 10.1103/PhysRev.71.717.

[89] A. M. Cowley and S. M. Sze. "Surface States and Barrier Height of Metal-Semiconductor Systems". In: *Journal of Applied Physics* 36 (10 July 1965), p. 3212. DOI: 10.1063/1.1702952.

[90] R. T. Tung. "The physics and chemistry of the Schottky barrier height". In: *Applied Physics Reviews* 1 (1 Jan. 2014), p. 011304. DOI: 10.1063/1.4858400.

[91] M. L. Cohen. "Schottky and Bardeen limits for Schottky barriers". In: *Journal of Vacuum Science and Technology* 16 (5 June 1998), p. 1135. DOI: 10.1116/1.570176.

[92] E. Rhoderick. "Metal-semiconductor contacts". In: *IEE Proceedings I Solid State and Electron Devices* 129 (1 1982), p. 1. DOI: 10.1049/IP-I-1.1982.000110.1049/IP-I-1.1982.0001.

[93] B. C. J. Brabec et al. "Origin of the Open Circuit Voltage of Plastic Solar Cells". In: (5 2001), pp. 374–380.

[94] P. Löper et al. "Organic–inorganic halide perovskite/crystalline silicon four-terminal tandem solar cells". In: *Phys. Chem. Chem. Phys.* 17.3 (2014), pp. 1619–1629. DOI: 10.1039/C4CP03788J.

[95] C. D. Bailie et al. "Semi-transparent perovskite solar cells for tandems with silicon and CIGS". In: *Energy and Environmental Science* 8 (3 2015), pp. 956–963. DOI: 10.1039/c4ee03322a.

[96] J. Werner et al. "Sputtered rear electrode with broadband transparency for perovskite solar cells". In: *Solar Energy Materials and Solar Cells* 141 (2015), pp. 407–413. DOI: 10.1016/j.solmat.2015.06.024.

[97] D. P. McMeekin et al. "A mixed-cation lead mixed-halide perovskite absorber for tandem solar cells". In: *Science* 351.6269 (2016), pp. 151–155. DOI: 10.1126/science.aad5845.

[98] F. Fu et al. "High-efficiency inverted semi-transparent planar perovskite solar cells in substrate configuration". In: *Nature Energy* 2.1 (2017), pp. 1–12. DOI: 10.1038/nenergy.2016.190.

[99] J. P. Mailoa et al. "A 2-terminal perovskite/silicon multijunction solar cell enabled by a silicon tunnel junction". In: *Applied Physics Letters* 106.12 (2015), pp. 30–33. DOI: 10.1063/1.4914179.

[100] S. Albrecht et al. "Monolithic perovskite/silicon-heterojunction tandem solar cells processed at low temperature". In: *Energy Environ. Sci.* 9.1 (2016), pp. 81–88. DOI: 10.1039/C5EE02965A.

[101] J. Werner et al. "Efficient Monolithic Perovskite/Silicon Tandem Solar Cell with Cell Area >1 cm2". In: *Journal of Physical Chemistry Letters* 7.1 (2016), pp. 161–166. DOI: 10.1021/acs.jpclett.5b02686.

[102] K. A. Bush et al. "23.6%-efficient monolithic perovskite/silicon tandem solar cells with improved stability". In: *Nature Energy* 2.4 (2017), p. 17009. DOI: 10.1038/nenergy.2017.9.

[103] F. Sahli et al. "Fully textured monolithic perovskite/silicon tandem solar cells with 25.2% power conversion efficiency". In: *Nature Materials* 17.9 (2018), pp. 820–826. DOI: 10.1038/s41563-018-0115-4.

[104] A. Al-Ashouri et al. "Monolithic perovskite/silicon tandem solar cell with >29% efficiency by enhanced hole extraction". In: *Science* 370.6522 (2020), pp. 1300–1309. DOI: 10.1126/science.abd4016.

[105] P. Tockhorn et al. "Nanostructures Enable Certified Efficiency of 29.80% in Perovskite/Silicon Tandem Solar Cells". In: (May 2022). DOI: 10.29363/NANOGE.HOPV.2022.101.

[106] M. Jošt et al. "Textured interfaces in monolithic perovskite/silicon tandem solar cells: advanced light management for improved efficiency and energy yield". In: *Energy & Environmental Science* 11.12 (2018), pp. 3511–3523. DOI: 10.1039/C8EE02469C.

[107] A. Cruz et al. "Optoelectrical analysis of TCO+Silicon oxide double layers at the front and rear side of silicon heterojunction solar cells". In: *Solar Energy Materials and Solar Cells* 236 (Mar. 2022), p. 111493. DOI: 10.1016/J.SOLMAT.2021.111493.

[108] L. J. van der Pauw. "A METHOD OF MEASURING SPECIFIC RESISTIVITY AND HALL EFFECT OF DISCS OF ARBITRARY SHAPE". In: *Semiconductor Devices: Pioneering Papers* (Mar. 1991), pp. 174–182. DOI: 10.1142/9789814503464_0017.

[109] A. Pflug et al. "Optical characterization of aluminum-doped zinc oxide films by advanced dispersion theories". In: *Thin Solid Films* 455-456 (May 2004), pp. 201–206. DOI: 10.1016/J.TSF.2004.01.006.

[110] D. Abou-Ras et al. "Electron Microscopy on Thin Films for Solar Cells". In: *Advanced Characterization Techniques for Thin Film Solar Cells*. John Wiley & Sons, Ltd, 2011. Chap. 12, pp. 299–345. DOI: https://doi.org/10.1002/9783527636280.ch12.

[111] M. H. Jung and H. S. Choi. "Characterization of octadecyltrichlorosilane self-assembled monolayers on silicon (100) surface". In: *Korean Journal of Chemical Engineering 2009 26:6* 26 (6 Feb. 2010), pp. 1778–1784. DOI: 10.1007/S11814-009-0249-9.

[112] M. Schwartzkopf et al. "From atoms to layers : in situ gold cluster growth kinetics during sputter deposition †". In: (2013), pp. 5053–5062. DOI: 10.1039/c3nr34216f.

[113] G. Benecke et al. "A customizable software for fast reduction and analysis of large X-ray scattering data sets: applications of the new DPDAK package to small-angle X-ray scattering and grazing-incidence small-angle X-ray scattering". In: *urn:issn:1600-5767* 47 (5 Sept. 2014), pp. 1797–1803. DOI: 10.1107/S1600576714019773.

[114] M. Schwartzkopf et al. "Real-Time Monitoring of Morphology and Optical Properties during Sputter Deposition for Tailoring Metal-Polymer Interfaces". In: *ACS Applied Materials and Interfaces* 7 (24 June 2015), pp. 13547–13556. DOI: 10.1021/ACSAMI.5B02901/SUPPL_FILE/AM5B02901_SI_002.PDF.

[115] M. Schwartzkopf and S. V. Roth. "Investigating Polymer–Metal Interfaces by Grazing Incidence Small-Angle X-Ray Scattering from Gradients to Real-Time Studies". In: *Nanomaterials 2016, Vol. 6, Page 239* 6 (12 Dec. 2016), p. 239. DOI: 10.3390/NANO6120239.

[116] M. Schwartzkopf et al. "Role of Sputter Deposition Rate in Tailoring Nanogranular Gold Structures on Polymer Surfaces". In: *ACS Applied Materials and Interfaces* 9 (6 Feb. 2017), pp. 5629–5637. DOI: 10.1021/ACSAMI.6B15172/SUPPL_FILE/AM6B15172_SI_006.AVI.

[117] E. Köhnen et al. "Highly efficient monolithic perovskite silicon tandem solar cells: analyzing the influence of current mismatch on device performance". In: *Sustainable Energy & Fuels* 3.8 (2019), pp. 1995–2005. DOI: 10.1039/C9SE00120D.

[118] J. Shi et al. "Opto-electro-modulated transient photovoltage and photocurrent system for investigation of charge transport and recombination in solar cells". In: *Review of Scientific Instruments* 87 (12 Dec. 2016), p. 123107. DOI: 10.1063/1.4972104.

[119] M. Stephen et al. "Charge transport and its characterization using photo-CELIV in bulk heterojunction solar cells". In: August (2016). DOI: 10.1002/pi.5274.

[120] C. M. Wolff et al. "Orders of Recombination in Complete Perovskite Solar Cells – Linking Time-Resolved and Steady-State Measurements". In: *Advanced Energy Materials* 11 (45 Dec. 2021). DOI: 10.1002/AENM.202101823.

[121] D. Kiermasch et al. "Revisiting lifetimes from transient electrical characterization of thin film solar cells; a capacitive concern evaluated for silicon, organic and perovskite devices". In: *Energy & Environmental Science* 11 (3 Mar. 2018), pp. 629–640. DOI: 10.1039/C7EE03155F.

[122] R. Hidayat et al. "Revealing the charge carrier kinetics in perovskite solar cells affected by mesoscopic structures and defect states from simple transient photovoltage measurements". In: *Scientific Reports 2020 10:1* 10 (1 Nov. 2020), pp. 1–13. DOI: 10.1038/s41598-020-74603-x.

[123] E. Knapp and B. Ruhstaller. "Numerical analysis of steady-state and transient charge transport in organic semiconductor devices". In: *10th International Conference on Numerical Simulation of Optoelectronic Devices, NUSOD 2010* (2010), pp. 35–36. DOI: 10.1109/NUSOD.2010.5595680.

[124] B. Hailegnaw, N. S. Sariciftci, and M. C. Scharber. "Impedance Spectroscopy of Perovskite Solar Cells: Studying the Dynamics of Charge Carriers Before and After Continuous Operation". In: *physica status solidi (a)* 217 (22 Nov. 2020), p. 2000291. DOI: 10.1002/PSSA.202000291.

[125] M. Burgelman, P. Nollet, and S. Degrave. "Modelling polycrystalline semiconductor solar cells". In: *Thin Solid Films* 361-362 (Feb. 2000), pp. 527–532. DOI: 10.1016/S0040-6090(99)00825-1.

[126] R. Santbergen et al. "GenPro4 Optical Model for Solar Cell Simulation and Its Application to Multijunction Solar Cells". In: *IEEE Journal of Photovoltaics* 7.3 (2017), pp. 919–926. DOI: 10.1109/JPHOTOV.2017.2669640.

[127] J. Werner et al. *Sputtered rear electrode with broadband transparency for perovskite solar cells.* 2015. DOI: 10.1016/j.solmat.2015.06.024.

[128] T. Wahl et al. "Sputtered indium zinc oxide rear electrodes for inverted semi-transparent perovskite solar cells without using a protective buffer layer". In: *Organic Electronics* 54 (Mar. 2018), pp. 48–53. DOI: 10.1016/J.ORGEL.2017.12.020.

[129] E. Aydin et al. "Sputtered transparent electrodes for optoelectronic devices: Induced damage and mitigation strategies". In: *Matter* 4 (11 Nov. 2021), pp. 3549–3584. DOI: 10.1016/J.MATT.2021.09.021.

[130] K. Liu et al. "Reducing sputter induced stress and damage for efficient perovskite/silicon tandem solar cells". In: *Journal of Materials Chemistry A* 10 (3 Jan. 2022), pp. 1343–1349. DOI: 10.1039/D1TA09143C.

[131] K. Ellmer and T. Welzel. "Reactive magnetron sputtering of transparent conductive oxide thin films: Role of energetic particle (ion) bombardment". In: *Journal of Materials Research 2012 27:5* 27 (5 Mar. 2012), pp. 765–779. DOI: 10.1557/JMR.2011.428.

[132] T. Welzel et al. "Ion Energy Distributions in Magnetron Sputtering of Zinc Aluminium Oxide". In: *Plasma Processes and Polymers* 6 (S1 June 2009), S331–S336. DOI: 10.1002/PPAP.200930805.

[133] T. Welzel and K. Ellmer. "Negative oxygen ion formation in reactive magnetron sputtering processes for transparent conductive oxides". In: *Journal of Vacuum Science & Technology A: Vacuum, Surfaces, and Films* 30 (6 Oct. 2012), p. 061306. DOI: 10.1116/1.4762815.

[134] G. Haacke. "New figure of merit for transparent conductors". In: *Journal of Applied Physics* 47 (9 Aug. 2008), p. 4086. DOI: 10.1063/1.323240.

[135] H. H. Li. "Refractive index of alkali halides and its wavelength and temperature derivatives". In: *Journal of Physical and Chemical Reference Data* 5 (2 Oct. 2009), p. 329. DOI: 10.1063/1.555536.

[136] H. Liu. "Growth Kinetics of Thin Film Epitaxy". In: *21st Century Surface Science - a Handbook* (Oct. 2020). DOI: 10.5772/INTECHOPEN.91224.

[137] J. A. Raiford et al. "Enhanced Nucleation of Atomic Layer Deposited Contacts Improves Operational Stability of Perovskite Solar Cells in Air". In: *Advanced Energy Materials* 9 (47 Dec. 2019), p. 1902353. DOI: 10.1002/AENM.201902353.

[138] A. F. Palmstrom et al. "Enabling Flexible All-Perovskite Tandem Solar Cells". In: *Joule* 3 (9 Sept. 2019), pp. 2193–2204. DOI: 10.1016/J.JOULE.2019.05.009.

[139] R. H. Cox and H. Strack. "Ohmic contacts for GaAs devices". In: *Solid-State Electronics* 10 (12 Dec. 1967), pp. 1213–1218. DOI: 10.1016/0038-1101(67)90063-9.

[140] A. Helbig et al. "Quantitative electroluminescence analysis of resistive losses in Cu(In, Ga)Se2 thin-film modules". In: *Solar Energy Materials and Solar Cells* 94 (6 June 2010), pp. 979–984. DOI: 10.1016/J.SOLMAT.2010.01.028.

[141] W. Tress et al. “Imbalanced mobilities causing S-shaped IV curves in planar heterojunction organic solar cells”. In: *Applied Physics Letters* 98 (6 Feb. 2011), p. 063301. DOI: 10.1063/1.3553764.

[142] W. Tress and O. Inganäs. “Simple experimental test to distinguish extraction and injection barriers at the electrodes of (organic) solar cells with S-shaped current–voltage characteristics”. In: *Solar Energy Materials and Solar Cells* 117 (Oct. 2013), pp. 599–603. DOI: 10.1016/J.SOLMAT.2013.07.014.

[143] A. Wagenpfahl et al. “S-shaped current-voltage characteristics of organic solar devices”. In: *Physical Review B - Condensed Matter and Materials Physics* 82 (11 Sept. 2010), p. 115306. DOI: 10.1103/PHYSREVB.82.115306/FIGURES/7/MEDIUM.

[144] D. Kim et al. “Efficient, stable silicon tandem cells enabled by anion-engineered wide-bandgap perovskites”. In: *Science (New York, N.Y.)* 368 (6487 Apr. 2020), pp. 155–160. DOI: 10.1126/SCIENCE.ABA3433.

[145] Y. Zhou et al. “A universal method to produce low-work function electrodes for organic electronics”. In: *Science* 336 (6079 Apr. 2012), pp. 327–332. DOI: 10.1126/SCIENCE.1218829/SUPPL_FILE/ZHOU.SOM.PDF.

[146] J. H. Kim and J. W. Park. “Designing an electron-transport layer for highly efficient, reliable, and solution-processed organic light-emitting diodes”. In: *Journal of Materials Chemistry C* 5 (12 Mar. 2017), pp. 3097–3106. DOI: 10.1039/C7TC00488E.

[147] A. M. Cowley and S. M. Sze. “Surface States and Barrier Height of Metal-Semiconductor Systems”. In: *Journal of Applied Physics* 36 (10 July 2004), p. 3212. DOI: 10.1063/1.1702952.

[148] C. Li et al. “Investigation on the Overshoot of Transient Open-Circuit Voltage in Methylammonium Lead Iodide Perovskite Solar Cells”. In: *Materials 2018, Vol. 11, Page 2407* 11 (12 Nov. 2018), p. 2407. DOI: 10.3390/MA11122407.

[149] Y. Chen et al. “Efficient and balanced charge transport revealed in planar perovskite solar cells”. In: *ACS Applied Materials and Interfaces* 7 (8 Mar. 2015), pp. 4471–4475. DOI: 10.1021/acsami.5b00077.

[150] M. Neukom et al. “Opto-electronic characterization of third-generation solar cells”. In: *Science and Technology of Advanced Materials* 19 (1 Dec. 2018), pp. 291–316. DOI: 10.1080/14686996.2018.1442091.

[151] A. Wang et al. “Vacancy defect modulation in hot-casted NiOx film for efficient inverted planar perovskite solar cells”. In: *Journal of Energy Chemistry* 48 (Sept. 2020), pp. 426–434. DOI: 10.1016/J.JECHEM.2020.02.034.

[152] T. Golubev et al. "Understanding the impact of C60 at the interface of perovskite solar cells via drift-diffusion modeling". In: *AIP Advances* 9 (3 Mar. 2019), p. 035026. DOI: 10.1063/1.5068690.

[153] N. Lakhdar and A. Hima. "Electron transport material effect on performance of perovskite solar cells based on CH3NH3GeI3". In: *Optical Materials* 99 (Jan. 2020), p. 109517. DOI: 10.1016/J.OPTMAT.2019.109517.

[154] A. Tapponnier, I. Biaggio, and P. Günter. "Ultrapure C60 field-effect transistors and the effects of oxygen exposure". In: *Applied Physics Letters* 86 (11 Mar. 2005), p. 112114. DOI: 10.1063/1.1883327.

[155] Y. Tanaka et al. "Oxygen effect on the interfacial electronic structure of C60 film studied by ultraviolet photoelectron spectroscopy". In: *Chemical Physics Letters* 441 (1-3 June 2007), pp. 63–67. DOI: 10.1016/J.CPLETT.2007.04.080.

[156] E. V. Hauff and D. Klotz. "Impedance spectroscopy for perovskite solar cells: characterisation, analysis, and diagnosis". In: *Journal of Materials Chemistry C* 10 (2 Jan. 2022), pp. 742–761. DOI: 10.1039/D1TC04727B.

[157] D. Prochowicz et al. "In the Quest of Low-Frequency Impedance Spectra of Efficient Perovskite Solar Cells". In: *Energy Technology* 9 (7 July 2021). DOI: 10.1002/ENTE.202100229.

[158] I. G. Samatov et al. "Room-temperature rf-magnetron sputter-deposited W-doped indium oxide: decoupling the influence of W dopant and O vacancies on the film properties". In: *Applied Physics A: Materials Science and Processing* 122 (4 Apr. 2016), pp. 1–10. DOI: 10.1007/S00339-016-9983-0/FIGURES/10.

[159] W. Tress et al. "Interpretation and Evolution of Open-Circuit Voltage, Recombination, Ideality Factor and Subgap Defect States during Reversible Light-Soaking and Irreversible Degradation of Perovskite Solar Cells". In: *Energy & Environmental Science* (2017). DOI: 10.1039/C7EE02415K.

[160] S. Schiefer et al. "Applicability of the suns-VOC method on organic solar cells". In: *IEEE Journal of Photovoltaics* 4.1 (2014), pp. 271–277. DOI: 10.1109/JPHOTOV.2013.2288527.

[161] J.-P. Correa-Baena et al. "Identifying and suppressing interfacial recombination to achieve high open-circuit voltage in perovskite solar cells". In: *Energy Environ. Sci.* 10.5 (2017), pp. 1207–1212. DOI: 10.1039/C7EE00421D.

[162] T. D. Anthopoulos et al. "Air-stable ambipolar organic transistors". In: *Applied Physics Letters* 90 (12 Mar. 2007), p. 122105. DOI: 10.1063/1.2715028.

[163] E. M. Speller. "The significance of fullerene electron acceptors in organic solar cell photo-oxidation". In: *http://dx.doi.org/10.1080/02670836.2016.1215840* 33 (8 May 2016), pp. 924–933. DOI: 10.1080/02670836.2016.1215840.

[164] R. Santbergen et al. "Minimizing optical losses in monolithic perovskite/c-Si tandem solar cells with a flat top cell". In: *Optics Express* 24.18 (2016), A1288. DOI: 10.1364/OE.24.0A1288.

[165] E. Köhnen et al. "27.9Cells on Industry Compatible Bottom Cells". In: *Solar RRL* 5 (7 July 2021), p. 2100244. DOI: 10.1002/SOLR.202100244.

[166] A. F. Palmstrom et al. "Interfacial Effects of Tin Oxide Atomic Layer Deposition in Metal Halide Perovskite Photovoltaics". In: *Advanced Energy Materials* 8 (23 Aug. 2018), p. 1800591. DOI: 10.1002/AENM.201800591.

[167] C. C. Boyd et al. "Understanding Degradation Mechanisms and Improving Stability of Perovskite Photovoltaics". In: *Chemical Reviews* 119 (5 Mar. 2019), pp. 3418–3451. DOI: 10.1021/ACS.CHEMREV.8B00336/ASSET/IMAGES/MEDIUM/CR-2018-00336Z_0018.GIF.

[168] L. Hoffmann et al. "Atmospheric pressure plasma enhanced spatial atomic layer deposition of SnOx as conductive gas diffusion barrier". In: *Journal of Vacuum Science & Technology A: Vacuum, Surfaces, and Films* 36 (1 Dec. 2017), 01A112. DOI: 10.1116/1.5006781.

[169] K. O. Brinkmann et al. "Suppressed decomposition of organometal halide perovskites by impermeable electron-extraction layers in inverted solar cells". In: *Nature Communications* 8 (Jan. 2017). DOI: 10.1038/NCOMMS13938.

[170] M. Jošt et al. "Subcell Operation and Long-Term Stability Analysis of Perovskite-Based Tandem Solar Cells Using a Bichromatic Light Emitting Diode Light Source". In: *Solar RRL* 5 (8 Aug. 2021). DOI: 10.1002/SOLR.202100311.

[171] M. V. Khenkin et al. "Consensus statement for stability assessment and reporting for perovskite photovoltaics based on ISOS procedures". In: *Nature Energy 2020 5:1* 5 (1 Jan. 2020), pp. 35–49. DOI: 10.1038/s41560-019-0529-5.

[172] H. Scherg-Kurmes et al. "Improvement of the homogeneity of high mobility In2O3:H films by sputtering through a mesh electrode studied by Monte Carlo simulation and thin film analysis". In: *physica status solidi (a)* 213 (9 Sept. 2016), pp. 2310–2316. DOI: 10.1002/PSSA.201532819.

[173] T. Majumder et al. "Photoelectrochemical and photosensing behaviors of hydrothermally grown ZnO nanorods". In: *Journal of Applied Physics* 116 (3 July 2014), p. 034311. DOI: 10.1063/1.4890978.

[174] F. Ruske et al. "Optical modeling of free electron behavior in highly doped ZnO films". In: *Thin Solid Films* 518 (4 Dec. 2009), pp. 1289–1293. DOI: 10.1016/J.TSF.2009.03.218.

[175] G. E. Jellison and F. A. Modine. “Parameterization of the optical functions of amorphous materials in the interband region”. In: *Applied Physics Letters* 69 (3 June 1998), p. 371. DOI: 10.1063/1.118064.

Chapter 7

Appendix

7.1 List of publications and conference contributions

Manuscripts:

- S. Mariotti, K. Jäger, M. Diederich, M.S. Härtel, B. Li, K. Sveinbjörnsson, S. Kajari-schröder, R. Peibst, S. Albrecht, L. Korte, T. Wietler.
  "**Monolithic Perovskite / Silicon Tandem Solar Cells Fabricated Using Industrial p-Type Polycrystalline Silicon on Oxide / Passivated Emitter and Rear Cell Silicon Bottom Cell Technology**".
  Solar RRL 4, 2101066 (2022). DOI: 10.1002/SOLR.202101066

- M. Härtel, B. Li, S. Mariotti, P. Wagner, F. Ruske, S. Albrecht, B. Szyszka.
  "**Reducing sputter damage-induced recombination losses during deposition of the transparent front-electrode for monolithic perovskite/silicon tandem solar cells**".
  Solar Energy Materials and Solar Cells, pending publication.

Poster conference contributions:

- M. Härtel, E. Köhnen, R. Muydinov, S. Albrecht, B. Szyszka.
  "**Impact of Sputter-Damage on Semitransparent Perovskite Devices for Application in Tandem Solar Cells**".

E-MRS - European Materials Research Society
Nice, France (2019)

- M. Härtel, B. Li, K. Sveinbjörnsson, S. Albrecht, B. Szyszka.
"**Sputtered indium zinc oxide top electrodes for high efficiency perovskite/silicon tandem solar cells without buffer layer**".
1st International tandemPV Workshop
Berlin, Germany (2021)

- M. Härtel, B. Li, P. Wagner, S. Albrecht, B. Szyszka.
"**Highly Efficient Monolithic Perovskite/Silicon Tandem Solar Cells Without Atomic Layer Deposited Buffer Layer By Damage-Free Sputter Deposition**"*.
International tandemPV Workshop
Freiburg, Germany (2022)
*Awarded the Poster Prize

7.2 List of symbols and abbreviations

Abbreviations

2-PACz - [2-(9H-carbazol-9-yl)ethyl]phosphonic acid
2T - two-terminal
4T - four-terminal
a-Si:H - Hydrogenated amorphous silicon
AFM - Atomic force microscopy
Ag - Silver
ALD - Atomic layer deposition
AM0 - Air mass outside the atmosphere
AM1.5G - Air mass 1.5G
AZO - Aluminum-doped zinc oxide
BCP - Bathocuproine
Br - Bromine
C_{60} - Buckminsterfullerene
c-Si - Crystalline silicon
CBM - Conduction band minimum
CELIV - Charge extraction by linearly increasing voltage
CIGS - Copper indium gallium selenide
CNL - Charge neutrality level
Cs - Caesium
CTL - Charge transport layer
DC - Direct current
DMF - dimethylformamide
DMSO - dimethyl sulfoxide
EDS - Energy dispersive X-ray spectroscopy
EQE - External quantum efficiency
ETL - Electron transport layer
FAI - Formamidinium iodide
FF - Fill factor
FLA - Flash lamp annealing
FOM - Figure of merit
FTO - Flourine doped tin oxide
FZ - Float zone
GISAXS - Grazing incidence small-angle x-ray scattering
GIWAXS - Grazing incidence wide-angle x-ray scattering
GFS - Gas flow sputtering
HTL - Hole transport layer
I - Iodine
I_2O_3 - Indium oxide

IO - Indium oxide
IO:H - Hydrogen-doped indium oxide
IQE - Internal quantum efficiency
IS - Impedance spectroscopy
ITO - Indium tin oxide
IZO - Indium zinc oxide
J-V - Current density-voltage
LED - Light-emitting diode
LFTS - Linear facing target sputtering
LiF - Lithium fluoride
MABr - Methylammonium bromide
MAPbBr- Methylammonium lead bromide
Me-4PACz - [4-(3,6-dimethyl-9H-carbazol-9-yl)butyl]phosphonic acid
MgF_2 - Magnesium fluoride
MoO_3 - Molybdenum trioxide
MPP - Maximum power point
$NH_2CHNH_2^+$ - Formamidinium NIR - Near-infrared
NiO_x - Nickel oxide
O^- - Negatively charged oxygen ions
O_2 - Oxygen
OCVD - Open-circuit voltage decay
Pb - Lead
PbI_2 - Lead iodide
PCBM - [6,6]-phenyl-C61-butyric acid methyl ester
PCE - Power conversion efficiency
PEDOT:PSS - Poly polystyrene sulfonate
PEIE - Polyethyleneimine ethoxylated
PL - Photoluminescence
PLD - Pulsed laser deposition
PSC - Perovskite solar cell
PTAA - Polytriarylamine
RF - Radio frequency
RFMS - Radio frequency magnetron sputtering
RPD - Rapid plasma deposition
SAM - Self-assembled monolayer
SDD - sample-detector distance
SE - secondary electrons
SEM - Scanning electron microscopy
SHJ - Silicon heterojunction
Si - Silicon

SnO_2 - Tin oxide
spiro-OMeTAD - 2,2',7,7'-tetrakis(N,N-di-p-methoxyphenylamine)-9,9'-spirobifluoren
SPV - Surface photovoltage
SRH - Shockley-Read-Hall
SQ - Shockley-Queisser
TCO - Transparent conductive oxide
TiO_2 - Titanium dioxide
TPC - Transient photocurrent
UPS - Ultraviolet photoelectron spectroscopy
UV - Ultraviolet
UV-Vis-NIR - Ultraviolet–visible-near infrared
VBM - Valence band maximum
WF - Work function
XRD - X-ray diffraction
ZnO - Zinc oxide

Symbols

α - Absorption coefficient
A - Absorption
C - Capacitance
CE - Charge extraction
C_{geom} - geometric capacitance
ΔE_{BM} - Burstein-Moss shift
d - Thickness
D - cluster center-to-center distance
D_n - Diffusion coefficient
η - solar cell efficiency
ϵ_0 - Vacuum permittivity
ϵ_x - Static dielectric constant
e - Elementary charge 1.60217662×10^{-19} C
E - Electric field
E_0 - Vacuum level energy
EA - Electron affinity
E_{CB} - Conduction band energy
E_{CNL} - Charge neutrality level energy
E_F - Fermi level energy
E_g - Optical band gap
E_{ph} - Photon energy
E_U - Urbach energy
E_{VB} - Valence band energy
FF - Fill factor
h - Planck constant 6.62607004×10^{-34} $m^2 \cdot kg \cdot s^{-1}$
I - Light intensity
I_{SM} - Ionization potential of a semiconductor
j(t) - Transient current density
j_0 - Dark saturation current density
J - Current density
J_{MPP} - Maximum power point current density
J_{ph} - Photo current density
J_{SC} - Short-circuit current density
k - Boltzmann constant $1.38\cdot10^{-23}$ $m^2 \cdot kg \cdot s^{-2} \cdot K^{-1}$
κ - Extinction coefficient
λ - Wavelength
$\lambda_{1,2}$ - Mean free path langth
L_n - Diffusion length

μ - Carrier mobility
m_e^* - Effective electron mass
ν - Photon frequency
N_e - Charge carrier density
n - Principal quantum number
n - Refractive index
n_2 - Number of gas particles per unit volume
ν - Photon frequency
n_{id} - Ideality factor
Φ_0 - Charge neutrality level height
Φ_E - Work function
Φ_B - Schottky-barrier height
Φ_{ph} - Photon flux
p - gas pressure
PCE - Power conversion efficiency
P_d - Power density
P_{in} - Incident irradiation power density
PLQY - Photoluminescence quantum yield
q - Unit charge
QFLS - Quasi-Fermi level splitting
$r(O_2)$ - Oxygen ratio
ρ - Specific resistivity
r_0^* - Effective Bohr radius
$r(O_2)$ - Oxygen content in percent / oxygen flow ratio
r_x - A particles spherical radius
R - Reflection
R - Recombination rate
r - cluster radii
R_{par} - Parallel/shunt resistance
R_{ser} - Series resistance
R_{sq} - Sheet resistance
σ - Conductivity
$\sigma_{1,2}$ - Effective collision or scattering cross-section
T - Transmission
T - Temperature
T_{ann} - Annealing temperature
τ - Time constant
τ_n - Charge carrier lifetime
T_{avg} - Average transmittance
V - Voltage

V_{MPP} - Maximum power point voltage
V_O^{++} - Doubly charged oxygen vacancy
V_{OC} - Open-circuit voltage
ω_p - Plasma frequency
WF - Work function

Acknowledgments

"While we might feel small, separate, and all alone,
our people have never been more tightly tethered.
The question isn't if we will weather this unknown,
but how we will weather the unknown together."

Amanda Gorman, "*The Miracle of Morning*", April 2020.

In her poem "The Miracle of Morning," Amanda Gorman referred to the great challenges we faced and are still facing as a human race during the Corona pandemic. She describes how this challenge has brought us closer together and asks not if we will get through this time but how we will get through it together. As I reflect on the past five years, both the pandemic and the ups and downs of my doctoral research have been very challenging for me. The sentiment expressed in the above quote by Amanda Gorman perfectly captures how I have felt during this time. It has connected me with many people along the way - in spirit, struggling, ambition, cooperation, and also in joy. Together with my colleagues, I "weathered the unknown". Therefore, I would like to take this opportunity to thank all the people I have met along the way who have contributed in their own way to the success of my work.

My deepest gratitude goes to Bernd Szyszka and Steve Albrecht, who made my research possible and supported me scientifically over the time. They have always given me valuable input, reviewed and corrected my scientific texts, and motivated me to try new approaches. Furthermore, I am also highly grateful to Monica Morales-Masis for agreeing to evaluate my thesis. We met at conferences and had wonderful scientific exchanges. I would also like to thank Bernd Rech for chairing my defense and for the many encouraging words throughout the years.

Additionally, I want to thank Lars Korte for the scientific interaction, which has always helped me fill my knowledge gaps, and Florian Ruske for his tremendously helpful support in reading my dissertation and providing measurements, data, and input for my ongoing publication.

Without the help of many great individuals, several of my experiments and simulations would not have been possible. These include Bor Li, Silvia Mariotti, Jiahuan Zhang, Amran Al-Ashouri, Philipp Wagner, Fengjiu Yang, Philipp Tockhorn, Kari Sveinbjörnsson, Ke Xu, Bharath Vinoth Kumar, Bilgrim Seibertz, Manuel Hartig, Carola Klimm, and Klaus Jäger. I am incredibly grateful to these people for their valuable contributions to my results.

Additionally, I am immensely grateful to Stephan Roth and Matthias Schwartzkopf for enabling the measurements at DESY and to Peter Müller-Buschbaum and his group for

their assistance in coordinating and accompanying the measurements.
My experiments relied heavily on the equipment's quality and functionality. Without the active technical support of Carola Ferber, Thomas Lußky, Martin Muske, Tobias Hänel, Hagen Heinz, Monika Gabernig, Mona Wittig, and Kerstin Jacob, I would have been lost.
I am thankful for the wonderful work environments I experienced at TU and HZB due to the fantastic ever-growing teams I was a part of. I have the utmost regard for Marion Krusche because she has consistently assisted me with administrative problems and practically everything.
I would also like to point out the wonderful time I had as a doctoral representative at HZB, where I had the pleasure to work with wonderful people: Daniel, Jakob, Felix, Sasha, Nina, Raphael, Radu, Vladimir, Hans, Ivona, Markus, Patrick, Jenni, and Ke.
I acknowledge the German Federal Ministry for Education and Research (BMBF), which funded the Young Investigator Group Perovskite Tandem Solar Cells within the program "Materialforschung für die Energiewende" (grant no. 03SF0540), the German Federal Ministry for Economic Affairs and Energy (BMWi) ("PersiST," grant no. 0324037C), and the Helmholtz Association through the HySPRINT innovation lab project, for funding my work.
Thank you so much to everyone I met while doing my Ph.D., whom I consider close friends, and who contributed to making the experience even more memorable. The "Corona Döner" gang Silvia, Jorge, Manuel, Florian and Jeronimo, my girls Ivona, Nina, Maryam and Sonal, and many individual people, Lucas, Erika, Bor, Jiahuan, Ke, Stefan, Josefa, Fangfang, Nivin, Bharath, Bilgrim, Alex, Sid, Moni and many more.
And finally, I would like to thank my partner Vlad for his patience and resilience in "times of crisis," of which I had quite a few during the course of my Ph.D. He often tried to build me up after hard days with footbaths and popcorn. I don't know how else I would have coped with all the stress. Moreover, I would like to thank my mother for her tremendous mental support and my cats, Mao and Mokka, who have always calmed me down just by their existence.

Thank you.